NITROGEN MONOXIDE STORAGE AND RELEASE PROPERTIES OF LOCAL NATURAL ZEOLITE FOR BIOLOGICAL APPLICATIONS

A Thesis Submitted to
the Graduate School of Engineering and Sciences of
İzmir Institute of Technology
in Partial Fulfillment of the Requirements for the Degree of

DOCTOR OF PHILOSOPHY

in Chemical Engineering

by
Güler NARİN

June 2009
İZMİR

We approve the thesis of **Güler NARİN**

Prof. Semra ÜLKÜ
Supervisor

Prof. Serdar ÖZÇELİK
Co-Supervisor

Prof. Devrim BALKÖSE
Committee Member

Prof. Hayrettin YÜCEL
Committee Member

Assoc. Prof. Fehime ÖZKAN
Committee Member

Assoc. Prof. Moghtada MOBEDİ
Committee Member

30 June 2009

Prof. Devrim BALKÖSE
Head of the Chemical Engineering Department

Prof. Hasan BÖKE
Dean of the Graduate School of Engineering and Sciences

ACKNOWLEDGEMENTS

I would like to express my sincere gratitude to my adviser Dr. Semra Ülkü for her guidance, constant support and continuous encouragement throughout this research. I would also like to thank to commitee members Dr. Hayrettin Yücel, Dr. Serdar Özçelik, Dr. Fehime Özkan and Dr. Moghtada Mobedi for their valuable discussions and encouragements. I would like to express my special appreciation to Dr. Devrim Balköse for her valuable discussions. I would like to thank Dr. Erol Şeker for his support in the research. I would also like to thank to Dr. Hürriyet Polat for her help in the particle size analysis in the Faculty of Science.

This research was financially supported by Turkish Republic Prime Ministry State Planning Organization (DPT-2006 K120690, Determination of Effects of Zeolite on Health on Cellular and Molecular Level).

I would like to extend my appreciation to the zeolite group members, especially to Çisem Bulut Albayrak for their friendship, help and discussions in accomplishing the antibacterial and bactericidal tests. I would also like to thank my lab-mate Hasan Demir for his patience and help.

I would also like to express my appreciation to all my friends for their friendship, helps and encouragements. In separate, my dedication goes to my parents for their constant support and encouragements throughout all my school years.

ABSTRACT

NITROGEN MONOXIDE STORAGE AND RELEASE PROPERTIES OF LOCAL NATURAL ZEOLITE FOR BIOLOGICAL APPLICATIONS

In this thesis, nitrogen monoxide (nitric oxide, NO) adsorption, storage and release properties of the local clinoptilolite-rich natural zeolite and its modified forms were investigated. The zeolite particles (75-150 μm, 150-250 μm) were prepared through treatment of the natural zeolite with NaCl and consecutively with aqueous metal (Co^{2+}, Ag^{+}, Cu^{2+}, Fe^{3+}) salt solutions under different conditions. The prepared zeolites were characterized in terms of particle size and morphology, density, mineral and elemental composition, dehydration behavior, porosity, surface area, and infrared spectroscopic characteristics. The total adsorption capacities of the zeolites for NO were calculated from the breakthrough curves obtained at 30 ^{o}C on a dynamic adsorption system and found to be in the range of 5.5-8.5 mmol/g. NO was adsorbed in the zeolites reversibly and irreversibly. The total adsorption capacity was mainly contributed from the irreversible adsorption. The irreversible adsorption capacity was related to the type and amount of metal cation in the zeolite. The temperature-programmed desorption (TPD) profiles provided information about the desorption kinetics of the NO species formed on the zeolite surface upon the adsorption. The bands detected in the DRIFTS spectra upon admission of NO were assigned to reversibly and irreversibly adsorbed NO species. The unmodified and iron-sorbed zeolites gained antibacterial activity against *E. coli* after NO loading. The unmodified zeolite also exhibited antibacterial activity against *B. subtilis* after NO loading. The NO-loaded unmodified zeolite also exhibited complete bactericidal activity upon contact with both bacteria cells. The unmodified and copper-sorbed zeolites exhibited similar NO release kinetics.

ÖZET

BİYOLOJİK UYGULAMALAR İÇİN YEREL DOĞAL ZEOLİTİN AZOT MONOKSİT DEPOLAMA VE SALMA ÖZELLİKLERİ

Bu tezde, klinoptilolit bakımından zengin yerel doğal zeolitin ve değiştirilmiş biçimlerinin azot monoksit (azot oksit, NO) gazını adsorplama, depolama ve salma özellikleri incelendi. Zeolit tanecikleri (75-150 μm, 150-250 μm), doğal zeolitin NaCl ve ardından metal (Co^{2+}, Ag^{+}, Cu^{2+}, Fe^{3+}) tuzlarının sulu çözeltileriyle işlenmesi yoluyla hazırlandı. Hazırlanan zeolitler parçacık boyut ve morfoloji, yoğunluk, mineral ve kimyasal bileşimi, su kaybetme davranışı, gözeneklilik, yüzey alanı ve kızıl ötesi spektrometre özellikleri açısından karakterize edildi. Zeolitlerin toplam NO adsorplama kapasiteleri dinamik adsorpsiyon sisteminde 30 ^{o}C'de elde edilen adsorpsiyon kinetik eğrilerinden hesaplandı ve 5.5-8.5 mmol/g aralığında bulundu. NO gazı zeolitlere tersinir ve tersinir olmayan biçimde adsorplandı. Toplam adsorplama kapasitesinin büyük bölümünü, tersinir olmayan biçimde adsorplanan miktar oluşturdu. Tersinir olmayan biçimde adsorplama kapasitesi zeolitin içerdiği metal katyonların türüne ve miktarına bağlı olarak değişti. Sıcaklık-kontrollü desorpsiyon (TPD) profilleri NO gazının zeolit yüzeyine adsorplanması sonucu oluşan NO bileşiklerinin desorplanma kinetikleri hakkında bilgi verdi. DRIFTS spektrumlarında NO gazının değişik basınçlarda adsorplanması sırasında gözlenen bantlar, tersinir ve tersinir olmayan biçimde adsorplanan NO bileşikleriyle açıklandı. Modifiye edilmemiş ve demir-sorplanmış zeolitler NO yüklenikten sonra *E. coli*'ye karşı antibakteriyel aktivite gösterdiler. Modifiye edilmemiş zeolit NO yüklendikten sonra *B. subtilis*'e karşı da antibakteriyel etki gösterdi. NO yüklenmiş bu zeolit her iki bakteriye karşı bakterisidal etki gösterdi. Modifiye edilmemiş ve bakır-sorplanmış zeolitler benzer NO salım kinetiği sergiledi.

TABLE OF CONTENTS

ABSTRACT iv
ÖZET v
TABLE OF CONTENTS vi
LIST OF FIGURES ix
LIST OF TABLES xv
LIST OF SYMBOLS xviii

CHAPTER 1.INTRODUCTION 1
1.1. Biochemistry of Nitric Oxide 2
1.2. Therapeutic Importance of Nitric Oxide 4
1.3. Adsorption 8
1.4. Clinoptilolite 10
1.5. Objective of the Study 12

CHAPTER 2. LITERATURE SURVEY 14
2.1. Adsorption in Microporous Adsorbents 14
2.2. Studies on NO Adsorption in Microporous Adsorbents 16
2.3. Studies on NO Adsorption in Zeolites 24
2.4. Studies on Supercritical Gas Adsorption in Natural Zeolites 37
2.5. Fourier Transform Infrared (FTIR) Spectroscopy Studies on NO Adsorption 39
2.6. Studies on Health Applications of Zeolites 48

CHAPTER 3. THEORY 56
3.1. Adsorption in Micropores 56
3.2. Dynamics of Adsorption in Packed Columns 57
3.3. Mass Transfer in Packed Column 60
3.3.1. Diffusion through External Film 60
3.3.2. Diffusion in Macropores 63
3.3.3. Diffusion in Micropores 68
3.3.5. Relative Importance of Micropore and Macropore Mass Transfer Resistances 71
3.4. Axial Dispersion 72
3.5. Pressure Drop 83

CHAPTER 4. MATERIALS AND METHODS 85
4.1. Preparation of Adsorbents 85
4.1.1. Preparation of Zeolite with High Clinoptilolite Content 85
4.1.2. Preparation of the Metal-Sorbed Zeolites 87
4.2. Characterization of Adsorbents 89
4.2.1. Particle Size Distribution 89
4.2.2. Determination of Density, Volume and Porosity 89
4.2.3. X-Ray Powder Diffraction 94
4.2.4. Elemental Analysis 96
4.2.5. Zeta-potential Measurements 97
4.2.6. Scanning Electron Microscopy–Back Scattered Electron-Energy Dispersive X-Ray (SEM-BSE-EDX) 97
4.2.7. Textural Properties 98
4.2.8. Thermogravimetric Analysis (TGA) 98
4.2.9. Infrared Spectroscopy 98
4.3. NO Adsorption, Desorption and Temperature - Programmed Desorption 99
4.3.1. Dynamic Adsorption Studies 99
4.3.2. Diffuse Reflectance Infrared Spectroscopy (DRIFTS) 103
4.4. NO Loading 105
4.5. NO Release 106
4.5.1. Antibacterial Properties of the NO-Loaded Zeolites 106
4.5.2. Bactericidal Properties of the NO-Loaded Zeolites 107
4.5.3. NO Release in PBS 108
4.5.4. NO Release in Deionized Water 109

CHAPTER 5. RESULTS AND DISCUSSION 110
5.1. Preparation of Zeolite with High Clinoptilolite Content 110
5.2. Characterization of the Zeolites 115
5.2.1. Particle Size Distribution 116
5.2.2. Determination of Density, Volume and Porosity 118
5.2.3. X-Ray Powder Diffraction 123
5.2.4. Elemental Analysis 128
5.2.4.1. Interaction of Na-Clin with Deionized Water 132
5.2.4.2. Metal Sorption - Solid Phase 138
5.2.4.3. Metal Sorption - Aqueous Phase 142

5.2.5. Zeta-potential Measurements 147
5.2.6. Scanning Electron Microscopy–Back Scattered Electron-Energy Dispersive X-Ray (SEM-BSE-EDX) 148
5.2.7. Textural Properties 158
5.2.8. Thermogravimetric Analysis (TGA) 181
5.2.9. Infrared Spectroscopy 186
5.3. NO Adsorption-Desorption-Temperature Programmed Desorption 193
5.3.1. Effect of NO Flow Rate on NO Adsorption 202
5.3.2. Effect of Zeolite Particle Size on NO Adsorption 205
5.3.3. Effect of Activation Period on NO Adsorption 207
5.3.4. Effect of Adsorption Temperature on NO Adsorption 209
5.3.5. Effect of Clinoptilolite Content of the Zeolite on NO Adsorption 211
5.3.6. Effect of NO Adsorption Period on NO Adsorption 213
5.4. Temperature-Programmed Desorption 230
5.5. Diffuse Reflectance Infrared Spectroscopy (DRIFTS) 233
5.6. NO Release 247
5.6.1. Antibacterial Properties of the NO-Loaded Zeolites 247
5.6.2. Bactericidal Activity Test 253
5.6.3. NO Release in PBS 255
5.6.4. NO Release in Deionized Water 257
5.6.5. Mathematical Modeling of NO Release 261

CHAPTER 6. CONCLUSION 268

CHAPTER 7. RECOMMENDATIONS FOR FUTURE STUDY 277

REFERENCES 279

APPENDICES
APPENDIX A. ANALYSIS OF THE ADSORPTION SYSTEM 308
APPENDIX B. CHANGES IN COLOR OF ZEOLITES 316

LIST OF FIGURES

Figure **Page**

Figure 1.1. Synthesis of NO in vivo. 3
Figure 1.2. Multifaceted biological effects of NO..... 3
Figure 1.3. Orientation of clinoptilolite channel axes. 9
Figure 1.4. Structure of clinoptilolite through c-axis and the preferential sites of the charge-balancing cations. 10
Figure 2.1. Schematic diagram of the NO micropore filling on α-FeOOH-dispersed activated carbon fiber. 16
Figure 2.2. The adsorption isotherms of NO on Fe-ACF at different temperatures. 20
Figure 2.3. The reduced adsorption isotherm of NO on Fe-ACF 21
Figure 2.4. Schematic diagram of the PSA apparatus. 24
Figure 2.5. Breakthrough and elution curves of NO over Cu-MFI(23.3)-60. 26
Figure 2.6. Correlation between the adsorbed NO amounts and the Al contents in copper ion-exchanged zeolites..... 27
Figure 2.7. Dependence of the amount of reversible adsorption of NO on the exchange level of copper ion in MFI zeolite..... 28
Figure 2.8. N-N and N-O stretching modes of surface N_xO_y species..... 46
Figure 2.9. Adsorption and desorption isotherms of NO in Co-exchanged zeolite A at 25 ^oC. 50
Figure 2.10. NO release profiles for NO-loaded Co-exchanged zeolite A.....51
Figure 2.11. NO release profiles of NO-loaded metal-exchanged zeolite-A 52
Figure 2.12. Integrated profiles of NO releasing from zeolites LTA and FAU..... 53
Figure 3.1. Typical adsorption and desorption breakthrough curves 57
Figure 3.2. Comparison of correlations for external film mass transfer coefficients. 61
Figure 3.3. Summary of literature data of axial dispersion of gases in beds packed with fine particles.. 74

Figure 3.4. Variation of limiting Péclet number (Pe_∞) with particle size for flow through beds.. 75
Figure 3.5. Representation of the agglomeration model. 76
Figure 3.6. Dependence of the agglomerate diameter of the particle diameter. 76
Figure 3.7. Effect of velocity on Péclet number. 79
Figure 4.1. Experimental set-up used in the NO adsorption, desorption and temperature-programmed desorption studies. 100
Figure 4.2. Experimental set-up for the diffuse reflectance infrared spectroscopy 104
Figure 5.1. X-ray powder diffractograms of the clinoptilolite reference (Idaho) and the separated fractions through the purification study. 110
Figure 5.2. Calibration curves prepared for the quantitative mineralogical analysis: a, for the RIR method; b, for the Nakamura's method. 112
Figure 5.3. SEM micrographs of the mineral phases separated during the purification process, ... 113
Figure 5.4. X-ray powder diffractograms of the purified clinoptilolite before and after thermal treatment at 450 ^{o}C for 16 hours (*H* stands for the thermally treated sample). 114
Figure 5.5. a) TG and D-TG curves; b) DTA curves for ClinRich 115
Figure 5.6. Particle size distributions of the zeolites: a, particles used as adsorbent in the NO adsorption studies; b, powders used in the preparation of the pellets. 116
Figure 5.7. XRD diffractograms of the reference clinoptilolite (Idaho) and Washed. 122
Figure 5.8. X-ray diffractograms of the zeolite samples. 123
Figure 5.9. XRD diffractograms for the metal sorbed zeolites before and after the activation. 125
Figure 5.10. X-ray diffractograms of the particles prepared by pelletization.. 127
Figure 5.11. Relationship between the real exchange capacity and clinoptilolite content of clinoptilolite-containing zeolites 131

Figure 5.12. Change in concentrations of H^+ and exchangeable cations in the aqueous phase during interaction of Na-Clin with water. 134
Figure 5.13. X-ray powder diffractograms of Na-Clin. 138
Figure 5.14. Change in concentrations of exchangeable and metal cations in the solid phase during interaction of Na-Clin with metal salt solutions. 140
Figure 5.15. Change in concentrations of H^+, exchangeable and metal cations in the aqueous phase during interaction of Na-Clin with metal salt solutions. 143
Figure 5.16. Dependence of the zeta potential of Na-Clin on the solution acidity. 148
Figure 5.17. Scanning electron micrographs of Washed and Na-Clin particles. 149
Figure 5.18. SEM micrographs of ClinRich-Kaolin and WGround-Kaolin particles. 149
Figure 5.19. SEM and BSE micrographs of the zeolite samples. 151
Figure 5.20. N_2 adsorption and desorption isotherms of the zeolites (-196 ^oC). 157
Figure 5.21. BET plots from the N_2 adsorption data. 160
Figure 5.22. Langmuir plots for the N_2 adsorption data 163
Figure 5.23. CO_2 adsorption isotherms of the zeolites (30 ^oC). 165
Figure 5.24. Langmuir model plots of the CO_2 adsorption data. 167
Figure 5.25. BET plots for the CO_2 adsorption. 169
Figure 5.26. D-R plots for CO_2 adsorption. 171
Figure 5.27. CO_2 adsorption isotherms of the ClinRich-Kaolin, WGround-Kaolin and pure kaolin 174
Figure 5.28. Mesopore size distributions of the zeolites. 176
Figure 5.29. Pore size distributions of the zeolites in the micropore range 178
Figure 5.30. Thermal gravimetric curves of the zeolites 180
Figure 5.31. Relationship between the integrated weight loss and the cation content of the zeolites. 181
Figure 5.32. Derivative thermal gravimetric curves of the zeolites. 183
Figure 5.33. Transmittance spectra of the zeolites. 184

Figure 5.34. Transmittance spectra of the zeolites after NO adsorption and helium purging. 189
Figure 5.35. Transmittance spectra of the zeolites after thermal treatment successive to NO adsorption. 190
Figure 5.36. Transmittance spectra of the NO-loaded zeolites after contacted with water at 37 ^{o}C..... 191
Figure 5.37. TCD signal change at the outlet of the empty column under helium flow and the temperature program. 192
Figure 5.38. Breakthrough curves for the helium adsorption and the subsequent NO adsorption on Washed zeolite. 193
Figure 5.39. Breakthrough curve obtained for Washed zeolite under helium flow and the temperature program. 194
Figure 5.40. NO adsorption breakthrough curves for empty and packed columns of the nonporous glass particles and Washed zeolite particles 195
Figure 5.41. Breakthrough curves for the successive adsorption of NO on Washed zeolite. 196
Figure 5.42. Temperature-programmed desorption profiles for the successive adsorption of NO on Washed zeolite. 197
Figure 5.43. Adsorption profiles for Washed and synthetic zeolites..... 198
Figure 5.44. TPD profiles for Washed and synthetic zeolites.. 199
Figure 5.45. Effect of feed flow rate on the adsorption of NO in Washed zeolite 200
Figure 5.46. Effect of NO feed flow rate on the NO adsorption breakthrough curve for Washed zeolite normalized with respect to the total amount of NO fed to the column per unit mass of the zeolite 201
Figure 5.47. Effect of particle size of Washed zeolite on the NO adsorption 202
Figure 5.48. Effect of particle size of Washed zeolite on the NO adsorption breakthrough curve normalized with respect to the total amount of NO fed to the column per unit mass of the zeolite. 203

Figure 5.49. Effect of activation period on the NO adsorption by Washed zeolite. 205
Figure 5.50. Effect of temperature on the NO adsorption breakthrough curve. 207
Figure 5.51. Total, reversibly and irreversibly adsorbed NO amounts as a function of adsorption temperature. 208
Figure 5.52. Effect of clinoptilolite content of the zeolite on its NO adsorption kinetics. 209
Figure 5.53. Effect of the clinoptilolite content on the TPD profiles. 210
Figure 5.54. Effect of NO adsorption time on the breakthrough curve. 211
Figure 5.55. Adsorption profiles for the zeolite samples with different cation contents. 213
Figure 5.56. NO desorption profiles of the zeolites. 215
Figure 5.57. NO adsorption and desorption profiles. 216
Figure 5.58. Relationship between the total, reversible and irreversible adsorption capacities of the zeolites. 220
Figure 5.59. Dependence of the NO adsorption capacity on the limiting micropore volumes. 223
Figure 5.60. Dependence of total, reversible and irreversible adsorption capacities on the cation contents of the zeolites. 224
Figure 5.61. Effect of ionic radius on the NO adsorption capacity of the zeolites. 225
Figure 5.62. Effect of cation type and amount on the NO adsorption capacity in terms of molecule NO adsorbed per cation atom. 226
Figure 5.63. Relationship between the NO adsorption capacity and the cobalt content of the zeolite. 227
Figure 5.64. Dependence of the total, reversible and irreversible NO adsorption capacities per cobalt cation on the zeolite cobalt content 228
Figure 5.65. TPD profiles for the zeolite samples with different cation content. 231
Figure 5.66. DRIFT spectra of Washed zeolite-KBr mixture 233
Figure 5.67. DRIFT spectra of Washed-KBr mixture during NO adsorption and successive evacuation at 30 ^{o}C 234

Figure 5.68. DRIFT spectra of Washed zeolite-KBr mixture obtained successive to the saturation with 1000 mbar NO. 237
Figure 5.69. DRIFT spectra collected after 1000 mbar NO adsorption at 30 ^{o}C 239
Figure 5.70. DRIFT spectra collected after evacuation at 30 ^{o}C successive to the 1000 mbar NO adsorption 240
Figure 5.71. Change in the area of 1358.8 cm^{-1} band upon NO adsorption and evacuation for Washed-KBr mixture and pure KBr. 241
Figure 5.72. Change in the intensity of 1358.8 cm^{-1} band as a function of NO pressure for pure KBr and for Washed-KBr mixture. 243
Figure 5.73. DRIFT spectra of Washed zeolite-KBr mixture collected during NO adsorption and evacuation. 244
Figure 5.74. DRIFT spectra of Washed zeolite-KBr mixture for adsorption of 1000 mbar NO. 246
Figure 5.75. Antibacterial activity of the metal-sorbed zeolites against *E. coli.* 248
Figure 5.76. Antibacterial activity of the zeolite samples before and after NO loading (NO-loaded), and after the thermal treatment (NO-Des). 249
Figure 5.77. Relationship between the irreversibly adsorbed NO and the antibacterial strength of the zeolites against *E. coli*. 250
Figure 5.78. Relationship between the intensity of the 1384.9 cm^{-1} band and the antibacterial strength of the zeolites against *E. coli*. 251
Figure 5.79. Antibacterial activity of Washed-NO against B. subtilis 252
Figure 5.80. Bactericidal activity of Washed-NO in PBS (pH 7.4, at 37 ^{o}C).. 254
Figure 5.81. Calibration curve obtained for the nitrite concentration measurements by the spectrophotometric Griess method 255
Figure 5.82. Cumulative NO release profiles for Washed, Washed-NO and Washed NO-Des samples in PBS (37 ^{o}C, pH 7.4). 256
Figure 5.83. Calibration curve obtained for the nitrite concentration measurements by the spectrophotometric Griess method 257
Figure 5.84. Cumulative NO release profile for Washed-NO in deionized water (37 ^{o}C). 258

Figure 5.85. Cumulative NO release profiles for freshly loaded Washed-NO and 0.05 M Cu-NO in deionized water (37 ^{o}C). 259
Figure 5.86. Cumulative NO release profiles for freshly NO loaded WGround-Kaolin-NO and ClinRich-Kaolin-NO particles in deionized water at 37 ^{o}C. 260
Figure 5.87. NO release profiles for Washed-NO in deionized water and in PBS at 37 ^{o}C. 261
Figure 5.88. NO release kinetics from Washed-NO in PBS fitted to the spherical particle model (short time region) 263
Figure 5.89. NO release kinetics from Washed-NO and 0.05 M Cu-NO samples in deionized water fitted to the spherical particle model 265
Figure A.1. SEM micrograph of the natural zeolite particles (75-150 μm) 311
Figure B.1. Changes in color of the zeolites upon metal sorption, NO loading and thermal treatment after NO loading 316

LIST OF TABLES

Table **Page**

Table 1.1. Physical adsorption and chemisorption. 8
Table 2.2. NO adsorption properties of various cation-exchanged MFI zeolites. 20
Table 2.3. Infrared absorption bands induced by adsorbing NO on zeolite. 40
Table 2.4. Infrared absorption bands produced by disproportionation reactions of NO on zeolites. 41
Table 2.5. Infrared spectra results of NO adsorbed on metal ion-exchanged zeolites. 44
Table 3.1. Empirical correlations for external mass transfer. 60
Table 4.1. Coding of the samples. 88
Table 4.2. Characteristics of the column and the adsorbents. 101
Table 5.1. Comparison of the methods applied for the determination of the clinoptilolite contents of the phases separated during purification study 111
Table 5.2. Properties of the adsorbates. 119
Table 5.3. Total pore volumes of the zeolites calculated based on the Gurvitsch Rule. 120
Table 5.4. Properties of adsorbate molecules used for calculation of the total pore volume. 120
Table 5.5. Total pore volumes of the zeolites calculated based on the Gurvitsch Rule 121
Table 5.6. Elemental compositions of the zeolites (oxide weight %). 129
Table 5.7. Elemental compositions of the clinoptilolite reference minerals and ClinRich (oxide weight %). 130
Table 5.8. Change in the aqueous phase cation concentrations during interaction of Na-Clin with deionized water (meq/g). 133

Table 5.9. Qualitative mineralogical analysis of Na-Clin and its acid-treated forms. 137
Table 5.10. Elemental compositions of the zeolites (meq/g zeolite). 139
Table 5.11. Ionic and hydrated radii, hydration enthalpy of the cations. 141
Table 5.12. Changes in the aqueous phase cation concentrations during the metal sorption (meq/g)..... 142
Table 5.13. Metal species present in the solution during metal sorption experiments..... 145
Table 5.14. Comparison of the bulk and surface elemental composition of the zeolites (by weight)..... 154
Table 5.15. BET model parameters from the N_2 adsorption data..... 161
Table 5.16. Langmuir model parameters from the N_2 adsorption data. 162
Table 5.17. Textural properties of the zeolites (CO_2 adsorption at 30 ^oC) 166
Table 5.18. CO_2 adsorption capacities of clinoptilolite-rich natural zeolites from different geographical origin at 100 mmHg. 166
Table 5.19. The Langmuir model constants for the CO_2 adsorption. 168
Table 5.20. BET model parameters for the CO_2 adsorption..... 170
Table 5.21. Dubinin-Radushkevich model parameters from CO_2 adsorption data..... 172
Table 5.22. Textural properties of the particles prepared by pelletization. 174
Table 5.23. Partial and integrated weight losses for the zeolites..... 181
Table 5.24. Temperatures corresponding to maximum rate of weight loss and the rate of weight losses for the zeolites..... 182
Table 5.25. Assignment of vibration bands for the natural zeolitic mineral. 185
Table 5.26. Equilibrium NO adsorption capacities of the zeolites 218
Table 5.27. Comparison of the NO adsorption capacity of Washed and the cobalt-sorbed natural zeolite with those reported for cobalt-exchanged zeolite A..... 219
Table 5.28. Total, reversible and irreversible adsorption capacities of the zeolites for NO..... 221
Table 5.29. Density estimations for the adsorbed NO..... 222
Table 5.30. Desorption temperatures and areas of the peaks in the TPD spectra..... 232
Table 5.31. Change in the area and the frequency of the 1358.8 cm^{-1} band. 241

Table 5.32. Change in the area and the frequency of the 1358.8 cm^{-1} band for pure KBr..... 242
Table 5.33. The diffusion coefficients calculated for the NO release from Washed-NO sample in PBS..... 264
Table 5.34. The diffusion coefficients calculated for the NO release from Washed-NO and 0.05 M Cu-NO samples in deionized water..... 264
Table 5.35. Color changes observed in the zeolites after different treatments..... 266
Table A.1. Reynolds and Schmidt numbers characterizing the adsorption system. 308
Table A.2. Effective macropore diffusion coefficients calculated using the diffusibility values estimated from different correlations (cm^2/s)..... 309
Table A.3. Sherwood numbers estimated using different correlations..... 310
Table A.4. External fluid film mass transfer coefficients, k_f (cm/s)..... 310
Table A.5. Biot numbers for mass transfer, *Bi*. 312
Table A.6. Axial dispersion coefficient, D_L (cm^2/s) (initial)..... 312
Table A.7. Axial dispersion coefficient, D_L (cm^2/s) (later period)..... 313
Table A.8. Péclet numbers for the column (initial). 314
Table A.9. Péclet numbers for the column (later period). 314
Table A.10. Geometrical criteria to avoid maldistribution of the flow. 314

LIST OF SYMBOLS

A	differential molar work of adsorption
a	affinity constant, Langmuir model parameter
a_u	total external area of particles per unit volume of bed
b	van der Waals co-volume, $b=RT_c8P_c$
C_o	inlet gas phase adsorbate concentration
C	outlet gas phase adsorbate concentration
C_s	adsorbate concentration at the particle surface
d_{aggl}	diameter of agglomerates
d_{column}	column internal diameter
d_p	average particle diameter
d_{eff}	effective diameter of the sorbed molecule
D_c	micropore diffusivity
D_p	effective macropore diffusivity
D_e	effective intraparticle diffusivity r
D_K	Knudsen diffusivity
D_P	effective macropore diffusivity
D	diffusivity in a straight cylindrical pore
D_m	molecular diffusion coefficient
D_s	surface diffusivity
D_{NO}	effective NO diffusion coefficient within particle in liquid
D_c/r_c^2	micropore diffusional time constant
D_P/R_p^2	macropore diffusional time constant
D_L	effective axial dispersion coefficient
E_o	characteristic energy of adsorption for the reference vapor
e	electric charge of the proton, 1.602×10^{-19} C
f	friction factor
ΔH_v	enthalpy of vaporization at the boiling point
ΔH_d	enthalpy of adsorption in the first layer
k_B	Boltzman constant
k_f	external mass transfer coefficient

k_1, k_2	NO release rate coefficients
k	overall mass transfer coefficient
k^*	tortuosity of a pore
K	adsorption equilibrium constant expressed in terms of total volume of particle
L	column length
L_p	total pore length
M	molecular weight
$m_{dryinair}$	mass of dry (dehydrated) solid in air
$m_{wetinair}$	mass of completely hydrated solid in water
$m_{wetinwater}$	mass of completely hydrated solid in air.
M_t	cumulative amount of NO released at time t
M_e	cumulative amount of NO released at equilibrium
n_1, n_2	amount of NO released per weight of adsorbent
P	pressure
P_o	saturated vapor pressure
P_o'	hypothetical saturated vapor pressure (of supercritical gas near the critical temperature)
P_c c	critical pressure of the adsorbate
P_r	reduced pressure, $P_r=P/P_c$
$P_o(NO)$	saturated NO vapor pressure at 30 ^oC in the micropores
P_{oq}	quasi-saturated vapor pressure
P/P_{oq}	quasi-relative pressure
q_{st}	isosteric heat of adsorption
$q_{st,\phi=1/e}$	isosteric heat of adsorption at fractional micropore filling of *1/e*
Δp	pressure drop across the length of the column
Q	volumetric flow rate of adsorbate fed to the column
q_o	equilibrium (saturation) capacity of the adsorbent
q^*	solid-phase adsorbate concentration in equilibrium with local fluid-phase adsorbate concentration
q	concentration of NO in zeolite
q_{rev}	reversibly adsorbed amount of adsorbate per weight of adsorbent
q_{irr}	irreversibly adsorbed amount of adsorbate per weight of adsorbent

q^*_{rev}	amount of reversibly and irreversibly adsorbed NO molecules per cation
q^*_{irr}	amount of reversibly and irreversibly adsorbed NO molecules per cation
$\bar{r}$	mean macropore radius
r_c	crystal radius
r_o	bond length
R	radial coordinate within the particle
R	gas constant
r_{chem}	rate of chemisorption
r_{dif}	rate of diffusion throughout microporous network of adsorbent
r_{ads}	rate of NO adsorption
S	bed crossectional area
S_w	adsorbent weight
S/L	solid-to-liquid ratio (mass of solid/volume of solution)
t_b	breakthrough time
t^*	saturation (exhaustion) time
T_c	critical temperature of the adsorbate
T_r	reduced temperature, $T_r=T/T_c$
v	interstitial velocity
u	superficial fluid velocity, $u=\varepsilon v$
W_L	limiting (inherent) micropore volume
$W_L(NO)$	volume of NO adsorbed at saturation
W/W_L	fractional filling
W_o	limiting micropore volume
W	volume of liquid adsorbate adsorbed
w	volume fraction of crystals in total solid material in particle,
V_{bed}	bed volume
V_c	volume of pores with diameter smaller than 0.7 nm
V_n	volume of pores with diameter smaller than 2 nm (narrowest micropores)
$V_n–V_c$	volume of supermicropore
V_l	saturation value for the amount sorbed expressed in number of molecules
V_{bulk}	bulk volume of the particle
V_{total}	total pore volume
V_{open}	open pore volume
V_{closed}	closed pore volume

$V_{skeletal}$	skeletal (true) volume
V_p	total pore volume per gram of dehydrated zeolite
V_f	total void fraction in the crystal
V	amount of adsorbate adsorbed at saturation
V_m	monolayer capacity
[asym]	asymmetric vibration
[sym]	symmetric vibration

Dimensionless Numbers:

Re	Reynolds number, $Re=v\varepsilon d_p\rho/\mu$
Sc	Schmidt number, $Sc=\mu/\rho D_m$
Bi	Biot number, $Bi=k_f R_p/3\varepsilon_p D_e$
Pe	particle-based Péclet number
Pe_m	Péclet number based on the molecular diffusion, $Pe_m=d_p v/D_m$
Pe	Péclet number based on the axial dispersion, $Pe=d_p v/D_L$
Pe_∞	limiting Pe as $Re\rightarrow\infty$
Pe_{bed}	Péclet number for the fixed bed

Greek Letters:

ρ_{water}	density of water at measurement temperature
ρ_{air}	density of air at 25 ^{o}C, 1 atm
ρ_{true}	true (skeletal) density of solid
$\rho_{particle}$	particle density including the volume of pores
ρ_{bulk}	bulk density of particle
ρ_f	framework density
ε	bed voidage
ε_p	particle porosity
ε_p'	particle porosity including closed pores
τ	bed tortuosity
τ_p	particle tortuosity
η_p	diffusibility, $\eta=\varepsilon_p/\tau_p$

σ_{12}	collision diameter of the diffusing molecules from the Lennard–Jones potential theory
α_m	parameter defining elative importance of external and internal mass transfer resistance
ζ	mechanical parameter representing ratio of the intraparticle and external film diffusion resistances
Φ_s	particle sphericity factor
Ψ	parameter defining relative importance of macropore and micropore diffusion resistances
γ_1	reciprocal of axial (bed) tortuosity factor, $\gamma_1=1/\tau$
γ_2	constant related with the geometry of the bed
β'	empirical constant, radial dispersion factor
χ	particle shape factor
	scale of dispersion
$\in_{12}$	energy of interaction
Ω	collision integral
λ	mean free path
ϕ	fractional micropore filling
β	affinity coefficient
2θ	X-ray diffraction angle
Q	quadrupole moment
μ	dipole moment
α	polarizability
λ	mean free path
σ_p	constriction factor t
ρ_c	critical density, $\rho_c=M/b$
α	thermal coefficient
ρ_b	density of liquid at normal boiling point
ρ^*	liquid density of the adsorbate adsorbed in the pores at the measurement temperature (corrected density)

CHAPTER 1

INTRODUCTION

Nitric oxide (nitrogen monoxide, NO) is one of the ten smallest molecules found in nature. It is a free-radical diatomic molecule and exists as a gas under atmospheric conditions. NO rapidly interacts with O_2 to yield a variety of nitrogen oxides; NO_2, N_2O_3, NO_2^-, NO_3^-. NO and its derivatives are atmospheric pollutants known as NO_x, which cause various serious diseases, such as carcinogenesis and asthma.

Ironically, in the late 1980s, NO was discovered to be one the smallest, lightest, and the first gas molecule to act as a biological messenger in mammals. This discovery eventually led to the Nobel Prize in medicine in 1998. The discoveries made in the 1980s showed that NO is synthesized by mammalian cells and acts as physiological messenger and cytotoxic agent. NO was first biologically characterized in 1987 as endothelial-derived relaxing factor and it was reported that it is synthesized by endothelial cells in blood vessels and diffuse to the adjacent smooth muscles to cause vasodilatation (Ignarro et al., 1987; Ignarro, 2000; Furchgott, 1988). Since these initial studies, there has been an explosion of researches showing that NO release endogenously (from endothelial cells, brain etc.) and from NO-donor materials (Bedioui and Villeneuve, 2003). Thus, a great number of studies on the NO molecule have been carried out in the field of biochemistry.

From the environmental perspective, catalytic methods for NO removal, such as catalytic decomposition and selective catalytic reduction with reducing agent are among the most interesting current topics in the field. Zeolite-based catalysts have been those most intensively investigated and some zeolite-based catalysts including transition metal cations exhibited high efficiency. Adsorption is the primary step in the catalytic reactions and therefore the elucidation of the adsorption characteristics is indispensable for understanding the catalytic reactions.

1.1. Biochemistry of Nitric Oxide

Nitric oxide is synthesized throughout the body by cells such as endothelial cells, macrophages, neutrophiles, fibroblasts, keratinocytes. NO is involved in a number of key physiological functions in the body such as blood pressure regulation (Kelm, 2003), neurotransmission (Yun et al., 1996), inhibition of platelet adhesion (Riddell and Owen, 1999), wound healing (Witte and Barbul, 2002), and nonspecific immune response to infection (Sasaki et al., 1998). This is why recent attention has been increasingly focused on possibilities of treating and preventing the NO-related metabolic disorders. Vascular endothelial cells continuously release NO at an estimated flux of approximately 1.0×10^{-10} mol/cm^{2}min (Vaughn et al., 1998; Radomski et al., 1987a,b). This endogenous NO supply diffuses into the lumen of blood vessels and into the smooth muscle cells that surround all arteries and plays an integral role in preventing platelet activation in healthy blood vessels and in maintaining normal blood pressure, respectively.

Nitric oxide is produced endogenously in the endothelium from L-arginine by the enzyme nitric oxide synthase (NOS). L-arginine and oxygen serve as substrates for NOS to produce nitric oxide and L-citrulline as shown in Figure 1.1. There are three isoforms of NOS: Type I (neuronal nitric oxide synthase, nNOS), type II (inducible nitric oxide synthase, iNOS), and type III (endothelium nitric oxide synthase, eNOS). Neuronal NOS (nNOS) and endothelial NOS (eNOS) enzymes are constitutively expressed in cells and synthesize NO in response to an increase in calcium or in some cases to calcium independent stimuli such as shear stress. The inducible NOS (iNOS) is constitutively expressed only in some tissues such as lung epithelium and is typically synthesized in response to inflammatory or pro-inflammatory mediators (Moncada et al., 1991; Cirino, 2003). The pathophysiology of a number of disorders have been associated with an altered level of NO or expression of these enzymes, i. e., nitric oxide synthases (NOS) (Bruch-Gerharz et al., 1998).

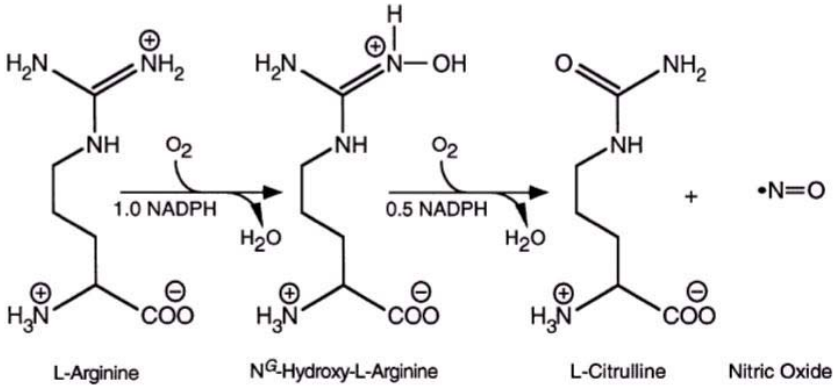

Figure 1.1. Synthesis of NO in vivo.
(Source: Andrew and Mayer, 1999)

NO is a rapidly diffusing, free radical gas with one unpaired electron exhibiting a diverse range of biological activity. Whether NO elicits physiological or pathophysiological responses is dependent on the concentrations of NO and the chemical composition of the biological environment. The physiological or pathophysiological functions of NO are summarized schematically in Figure 1.2.

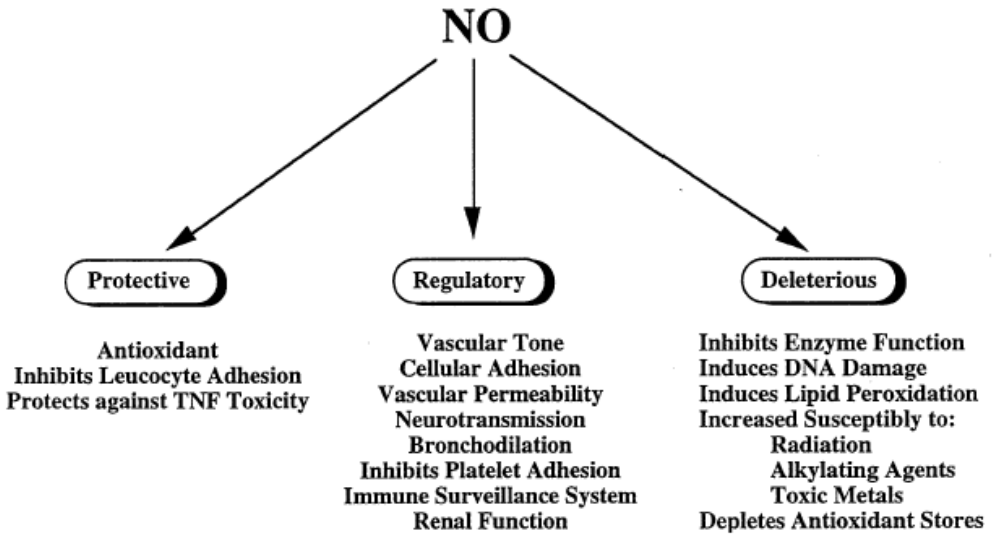

Figure 1.2. Multifaceted biological effects of NO.
(Source: Wink and Mitchell, 1998)

There are direct chemical reactions in which NO interacts directly with biological molecules. Such reactions are generally rapid, require low concentrations of NO and most likely account for the majority of physiological effects of NO. The most common direct reaction is between NO and heme-containing proteins. The reaction with the Hb-haem group is the main metabolic pathway for endogenous NO. Therefore Hb is a scavenger for NO and prevents it from reaching the tissue components (Mateo and de Artinano, 2000).

Indirect effects are derived from the reaction of NO with either superoxide or oxygen, which yields reactive nitrogen oxide species (RNOS). NO reacts with the superoxide anion to generate peroxynitrite at a rate that is limited only by its diffusion coefficient. Peroxynitrite is a selective oxidant and nitrating agent that interacts with various biological molecules, in that way damaging them. These effects are often associated with pathophysiological effect of NO (Mateo and de Artinano, 2000).

1.2. Therapeutic Importance of Nitric Oxide

Categorizing the chemical reactions of NO into direct or indirect effects allows for consideration of both the amount and duration of time NO is present in a specific environment. Direct effects occur at low NO concentrations (<1 mM) whereas indirect effects of NO involving the formation of RNOS become significant at higher local concentrations of NO (>1 mM). This behavior of NO carries a great therapeutic value that appropriate pharmacological treatment is developed to either promote NO production or inhibit it. Development of such treatments has been complicated by the fact that NO is involved in such a wide range of processes and that increases or decreases in NO levels might be therapeutically desirable depending on the type or stage of disease provides a considerable challenge for development of treatments.

The discovery of the bioregulatory roles of NO demands new methods for generating NO in a controlled manner to facilitate both an improved understanding of role of nitric oxide in physiology and the development of NO-associated therapies.

The NO release strategy may provide a solution to the long-lasting biocompatibility problems encountered when small chemical sensors are implanted in

vivo to monitor clinically important analytes such as oxygen, carbon dioxide, pH, electrolytes, glucose and lactate in a continuous, real-time manner. The erroneous analytical results have been often obtained when such devices are implanted in vivo. One major factor that has influenced the analytical performance of indwelling sensors is the biological response they exhibit when in contact with blood or tissue including thrombus formation on the sensor surface and inflammatory response. When these sensors contact with blood or tissue, proteins such as fibrinogen and von Willebrand Factor may adsorb onto the sensor surface providing sites for platelet adhesion. Platelet adhesion and activation can lead to thrombus formation on the surface of the device. Moreover, if the sensor contact with the blood vessel wall, the metabolism of the endothelial cells affect the flux of analyte to the sensor. Furthermore, vasoconstriction of the artery or vein around the sensor may occur. All these processes affect the performance of the sensor.

The therapeutic approach targeting promotion of endogenous NO is important particularly in the cardiovascular system. Since NO has a short half-life in vivo, the development of NO donors which have the capacity to release NO selectively with a prolonged half-life and with a reduced incidence of drug tolerance has supreme importance. Organic nitrates and S-nitrosothiols represent the important functional groups of many of the NO donors. The major limitation for the long-term use of NO-donors is the toxic effect on the gastrointestinal system. Preexisting compounds have been modified in order to exploit the beneficial effects of NO without the loss of pharmacological efficacy of the parent compound.

Moreover the data on the toxicological effects and biological role of NO collected through in vitro experiments performed using various NO delivery methods revealed that one of the major obstacles in such studies is to ascertain a direct and continuous delivery system for exposing various cells to exogenous nitric oxide. NO delivery by NO donors does not provide stable and consistent release rate, since the release rate can be affected by a variety of factors such as pH of the solution, light and nature of the aqueous medium. Also the residual donor compounds following the release of NO may cause toxicity especially in long-term exposures (Feelisch and Stamler, 1996). Moreover, NO produced by the stimulation of NOS enzymes can react intracellularly with other nitrogen species generated or oxidants within the cytoplasm, such as superoxide, to form other potentially damaging species like peroxynitrite (Kavdia et al., 1998).

As a consequence, more controlled and predictable way of delivering NO into aqueous solutions is required. Ghaffari and co-workers reported the design of a versatile gaseous NO (gNO) exposure chamber to test its effectiveness on various cells such as *Escherichia coli, Pseudomonas aeruginosa, Staphilococcus aureus* and human dermal fibroblasts to investigate the potential therapeutical role of exogenous nitric oxide gas as an antimicrobial agent as well as mediator in cutenous wound healing. In this study, gNO was supplied to the cells in both solid and aqueous media enclosed in the designed chamber. The design gNO exposure chamber was tested by comparing the growth of the bacterial strains as well as human skin fibroblasts in presence and absence of gNO with identical cells incubated in a conventional incubator. It was claimed that the gNO could be delivered in a controlled and reproducible manner for long-term exposure experiments using the designed exposure chamber. The kinetics of gNO uptake was characterized in the system by measuring the total NOx concentration in the solution, allowing for indirect estimation of gNO delivery. The device also allows continuous monitoring of several parameters such as concentrations of gNO, NO_2, O_2, temperature and humidity levels (Ghaffari et al., 2005).

There is currently particular interest in using NO delivery materials to prevent life-threatening complications associated with thrombosis formation at the surface of medical devices. The thrombogenic nature of these materials can cause serious complications and performance reduction (Nathan and Xie, 1994; Fleming et al., 1998; Sefton et al., 2000). As a result, systemic anticoagulants are almost always required clinically to reduce the risk of thrombus formation. However, the long-term use of these anticoagulants can also have adverse effects, especially an increased possibility of hemorrhage. Recent efforts have focused on coating the stents with drug eluting polymers (Regar et al., 2001; Gruberg et al., 2000; Frost et al., 2005). But the long-term effects of these non-natural, anti-cell proliferation agents are suspicious in terms of the structural integrity. Furthermore, polymeric materials were developed those mimicking endothelial cells and use of chemical surface moieties that suppress blood–material interactions (e.g., polymeric surfaces that exhibit decreased protein and cell adhesion) (Annich et al., 2000; Schoenfisch et al., 2000; Zhang et al., 2002; Feng and Chaikof, 2000; Bamford et al., 1992). It was reported that the molecules contributing to this non-thrombogenic and antiplatelet properties of the endothelial cells include NO, thrombomodulin, prostacyclin, and heparans (Colman, 1993; Makrides and Ryan, 1998). Therefore, if polymers can be prepared that can release and/or possess

immobilized forms of some of these species the surfaces are likely to be more thromboresistant. NO is well known as a potent anti-platelet agent and its continuous release from the surface of endothelial cells effectively prevents the adhesion/activation of platelets on normal blood vessel walls (Radomski et al., 1987a,b; Sneddon and Vane, 1988; Siney and Lewis, 1992). The NO releasing polymeric materials have had some success, but NO might be expected to be efficient if delivered at the appropriate rate for a sufficient duration. Another concern in the delivery of exogenous NO is the target specificity. For this purpose, materials that can store significant quantities of NO and then deliver it to specific sites in the body are under development.

The storage of a gas in solids is more advantageous than storing it in a tank at high pressure. The solid may have higher storage capacity and storage in solid eliminates the gas of high pressures. It is more advantageous in cases when the gas is required in small amounts. Adsorption in an adsorbent can be a strategy of storing gas. The porous adsorbents in which the gas is adsorbed through physical adsorption or chemical adsorption can be applied for this purpose.

1.3. Adsorption

These are two classes of adsorption, physical adsorption and chemisorption, which are distinguished on the nature of the surface forces (Table 1.1). In physical adsorption, when an adsorbate molecule contacts the surface of an adsorbent, it is subjected to various forces including the nonspecific forces (dispersion and repulsion, i.e. van der Waals forces) and electrostatic forces (polarization, field-dipole, field-quadrupole, adsorbate-adsorbate). The latter forces are significant only if the adsorbent has ionic structure such as zeolites. In chemisorption, the forces involved are much stronger and involve a considerable degree of transfer or sharing of the electrons. As a result, chemisorption is highly specific and the adsorption energies are generally greater than those for physical adsorption (Ruthven, 2006, Roque-Malherbe, 2000).

Table 1.1. Physical adsorption and chemisorption.
(Source: Ruthven, 2006)

Physical adsorption	Chemisorption
Low heat of adsorption (1.0 to 1.5 times latent heat of evaporation)	High heat of adsorption (>1.5 times latent heat of evaporation)
Nonspecific	Highly specific
Monolayer or multilayer	Monolayer only
No dissociation of adsorbed species	May involve dissociation
Only significant at relatively low temperatures	Possible over a wide range of temperatures
Rapid, nonactivated, reversible	Activated, may be slow and irreversible.
No electron transfer, although polarization of adsorbate may occur.	Electron transfer leading to bond formation between sorbate and surface.

The chemisorption of NO on transition-metal exchanged zeolites has been the subject of numerous studies. The highly dispersed cations in the microporous structure of zeolite having unsaturated coordination are the major cause of high activity of the zeolites. The NO coordination to the unsaturated metal cations in dehydrated zeolites involves electron transfer between them.

NO is an electron donor and acceptor and tends to form metal nitrosyl complexes in the transition metal-exchanged zeolites. The interaction of d-block transition metals with NO often involves a d-electron and/or an empty d-orbital. It was stated that the NO interacts with the cations in zeolites through the nitrogen atom to form either mononitrosyl or dinitrosyl complexes (Lunsford et al., 1978). The most common bonding mode of NO is the terminal linear type (M-NO) (M is the metal cation). In this type of bonding, the angle of the M-N-O group can vary from 160-180° and the NO group is considered as a 3-electron donor. Such complexes can be considered as derived from nitrosyl cation (NO^+). In another bonding mode of NO, the M-N-O group is characterized by an angle of 120-140^o, i.e. in a form of bent geometry. Such complexes can be considered as derived from nitroxyl anion (NO^-). The NO group can also bridge between metal centers through the nitrogen atom in a variety of geometries (Enemark and Feltham, 1974a; Feltham and Enemark, 1981). The NO group geometry is governed by the charge of NO group together with other parameters such as the coordination number, the coordination geometry and the nature of the highest occupied molecular orbital (Enermark and Feltham, 1974a,b).

Besides, since NO has an unpaired electron, it tends to be adsorbed as dimers. These dimmers can be regarded as adsorbed N_2O_2, since the existence of two coordinative vacancies is not needed for their formation (Hadjiivanov et al., 1999; Hadjiivanov, 2000). Even at room temperature, diamagnetic dimers $(NO)_2$ were shown to be formed and stabilized in the micropores of activated carbon fibers (Kaneko et al., 1987b).

1.4. Clinoptilolite

Clinoptilolite belongs to the heulandite group, with a three dimensional framework of silicon and aluminum tetrahedral. The theoretical composition of clinoptilolite is $(K_2, Na_2, Ca)_3[Al_6Si_{30}O_{72}] \cdot 24H_2O$, it can also contain some Mg^{2+} and Fe^{2+} ions. The content of non-tetrahedral cations (K^+, Na^+, Ca^{2+} and Mg^{2+}) as well as Si/Al ratio can change depending on the mineral (Breck, 1974). The total pore volume based on cm^3 H_2O/cm^3 crystal was reported as 34 % (Barrer, 1978). Clinoptilolite crystallizes in monoclinic C2/m group with the following unit cell parameters: a=17.62 Å, b=17.91 Å, c=7.39 Å and β=116.40° (Baerlocher et al., 2001; Gottardi and Galli, 1985; Joshi et al., 1997).

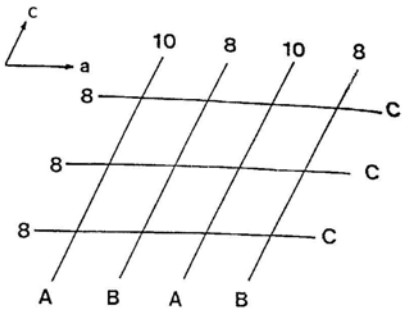

Figure 1.3. Orientation of clinoptilolite channel axes.
(Source: Ackley and Yang, 1991b)

The clinoptilolite channel system is shown in Figure 1.3. The channels of ten-membered (channel A) and eight-membered tetrahedral rings (channel B) are parallel to the c-axis. Another eight-membered ring channel (channel C) runs parallel to the a-axis giving rise to a two-dimensional channel system.

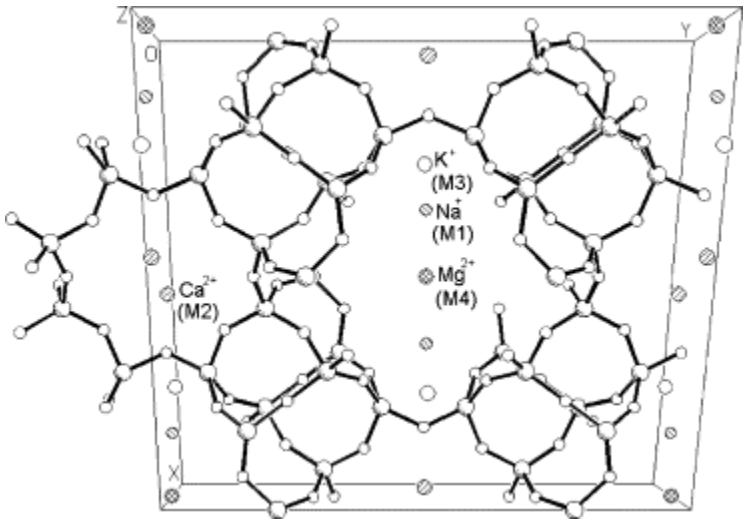

Figure 1.4. Structure of clinoptilolite through c-axis and the preferential sites of the charge-balancing cations. (Source: Koyama and Takeuchi, 1977)

The structure of clinoptilolite through c-axis and the preferential sites occupied by the charge-balancing cations are shown in Figure 1.4 (Koyama and Takeuchi, 1977). The clinoptilolite has four cationic sites (M1, M2, M3 and M4) where ion exchange occurs. Information on the channel orientation, dimensions and cation sites for clinoptilolite is given in Table 1.2.

Table 1.2. The orientation and dimensions of the channels, and cation sites in the channels. (Source: Ackley and Yang, 1991a, b)

Channel	Tetrahedral Ring Size/Channel Axis	Cation Site	Major Cations	Approximate Channel Dimensions (nm×nm)
A	10/c	M(1)	Na, Ca	0.72×0.44
B	8/c	M(2)	Ca, Na	0.47×0.41
C	8/a	M(3)	K	0.55×0.40
D	10/c	M(4)	Mg	0.72×0.44

The adsorption characteristics of zeolites are dependent upon their chemical and structural properties. The cation type, size, charge density, location and the extent to which it is exposed to the adsorbate molecules as well as the Si/Al ratio have a strong effect upon both adsorption capacity and selectivity. The Si/Al ratio of natural zeolites cannot be modified except by acid treatment to dealuminate the structure. The same Si/Al ratio does not dictate the same cation locations, since cation location can be affected by the Al ordering or distribution, thus resulting in different adsorption characteristics (Armbruster, 2001). The level of dehydration may also affect the adsorption properties. Dehydration and thermal treatment can result in migration of cations, thereby influencing cation location and pore openings (Ackley et al., 2003). Modifications induce structural and chemical changes, therefore adsorption and diffusion characteristics of the zeolite can be tailored for specific adsorption process (Munson, 1973; Breck, 1974; Ackley and Yang, 1991a,b; 1992).

1.5. Objective of the Study

Clinoptilolite has been studied for adsorption, separation and ion exchange applications in industrial scale. Furthermore in the recent review by Ackley and co-workers, natural zeolites were proposed for gas purification applications especially at trace concentrations due to their small pores and small pore volumes (Ackley et al., 2003).

Although NO is an important gas from the biological and environmental points of view. NO is a supercritical gas under ambient conditions. Previous studies on adsorption of supercritical gases revealed that these gases can be adsorbed by microporous adsorbents through micropore filling mechanism. However, almost no study has been performed on adsorption of NO in clinoptilolite. The theory of volume filling of pores of Dubinin is consistent with the micropore-adsorbate interaction concept where the size of an adsorbate molecule and pore size is comparable. Since clinoptilolite pore size is comparable to the kinetic diameter of a NO molecule, it was expected that NO can be adsorbed by clinoptilolite through the micropore filling mechanism. Previous studies showed that the adsorption and diffusion characteristics of

clinoptilolite could be modified by ion exchange for specific gas adsorption applications (Ackley and Yang, 1991a,b; Ackley et al., 1992; Ma and Mancel, 1972). The tendency of NO molecule to metal ions is known from the biological and catalytic studies. Regarding the crucial effect of small doses of NO in the biological systems, even minute amounts of NO adsorbed in clinoptilolite may have important applications.

Clinoptilolite is the most common natural zeolite. Its low cost makes the zeolitic tuffs rich in clinoptilolite commercially attractive. However, natural zeolites are not utilized as extensively as synthetic ones due to heterogenities in terms of mineral purity and cation composition. The clinoptilolite content of the natural zeolitic sample influences its ion-exchange and adsorption characteristics (Mumpton, 1998, 1999). Special interest has been devoted to clinoptilolite-rich natural zeolite in this study due to the large amount of reserves in the Western Anatolia region. The natural zeolite reserve in Turkey is estimated to be about 50 billion tons. Gördes basin has one of the most important clinoptilolite occurences in Turkey with high mineral purity and homogenity with an estimated reserve of 1 billion tons (Esenli, 2002). Recently, the clinoptilolite-rich natural zeolite from Western Anatolia and its acid-modified and ion-exchanged forms were investigated for its thermal stability, antibacterial activity, water vapor, carbon dioxide and carbon monoxide adsorption and diffusion properties (Çakıcıoğlu-Özkan and Ülkü, 2004, 2008; Top, 2001; Top and Ülkü, 2004; Narin, 2001; Narin et al., 2004; Akdeniz and Ülkü, 2007, 2008).

Clinoptilolite-rich natural zeolites have been applied for drug delivery purposes and found to be efficient in order to attenuate the side effects of the drugs. Therefore, study on interaction of nitrogen monoxide with clinoptilolite offers many potential applications for the adsorption, storage and release of NO for biological purposes. Regarding the importance of storage and release of biological gases such as NO, a microporous natural adsorbent clinoptilolite with high pore volume can be a good candidate for these purposes. This thesis aims investigation of the adsorption, storage and release characteristics of the local clinoptilolite-rich natural zeolite for nitric oxide.

CHAPTER 2

LITERATURE SURVEY

Some of those studies on adsorption in microporous adsorbents, NO adsorption in synthetic and natural zeolites as well as in other microporous adsorbents using dynamic and static adsorption systems as well as *insitu* infrared spectroscopy, NO storage and release properties of zeolites, health applications of zeolites, ion exchange and antibacterial properties of natural zeolites were reviewed in this chapter.

2.1. Adsorption in Microporous Adsorbents

Gas adsorption relies on diffusion of gas molecules to the surface of an adsorbent where weak intermolecular forces hold them. The concept of the adsorbed layer on the walls of large pores by a layer-by-layer mechanism is not applicable adsorption in micropores of size comparable to the size of adsorbate molecule. In this case, the adsorption occurs by micropore filling mechanism, i. e., the pore space is filled in a volumetric fashion (Dubinin and Astakhov, 1971). The characteristic of micropore filling is a remarkable adsorption uptake in the low-pressure region due to overlapped interaction potential of the pore walls

Dubinin and Radushkevich developed the concept of micropore filling for activated carbons and an equation describing micropore filling by the Dubinin and Radushkevich (D-R) equation (Dubinin and Radushkevich, 1947):

$$\frac{W}{W_L} = \exp\left[-\left(\frac{A}{\beta E_o}\right)^2\right] \tag{2.1}$$

where W is the volume of liquid adsorbate adsorbed at relative pressure P/P_o and temperature T, W_L is the limiting micropore volume, E_o is the characteristic energy of adsorption for the reference vapor (benzene), β is the affinity coefficient which has a value of unity when the adsorptive is the reference vapor (benzene), and A is the differential molar work of adsorption given as:

$$A = RT \ln\left(\frac{P_o}{P}\right) = -\Delta G \tag{2.2}$$

where R is the universal gas constant and ΔG is the change in the Gibbs free energy. Substituting Equation (2.2) in Equation (2.1) yields:

$$\ln\left(\frac{W}{W_L}\right) = -\left(\frac{RT}{\beta E_o}\right)^2 \ln^2\left(\frac{P_o}{P}\right) \tag{2.3}$$

As the saturated vapor pressure, P_o, is not defined for a supercritical gas, the D-R equation is not valid for description of adsorption of a supercritical gas. Dubinin extended the D-R equation to deal with supercritical gases (Dubinin, 1960). He introduced a hypothetical saturated vapor pressure (P_o') of supercritical gas near the critical temperature can be estimated from:

$$P_o' = \left(\frac{T}{T_c}\right)^2 P_c \tag{2.4}$$

where P_c and T_c are the critical pressure and temperature, respectively. The hypothetical saturated vapor pressure was also considered as the fitting parameter in

addition to the characteristic energy. Then the extended D-R equation for the supercritical gases was given as follows:

$$\ln\left(\frac{W}{W_L}\right) = -\left(\frac{RT}{\beta E_o}\right)^2 \ln\left(\frac{T_r}{P_r}\right)^2 \qquad (2.5)$$

where $T_r=T/T_c$ and $P_r=P/P_c$ are the reduced temperature and pressure, respectively. In this model the adsorption mechanism of supercritical fluids was assumed to be the same with the pore filling mechanism as for subcritical fluids.

2.2. Studies on NO Adsorption in Microporous Adsorbents

Kaneko reported that the activated carbon fiber (ACF) modified with fine α-FeOOH (α-FeOOH-ACF) could adsorb abundant NO at 30 ^oC by chemisorption-assisted micropore filling mechanism (Kaneko, 1987a). They previously found that α-Fe_2O_3 produced by decomposition of α-FeOOH in vacuum had greater chemisorption activity for NO than α-FeOOH (Hattori et al., 1979), therefore they decided to decompose α-FeOOH dispersed on ACF in vacuum in order to obtain an adsorbent with higher NO adsorption capacity. This adsorbent adsorbed NO up to 300 mg/g adsorbent at 30 ^oC (Kaneko and Inouye, 1988).

Kaneko and co-workers carried out N_2 adsorption on the iron oxide-dispersed ACF with preadsorbed NO. The adsorbent was prepared by dispersion of ultrafine α-FeOOH particles on the ACF. The ACF having uniform size of micropores was treated with 0.6 M $Fe_2(SO_4)_3$ solution at 30 ^oC and at pH 13. X-ray diffraction and X-ray photoelectron spectroscopic analysis confirmed formation of ultrafine α-FeOOH particles on the ACF. Adsorption isotherms of NO at 30 ^oC and N_2 at -196 ^oC on the α-FeOOH-dispersed ACF were compared. The isotherms indicated micropore filling of both gases on the adsorbent. The NO adsorption capacity was reported as 320 mg NO/g at 80 kPa and 30 ^oC. The adsorption isotherm of NO at 30 ^oC was found to be similar to

that of N_2 at -196 ^oC, being of the Type I according to the IUPAC classification. The amount of NO filled in the micropores was found to be 1045 % of those of N_2 at -196 ^oC, although the NO adsorption temperature was much higher than the boiling temperature of NO. The D-R plot was applied to the NO adsorption isotherms. It was concluded that NO was adsorbed by a special micropore filling mechanism which chemisorption partially assisted; the ultrafine α-FeOOH particles on the ACF assisted the micropore filling of NO through the chemisorptive action as schematically shown in Figure 2.1. The TPD studies revealed that the adsorbed NO species were NO. The magnetic susceptibility measurements on the NO-adsorbed ACF showed that NO molecules formed dimmers in the micropores (Kaneko et al., 1987b).

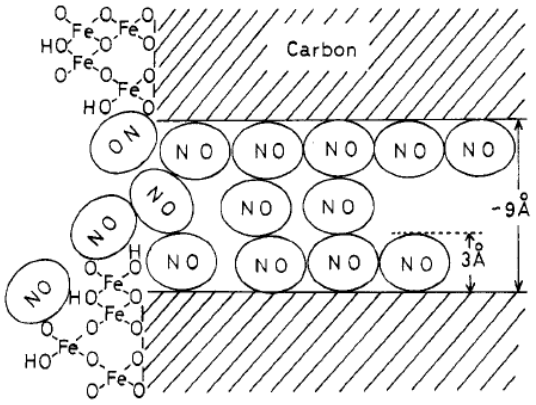

Figure 2.1. Schematic diagram of the NO micropore filling on α-FeOOH-dispersed activated carbon fiber. (Source: Kaneko et al., 1987b)

Kaneko examined the adsorption isotherms of NO at 30 ^oC and N_2 at -196 ^oC on the α-Fe_2O_3 dispersed ACF. The adsorbent was obtained by decomposing the α-FeOOH dispersed on the ACF in vacuum at 300-500 ^oC. The adsorption of N_2 after preadsorption of NO decreased remarkably. The difference in the amount of N_2 adsorbed before and after the NO adsorption was found to be almost equal to the amount of adsorbed NO. Since the NO adsorption isotherm was of Langmuir type, the volume of NO adsorbed at saturation, $W_L(NO)$, was regarded as the pore volume of the adsorbent and the D-R equation was modified yielding:

$$\ln\left[\frac{W_L(NO)}{W}\right] = \left(\frac{RT}{\beta E_o}\right)^2 \ln^2\left[\frac{P_o(NO)}{P}\right] \qquad (2.6)$$

where $P_o(NO)$ is the saturated NO vapor pressure at 30 ^oC in the micropores. The modified D-R plots obtained by fitting the experimental data were found to be linear from which $P_o(NO)$ and βE_o were calculated. The ratios of the amount of NO filled to that of N_2 were found to be in the range of 0.6-0.8. The saturated vapor pressures of NO at 30 ^oC in the micropores were obtained by the modified D-R plot as 820-1250 torr. He discussed the relationship between the state of micropores and the NO micropore filling. The role of the modification with iron oxides was related to the dimer formation through weak chemisorption (Kaneko, 1988).

Kaneko also studied the temperature dependence of NO adsorption on h-ox-ACF (Fe_2O_3-dispersed ACF prepared by decomposing fine α-FeOOH on the ACF at 500 ^oC and 1 mPa for 15 hours) at 1, 30, 45 and 100 ^oC in order to elucidate the role of chemisorption in the NO micropore filling. The adsorption isotherms of N_2 at –196 ^oC and of NO at 1-100 ^oC were obtained gravimetrically. The amount of Fe deposited on ACF was determined as 7 % by weight by chemical titration. The iron oxides on the ACF were found to be highly dispersed α-Fe_2O_3 by EXAFS. The relationship between the initial rate of NO adsorption and the temperature was inspected. Regarding that almost all adsorptions completed within 10 minutes, the author stated that supercritical NO was rapidly adsorbed like a vapor. The initial rate of NO adsorption was estimated by the amount of NO adsorbed after 2 minutes of the NO introduction. The rate has a minimum near 47 ^oC. When the adsorption temperature decreased, the adsorption rate increased below 47 ^oC, but a reverse tendency was observed above this temperature. The percentage of the micropore volume occupied by NO relative to the micropore volume (determined from N_2 adsorption) decreased from 83 to 45% with increasing temperature. The changes in the initial rate of NO adsorption and in the saturated amount of NO adsorption with temperature were attributed to the assistance of chemisorptive process in the micropore filling of supercritical NO. All the isotherms were of the Langmuir type and exhibited remarkable hystereses regardless the adsorption temperature. The maximum NO adsorption occurred at 1 ^oC. The micropore volume of h-ox-ACF for NO was approximated by the amount of NO adsorbed at

saturation. Application of the extended D-R equation yielded straight lines designating the applicability of the equation to describe the NO micropore filling. The micropore volume for NO was determined from the extended D-R plots and the saturated NO vapor pressure, $P_o(NO)$, was calculated from Equation (2.4). The modified D-R plots given by Equation (2.6) were also found to be linear. The $P_o(NO)$ and βE_o values were determined from the modified D-R plots and compared with the values obtained from the extended D-R plots. The values determined from the extended D-R plots were higher than the micropore volume for N_2 despite the similar molecular volumes of N_2 and NO. The $P_o(NO)$ determined from the extended D-R plots was very large. The smaller $P_o(NO)$ values obtained from the modified D-R plots were attributed to the depression of the saturated NO vapor pressure by the micropore field. The temperature dependences of the adsorption rate and the adsorption isotherms indicated the assistance of the chemisorption process in the micropore filling of supercritical NO. It was concluded that the micropore filling of supercritical NO could be briefly described by the extended and modified D-R equations, but further study was required to describe the NO micropore filling definitely (Kaneko, 1989).

Kaneko and Murata criticized the extended D-R equation given by Dubinin in terms of the extrapolation of the pressure versus temperature relationship. They claimed that the saturation vapor pressure was not defined for a supercritical gas, thus the D-R equation was not valid for description of adsorption of a supercritical gas. They pointed out a need for a concise analytical method for determination of saturation vapor pressure of a supercritical gas from the experimental point of view. They assumed that supercritical gas molecules were concentrated in the micropore volume by the strong adsorbate-adsorbent and thereby the supercritical gas was transformed into a quasi-vapor. The quasi-vapor state depends strongly on the micropore size and the quasi-vapor has own intermolecular structure (Kaneko, 1986) and the quasi-saturated vapor pressure, P_{oq}. Each quasi-vapor has its inherent micropore volume (W_L) and it can be filled in the micropore of the capacity W_L with the micropore filling mechanism. The modified D-R equation was extended to the quasi-vapor state of supercritical gas. The plot of $[ln(W_L/W)]^{1/2}$ versus lnP was called the supercritical D-R plot. The quasi-saturated vapor pressure of supercritical gas under the micropore field (P_{oq}) and βE_o were determined from the plot. βE_o was associated with the isosteric heat of adsorption

at the fractional filling (ϕ) of 1/e ($q_{st,\phi=1/e}$) using the enthalpy of vaporization at the boiling point (ΔH_v):

$$q_{st,\phi=1/e} = \Delta H_v + \beta E_o \tag{2.7}$$

The supercritical D-R equation gave the reduced adsorption isotherm of the supercritical gas using the concepts of P_{oq} and W_L which was experimentally estimated by the Langmuir plot of the adsorption isotherm. P_{oq} and W_L were related to the intermolecular interaction of supercritical gas in the quasi-vapor state and the adsorbate-adsorbent interaction, respectively. The amount of adsorption at a pressure P (W) was expressed in terms of the fractional filling (W/W_L) and the quasi-relative pressure (P/P_{oq}), so the reduced adsorption isotherm was obtained. The reduced D-R equation was given as (Kaneko and Murata, 1997):

$$\frac{W}{W_L} = \exp\left[-\left(\frac{RT}{\beta E_o}\right)\ln\left(\frac{P_{oq}}{P}\right)^2\right] \tag{2.8}$$

The adsorption isotherm of NO on the iron oxide-dispersed ACF (Fe-ACF) at 1, 30 and 100 ^{o}C are shown in Figure 2.2. The supercritical D-R equation applied to the NO adsorption on the Fe-ACF gave straight lines designating that the supercritical D-R equation described the NO micropore filling. The values of P_{oq} and βE_o were determined at each temperature and given in Table 2.1. The P_{oq} values were found to be greater than 101 kPa, but they were in a reasonable range. On the contrary, the estimated value of the saturated vapor pressure with the D-R model was found to be higher than 1 GPa. The $q_{st,\phi=1/e}$ for NO was determined using ΔH_v value of 13.8 kJ/mol which was close to the stabilization energy of the NO dimer in the micropore of ACF was reported previously as 22-24 kJ/mol (Kaneko, 1989).

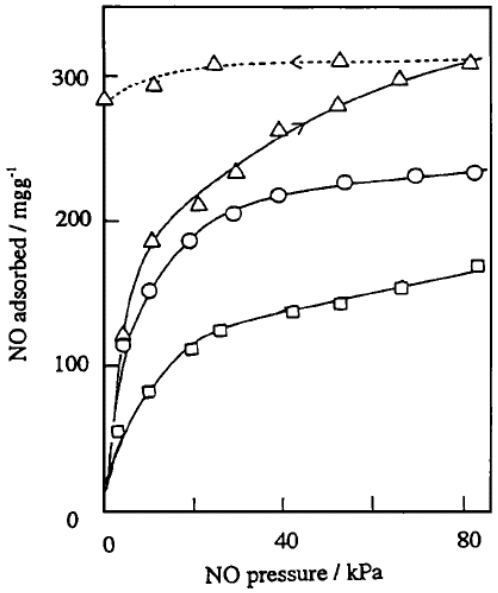

Figure 2.2. The adsorption isotherms of NO on Fe-ACF at different temperatures: △, 1 °C; ○, 30 °C; □, 100 °C. (Source: Kaneko and Murata, 1997)

Table 2.1. Inherent micropore volume (W_L), saturated vapor pressure (P_{oq}) and characteristic adsorption energy (βE_o) for supercritical NO on Fe-ACF. (Source: Kaneko and Murata, 1997)

Temperature (°C)	W_L(ml/g)	P_{oq} (kPa)	βE_o (kJ/mol)
1	0.32	360	10.0
30	0.23	230	11.5
100	0.17	370	12.4

The reduced adsorption isotherms were determined from the W_L and P_{oq} values and shown in Figure 2.3. The adsorption isotherms at different temperatures given in Figure 2.2 were well expressed by a single reduced adsorption isotherm irrespective of the adsorption temperature. The goodness of the reduced adsorption isotherm also supported the applicability of the supercritical D-R method-proposed (Kaneko and Murata, 1997).

The micropore volume for each adsorptive depends on the pore width and characteristic quantities of the potential well depth and effective diameter for the adsorbate molecule-adsorbent surface atom. The micropore volume can be determined experimentally due to a considerably strong adsorption which provides the Langmuir type isotherm. The micropore volume for vapor molecules is almost equal to the

micropore volume obtained from N_2 adsorption at –196 ^oC, i.e. the Gurvitsch rule is held. On the other hand, the micropore volume filled by a supercritical gas, which can be evaluated from the Langmuir plot of the adsorption isotherm, is less than the micropore volume obtained from N_2 adsorption at –196 ^oC (Kaneko and Murata, 1997).

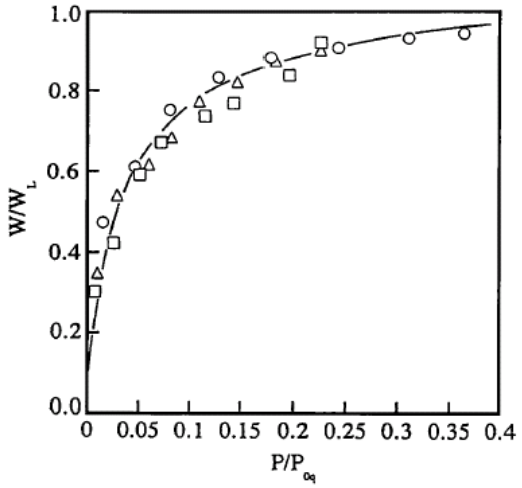

Figure 2.3. The reduced adsorption isotherm of NO on Fe-ACF: △, 1 ^oC; ○, 30 ^oC; □, 100 ^oC. (Source: Kaneko and Murata, 1997)

Claudino and co-workers studied the NO adsorption equilibrium and kinetic behavior of different carbons in the temperature range of 45-85 ^oC using gas chromatography. The inlet NO concentration was set to 0.05, 0.5 and 5 % (by volume) in helium. 0.3 mm activated carbon particles were packed into the column with internal diameter of 0.28 cm and length of 52 cm and activated at 100 ^oC for 3 hours under helium flow. The column flow rate was 30 ml/min. The column outlet NO concentration was recorded by TCD. After the saturation of the column, pure helium was passed through the column to measure the desorption curve under the same flow rate and temperature. The adsorption of NO on activated carbons was described by the interaction of NO with surface oxygen complexes present on the carbon surface forming NO_2 adsorbed on the carbon surface. The NO adsorption capacity was found to be dependent indirectly on both the BET surface area and oxygen functional group content of the carbon, and increased as the oxygen content increased. The adsorption was reversible and the enthalpy of adsorption was found to be in the range of 3.3-11 kJ/mol.

The desorption results showed that all NO could be desorbed under helium flow at the adsorption temperature. The linear driving force model was used to describe the breakthrough curves and the results showed that this model was suitable to describe the adsorption of NO on activated carbons in a fixed-bed. It was claimed that FTIR studies were required in order to elucidate the adsorption meachanism as well as for the identification of the adsorbed species and their stabilities (Claudino et al., 2004).

Recently, Alcañiz-Monge and colleauques studied the NO adsorption on iron-containing activated carbon fibers (Fe-ACF) at 27 ^{o}C. The adsorbents were prepared by mixing an iron precursor ($FeCl_3$) with raw pitch before carbon fiber formation (CF), and further CO_2 activation of the Fe-CF. The prepared Fe-ACF samples were denoted by CFe%, % indicating the burn-off in weight percent after the activation step. The NO adsorption capacities for NO were determined from the NO adsorption curves obtained under feed stream of 5% NO in helium. The NO adsorption capacity of the ACF containing iron was found to be higher than that of the Fe-free ACF. The non-activated fiber (CFe) showed the lowest NO adsorption capacity. The higher the activation of the fiber, the lower the NO adsorption capacity. It was suggested that the NO adsorption capacity of the Fe-ACF probably depended on the pore volume and pore size distribution of the fiber and on the nature of the iron species. The volumes of pores with diameter smaller than 0.7 nm (V_c) and smaller than 2 nm (narrowest micropores, V_n) were determined by CO_2 and N_2 adsorption, respectively. The samples with higher burn-off showed lower V_n but higher supermicropore volumes (V_n–V_c). Thus NO adsorption capacity was related to the V_n. The XRD analysis revealed that oxidized iron species (FeO, Fe_3O_4, Fe_2O_3) were formed on the samples during activation of the fibers. The nature of these oxidized iron species was related to the burn-off percentage. The sample with metallic iron and/or partially reduced iron species (Fe, FeO) showed the highest NO adsorption capacity implying the higher activity of the reduced iron species in NO adsorption. It was reported that not all of iron located in the carbon bulk participated in NO adsorption. Most of the samples showed similar adsorption kinetic behaviour, except for the sample CFe. The NO adsorption rate was slow and in some samples more than 4 hours were required for complete saturation. The higher NO adsorption rates were found for the samples with wider pores. The low NO adsorption rate was attributed to the relative rates of the different steps involved in the adsorption: rate of chemisorption of NO on iron species (r_{chem}) and rate of diffusion of NO throughout the microporous network of the fiber (r_{dif}). The rate of NO adsorption (r_{ads})

was expressed as $1/r_{ads}=1/r_{chem}+1/r_{dif}$. Regarding the adsorption temperature of 27 ^{o}C, the chemisorption step was assumed to be slow except for the sample with the very narrow micropores. Different kinetic models were applied to the experimental NO adsorption data. The first model assumed that NO adsorption rate was controlled by NO diffusion throughout the micropores of the adsorbent and was described by the Fick's Law (Ruthven, 1984). The experimental data was not described by this model indicating that the adsorption rate was not controlled by the diffusion of NO in the micropores of the fiber. The second model described the NO chemisorption by the Elovich model.The experimental data were fitted well to this model after an early period of time. The slopes of the curves were related to the geometry of the solid porous network. NO chemisorption on carbon or on surface oxygen–carbon complexes was neglected regarding the low adsorption temperature and therefore chemisorption of NO was proposed to occur on iron species. It was proposed that the NO adsorption on Fe-ACF samples took place in two steps: first chemisorption of NO and formation of the dimer N_2O_2, and then diffusion of the dimer into the micropores. For the adsorption of NO, the former step was the rate-limiting step for the Fe-ACF samples while the later step was the rate-limiting step for the CFe sample having very narrow micropores. The adsorbed NO was desorbed by heating the adsorbents at 227 ^{o}C, and the NO adsorption capacity of the adsorbent did not change after desorption (Alcañiz-Monge et al., 2008).

2.3. Studies on NO Adsorption in Zeolites

Zhang and co-workers measured the amount of reversibly and irreversibly adsorbed nitrogen monoxide on metal-exchanged zeolites using a dynamic adsorption apparatus, and investigated the nature of the adsorbed species of NO and the adsorption mechanism by infrared and temperature-programmed desorption (TPD) techniques. The effects of the metal cations, zeolite structure, aluminum content, ion exchange level, adsorption temperature and pressure, and preadsorbed gases on the NO adsorption and desorption properties of the zeolites were discussed. Various metal-exchanged forms of the zeolites including ZSM-5(23.3), mordenite(10.5), ferrierite(12.3) offretite/erionite(7.7), and Y(5.6), L(6.0), and X(2.6) (the numbers in the parantheses

denotes SiO_2/Al_2O_3) were examined. The metal-exchanged zeolites were prepared from the sodium-exchanged forms. The sodium forms were obtained through treating the zeolites with dilute $NaNO_3$ solution and metal-exchanged forms through treating the zeolites with the metal acetate or nitrate solutions of 10^{-11} mmol/l initial concentration in zeolite mass/solution volume (*S/L*) ratio of 15 g/l overnight. The wet cake obtained by filtration was again metal exchanged in the new metal salt solution. After the desired repetition, the sample was washed and dried at 110 ^{o}C.

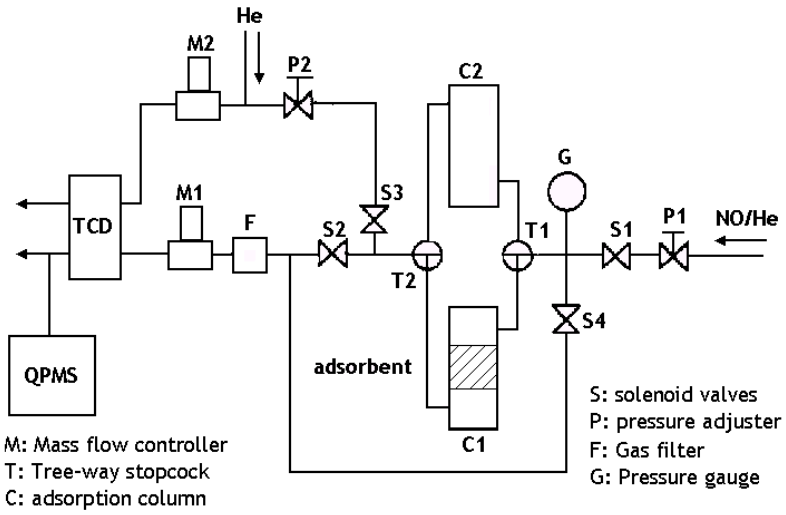

Figure 2.4. Schematic diagram of the PSA apparatus.
(Source: Zhang et al., 1993, 1999)

The adsorption-desorption measurement was carried out in a fixed bed as shown in Figure 2.4. Two adsorption columns were used; the packed one was for the usual adsorption-desorption measurement, and the empty one was for a blank test. Adsorption and desorption runs were periodically controlled by solenoid valves. The adsorbent of 0.5-1.0 g was placed in a stainless steel column (7.4 mm internal diameter, 22 cm length) and was activated by heating at 500 ^{o}C for 5 hours under a helium stream (50 ml/min) before the adsorption run. In the adsorption run, the gas mixture of NO (1000-20000 ppm) and helium was fed to the packed column at a rate of 100 ml/min. After the adsorption run, pure helium (100 ml/min) was passed through the column in a countercurrent direction to desorb the reversibly adsorbed NO from the adsorbent. The

adsorption temperature was -78-100 ^{o}C and the adsorption (or desorption) time was 45-120 minutes. The effluent concentration and composition were continuously monitored by using an on-line thermal conductivity detector (TCD) and a quadrupole mass spectrometer (QPMS), respectively (Zhang et al., 1993).

Infrared absorption spectra were recorded by using an infrared spectrometer and a quartz infrared cell with potassium bromide (KBr) windows. The self-supporting sample wafer was heated to 500 ^{o}C for 2 hours and cooled to room temperature under a dynamic vacuum. Infrared measurements were performed at ambient temperature. The same apparatus shown in Figure 2.4 was used for the temperature-programmed desorption (TPD) analyses. After the adsorption of NO at 0 ^{o}C in a NO flow (5000 ppm) for 3 hours, the column was purged with pure helium for 5 hours. Subsequently, the TPD experiment was carried out with a heating rate of 5 K/min in a helium flow (50 ml/min at 101.3 kPa, 25 ^{o}C) in the temperature range of 50–600 ^{o}C. The amount of NO desorbed was estimated from the profiles measured by TCD, and the composition of the desorbed gas was monitored by QPMS. When the adsorption and desorption runs were repeated, almost the same breakthrough and elution curves were obtained for all the zeolites as shown in Figure 2.5. N_2 and N_2O were formed in the first adsorption run. The amount of NO adsorbed was estimated from the hatched area (denoted as a_n where n is the number of adsorption-desorption cycles) while that of NO desorbed was calculated from the dotted area (b_n). The a_n values decreased with increasing n and reached a constant value while the b_n value was almost constant, independent of n. Usually a_n became approximately equal to b_n at the fifth or sixth adsorption-desorption cycle. Then, the amount of reversible adsorption of NO per weight of adsorbent (q_{rev}) was defined by a_m/S_w (where S_w is the sample weight) at $a_m=b_m$. The amount of irreversible adsorption of NO per weight of adsorbent (q_{irr}) was defined by

$$q_{irr} = \sum_{n=1}^{m} (a_n - b_n)/S_w \qquad (2.9)$$

The measured q_{rev} and q_{irr} at 0 ^{o}C on various cation-exchanged MFI zeolites are given in Table 2.2. The q_{rev} and q_{irr} greatly changed with the metal exchanged. In the case of transition metal-exchanged zeolites, generally q_{irr} were larger than q_{rev}. On the

contrary, q_{rev} was greater than q_{irr} for alkaline earth metal-exchanged zeolites. Both q_{rev} and q_{irr} were very small on alkali metal-, rare earth metal- and proton-exchanged zeolites. The ratio of the irreversibly adsorbed NO to Co^{2+} ion was found to be 1.69 and did not change at 50 ^{o}C. This indicated that NO was strongly adsorbed on Co^{2+} at room temperature and some of the cobalt nitrosyl complexes on MFI zeolite existed in the form of $[Co\text{-}(NO)_2]^{2+}$ (Zhang et al., 1993).

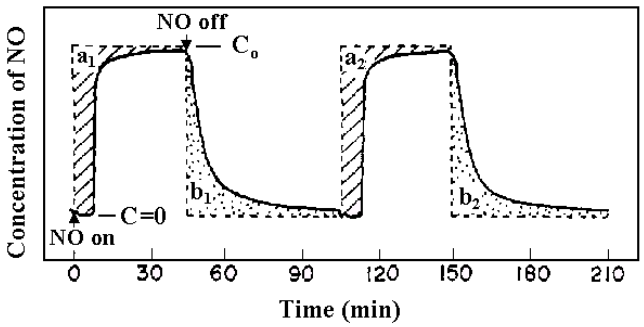

Figure 2.5. Breakthrough and elution curves of NO over Cu-MFI(23.3)-60: solid line: with adsorbent, broken line: without adsorbent, C_o: initial concentration of NO, adsorption time: 45 minutes, desorption time: 60 minutes, concentration of NO: 1910 ppm; flow rate: 100 ml/min, adsorption temperature: 0 ^{o}C, adsorbent weight: 1 g. (Source: Zhang et al., 1993)

Table 2.2. NO adsorption properties of various cation-exchanged MFI zeolites. (Source: Zhang et al., 1993)

Adsorbent	Cation content (% by weight)	Amount of NO adsorbed (cm^3/g)		
		Reversible	Irreversible	Total
Na-MFI(23.3)-100b	2.81	0.16	0	0.16
Cu-MFI(23.3)-157	5.9	4.28	14.9	19.18
Co-MFI(23.3)-90	3.06	1.52	19.69	21.21
Mn-MFI(23.3)-127	4.2	1.19	5.81	7.00
Ni-MFI(23.3)-68	2.41	1.03	6.64	7.67
Zn-MFI(23.3)-96	3.79	1.01	0.50	1.51
Ag-MFI(23.3)-90	10.85	3.38	0.54	3.92

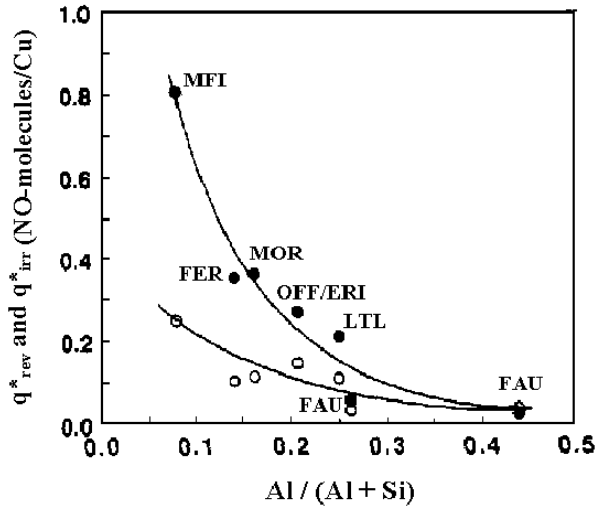

Figure 2.6. Correlation between the adsorbed NO amounts and the Al contents in copper ion-exchanged zeolites: ○, q^*_{rev}; ●, q^*_{irr}. (Source: Zhang et al., 1993)

Among the adsorbents Co-MFI(23.3)-90 showed the largest q_{irr} and the copper-exchanged ZSM-5 zeolites showed the greatest ability for reversible adsorption. Since the aim of the study was examination of the adsorption-desorption properties of the adsorbents for PSA applications that requires reversible adsorption, the copper exchanged ZSM-5 sample was studied in more detail. Both the amount of reversibly and irreversibly adsorbed NO per copper ion significantly changed with the zeolite structure and decreased in the following order: MFI>OFF/ERI>MOR>LTL>FER>FAU. As seen in Figure 2.6, both q^*_{rev} and q^*_{irr} (NO molecules/Cu) decreased with the increment in the aluminum content of the copper ion-exchanged zeolites and independent of the zeolite structure. It was concluded that the adsorption of NO was mainly controlled by the aluminum content, since the catalytic activity per acidic site increased with decreasing aluminum content for acidic zeolites. A good correlation was obtained between the infrared vibration frequencies of acidic hydroxyls and the Al content of the zeolite implying the dependence of the acid strength on the Al content (Zhang et al., 1993).

Figure 2.7 shows the dependencies of the adsorbed NO amounts at 0 ^{o}C on the exchange level of copper ion. q_{rev} and q_{irr} were found to be proportional to the exchange level. The q^*_{rev} and q^*_{irr} were found to be independent of exchange level and remained constant approximately at 0.23 and 0.64 NO molecules/Cu, respectively. The higher the exchange level of copper ion in MFI zeolite was the higher q_{rev} and q_{irr} were. With decreasing adsorption temperature, q_{irr} significantly increased at about -23 ^{o}C. On the other hand, q_{rev} gradually increased with decreasing adsorption temperature, reached the maximum (4.35 cm^3/g) at -30 ^{o}C and then decreased. The temperature dependence of q_{rev} was discussed in terms of the possibilities of either the decrease in the sites for reversible adsorption of NO by the abrupt increase in the amount of irreversible adsorption of NO (reversibly adsorbed NO is converted into irreversibly adsorbed NO at low temperatures) or decrease in the effective pore size of MFI zeolite (0.54 nm) by increasing amount of irreversibly adsorbed NO or nonattainment of the adsorption equilibrium due to the small diffusion coefficient at low temperature (Zhang et al., 1993).

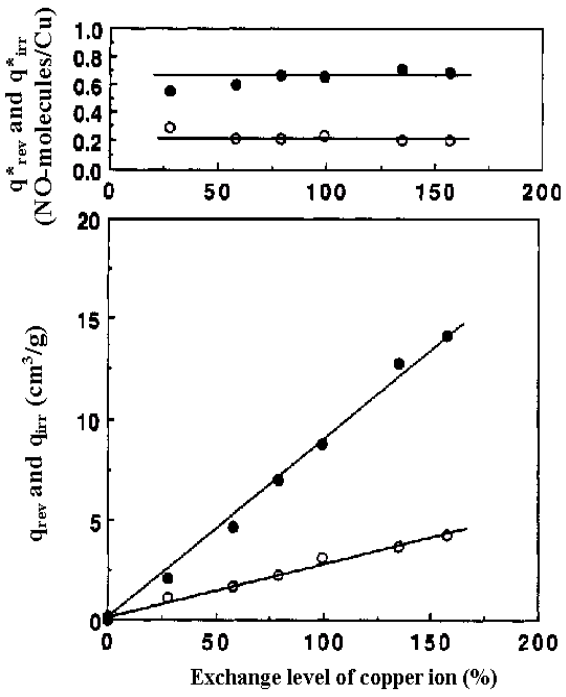

Figure 2.7. Dependence of the amount of reversible adsorption of NO on the exchange level of copper ion in MFI zeolite: ○, q_{rev}; ●, q_{irr}. (Source: Zhang et al., 1993)

The effect of partial pressure of NO on the adsorption isotherms were also investigated for q_{rev} and q_{irr} on Cu-MFI(23.3)-157 at 0 ^{o}C. It was found that both q_{rev} and q_{irr} increased with increasing concentration of NO. The isotherms of q_{rev} and q_{irr} were roughly expressed by the Langmuir isotherm. The q_m and the Langmuir adsorption equilibrium constant for q_{rev} were found as 10.14 cm^3/g and 357 atm^{-1}, respectively, and for q_{irr} 27.61 cm^3/g and 745 atm^{-1}, respectively. The effect of preadsorbed gas was examined on Cu-MFI(23.3)-157. The preadsorption of NO_2 resulted in the enhancement of q_{rev}. This suggested that irreversibly adsorbed NO_2 could act as new active sites for the reversible adsorption of NO. On the other hand preadsorption of O_2, CO, CO_2, H_2O or SO_2 reduced q_{rev} and q_{irr}. The bands observed in the infrared spectra upon admission of NO onto Cu-MFI(23.3)-157 and evacuation at 500 ^{o}C were assigned to N_2O (2238 cm^{-1}), NO_2^+ (2125 cm^{-1}), NO^+ (1906 cm^{-1}), gaseous NO (1876 cm^{-1}), NO^- (1813 cm^{-1}), and $(NO)_2^-$ (1827 and 1734 cm^{-1}). No bands of NO adsorbed were observed on Na-MFI(23.3)-100, designating that the adsorbed species of NO were associated with copper ions. The change of the intensities of the bands with time was also examined. The intensities of IR bands of NO^- and $(NO)_2^-$ were found to decrease, that of NO^+ to increase while that of NO_2^+ did not change with time. When the sample was evacuated for 30 min at room temperature, the bands of NO^- and $(NO)_2^-$ completely disappeared and the intensity of the NO^+ band decreased. The intensity of NO^+ recovered to the original value by the second admission of 52 torr of NO while the bands of NO^- and $(NO)_2^-$ did not appear. The same results were reproduced when NO was adsorbed and evacuated subsequently. The major species of the reversible adsorption of NO on copper-exchanged MFI zeolite was the NO^+ species. In order to clarify irreversibly adsorbed NO species on Cu-MFI(23.3)-157, TPD was performed after NO adsorption. No desorption peak was observed for a Na-MFI(23.3) zeolite in the TPD profile indicating that the irreversible NO adsorption was associated with copper ion (Zhang et al., 1993).

Zhang and co-workers also studied the adsorption properties of NO on various silver-exchanged zeolites using the same dynamic adsorption apparatus shown in Figure 2.4. In this study, the effects of aluminum content, silver exchange level, adsorption temperature, adsorption pressure and preadsorbed gases on the adsorption properties were discussed. In addition, the adsorbed species of NO on Ag-MOR were also investigated by means of infrared spectroscopy. 0.1-2% of NO in helium was introduced into the column at a rate of 100 ml/min. The desorption runs were performed

as in the previous study. The adsorption or desorption time was about 45-120 minutes. The temperature of adsorbent was controlled in the range of -78-0 ^{o}C by using an icebox and a cooling system. The reversibly adsorbed NO molecule/cation exchanged was found to be constant fot Ag-MFI(23.3) while increased monotonically with the exchange level of silver ion for Ag-MOR(15.0). This behavior was explained by the effectiveness of silver ion introduced to the zeolite structure. Constant reversibly adsorbed NO molecule/cation exchanged of Ag-MFI(23.3) was attributed to uniform exchange sites in MFI. It was stated that the silver ions exchanged into MOR zeolite had selectivity for NO adsorption or exchange sites in MOR had selectivity for silver ion exchange. The reversibly and irreversibly adsorbed amounts of NO on Ag-MOR(15.0)-112 at -78 ^{o}C were found to be 11.49 and 25.78 cm^3/g, respectively. The reversibly and irreversibly adsorbed NO species on Ag-MOR(15.0)-112 were characterized by infrared spectroscopy technique. For Ag-MOR, the reversibly adsorbed species were $NO^{\delta+}$ and N_2O, and the irreversibly adsorbed NO species were N_2O, $NO^{\delta+}$, as well as a small amount of $NO^{\delta-}$, $NO_2^{\delta+}$ (Zhang et al., 1999).

Matsumoto and co-workers measured the adsorption and desorption isotherms of NO for hydrogen, sodium and calcium forms of mordenite gravimetrically at 0 ^{o}C and -72 ^{o}C. The saturation adsorption capacities were calculated assuming that the density of adsorbed NO was equal to that of liquid NO at the critical temperature. The saturation capacities of H, Na and Ca mordenites for NO at -72 ^{o}C were determined in the range of 20.1-24.9 molecules/unit cell (0.16-0.20 cm^3/g) by the application of the Langmuir model. From the adsorption isotherms of NO at 0 ^{o}C, it was found that the adsorbed amounts increased more gradually with increase in equilibrium pressure than those at -72 ^{o}C. The saturation capacity decreased to 7–14 molecules/unit cell (0.06-0.13 cm^3/g) at 0 ^{o}C. The order of the saturation capacity was reported to be HM-10>NaM-10≈CaM-10. The measured saturation capacities were compared with the micropore volumes estimated by the application of the Dubinin-Raduskevich (D-R) model on the N_2 adsorption data. It was found that the saturation capacities corresponded to 88-100% of the micropore volumes implying that the NO molecules filled up zeolite cavities at -72 ^{o}C regardless of the kind of cations. The enhanced adsorption of molecules in micropores was explained by the overlapping of potential field from pore walls (Everett and Powl, 1976; Gregg and Sing, 1982). The enhancement of dispersion interaction between an NO molecule and pore walls was estimated assuming that NO was a

spherical molecule with mean radius of 0.33 nm and the mordenite micropore was cylindrical with diameter of 0.68 nm (Stoeckli, 1974; Everett and Powl, 1976). The potential depth of the interaction at the center of the main channel of mordenite was found to be 1.4-1.6 times deeper than the energy minimum on flat surface. It was further stated that the cation sites in micropores of zeolites exhibit strong electrostatic field, which caused strong adsorption of polar molecules. On the other hand the mean kinetic energy of NO at -72 ^{o}C was only 1.1 times higher than that at its critical temperature. It was concluded that the strong adsorption of NO and the hysteresis at -72 ^{o}C were possibly attributable to combination of the enhancement of dispersion potential and the electrostatic interaction in micropores of mordenite. They obtained lower saturation capacities at 0 ^{o}C corresponding to only 30-76 % of the relevant micropore volumes. This was explained by that the cavities of mordenite could not be filled up by NO molecules at 0 ^{o}C due to the mean kinetic energy of NO at this temperature. The mean kinetic energy of NO at 0 ^{o}C was 1.5 times higher than that at the critical temperature, so NO molecules moved vigorously which decreased the frequency of adsorption in the micropore. However, a clear hysteresis was still observed in desorption branch of each isotherm at this temperature. These results suggested that the interaction between NO and the mordenite was strong enough at 0 ^{o}C to adsorb NO in the mordenite cavity (Matsumoto et al., 2000).

Furuyama and Morimoto studied the sorption of nitric oxide, carbon monoxide and nitrogen by sodium mordenite and found that the strength of the sorption affinity varied in the order of N_2<NO<CO. The isotherms were almost linear (obeying the Henry's Law) at lower coverage for all gases. At higher coverages, the slope for NO rose steeply while those for CO and N_2 decreased gradually. In the steep rise region, it took several days to attain equilibrium. This phenomenon was attributed to the dimerization of NO. The saturation adsorption amount was reported as 25.0 ml (STP)/g for CO and N_2 from the Langmuir model. On the other hand, the Langmuir equation could not be applied to the isotherm of NO. However, the molecular dimension of NO (bond length, r_o=0.114 nm) was almost the same as that of CO and N_2 (r_o=0.113 and 0.106 nm, respectively), so the saturation value for the amount sorbed for NO was estimated to be close to 25 ml (STP)/g. The one-dimensional gas model was applied for the sorbate in mordenite pores assuming the sorbates were aligned linearly. Then the effective diameter of the sorbed molecule (d_{eff}) was calculated as 0.4 nm from:

$$d_{eff} = L_p / V_1 \quad (2.10)$$

where L_p is the total pore length and V_l is expressed in number of molecules. Using crystal structure data, L_p was expressed as:

$$L_p = (\text{number of unit cell/g}) \times (\text{length of c axis}) \quad (2.11)$$

The isosteric heat of sorption changed with temperature and coverage. At fractional coverage of 0.02, the isosteric heat of sorption values for CO, N_2, and NO were 8.8, 8.0, and 7.1 kcal/mol at -30 ^oC, and 8.1, 6.6, and 6.6 kcal/mol at 30 ^oC, respectively. For NO, the isosteric heat of sorption could not be determined above fractional coverage of 0.1 due to the occurrence of dimerization. The examination of effect of the dipole moment on the thermodynamic properties of sorbates in mordenite showed that the magnitude of the isosteric heat of adsorption and the degree of rotational hindrance were affected slightly by the presence of a dipole moment. This indicated that the electrostatic field was very weak in the pores of mordenite and the magnitude of the isosteric heat of sorption was mainly determined by dispersion forces and that the contributions of the quadrupole and dipole moments were less significant (Furuyama and Morimoto, 1978).

Furuyama and Nagato performed argon, oxygen, nitrogen, nitric oxide, and carbon monoxide sorption experiments by magnesium, calcium, and barium mordenites over a temperature range of -50 to 150 ^oC. The sorption affinities were found to be in the order Ar<O_2<<N<NO<CO irrespective of the kind of mordenite. The order of gas sorbability of mordenite was Ba-M<Ca-M<Mg-M (M denotes mordenite). The isosteric heat of sorption at the coverage of 0.02 was found to be in the order of Ar≈O_2<<N_2≈NO<CO (5.7, 7.4, 12.8, 10-15, 15.8 for Mg-M; 6.3, 6.4, 9.9, 9-10, 12.1 for Ca-M; and 5.6, 5.7, 7.5, 7.8, and 9.3 for Ba-M, in kcal/mol). The differential molar entropy of the sorbate was divided into two terms: the thermal entropy and the configurational entropy. The configurational entropy was defined as a function of the coverage and subtracting it from the differential molar entropy of the adsorbate, the

thermal entropy was determined. The temperature dependency of the thermal entropy demonstrated the changes in the sorbed state. The steep increase in the thermal entropy with temperature indicated that the sorbed molecule translated one-dimensionally with free rotation and two-dimensional oscillation in the mordenite channels. Energies of dispersion, repulsion, induced dipole-field strength, permanent dipole-field strength, and molecular quadrupole-field gradient interactions were calculated quantitatively on the basis of the point charge model to determine the calculated isosteric heat of adsorption value. The comparison of the calculated and experimental isosteric heat of adsorption values indicated that the frequency of the rotation of the sorbed molecule was regulated by the periodic location of the alkaline-earth cation in the mordenite channels. They have succeeded in drawing a picture of the dynamic behavior of the sorbed molecule in the mordenite channels (Furuyama and Nagato, 1984).

Furuyama and co-workers also studied sorption of argon, oxygen, nitrogen, nitric oxide, and carbon monoxide by hydrogen mordenite (H-M), hydrogen ZSM-5 (H-ZSM-5), and sodium hydrogen mordenites (Na-H-M) over a temperature range of -60 to 70 ^{o}C. The hydrogen mordenite and ZSM-5 exhibited the sorption affinities in the order $Ar \leq O_2 << N_2 < NO < CO$. The gas sorbability of H-M was found to be lower than those of Li-M and Na-M which violated the general rule that the gas sorbability increases with a decrease in the cation size, if the electric charges of the cations are the same. The lower gas sorbability of H-ZSM-5 as compared to than that of Cs-M was attributed to the fewer cations present in H-ZSM-5, resulting in a weaker electrostatic field than that of Cs-M. The isosteric heats of sorption of Ar, O_2, N_2, NO, and CO were determined as 4.3, 4.4, 5.6, 5.6, and 6.9 for hydrogen mordenite and 3.5, 3.6, 4.3, 4.4, and 5.1 for hydrogen-ZSM-5 at the coverage of 0.02. The sums of the dispersion and repulsion energies were calculated for H-M, H-ZSM-5, and three kinds of hypothetical zeolites having 8- to 12-membered-ring channels and compared with each other. It was concluded that the sums of the dispersion and repulsion energies were remarkably affected by the size and shape of the zeolite channel (Furuyama et al., 1984).

Galán studied the adsorption of NO on 13X and 5A, alumina and nickel-kieselguhr and copper zinc oxide catalysts by using a chromatographic technique and moment theory. Molecular sieve pellets were crushed to average particle diameter of 272 μm and packed into the column with length of 20.46 cm and internal diameter of 7.75 mm. Carrier gas flow rate was set between 10-70 cm^3/min (25 ^{o}C, 1 atm). 1-cm^3 pulses of 5 mol% NO in helium balance was injected to the column and the response

peak was obtained using a thermal conductivity detector. The adsorbents were activated at 300 ^{o}C under 20-30 cm^3/min (25 ^{o}C, 1 atm) pure helium flow. It was found that NO was physically adsorbed on 13X in the temperature range between 50 and 100 ^{o}C, and the NO adsorption capacity of 13X was reported to be 0.5 cm^3/g at 50 ^{o}C. The low adsorption capacity of 13X was explained by absence of interaction between NO molecules and 13X due to the low molecular size of NO in comparison with the effective pore diameter of 13X (10 Å), i. e., NO molecules pass through 13X pores without any interaction. In the same study, the first moments (retention times) of the peaks for 5A were reported to decrease as the run number increases. It was suggested that NO interacted irreversibly with 5A and decreased its adsorption capacity with time (Galán, 1984).

Despres and co-workers studied the adsorption and temperature-programmed desorption of NO_x on copper-exchanged ZSM-5 (Cu-ZSM-5) and showed that NO could not be stored at 200 ^{o}C. In order to store NO, NO must be oxidized to NO_2. NO_2 was stored over a wide temperature range from both dry and humid feeds. However, water in the feed inhibited the oxidation of NO to NO_2, thereby its adsorption. This was probably attributed to competition of the sites for NO oxidation and for H_2O adsorption. It was reported that the over-exchanged zeolite catalyst used in the study tended to form species containing extra-lattice oxygen under oxidizing conditions, such as [Cu–O–Cu]$^{2+}$and [Cu^{+}–O–Cu^{2+}]. It was assumed that these extra-lattice oxygens were also involved in the oxidation of NO. The following reactio was proposed for the adsorption of NO_2:

$$3NO_2 + [CuO] \leftrightarrow NO + Cu(NO_3)_2 \qquad (2.12)$$

This reaction involves disproponation of NO_2 and production of two stored nitrate species bound to copper cations and release of one NO molecule to the gas phase. NO has also a negative effect on the storage of NO_2. This effect was attributed to reaction of the NO with the stored nitrates, resulting in a shift in the equilibrium of the above reaction back to NO_2. The TPD profiles revealed that the stored NO_x-species

were completely desorbed by heating up to 450 ^{o}C. The following overall reaction was proposed for the desorption process:

$$Cu(NO_3)_2 \rightarrow 2NO_2 + [CuO] + 1/2\,O_2 \qquad (2.13)$$

The decomposition of the stored species by heating resulted in the complete restoration of the adsorption sites. The maximum desorption of 380 ^{o}C implied high thermal stability of the stored species. In the presence of NO, the complete desorption of the nitrates occurred at temperatures at 150 ^{o}C instead of 300–400 ^{o}C. It was concluded that an ideal storage material should possess both the capabilities of oxidizing NO to NO_2 and of storing the NO_2 formed (Despres et al., 2003).

There are studies on adsorption of NO with natural zeolites regarding the catalytic activity of zeolites in selective catalytic reduction (SCR) of NO_x. These studies were performed at high temperatures and in the presence of other gases (H_2O, SO_2 and hydrocarbons) which coexist with NO_x in the exhaust gases.

Moreno-Tost and co-workers investigated the catalytic selective reduction of NO over Cu-exchanged natural zeolites (mordenite and clinoptilolite) using NH_3 as reducing agent and in the presence of excess oxygen. Cu (II)-exchanged zeolites were found to be very active catalysts in excess oxygen exhibiting good water tolerance. The samples displayed conversions of 95% at 177- 327 ^{o}C. No N_2O formation was observed by TPR analysis. The chemical state of the Cu(II) in exchanged zeolites was characterized by XPS and found that copper exists as Cu(II) ions coordinated with oxygen atoms of the zeolite and as CuO species (Moreno-Tost et al., 2004).

Kim and his colleagues studied the selective reduction of NO by CH_4 in the presence of excess O_2 on cobalt-exchanged synthetic clinoptilolite (Co-CLI). The catalytic results were compared with those obtained from Co-ZSM-5 and Co-FER. At temperatures above 500 ^{o}C, Co-CLI was found to be much more active for NO reduction than Co-ZSM-5, but less active than Co-FER. However, it was found that the selectivity for CH_4 toward reacting with NO at high temperatures (≥450 ^{o}C) was higher on Co-CLI than on Co-ZSM-5 or Co-FER. The importance of zeolite pore size as a structural parameter influencing the activity of intrazeolitic Co^{2+} ions for NO reduction

by CH_4 was discussed. They concluded that Co^{2+} ions were located at the thermodynamically more stable sites in 8-ring channels than in Co-ZSM-5 and Co-FER (Kim et al., 1999).

Long and Yang studied the SCR-NO with ammonia over different Fe^{3+}-exchanged zeolites (mordenite, clinoptilolite, beta, ferrierite, chabazite). It was found that Fe^{3+}-mordenite and Fe^{3+}-clinoptilolite were much more active than the commercial vanadia catalyst. They proposed that the NO oxidation to NO_2 was the rate-determining step. NO, N_2O_3, NO_2, and nitrate species were adsorbed to the iron sites while NH_3 molecules were adsorbed on Brønsted acid sites forming NH_4^+ (Long and Yang, 2002).

2.4. Studies on Supercritical Gas Adsorption in Natural Zeolites

Ma and Mancel studied the diffusion of NO and other gases in molecular sieve zeolites by gas chromatography in the temperature range of 133–325 ^oC. 1.8-3.6 mm adsorbent particles were packed in to the column with 1 cm inside diameter and 213 cm length and activated at 400 ^oC for 15 hours under helium flow. A pulse of gas was injected at the column inlet and the broadening of the peak was then analyzed for different carrier gas flow rates. The diffusion coefficients, isosteric heats of adsorption and activation energies were measured and found to decrease in the order of natural mordenite>Na-mordenite>H-mordenite>13X≈5A indicating the increased ease of diffusion in the three-dimensional pore system. The variation between the adsorbents were discussed in terms of the interaction between the surface and diffusing gas molecules as well as the pore size of the adsorbents with respect to the size of the diffusing gas molecules. The heats of adsorption of NO for 5A, 13X and natural mordenite were found as 8.9, 2.2 and 4.8 kcal/mole, respectively. The diffusion coefficients for NO were measured as 0.0034, 0.049 and 0.0036 cm^2/s for 5A, 13X and natural mordenite, respectively. The diffusion coefficients measured was the overall effective diffusion coefficient which include the contribution from both the micropores and macropores. The larger effective diffusion coefficient of 13X with respect to that of 5A was explained by the large pores of 13X. For some of the studied gas-adsorbent pairs, no chromatographic peak was observed although the pore size of the adsorbent

was larger than the diffusing molecule. This was attributed to the strong interaction between the cations in the case of the adsorbent and the gas molecule as well as to blockage of the paths of diffusion by the presence of relatively large cations. Since the gas chromatography method does not give information concerning the microscopic (molecular level) of the system, the interactions between the diffusing gas molecules and the adsorbent surface could be discussed at the macroscopic level (Ma and Mancel, 1972).

Triebe and Tezel carried out a study on adsorption of NO on a natural clinoptilolite. They used gas chromatographic method to examine the adsorption of NO on different zeolites in the temperature range of 150-200 ^{o}C to determine the potential for separation of the common pollutant (NO) from air. It was found that NO was the most strongly adsorbed adsorbate in the natural clinoptilolite and this strong interaction was attributed to the strong dipole-cation interaction of NO. The heat of adsorption was determined as 9.4 kcal/mol (Triebe and Tezel, 1995). On the other hand, it had been previously reported that in typical adsorption processes for removal of NO, the NO was converted to NO_2 in the presence of O_2 and subsequently adsorbed (Joithe et al., 1972; Sundaresan et al., 1967).

There are also studies in the literature on adsorption of supercritical gases in natural clinoptilolite. Ackley and Yang investigated adsorption and diffusion characteristics of N_2 and CH_4 on modified natural clinoptilolites. The fully exchanged forms of clinoptilolite with monovalent cations (K^+, Na^+ and H^+) and highly exchanged bivalent cations (Ca^{2+} and Mg^{2+}) were produced. A purified form of the raw natural zeolite was also tested in the study. The supercritical adsorption data was obtained gravimetrically at 27 and 50 ^{o}C for both N_2 and CH_4. These gases were selected as probe molecules of similar kinetic diameter but different shape. The Dubinin-Astakhov volume filling model was applied to the supercritical isotherm data to estimate adsorption capacities and the pore volumes at the normal boiling temperatures of N_2 and CH_4. However, it was stated that the normal boiling temperatures were low for practical isotherm measurement due to the slow diffusion of these gases. Therefore, they decided to predict the limiting adsorption volume or pore volume at the normal boiling point using the isotherms measured above the critical temperature. Adsorption isotherms and energetic heterogeneity have been discussed in terms of the types of cations and their locations in the clinoptilolite channels. Adsorption of N_2 and CH_4 molecules was strongly affected by the internal electrostatic fields that envelop the entire pore space. It

was affirmed that the contributions of the framework ions, charge-balancing cations, and adsorbate molecules to these internal fields were important and interdependent. Molecular sieving was confirmed for CH_4 in the Na^+ and Ca^{2+} clinoptilolites and for N_2 in Ca^{2+} clinoptilolite. It was stated that presence of mixture of cations in natural clinoptilolites complicates any attempt to associate structural properties to the adsorption and diffusion characteristics of the adsorbent. Therefore, it is required to obtain homoionic form of the zeolite in order to correlate the adsorption and diffusion properties to the structural properties. It was concluded that adsorption characteristics of the clinoptilolite have been significantly changed through cation modification (Ackley and Yang, 1991a).

Ackley and Yang also studied the effects of cation type, size, location and distribution of the diffusion of N_2 and CH_4 molecules by changing the channel structure of clinoptilolite by ion exchange. The plane sheet and parallel channel diffusion models were developed from the one-dimensional plane sheet diffusion equation to represent the rapid and slow components of diffusion evident from the experimental data. Concentration-dependent diffusion time constants for both the eight- and ten-member ring channels of the clinoptilolite structure were determined from gravimetric uptake measurements. It was found that the concentration-dependent diffusion time constants varied by a factor of more than 1000 for N_2 and CH_4 (Ackley and Yang, 1991b).

2.5. Fourier Transform Infrared (FTIR) Spectroscopy Studies on NO Adsorption

NO species adsorbed on metal ion–exchanged zeolites and its derivatives have been extensively investigated by infrared spectroscopy. This technique is widely used for assigning the state of NO species adsorbed on zeolites. Infrared spectroscopy gives information on the state of the adsorbed species on the zeolite surface upon NO adsorption, evacuation and temperature-programmed desorption. Infrared spectroscopy coupled with probe molecule adsorption is a sensitive technique for investigations of the properties of solid surfaces. The interaction of molecular species with active metal sites is usually studied with NO probe molecule using the FTIR technique. Therefore, the

various transition metal species located in the structure of the zeolite can be differentiated and the nature and properties of adsorption sites present on the surface (e.g. types of sites, the oxidation state of the metal, the state and localization of the cations) can be examined (Ryczkowski, 2001).

Hadjiivanov and his colleagues proposed the following reaction sequence for the adsorption of NO on Cu-ZSM-5 in the presence of oxygen at room temperature:

$$NO \rightarrow N_2O_3 \rightarrow N_2O_4 \rightarrow NO_2 \rightarrow NO_3 \qquad (2.14)$$

It was reported that the spectra showed only the bands typical for nitrate species at 180 ^{o}C. The stability of these nitrates in the presence of water or NO was also investigated and it was deduced that once formed, nitrates were only slightly affected by water and NO (Hadjiivanov et al., 1996).

Mihaylov and co-workers adsorbed NO at ambient temperature on NiNaY at different equilibrium pressures. After admission of NO at equilibrium pressure of 670 Pa for 10 minutes, a series of low-intensity bands with maxima at 1507, 1457, 1410, 1378, 1335, 1315 and 1270 cm^{-1} were observed and assigned to NO_y^- species (Hadjiivanov, 2000; Pozdnyakov and Filimonov, 1973). They noticed that the bands at 1410, 1378 and 1270 cm^{-1} have also been observed with NaY and ascribed to symmetric nitrates (1410 and 1380 cm^{-1}) and bidentate nitrites (1270 cm^{-1}) formed with the participation of Na^+ ions (Ivanova et al., 2001; Szanyi et al., 2003). Therefore, the remaining bands (1507, 1457, 1335 and 1315 cm^{-1}) were attributed to NO_y^- compounds of nickel. It was concluded that although it was difficult to make a detailed interpretation of the spectra but the bands were elucidated mainly of the presence of nitrates. The free nitrate ion was characterized by ν_3 and ν_1 vibrations at 1380 and 1050 cm^{-1}, respectively and ν_1 vibration is not IR active (Nakamoto, 1966). The bands of NO_y^- complexes formed on NiNaY upon adsorption of NO on at ambient temperature at different equilibrium pressures resisted evacuation (Mihaylov et al., 2004).

Chao and Lunsford investigated the adsorption of NO on CaY, NaY, decationated Y and HY. They detected at least eight absorption peaks on each zeolite in the infrared spectra. The infrared absorption peaks were identified by examining the

equilibrium between the adsorbed molecules and nitrogen oxides in the gas phase, and by comparing the spectra of the adsorbed species with infrared spectra produced upon adsorption of various nitrogen oxides on zeolites. The bands in the spectra were assigned to the adsorbed N_2O, NO_2^+, N_2O_3, NO_3-, a nitrito complex, and covalently bonded nitrite. The doublet observed at 1400 cm^{-1} induced upon adsorption of NO on NaY and CaY zeolites were assigned to NO_3^- species (Nakamoto, 1966). This doublet was also produced by doping NaY with small amounts of $NaNO_3$. The formation of this doublet upon adsorption of NO_2 on NaY indicated that there were some easily extractable oxygen ions in NaY (Chao and Lunsford, 1971).

Table 2.3. Infrared absorption bands induced by adsorbing NO on zeolite.
(Source: Chao and Lunsford, 1971)

Zeolite	23 ^oC	Cooled to -78 ^oC	Degassed at 23 ^oC	Degassed at 200 ^oC	Degassed at 300 ^oC	Degassed at 400 ^oC
NaY	none	1260, 1305, 1555, 1920, 2000, 2100, 2240	1260, 1400, 3650	1400	1400	none
CaY	1305 (unresolved), 1565, 1935, 2040, 2200, 2250	1305, 1565, 1935, 2040, 2200, 2250	2040, 2200, 3640	1400, 1470	1400, 1470	none
DecY	none	1300, 1570, 1910, 1980, 2120, 2240	1585, 1650, 2000, 2120	1585, 1650	none	none
HY	none	2200	none	none	none	none

Addison and Barrer claimed that nitrite and nitrate ions were resulted from the reaction of NO_2 with residual intracrystalline water to produce HNO_2 and HNO_3 (Addison and Barrer, 1955). On the other hand, Chao and Lunsford proposed that although such a reaction might be the source of protons and nitrite ions, it was not the major source of nitrate ions, since the disproportionation reaction on decationated zeolites produced SiOH groups, but very few nitrate or nitrite ions, and also very few SiOH groups were produced when 0.2 molecule per cage of NO_2 was adsorbed on CaY. At this NO_2 level, the nitrate ion concentration was comparable to that from the disproportionation reaction. Table 2.3 shows the infrared absorption bands induced due to NO adsorption and disproportionation on NaY, CaY, decationized Y (DecY) and HY zeolites (Chao and Lunsford, 1971).

Table 2.4. Infrared absorption bands produced by disproportionation reactions of NO on zeolites. (Source: Ivanova et al., 2001)

Sample	Assignment	Bands (cm^{-1})	Note
CoY	NO^+	2194, 2133	Easily removed by evacuation, the 2194 cm^{-1} band alternatively assigned to NO_2^+
	$Co^{2+}(NO)_2$	1900, 1819	Disappear in oxygen atmosphere
	N_2O_3	1900-1886, 1583, 1300	Easily removed by evacuation
	N_2O_4	1747	Easily removed by evacuation
	NO_2	1662	Reacts with NO
	Bridged nitrates	1640-1610, 1340-1320	Tentative assignment
	Nitro species	1563, 1383	Very stable
	Bidendate nitrites	1270	Bonded to Na^+ sites
Co-ZSM-5	Co^{2+}-$(NO)_2$	1894, 1812	Disappear in oxygen atmosphere
	Co^{3+}-NO	1940	Easily removed by evacuation
	Co^{2+}-NO	1857	Produced after decomposition of dinitrosyls
	NO^+	2133	Easily removed by evacuation
	Bridged nitrates	1646	Stable up to 573 K
	Bidendate nitrates	1598, 1575	Stable up to 573 K
	Bridged nitrates	1539-1507	Stable up to 473 K, react easily with methane
NaY	Symmetric nitrates	1415, 1383	Stable to ≈ 400 ^oC
	Bidendate nitrites	1270	Also formed on CoY
	NO^-	1260	Disappears in oxygen atmosphere

Ivanova and co-workers studied the species formed upon NO adsorption on NaY, CoY and Co-ZSM-5. The bands and the assignments are given in Table 2.4. The bands at 1415 and 1383 cm^{-1} observed for NaY were attributed to symmetric-like nitrates. The nitrates (formed in CoY, exhibited bands at 1488 and 1473 cm^{-1}) and the respective nitrospecies (formed in CoY, exhibited bands at 1563 and 1383 cm^{-1}) showed very high thermal stability (stable at ~400 ^{o}C). The detection of these bands in the absence of oxygen was attributed to the oxidation of NO using the surface hydroxyls or lattice oxygen atoms as oxidation source (Ivanova et al., 2001):

$$2NO_2 + \frac{1}{2}O_2 + O^{2-} \rightarrow 2NO_3^- \tag{2.15}$$

$$N_2O_3 + O^{2-} \rightarrow 2NO_2^- \tag{2.16}$$

Salama and colleagues studied the in situ interaction of NO gas on the cerium framework-substituted ZSM-5 and mordenite zeolites by FTIR spectroscopy. Samples of ZSM-5 and mordenite-containing cerium (7.5 % by weight expressed as CeO_2) have been hydrothermally synthesized from starting gel upon which the introduction of cerium is being made during synthesis of zeolites. The adsorption of NO led to the formation of a series of nitrosyl species: N_2O (2245 cm^{-1}), NO^+ (2160 cm^{-1}), NO (1910 cm^{-1}), N_2O_3 (1880, 1580 cm^{-1}), $(NO)_{2s,as}$ (1844, 1734–1720 cm^{-1}), NO_2 (1630 cm^{-1}) and ionic compounds, i.e. nitrato and nitrito NO_x^- (x=2-3) (1300-1500 cm^{-1}). The ionic compounds formed were stable upon evacuation. Such nitrosyl complexes were favorably formed on Ce-ZSM-5 than on Ce-mordenite due to facilitated intervention of the cerium couple (Ce^{III}/Ce^{IV}) on the former than on the latter (Salama et al., 2005).

Huang and Yang studied NO adsorption on the Fe-Mn-Ti oxides by FTIR spectroscopy. It was shown that the nitrate was the final species for NO adsorption. NO_2 and nitrite were the intermediates during nitrate formation on the oxides. TPD profiles indicated that NOx species could desorb at temperatures below 400 °C. The high efficiency for NO removal on these oxides was related to their high activities in NO

oxidation to NO_2 at 25 °C. The effect of H_2O on NOx adsorption was also studied. When a mixed gas containing 500 ppm NO, 10% O_2, 2.5% H_2O, and helium was passed over the oxides for 60 minutes, two infrared bands were observed at 1635 and 1383 cm^{-1}. The 1635 cm^{-1} band was assigned to adsorbed H_2O while that at 1383 cm^{-1} was due to nitrate species (Pinna, 1998; Laane and Ohlsen, 1980). The strength of the band due to nitrate species was found to be lower in the presence of H_2O suggesting an inhibiting role for H_2O. When H_2O supply was stopped while the other conditions were kept the same, the band at 1635 cm^{-1} decreased while the band at 1383 cm^{-1} increased gradually with time. This indicated replacement of adsorbed H_2O by nitrate species. According to these results, they proposed a possible mechanism for the formation of nitrate in which the lattice oxygen in the transition metal oxides was involved as follows:

$$NO + \tfrac{1}{2}O_2 \rightarrow NO_2 \tag{2.17}$$

$$NO + NO_2 \rightarrow N_2O_3 \tag{2.18}$$

$$N_2O_3 + O^{2*} \rightarrow 2NO_2^- \tag{2.19}$$

$$2NO_2 + O^{2-} \rightarrow NO_3^- + NO_2^- \tag{2.20}$$

$$NO_2^- + \tfrac{1}{2}O_2 \rightarrow NO_3^- \tag{2.21}$$

$$2NO_2 + \tfrac{1}{2}O_2 \rightarrow N_2O_5 \tag{2.22}$$

$$N_2O_5 + O^{2-} \rightarrow 2NO_3^- \tag{2.23}$$

In reaction (2.17), NO is oxidized to NO_2 by O_2 on the oxides. Subsequently, the formed NO_2 reacts with NO to produce N_2O_3 (reaction 2.18), which then reacts with lattice oxygen to form nitrite species (reaction 2.19). On the other hand, the NO_2 can also react with lattice oxygen and disproportionate to nitrate and nitrite species (reaction 2.20). The nitrite species can be oxidized to nitrate by oxygen (reaction 2.21). Moreover, NO_2 may also react to form nitrate by oxidization with oxygen (reactions 2.22 and 2.23). The formed nitrate is then stored on the oxides. NO oxidation to NO_2 is a very important step for NOx adsorption. Since Fe-Mn-based sorbents had very high

NO conversions to NO_2, they showed high NOx adsorption rates (Huang and Yang, 2001).

Table 2.5. Infrared spectra results of NO adsorbed on metal ion-exchanged zeolites. (Source: Iwamoto and Yahiro, 2003)

Metal	Zeolite	Frequency (cm^{-1})	Adsorbed species	Note	Reference
Fe	MFI	1920	$(NO)_2$[sym]	On Fe^{2+}	(Hadjiivanov et al., 1999)
		1880-1878	NO	On Fe^{2+}	
		1835	$(NO)_2$[asym]	On Fe^{2+}	
		1620	NO_3	Bidendate	
		1570	NO_3	Monodendate	
	FAU(Y)	1917	$(NO)_2$[sym]	on a highly accessible Fe^{2+}	(Segawa et al., 1982)
		1870	NO	on a sterically hindered Fe^{2+}	
		1845	NO	on an intermediate accesible Fe^{2+}	
		1815	$(NO)_2$[asym]	on a highly accessible Fe^{2+}	
		1767	NO	on a highly accessible Fe^{2+}	
Co	MFI	2120	NO_2^+		(Zhang et al., 1995)
		1940-1935	NO^+	On Co^{2+}	
		1894	$(NO)_2$[sym]	On Co^{2+}	
		1810	$(NO)_2$[asym]	On Co^{2+}	
	FER	1930	NO^+		(Li et al., 1994)
		1890	$(NO)_2$[sym]	On Co^{2+}	
		1810	$(NO)_2$[asym]	On Co^{2+}	
		1630	NO_2	Nitro	
		1610	NO_2	Monodendate nitrito	
		1560-1540	NO_3		
	FAU(Y)	1930-1886	NO	(unstable at room T)	(Li et al., 1994)
		1910	$(NO)_2$[sym]	on Co^{2+}	
		1830	$(NO)_2$[asym]	on Co^{2+}	
		1800	NO	(Unstable at room T)	
	BEA	1935	NO	On Co^{n+}	(Tabat et al., 1998)
		1898	$(NO)_2$[sym]	On Co^{n+}	
		1816	$(NO)_2$[asym]	On Co^{n+}	
		1540	NO_2	Monodendate nitrito	
		Below 1300	NO_2	Chealating nitrito	

(cont. on next page)

Table 2.5 (cont.). Infrared spectra results of NO adsorbed on metal ion-exchanged zeolites. (Source: Iwamoto and Yahiro, 2003)

Metal	Zeolite	Frequency (cm^{-1})	Adsorbed species	Note	Reference
Cu	MFI	2240-2230	N_2O		(Iwamoto et al., 1992; Valyon and Hall, 1993)
		1905-1904	NO^+	On an accessible isolated Cu^{2+}	
		1895	NO	On Cu^{2+} carrying extralattice oxygen	
		1906-1895	NO	On Cu^{2+}	
		1827-1825	$(NO)_2^-$[sym]	On Cu^+	
		1815-1807	NO^-	On Cu^+	
		1734-1730	$(NO)_2^-$[asym]	On Cu^+	
		1630-1619	NO		
		1340-1300	NO_2[sym], NO_3		
	FAU(Y)	1951-1946	NO	On an accessible isolated Cu^{2+}	(Valyon and Hall, 1993)
		1912-1907	NO	On Cu^{2+} carrying extralattice oxygen	
		1902-1891	NO	On isolated Cu^{2+} moved to accessible positon	
		1825	$(NO)_2$[sym]	On Cu^+	
		1732-1740	NO	On Cu^+	
		1796-1802	$(NO)_2$[asym]	On Cu^+	
		1400	NO_3		
Ag	MFI	1630	NO_3	bridging	(Hadjiivanov, 1998)
		1576	NO_3	bidendate	
		1440	NO_2	Monodendate nitrito	
	FAU(Y)	1884	NO	in $[Ag(I)NO]^+$	(Hadjiivanov, 1998)

Recently, Iwamoto and Yahiro reviewed the studies on the nitrogen monoxide removal by metal ion-exchanged zeolites. Cobalt and copper-containing zeolites have been extensively studied. The IR bands associated with NO species on metal ion-exchanged zeolites are listed Table 2.5 (Zhang et al., 1995; Iwamoto et al., 1992; Valyon and Hall, 1993; Hadjiivanov et al., 1999; Segawa et al., 1982; Li et al., 1994; Tabata et al., 1998; Hadjiivanov, 1998; Chao and Lunsford, 1974). The stretching frequency of NO adsorbed on metal ion–exchanged zeolite spans a wide range, 1940–1780 cm^{-1}, depending mainly on the type of cation present in the zeolite. NO species detected on metal ion–exchanged zeolites were mainly classified into three types:

mononitrosyl species with or without the electron transfer from and to metal ion in zeolites, dinitrosyl species, $(NO)_2$, and NO derivatives such as NO_2, N_2O, NO_3, and N_2O_3, which are produced by disproportionation and oxidation reactions of NO (Iwamoto and Yahiro, 2003).

Hadjiivanov summarized the position of IR bands for surface NO_x species on metals, metal oxides, and zeolites containing metal ions (Figure 2.8) (Hadjiivanov, 2000).

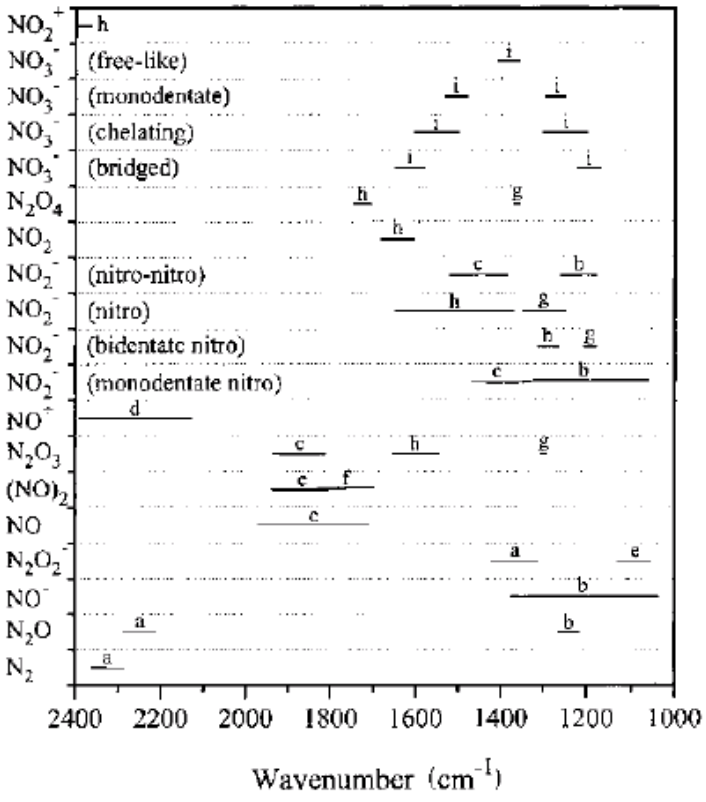

Figure 2.8. N-N and N-O stretching modes of surface N_xO_y species. a, ν(N-N); b, ν(N-O); c, ν(N=O); d, ν(N=O); e, $\nu_s(N\text{-}O)_2$; f, $\nu_{as}(N\text{-}O)_2$; g, $\nu_s(NO_2)$; h, $\nu_{as}(NO_2)$; i, $\nu(NO_3)$. (Source: Hadjiivanov, 2000)

Nitric oxide has been used as a probe to study the state of supported transition metal ions. It has been shown that $Cu^{+,}$ Ag^+, Ni^{2+}, Fe^{2+} and Cr^{2+} ions form complexes with NO in zeolites and the interaction was interpreted in terms of either covalent bonding or the donation of an electron from the NO to the metal ion. It was reported

that the latter strengthened the N-O bond and to increased the stability of the nitric oxide molecule (Chao and Lunsford, 1972, 1974; Huang, 1974; Jermyn et al., 1973; Naccache and Ben Taarit, 1973).

2.6. Studies on Health Applications of Zeolites

The clinoptilolite-rich natural zeolite and their modified forms have been evaluated as a gastric antacid, anti-diarrheic, antihyperglicemic, hipocholesterolemic and as a matrix for the release of ions and organic molecules (Rivera et al., 1998; Rodriguez-Fuentes et al., 1997; Conception-Rosabal et al., 1997, 2000; Simón-Carballo et al., 2001; Lam et al., 1998). The zeolites have been studied also as a potential adjuvant in anticancer treatment (Parlat et al., 1999; Seidel et al., 1997; Pavelic et al., 2001, 2002). The use of clinoptilolite-rich natural zeolites as slow release of drug matrix has been studied in order to create synergetic interaction between the inherent properties of zeolites (antacid, antibacterial, antiviral, immunostimulatory etc.) and the loaded drug, and/or to attenuate the side effects of the drug. For this purpose, Lam and co-workers performed a theoretical study to investigate the adsorption of aspirin in the natural clinoptilolite–heulandite. The aim was development of antacid-aspirin formulation. The results showed the possibility of the physical adsorption of aspirin by clinoptilolite. It was reported that the presence of more aluminum and compensating cations in the zeolite structure did not significantly change the results (Lam et al., 1998).

Farías and co-workers studied the physicochemical interaction between the sodium and calcium enriched forms of natural clinoptilolite and two drugs (metronidazole and sulfamethoxazole) whether the buffering character (antacid) of the natural clinoptilolite could attenuate the gastrointestinal side effects in a parallel administration. The oral administration of these drugs may cause side effects associated with gastrointestinal disturbances. The chemical behavior of these organic molecules in the presence of the zeolite was investigated in simulated aqueous medium of the gastrointestinal tract by using UV and infrared spectroscopy. The structure of the two drugs remained unaltered after interaction with the zeolites. It was demonstrated that metronidazole was not adsorbed on the natural zeolite but adsorbed on the washed

zeolite demonstrating the effect of non-zeolitic mineral phases on the adsorption behavior. They observed moderate incorporation of protonated form of metronidazole for sodium and calcium enriched zeolites at pH=1.2. The interaction with sulfamethoxazole was found to be negligible at the pH values considered. It was claimed that the interaction between the drugs and the zeolites depended on the polarity of the drug molecules and on the nature of the zeolite mineral. These results suggested that zeolites and drugs could be administrated in parallel without any loss of the individual pharmaceutical effect of each product (Farías et al., 2003).

Rivera and colleagues also studied the influence of different treatments (sodium exchange, surfactant adsorption, drug adsorption) on the structural behavior of natural clinoptilolite in connection to its potential utilization as host material for slow release of drugs. The results indicated sodium exchange had little influence on the appearance of the octahedral aluminum, but the Al extraction from the framework seems to occur in preferential and different sites of both samples, when submitted to an acid environment close to stomach conditions (pH 1.2). Similar conditions to those expected in the duodenum (pH 5.5) did not affect the framework neither natural or sodium clinoptilolite. The presence of surfactant and drugs on the zeolite did not produce structural changes and resulted in a strong decrease of the specific surface area. It was concluded that the zeolitic materials could be used as drug support drugs of very different nature (Rivera et al., 2003).

Rivera and Farías carried out a preliminary study to explore capability of the purified natural clinoptilolite as a convenient support to host molecules of pharmaceutical interest. They studied the incorporation of two model drugs (sulfamethoxazole and metronidazole) with different surfactant/clinoptilolite composites. The composites and zeolite–surfactant-drugs systems were characterized chemically and physically. The studies by infrared spectroscopy indicated that the zeolite structure remained unchanged after the modification with the surfactant and the drug. They have shown that a cationic surfactant was noticeably adsorbed by natural clinoptilolite and the model drug sulfametoxazole (the least polar drug) was adsorbed by this zeolite-cationic surfactant system. The adsorption of this drug increased with the amount of the cationic surfactant on the zeolite and with the concentration of drug in solution. The thermal stability of this formulation increased when the admicelles hosted drug (sulfamethoxazole) in their interior. Approximately 80% of the drug was released

from the drug-zeolite-surfactant formulation in about 24 hours (Rivera and Farías, 2005).

In the area of improvement of diagnostic methods and development of better drug delivery systems, recently, zeolites (zeolite Y, mordenite, silicalite) were proposed as a tool for in-cell chemistry. The adsorption and delivery of a low molecular bioactive substance, N-nitro-l-arginine methyl ester (L-NAME) which is known as inhibitor of the cellular synthesis of NO, into viable cells were investigated by the dealuminated forms of the zeolites (Dahm and Eriksson, 2004). More recently, zeolite-Y powder was functionalized with ferric iron-diethyldithiocarbamate complexes and applied to trap nitric oxide radicals in liquids and biological systems (van Faassen and Vanin, 2006).

Khare and co-workers examined the effect of a silver zeolite-impregnated catheter on catheter-related colonization and infection in adult critical care patients. The study was conducted in vivo and involved 246 CVC insertions (122 silver-impregnated and 124 non-impregnated). CVC tip colonization (biofilm-forming micro-organisms including coagulase negative staphylococci, *Staphylococcus aureus, Enterococcus faecalis, Escherichia coli, Pseudomonas aeruginosa, Candida albicans*) and catheter-related bloodstream infections (CR-BSI) after insertion were analyzed. The overall colonization rate was significantly lowered in the silver zeolite-impregnated CVC tips as compared with the control CVC tips. In addition, there was a lower rate of tip colonization by coagulase negative staphylococci in the silver zeolite-impregnated CVC tips as compared with the control CVC tips. Silver zeolite powder was mixed with the bulk polyurethane material during the manufacturing of the CVC tips. The mechanism of silver impregnated CVC tips were explained by the release of silver ions tightly bonded to the zeolite by active ion-exchange upon contact with blood and body fluids in biological environment (Khare et al., 2006).

Recently, Wheatley and his colleagues measured the adsorption/desorption of nitric oxide gas in Co-exchanged zeolite A at 25 ^{o}C gravimetrically. The zeolite (~130 mg) was initially outgassed at 300 ^{o}C under 1×10^{-4} mbar until no further weight loss was observed. NO gas was introduced into the system until the desired pressure was achieved, and the mass uptake of the sample was measured as a function of time until the adsorption equilibrium was achieved. In this manner an adsorption isotherm was collected by incrementally increasing the pressure and recording the increase of the adsorbent weight at equilibrium. Desorption of adsorbed nitric oxide gas in the samples was performed by gradually decreasing the system pressure to 2×10^{-2} mbar. The

adsorption and desorption isotherms shown in Figure 2.9 indicated that the Co-exchanged zeolite A exhibited affinity for NO, even at low pressures the majority of the gas was adsorbed irreversibly. The hysteresis observed in the adsorption/desorption isotherm indicated that the zeolite could hold NO at pressures below those needed to load NO into the adsorbent (Wheatley et al., 2006).

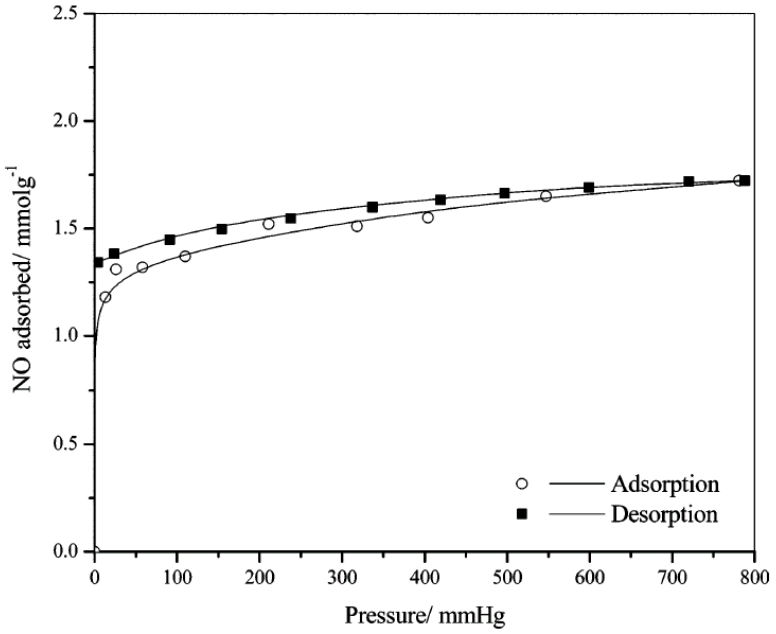

Figure 2.9. Adsorption and desorption isotherms of NO in Co-exchanged zeolite A at 25 ^{o}C. (Source: Wheatley et al., 2006)

The NO release profile for the NO-loaded cobalt-exchanged zeolite A (31 mg) under 200 ml/min flow of argon with relative humidity of 11% as a cumulative total amount of NO released per gram of zeolite are shown in Figure 2.10. The total amount of NO released was approximately 1 mmol NO/g of zeolite. They also stated that the amount of moisture present in the gas flow is important in controlling the release rate of the NO. Increasing the relative humidity (while keeping the flow rate constant) to 22% increased the rate of NO release (Wheatley et al., 2006).

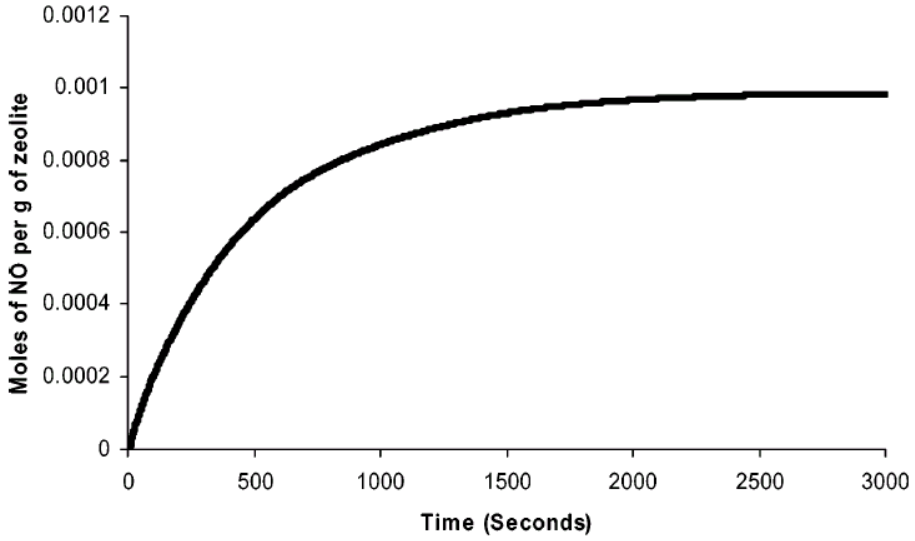

Figure 2.10. NO release profile for NO-loaded Co-exchanged zeolite A.
(Source: Wheatley et al., 2006)

They also measured the release of NO from the zeolites alternatively by contacting the zeolite with moist argon (5 ml/min) that was subsequently bubbled through a liquid phase (phosphate buffered saline, pH 7.4 at 25 ^{o}C). The amount of NO dissolved in the solution was then measured electrochemically. The NO release profiles for the transition metal-exchanged zeolite-A samples obtained are shown in Figure 2.11. Due to slow flow rate of the argon even in moisture-saturated argon, the release of the NO took place much more slowly and lasted up to 10 hours. The amount of NO released was found to be different for each zeolite and in good agreement with those in the previously reported studies on NO adsorption properties of transition metal zeolites. It was found that Co-exchanged zeolites released the most NO (~32 nM NO/mg zeolite) while the original Na-form of the zeolite released the least NO (~6 nM NO/mg zeolite). The low NO release from the Cu-exchanged zeolite A (over-exchanged) was explained by the presence of Cu cations as hydroxide species in the zeolite reducing the availability of the metal cations for NO coordination. It was concluded that the amount of NO released by the zeolite was correlated with the type and amount of the transition metal present (Wheatley et al., 2006).

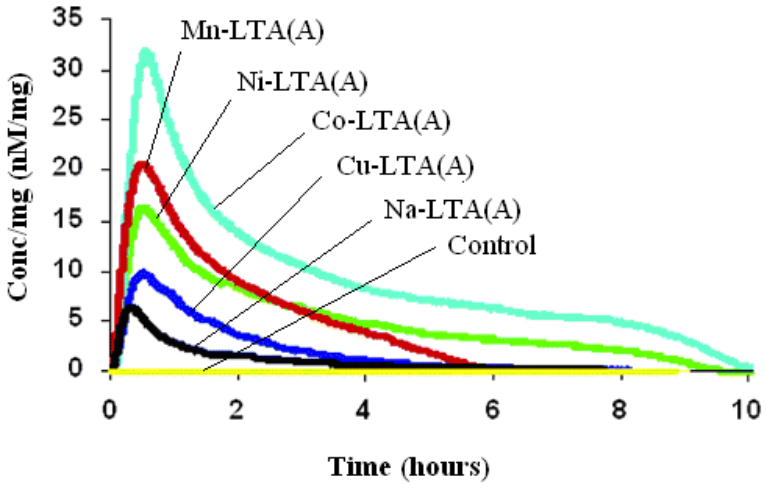

Figure 2.11. NO release profiles of NO-loaded metal-exchanged zeolite-A. (Source: Wheatley et al., 2006)

In another study, from the same research group Xiao and co-workers showed that zeolites (LTA, FAU) exchanged with transition metal cations Co^{2+}, Mn^{2+}, Zn^{2+} and Cu^{2+} were capable of storing and delivering a large quantity of NO in the range of 1.2-2.7 mmol/g. But these values were not in agreement with those given in the figures (Figure 2.12). The maximum amount of NO released was measured as about 0.82 mmol/g for the Zn-LTA and the minimum as 0.02 mmol/g Co-FAU. The differences in NO adsorption capacities of the zeolites were explained by the differences in the pore volumes of the zeolites exchanged with different metals. The NO adsorption capacities of zeolites FAU and LTA exchanged with the same metal were found to be different from each other. This was attributed to that the metal ion exchange affected the pore volume of zeolite FAU more significantly than that of LTA. The storage of NO mainly involved coordination of NO to metal cation sites. The stored nitric oxide was released by exposing the zeolites to a moisture atmosphere. The NO release took more than 2 hours for the NO concentration decreasing below ~5 ppb in outlet gas. It was also stated that the NO release rate could be controlled by tailoring the zeolite framework and the release conditions (Xiao et al., 2007).

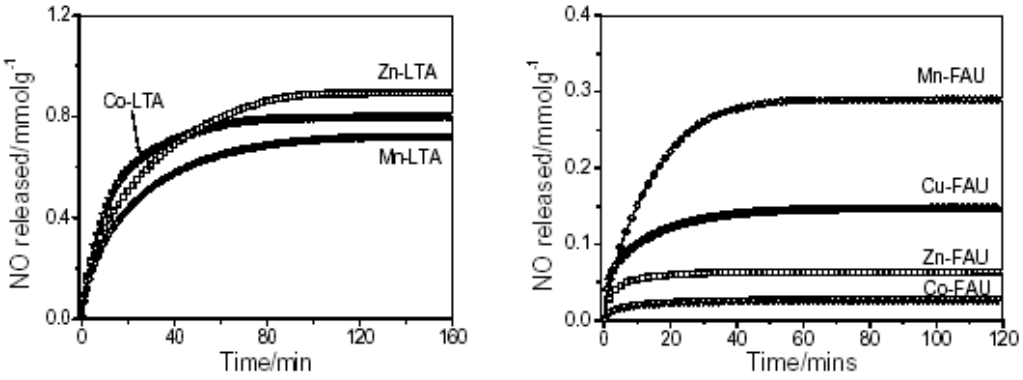

Figure 2.12. Integrated profiles of NO releasing from zeolites LTA and FAU. (Source: Xiao et al., 2007b)

The release of NO from the zeolites was studied under dynamic conditions by passing humid inert gas through samples, it was suggested that the NO release mechanism involved transport of the water molecules in carrier gas to the external surface of zeolite and then diffusion in pores, adsorption of the water at metal cation sites, displacement of the water molecule with the adsorbed NO molecules and diffusion of NO along pore into the gas that passed through. A double first order kinetic equation was fitted to the NO release kinetic data assuming that NO release might have occurred simultaneously from two individual parts inside zeolites characterized by releasing rate coefficients of k_1 and k_2 (Xiao et al., 2007):

$$n = n_1\left(1 - e^{-k_1 t}\right) + n_2\left(1 - e^{-k_2 t}\right) \tag{2.24}$$

where n is the amount of NO released (mmol/g zeolite). It was stated that $n_2=0$ for kinetically uniform release of NO. This case was observed for Mn-FAU (k_1=8.67×10^{-4} s^{-1}) and Co-FAU (k_1=2.45×10^{-3} s^{-1}). Cu-FAU and Zn-FAU zeolites exhibited kinetically nonuniform NO release profiles with k_1/k_2 ratios of 1.79×10^{-2}/1.03×10^{-3} and 9.50×10^{-3}/1.10×10^{-3}, respectively. The greater n and lower k values indicated that NO release lasted longer and a higher quantity of NO was delivered (Xiao et al., 2007).

The motivation of the present study was to test the NO adsorption, storage and release capability of the clinoptilolite-rich local natural zeolite. This requires the adsorption equilibrium and kinetic data. These data are not available in the literature. For the storage purposes the irreversible adsorption capacity is also required. Furthermore, in order to tailor the NO adsorption properties of the zeolite and elicit the mechanism of the interaction of NO with the zeolite, the data on the effect of type and amount of cations present in the zeolite on its adsorption properties are necessary.

CHAPTER 3

THEORY

For applications of the adsorbent for adsorption, storage and release of an adsorbate, it is necessary to determine the total, reversible and irreversible adsorption capacities of the adsorbent. Furthermore, the equilibrium and kinetics of NO adsorption in the natural zeolite are required in order to define the adsorption system. These parameters are determined by fitting the experimental data to the appropriate model of the process. The model should include all the mass and heat transfer processes taking place within the bed and the particles in order to define the system realistically.

3.1. Adsorption in Micropores

In micropores of size comparable to the size of adsorbate molecule, adsorption takes place by attractive forces from the micropore wall, and the adsorbate molecules begin to fill the micropore volumetrically. (Suzuki, 1990). Adsorption in micropores is affected by the adsorbent structure and surface composition, pore size and shape, polarizabilities and polarities of the interacting centers, size and shape of the adsorptive molecule and adsorption temperature (Sing et al., 2004). The cations in the micropores of zeolites exhibit strong electrostatic field and cause strong adsorption of polar molecules. On the other hand, the cation may effectively block the pore such that certain molecules are excluded (steric effect). In this case the micropore volume measured is lower than the actual one. The steric effect can also be caused by the shape of the pore. Micropore volume capacity is also dependent on the packing of the adsorbed molecules in the micropore (Sing et al., 2004).

The micropore volume can be determined experimentally from the adsorbed amount at saturation provided that the isotherm is Type 1. If the adsorbent contains only

micropores, then the total adsorption capacity approaches the micropore volume. Gurvitsch's rule states that the adsorption uptake at relative pressure of approximately 1, when expressed as a volume of liquid (using the normal liquid density) is the same for all adsorptives on a given adsorbent (Gurvitsch, 1915).

Kaneko and Murata claimed that in micropores of size comparable to the size of the supercritical adsorbate molecule has a very deep molecular potential well gives rise to adsorption of the supercritical gas to some extent, but not in abundant amounts. The volume of vapor molecules adsorbed is almost equal to the micropore volume. On the other hand, the volume of supercritical gas molecules adsorbed was found to be less than the micropore volume (Kaneko and Murata, 1997).

3.2. Dynamics of Adsorption in Packed Columns

The amount of gas adsorbed is one of the basic parameters required in the adsorption studies. The amount adsorbed may be calculated from variations of the gas pressure in a specified volume (volumetric adsorption system) or from variations of the weight of the adsorbent in a static or continuous flow apparatus (gravimetric adsorption system). It is also possible to determine the adsorption capacity by means of a dynamic adsorption system where the adsorption occurs under the flow of adsorbate. Generally in dynamic adsorption systems packed columns are used.

Dynamics of adsorption in packed columns is studied by analysis of the response of an initially adsorbate-free adsorbent in the column to either a step change in the inlet adsorbate concentration (step input) or to the injection of a small pulse of the adsorbate at the column inlet (pulse input). The response to a step input is called the breakthrough curve and that to the pulse input is called the chromatographic response. A perfect pulse is the derivative of the perfect step for a linear system, therefore the chromatographic response is the derivative of the breakthrough curve. As a result, the response to either input provides the same information (Ruthven, 1984; Kärger and Ruthven, 1992).

In a typical breakthrough experiment, a steady flow of adsorbate is introduced to the bed and the exit gas phase composition is recorded as a function of time. The

concentration of the adsorbate at the outlet of the column is initially zero and then gradually increases to an equilibrium (steady-state) value reflecting the fact that the adsorbent has become saturated with the adsorbate.

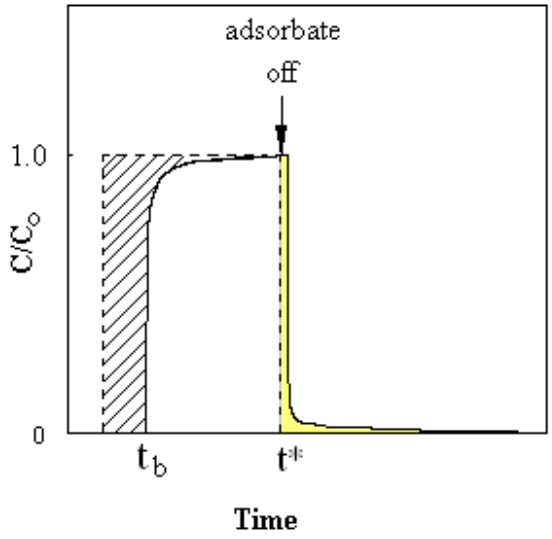

Figure 3.1. Typical adsorption and desorption breakthrough curves.

A typical response of a packed column to a step input (breakthrough curve) is shown in Figure 3.1. The dashed line is the empty column (blank) data and the solid line is for the packed column. The scanned and shaded areas are related with the total and reversible adsorbed amounts, respectively. The time at which the breakthrough is attained is called the breakthrough time (t_b), while the time at which the saturation is attained is called the exhaustion time (t^*). Adsorption takes place from the column inlet and proceeds to the exit. At any instant, the packed bed can be divided into two zones: the equilibrium zone and the adsorption (mass transfer) zone. In the equilibrium zone, the adsorbed phase concentration is in equilibrium with the solute concentration in the feed. The transfer of the adsorbate from the fluid phase to the solid phase occurs only in the mass transfer zone. The length of the mass transfer zone depends on the adsorption kinetics and equilibrium, nature of the adsorbent and the flow rate. The length of the mass transfer zone may expand (proportionate pattern) or remain constant (constant pattern) as it moves through the column (Ülkü, 1991). The velocity of the mass transfer

zone is determined by the equilibrium isotherm. The shape of the breakthrough curve is determined by the nature of the adsorption isotherm and the individual transport processes taking place within the bed and the particles. These factors tend to make the breakthrough curve more dispersive. In general, the breakthrough time increases by decreased concentration of adsorbate in the fluid phase, decreased flow rate, increased bed length and for smaller adsorbent particles. For the column with axial dispersion and mass transfer resistances to an input, the time delay of the response gives information about the adsorption equilibrium while the dispersion provides information on the adsorption kinetics and the extent of axial dispersion in the column. The location of the front at any time can be found from an overall mass balance, but determination of the form of the concentration front necessitates solution of the differential mass balance equations for the fluid and solid phases.

In the desorption mode, the flow passing through the column is switched from the adsorbate to the carrier gas and the decrease of concentration of adsorbate with time at the column effluent stream is followed until input and output concentrations are equal.

The equilibrium adsorption capacity of the adsorbent (q_o) is determined from the breakthrough curve based on the overall mass balance on the column. The total adsorbate adsorbed from the feed stream upon complete saturation of the bed equals to the sum of the amount of adsorbate left the bed, amount of adsorbate retained in the interparticle voids within the bed and adsorbed in the solid phase:

$$QC_o t^* - \int_0^{t^*} C(t)dt = \varepsilon V_{bed} C_o + (1-\varepsilon) V_{bed} q_o \qquad (3.1)$$

where Q is the volumetric flow rate of adsorbate fed to the column, C and C_o is the outlet and inlet gas phase adsorbate concentration, respectively, V_{bed} is the bed volume, ε is the bed voidage and q_o is in equilibrium with C_o. Rearranging Equation (3.2) yields:

$$\int_0^{\infty}\left(1-\frac{C}{C_o}\right)dt=\frac{L}{v}\left[1+\left(\frac{1-\varepsilon}{\varepsilon}\right)\frac{q_o}{C_o}\right]=t^* \qquad (3.2)$$

where L is the column length, and v is the interstitial velocity (Ruthven, 1984).

3.3. Mass Transfer in Packed Column

A zeolite particle is made up of zeolite crystals and a mesoporous and macroporous binder between these crystals. The transfer of adsorbate from the fluid phase to the solid phase with bidisperse pore structure involves several steps: transfer of the adsorbate molecules from the bulk fluid phase to the particle surface (diffusion through the immobile gas layer around the zeolite particle), diffusion of the adsorbate molecules through the macropores within the particle, and diffusion of the adsorbate molecules within the micropores of the zeolite crystals.

3.3.1. Diffusion through External Film

Diffusion of adsorbate molecules prior to adsorption takes place in two regions: the fluid phase outside the particle and within the particle. The transport resistance outside the particle occurs in the film surrounding the particle. When there is more than one component in the fluid phase, the surface of an adsorbent particle is surrounded by a laminar boundary layer through which transport can occur by molecular diffusion. The film resistance depends on the hydrodynamic conditions around the adsorbent particles in the bed, the properties of the fluid, the particle size and particle surface roughness (Ülkü, 1991).

The external mass transfer coefficient (k_f) describes the transport of the adsorbate molecules from the bulk fluid phase to the external surface of the adsorbent particle. The magnitude of k_f can be calculated via the Sherwood number (Sh) according to:

$$k_f = \frac{ShD_m}{d_p} \tag{3.3}$$

For an isolated spherical adsorbent particle in a stagnant fluid, *Sh* is equal to 2. *Sh* is usually estimated by using the empirical correlations. Many empirical correlations were developed from experimental data for particle to fluid mass transfer processes measured for specific adsorbates and adsorbent particles to express the *Sh* as a function of *Re* and *Sc*.

Table 3.1. Empirical correlations for external mass transfer.

Reference	Empirical correlation	Range of validity
Ranz and Marshall, 1952	$Sh = 2 + 0.6Sc^{0.33}\,Re^{0.5}$	$2 \le ReSc^{0.67} \le 50000$
Williamson et al., 1963	$Sh = 2.4\varepsilon\,Re^{0.34}\,Sc^{0.42}$	$0.08<Re<125$ $150<Sc<1300$
Wilson and Geankoplis, 1966	$Sh = \frac{1.09}{\varepsilon^{0.66}}Re^{0.33}\,Sc^{0.33}$	$0.0016<Re<55$ $165<Sc<70600$
Karabelas et al., 1971	$Sh = 4.58\,Re^{0.33}\,Sc^{0.33}$	$0.4<Re<10$
Kataoka et al., 1972	$Sh = 1.85\left(\frac{1-\varepsilon}{\varepsilon}\right)^{0.33} Re^{0.33}\,Sc^{0.33}$	$Re/(1-\varepsilon)<10$ or $Re<100$
Coeuret, 1976	$Sh = 5.4\,Re^{0.33}\,Sc^{0.25}$	$0.04<Re<30$
Kumar et al., 1977	$Sh = \frac{1.13}{\varepsilon}Re^{0.21}\,Sc^{0.33}$	$Re<10$
Dwivedi and Upadhyay, 1977	$Sh = \frac{ReSc^{0.33}}{\varepsilon}\left(\frac{0.765}{Re^{0.82}} + \frac{0.365}{Re^{0.386}}\right)$	$0.01<Re<15000$
Wakao and Funazkri, 1978	$Sh = 2 + 1.1Sc^{0.33}\,Re^{0.6}$	$Re=3\text{-}10000$
Olive and Lacoste, 1979	$Sh = 4.3\,Re^{0.35}\,Sc^{0.25}$	$0.1<Re<3$
Ohashi et al., 1981	$Sh = 2 + 1.58\,Re^{0.4}\,Sc^{0.33}$	$10^{-3}<Re<5.8$
	$Sh = 2 + 1.21\,Re^{0.5}\,Sc^{0.33}$	$5.8<Re<500$
	$Sh = 2 + 0.59\,Re^{0.6}\,Sc^{0.33}$	$Re>500$
Roberts and Cornal, 1985	$Sh = \left(2 + 0.644Re^{0.5}\,Sc^{0.33}\right)\left[1 + 1.5(1-\varepsilon)\right]$	$Re=0.8\text{-}5$

The collection of common external mass transfer coefficient correlations is given in Table 3.1. The comparison of the correlations for external film mass transfer coefficients is shown in Figure 3.2.

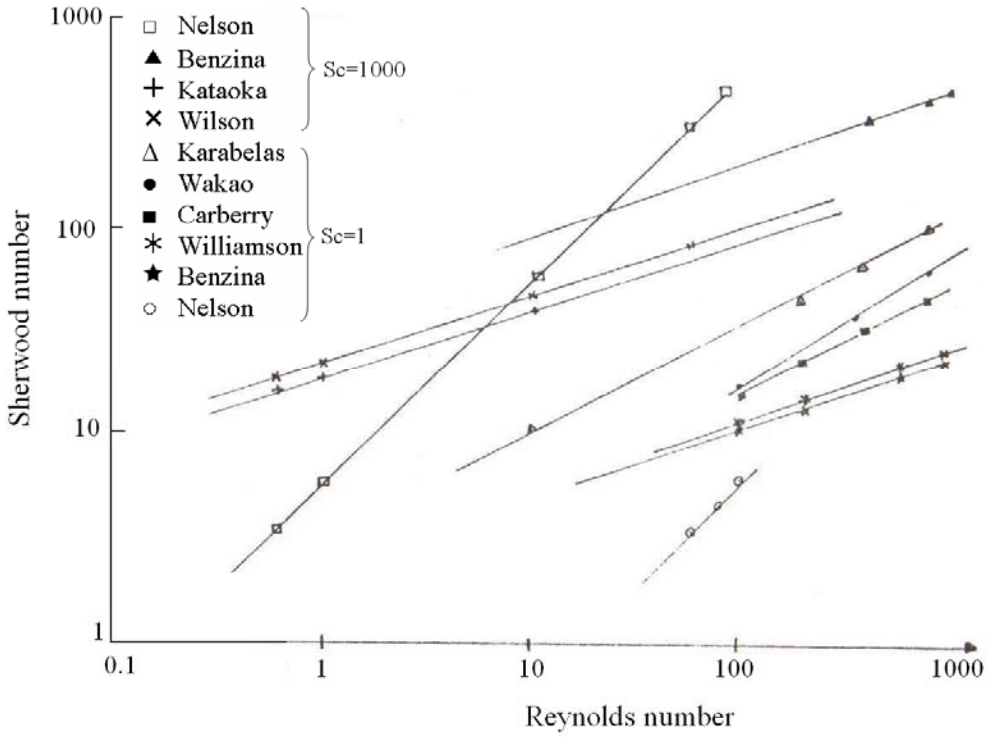

Figure 3.2. Comparison of correlations for external film mass transfer coefficients. (Source: Ülkü, 1991)

The inconsistency between the correlations can be attributed to the geometric parameters. The reported limiting *Sh* values below 2 may be attributed to the underestimation of axial dispersion for porous particles and the values higher than 2 can be explained by the invalidity of limiting single sphere boundary in the adsorbent bed and importance of geometric similarity (Ülkü, 1991). Furthermore, since these correlations were developed with adsorbents that are different in chemical and physical character, they ignore impacts of surface topography and roughness. Significantly different external film mass transfer coefficients were obtained for microporous adsorbents with different surface roughness characteristics. The rough spheres exhibited notably higher mass transfer rates over the smooth spheres. It was concluded that mass

transfer enhancement was more dependent on surface roughness than on overall particle shape (Roberts and Cornal, 1985; Young and van Vliet, 1988).

The particle shape was quantified by a parameter called sphericity. The sphericity of the particles (Φs) is a measure of how close a particle is to being a sphere and is defined as:

$$\Phi_s = \frac{\text{surface area of a sphere with same volume as the particle}}{\text{actual surface area of the particle}} \tag{3.4}$$

For granular particles, typical values of sphericity range between 0.6 and 0.95. The sphericity of crushed glass and zeolite was reported as 0.65 (Inglezakis and Poulopoulos, 2006).

Significance of the external film resistance depends on the hydrodynamic conditions. In general, for porous particles, the external resistance to mass transfer is smaller than the intraparticle diffusion resistance but it may still be large enough and have a significant contribution to overall mass transfer resistance. The adsorption capacity of the fluid film is smaller than that of the adsorbent particle, thus there is very little accumulation of sorbate within the film. This implies a constant flux and a linear concentration gradient through the film (Ruthven, 1984).

3.3.2. Diffusion in Macropores

Diffusion in a random pore network is slower as compared to that in a set of straight cylindrical pores as a result of increasing diffusion path length, connectivity of the pores and variations in the pore diameters. Considering the diffusion in a particle, these effects are lumped into the particle tortuosity factor (τ_p). The effective macropore diffusivity (D_P) is given by:

$$D_P = \frac{\varepsilon_p}{\tau_p} D \tag{3.5}$$

where D is the diffusivity in a straight cylindrical pore of same diameter. τ_p is the tortuosity of the solid structure, which is defined as the ratio of the actual distance a molecule travels between two points and the shortest distance between these points.

Fogler described the variation in the pore cross-sectional area normal to diffusion by constriction factor (σ_p) as:

$$D_P = \frac{\varepsilon_p \sigma_p}{\tau_p} D \tag{3.6}$$

where σ_p accounts for the variation in the cross-sectional area that is normal to diffusion. A typical value of σ_p is 0.8 (Fogler, 1999).

Diffusion of a molecule in a macropore occurs through two mechanisms: molecular and Knudsen diffusion. Relative importance of molecular or Knudsen diffusivity is largely determined by diameter of the macropore and the mean free path of the diffusing molecule. Molecular diffusion is the dominant mechanism if the mean free path of the gas molecule is smaller than the pore diameter. The mean free path (λ) is defined as the average distance traveled between molecular collisions and can be estimated from the following expression (Cunningham and Williams, 1980):

$$\lambda = \frac{k_B T}{\sqrt{2}\pi \sigma_{12}^2 P} \tag{3.7}$$

where k_B is the Boltzman constant, σ_{12} is the collision diameter of the diffusing molecules from the Lennard–Jones potential theory, and P is the pressure.

In small pores and at low pressure, the mean free path becomes greater than the pore diameter. Under these conditions, the diffusing molecules collide with the pore walls more frequently than they collide with each other. Thus the Knudsen diffusion predominates in the macropores and Knudsen diffusivity can be calculated as:

$$D_K = \frac{2}{3}\bar{r}\left(\frac{8RT}{\pi M}\right)^{1/2} = 9700\bar{r}\left(\frac{T}{M}\right)^{1/2} \tag{3.8}$$

where D_K is the Knudsen diffusivity, $\bar{r}$ is the mean macropore radius and M is the molecular weight of the diffusing molecule (Kärger and Ruthven, 1992; Ruthven, 1984).

If the pore diameter is large relative to the mean free path of the diffusing molecules, the diffusing molecules collide with each other more frequently than they collide with the pore walls. Under these conditions, the molecular diffusion is significant diffusion mechanism in the macropores and the effective macropore diffusivity can be estimated from Equation (3.5) by substituting D with the molecular diffusion coefficient (D_m) (Ruthven, 1984).The theoretical estimation of molecular diffusion coefficient was developed by Chapman and by Enskog (Chapman and Cowling, 1970):

$$D_m = \frac{0.00186T^{3/2}\sqrt{\frac{1}{M_1}+\frac{1}{M_2}}}{P\sigma_{12}^2\Omega} \tag{3.9}$$

where Ω is collision integral, T is absolute temperature, and M_1 and M_2 are molecular weights of gases. The collision diameter is given by,

$$\sigma_{12} = \frac{1}{2}(\sigma_1 + \sigma_2) \tag{3.10}$$

The calculation of Ω depends on an integration of the interaction between the two species. This interaction is usually described by the Lennard-Jones 12-6 potential. The integral depends on the temperature and the energy of interaction ($\in_{12}$). The $\in_{12}$ is a geometric average of contributions from the two species:

$$\in_{12} = \sqrt{\in_1 \in_2} \tag{3.11}$$

Then Ω can be found as a function of $k_B T/\in_{12}$ using the tabulated data (Cussler, 1987).

In the transition region where the mean free path is comparable with the pore diameter, the collisions of diffusing molecules with each other and with the pore wall are both significant. In this case, D can be calculated by (Ruthven, 1984):

$$\frac{1}{\mathrm{D}} = \frac{1}{\mathrm{D_m}} + \frac{1}{\mathrm{D_K}} \tag{3.12}$$

The coefficient of ε_p/τ_p in Equation (3.7) is defined as diffusibility (η) by Suzuki (Suzuki, 1990). It can be correlated to the porosity (ε) and particle shape factor (χ) as (Suzuki and Smith, 1972):

$$\eta = \frac{\varepsilon}{\varepsilon + \chi(1-\varepsilon)} \tag{3.13}$$

The diffusibility can also be expressed as a function of bed porosity (Wakao and Smith, 1962):

$$\eta = \varepsilon^2 \tag{3.14}$$

The diffusibility is related to the tortuosity of a pore, k^* (Suzuki, 1990):

$$\eta = \frac{\varepsilon}{k^*} \tag{3.15}$$

Since the diffusion within the particle is of concern, bed porosity and pore tortuosity should be replaced by the particle porosity (ε_p) and particle tortuosity (τ_p) in these correlations.

Experimental particle tortuosity factors reported generally in the range of 1.7 to 6. An average value of 3 of the tortuosity corresponds to straight, randomly oriented, cylindrical pores with equal probability of all possible orientations (Ruthven, 1984). Complicated correlations which relate particle tortuosity factors to pore diameter to length ratio or configuration of the pores are available in the literature (Suzuki, 1990). The tortuosity factor should be handled as an empirical constant, which is characteristic for each material, and should be evaluated experimentally (Perry and Green, 1999).

The Knudsen and molecular diffusion occur through the adsorbed gas phase in the center region of the macropores. However, if there is adsorption also on the surface of the macropore, there exists an adsorption layer on the pore surface. Additional flux occurs due to diffusion through this layer and its contribution becomes significant if the adsorption equilibrium is favorable. Diffusion through this layer is called surface diffusion. Surface diffusion is significant only in small macropores. Diffusion in these macropores pores occurs by Knudsen mechanism. The effective macropore diffusivity is then expressed as:

$$D_p = D_K + K\left(\frac{1-\varepsilon_p}{\varepsilon_p}\right)D_s \tag{3.16}$$

where D_s is the surface diffusivity and K is the adsorption equilibrium constant expressed in terms of the total volume of the porous solid (Ruthven, 1984). The relative importance of surface diffusion depends on the ratio of KD_s/D_K. Since surface diffusion is an activated process, KD_s increases with decreasing temperature. Therefore surface diffusion is generally significant at temperatures not much higher than the normal boiling temperature of the adsorbate. At higher temperatures, the surface flux can be neglected (Ruthven, 1984; Kärger and Ruthven, 1992).

3.3.3. Diffusion in Micropores

In the pores or which the diameter is comparable to that of the diffusing molecule, the diffusing molecules cannot escape from the force field of the pore walls. In this pore region diffusion occurs by an activated process in which the molecules jump randomly between neighboring low energy sites. This diffusion regime is referred as configurational diffusion, activated diffusion or zeolitic diffusion. In micropores**,** interactions between the diffusing molecule and the pore wall are dominated. Therefore, the micropore diffusivity changes considerably with the molecular dimensions of the sorbate molecule and the free dimensions of the channels. The geometry of the pores, chemical composition of the zeolite (type, charge and distribution of the cations), shape, size, polarity and concentration of the diffusing molecules, and temperature strongly affect diffusion in the micropores. Micropore diffusion is sensitive to the complete or partial blockage of the certain channels (Ruthven, 1984; Kärger and Ruthven, 1992).

3.3.4. Relative Importance of External and Internal Mass Transfer Resistances

The relative importance of internal and external mass transfer resistances can be determined by the Biot number which is the ratio of the external film mass transfer rate to the intraparticle mass transfer rate and expressed as:

$$\mathrm{Bi} = \frac{k_f R_p}{3\varepsilon_p D_e} \tag{3.17}$$

where D_e is the effective intraparticle diffusivity representing the contribution from the macropore and micropore diffusion within the particle. The criterion for negligible external mass transfer resistance is given as $Bi>20$ (Ruthven, 1984). As the rate of mass transfer in the external film increases as compared to the intraparticle mass transfer rate, Bi increases.

A similar criterion for the determination of the relative importance of external and internal mass transfer resistance was proposed by Kärger and Ruthven. A parameter (α_m) was derived from the steady state mass balance:

$$\alpha_m = \frac{(C_o - C_s)/C_o}{\left[\frac{d}{dR}\left(\frac{C}{C_o}\right)\right]_{R_p}} = \frac{D_e}{k_f R_p} \tag{3.18}$$

where C_o and C_s are the adsorbate concentrations in the bulk fluid and at the particle surface, respectively. In fact α_m is the reciprocal of $\varepsilon_p Bi$. Since $\mathrm{Sh} \geq 2$ and $D_e < D_m$, α_m is always lower than 1 implying that the external mass transfer resistance is less important than internal diffusional resistance (Kärger and Ruthven, 1992).

Another criterion for the determination of relative importance of external and internal mass transfer resistances was given as follows:

$$\zeta = \frac{k_f a_u}{K \frac{q_o}{C_o}} \tag{3.19}$$

$$K = \frac{15 D_e \rho_{bulk}}{R_p^2} \tag{3.20}$$

$$a_u = \frac{3(1-\varepsilon)}{R_p} \tag{3.21}$$

Here ζ is a mechanical parameter and represents the ratio of the intraparticle and external film diffusion resistances, q_o is the saturation capacity of the adsorbent (in equilibrium with C_o) and a_u is the total external area of particles per unit volume of bed. The value of ζ close to zero designates that the external film diffusion controls the process rate, while if ζ is infinite, then the intraparticle diffusion controls the process rate. This criterion was derived for a system with favorable adsorption isotherm. They noted that for ζ>7.6, the particle diffusion is more significant, whereas if ζ<0.14, the external mass transfer controls the adsorption rate (Miura and Hashimoto, 1977).

There exist different definitions for the Biot number in the literature. Cooney defined the Biot number as:

$$Bi = \frac{k_f R_p C_o}{D_e q_o} \tag{3.22}$$

It was pointed out that for *Bi* lower than 0.5, the fluid film resistance is dominant, while for *Bi* greater than 30, dominance of intraparticle resistance exists. The only restriction is that the isotherm be favorable (Cooney, 1993).

Another expression defines the Biot number as follows:

$$\mathrm{Bi} = \frac{k_f R_p C_o}{D_e q_o} \frac{1}{\Phi_s} \tag{3.23}$$

where Φ_s is the sphericity of the particles given by Equation (3.2). This criterion is also valid for the systems with favorable adsorption isotherm. The value of *Bi* larger than 30 implies the dominance of the intraparticle diffusion (Hand et al., 1984).

3.3.5. Relative Importance of Micropore and Macropore Mass Transfer Resistances

For diffusion in a biporous adsorbent particle, the relative importance of micropore and macropore diffusional resistances depends on the ratio of the diffusional time constants, i. e., $(D_c/r_c^2)/(D_P/R_p^2)$, where D_c is the micropore diffusivity and r_c is the crystal radius. The diffusion time constant for macropore diffusion depends on the particle radius, whereas that for micropore diffusion is independent of the particle size and only a function of the crystal radius. Therefore, the relative dominance of the micropore diffusion can be confirmed experimentally by making replicate experiments with particles with different size. Under conditions of micropore diffusion control, the adsorption rate is independent of particle size (Kärger and Ruthven, 1992). The macropore diffusion resistance can be reduced by reducing the particle size but in this case the pressure drop across the bed increases (Ruthven, 1984).

Garg and Ruthven defined a parameter for the determination of the relative importance of macropore and micropore diffusion resistance:

$$\psi = \frac{3w\left(1-\varepsilon_p\right)}{\varepsilon_p}\frac{D_c}{D_p}\left(\frac{R_p}{r_c}\right)^2\frac{dq*}{dC} \tag{3.24}$$

Here w is the volume fraction of zeolite crystals to the total solid material in a particle, q^* is the solid-phase adsorbate concentration in equilibrium with local fluid-phase adsorbate concentration. For the values of Ψ smaller than 1, micropore diffusion controls and for the values greater than 100, macropore diffusion controls (Garg and Ruthven, 1973).

3.4. Axial Dispersion

Axial dispersion contributes to the broadening of the adsorption front due to flow in the interparticle void spaces. The axial dispersion of a gas through a packed column occurs due to contributions from molecular diffusion in the interparticle void spaces and turbulent mixing due to the splitting and recombination of flows around the adsorbent particles and is represented by:

$$D_L = \gamma_1 D_m + \gamma_2 v d_p \tag{3.25}$$

where D_L is effective axial dispersion coefficient in which the effects of all mechanisms which contributes to axial mixing are lumped together, and γ_1 and γ_2 are constants related with the geometry of the bed and normally have values of about 0.7 and 0.5, respectively (Ruthven, 1984).

The axial dispersion can also be expressed in terms of particle-based Péclet number (*Pe*) as follows:

$$\frac{1}{Pe} = \frac{D_L}{vd_p} = \gamma_1 \frac{D_m}{vd_p} + \gamma_2 = \frac{\gamma_1 \varepsilon}{ReSc} + \gamma_2 \tag{3.26}$$

where *Sc* is Schmidt number, $Sc=\mu/\rho D_m$, and *Re* is Reynolds number, $Re=v\varepsilon d_p\rho/\mu$.

The contribution from the molecular diffusion in the interparticle void spaces represented by the $\gamma_1 D_m$ term is determined by the bed voidage and tortuosity of the diffusion path in the interparticle voids (Suzuki, 1990). γ_1 is the reciprocal axial (bed) tortuosity factor representing the ratio of the distance between two cross sections of a column to the true distance traveled by flowing molecules due to their zig-zag motion between solid particles. The bed tortuosity ($\tau=1/\gamma_1$) is related to the bed voidage by (Wicke, 1973):

$$\gamma_1 = 0.45 + 0.55\varepsilon \tag{3.27}$$

For typical bed voidages of 0.35-0.40, γ_1 is obtained in the range of 0.64-0.67. For packed bed of randomly oriented cylindrical pores, $\gamma_1 = 1/\sqrt{2} \approx 0.7$ (Ruthven, 1984).

In laminar flow regime ($Re<100$), axial dispersion in a packed column is expected due to the local velocity distribution of gas in the interparticle void spaces (Suzuki, 1990). In this flow regime, axial dispersion occurs primarily by molecular diffusion, thus D_L is independent of velocity and expressed as:

$$D_L = \gamma_1 D_m \tag{3.28}$$

or in terms of *Pe*:

$$Pe = \frac{\tau Re Sc}{\varepsilon} \tag{3.29}$$

Generally, the contribution of molecular diffusion to axial dispersion becomes dominant for $ScRe<10$ (Suzuki, 1990). The conditions corresponding to low Re are selected in the case of columns packed with small particles in order to avoid the problems of channeling and high order dependence of axial dispersion on velocity (Ruthven, 1984).

$\gamma_2 v d_p$ term in Equation (3.25) represents the turbulent mixing which is dominant in the turbulent flow regime ($Re>100$). At high Reynolds numbers, the fluid entering each interparticle void is considered to be fully mixed. For this case, Pe approaches the limiting value (Pe_∞) as $Re \rightarrow \infty$. The theoretical value of $Pe_\infty = 1/\gamma_2$ is 2.0 for $\gamma_2 \approx 0.5$ (Ruthven, 1984).

The axial dispersion of gas in packed beds has been extensively studied in the literature and the experimental data was correlated according to the following equation (van Deemter et al., 1956; McHenry and Wilhelm, 1957; Evans and Kenney, 1957; Edwards and Richardson, 1968; Urban and Gomezplata, 1969; Suzuki and Smith, 1972; Scott et al., 1974; Kawazoe et al., 1974; Moulijn and van Swaaij, 1976; Hsu and Haynes, 1981):

$$\frac{1}{Pe} = \frac{D_L}{v d_p} = \frac{\gamma_1 D_m}{Re Sc} + \frac{1}{Pe_\infty \left(1 + \frac{\beta' \gamma_1 D_m}{v d_p}\right)} \tag{3.30}$$

The $\beta' \gamma_1 D_m / v d_p$ term accounts for the effect of radial dispersion on the concentration gradient caused by axial dispersion (Ruthven, 1984). β' is the radial dispersion factor and its theoretical value obtained from a highly turbulent random walk model is 8. The empirical constants β' and Pe_∞ obtained by fitting Equation (3.26) to the experimental data exhibited significant deviation from the theoretical values especially

for packed beds of small particles as shown in Figure 3.3 (Moulijn and van Swaaij, 1976).

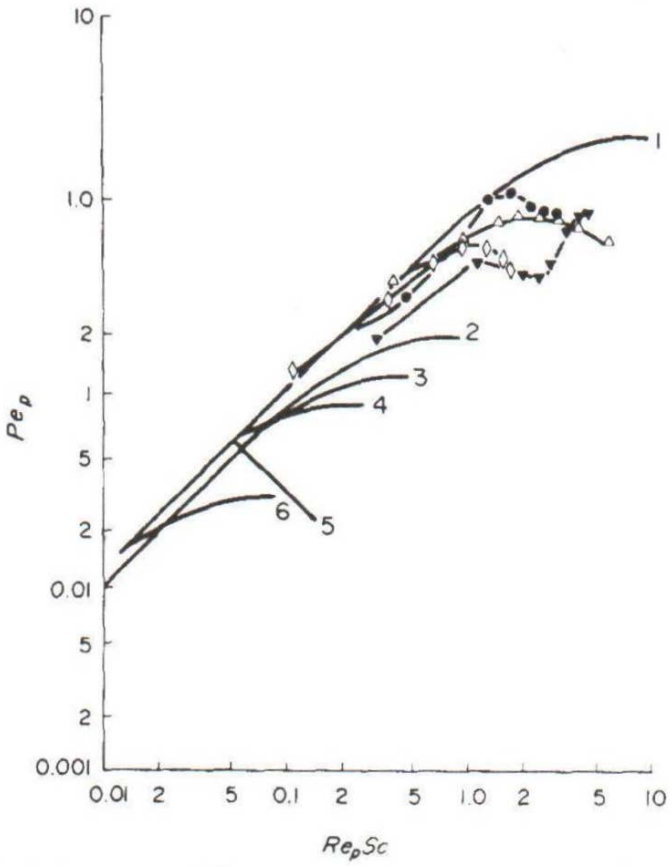

Figure 3.3. Summary of literature data of axial dispersion of gases in beds packed with fine particles. 1, d_p> 500 μm; 4, d_p=158 ± 90 μm; 5, d_p=97 ± 30 μm; 6, d_p=146 ± 70 μm (Edwards and Richardson, 1968); 2, d_p=160 ± 25 μm; 3, d_p=114 ± 10 μm (Suzuki and Smith, 1972); ●, d_p=117 ± 3 μm; ◊, d_p=101 ± 22 μm; Δ, d_p=195 ± 26 μm; ▼, d_p=216 ± 7 μm (Moulijn, 1974).
(Source: Moulijn and van Swaaij, 1976)

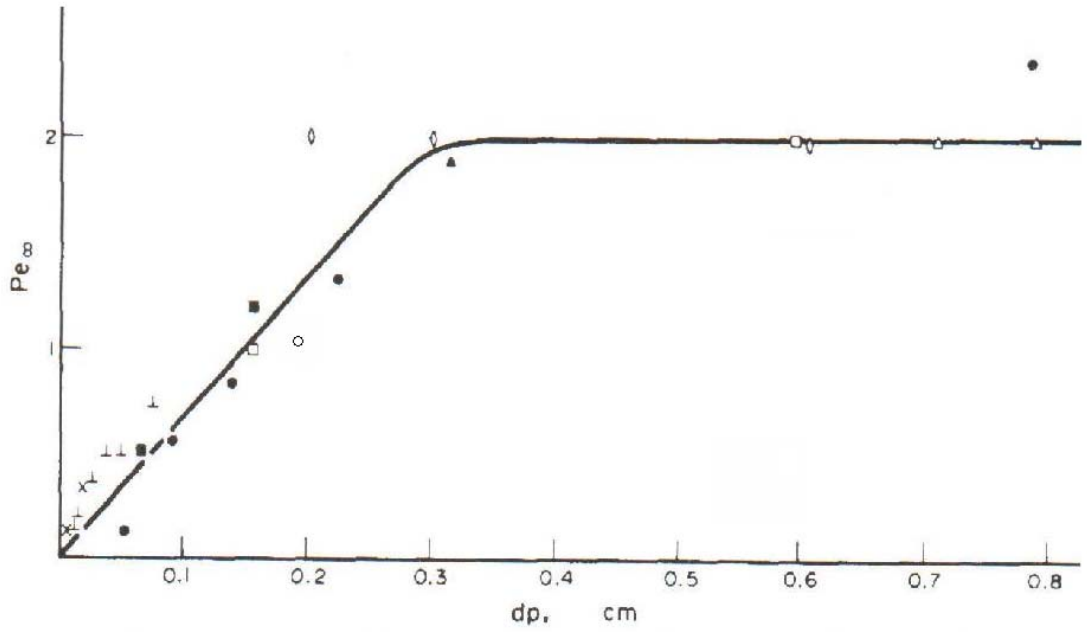

Figure 3.4. Variation of limiting Péclet number (Pe_∞) with particle size for flow through beds: ●, Langer et al., 1978; ×, van Deemter et al., 1956; ■, Kawazoe et al., 1974; ◊, Edwards and Richardson, 1968; Δ, Scott et al., 1974; ▲, McHenry and Wilhelm, 1957; □, Urban and Gomezplata, 1969; ○, Evans and Kenney, 1965; ⊥, Suzuki and Smith, 1972.
(Source: Langer et al., 1978)

From Figure 3.4, it was concluded that the limiting *Pe* values were close to the theoretical value of 2 only for beds packed with particles larger than 0.3 cm. But for the beds of smaller particles, the Pe_∞ values obtained were smaller than the theoretical value and increased linearly with the particle diameter as follows (Langer et al., 1978):

$$\text{for } d_p \leqslant 0.25 \text{ cm} \qquad Pe_\infty = 6.7 d_p \tag{3.31}$$

This indicates that the axial dispersion is enhanced in packed beds of small particles. In these beds, channeling of flow induced by the local irregularity of the packing occurs especially at very low Reynolds numbers (Ruthven, 1984; Suzuki, 1990). This behavior was attributed to tendency of small particles to stick together so that their hydrodynamic behavior is similar to that of larger particles (Scott et al., 1974).

Moulijn and van Swaaij considered these packed beds to be composed of agglomerates of equal diameter of d_{aggl} as shown in Figure 3.5.

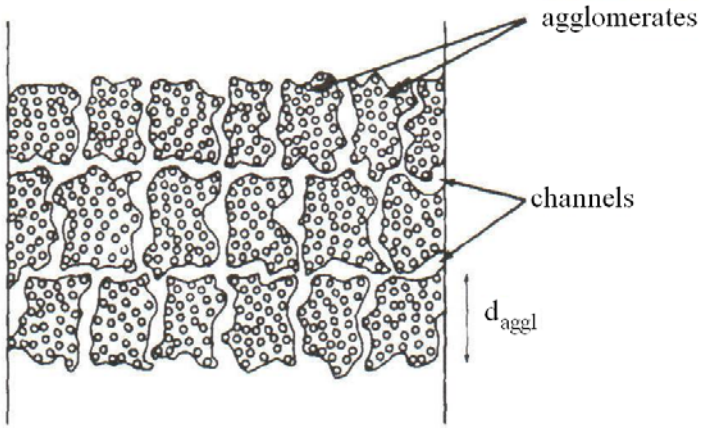

Figure 3.5. Representation of the agglomeration model.
(Souce: Moulijn and van Swaaij, 1976)

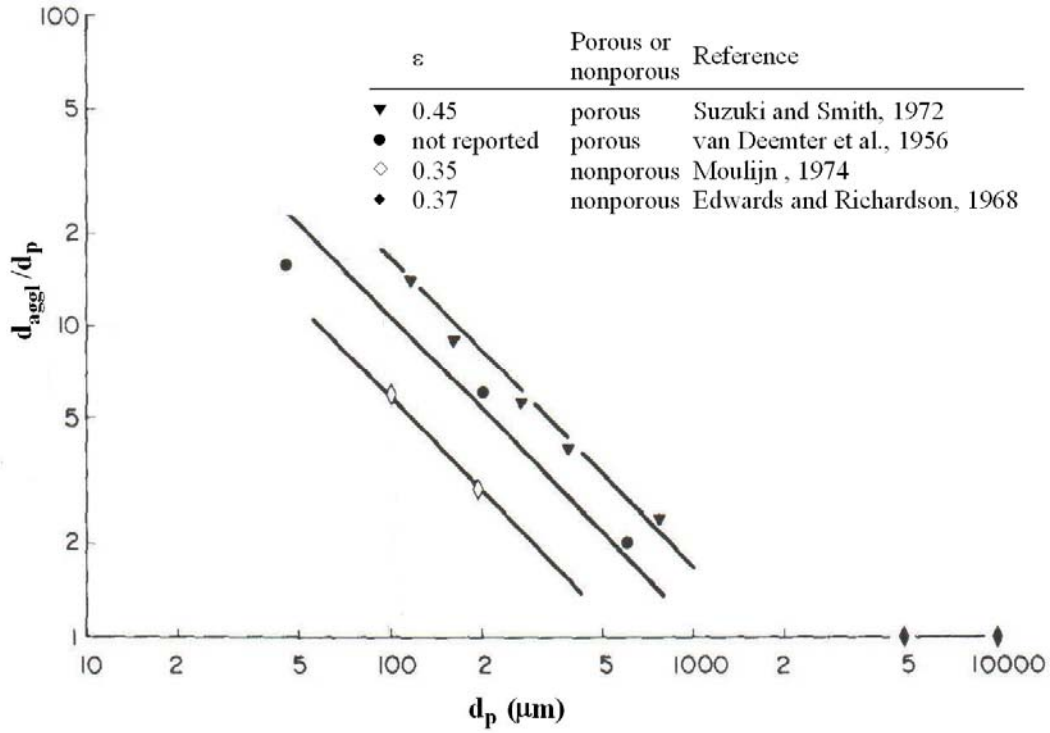

Figure 3.6. Dependence of the agglomerate diameter of the particle diameter.
(Souce: Moulijn and van Swaaij, 1976)

For particles with diameter below 500 μm, it was shown that clustering of particles in packed beds were important and the size of the clusters was inversely proportional to the particle diameter (Figure 3.6). This phenomenon results in severe channeling of gas (Moulijn and van Swaaij, 1976). Schlünder suggested that the clustering of particles was probably due to interparticle forces, and their effect was due to the flow properties at low Re numbers (Schlünder, 1977).

Suzuki and Smith used a chromatographic technique to evaluate the axial dispersion coefficients in beds of small porous CuO•ZnO catalyst particles (diameter of 0.1-1 mm) and beds of nonporous glass beads (diameter of 0.51 mm) over a wide range of velocities corresponding Re in the range of 0.00237-11.9. In the low velocity region, the relationship was found between the Péclet number based on the molecular diffusion ($Pe_m=d_pv/D_m$) and D_L/D_m for the porous catalyst particles and nonporous glass beads. As the velocity decreased, D_L/D_m reached a constant value. In this region D_L was found to be proportional to the molecular diffusion coefficient and to the diffusibility (η) as follows (Suzuki and Smith, 1972):

$$D_L = \eta D_m \tag{3.32}$$

The value of η was experimentally found to be 0.44 and 0.30 for the porous catalyst particles and for the nonporous glass beads, respectively. The η/ε ratios which is a measure of the tortuosity of the axial dispersion path (ε/η is tortuosity factor) were reported as ~0.97 and ~0.79 for the catalyst particles and nonporous glass beads, respectively. The higher η/ε value for the porous particles as compared to that for the nonporous glass beads was attributed to possible contribution of intraparticle diffusion to axial dispersion. D_L was expressed as the sum of contributions from the gas and particles phases (Suzuki and Smith, 1972):

$$D_L = \delta D_m + (1-\delta) D_e \tag{3.33}$$

where δ is related to the bed voidage by:

$$\delta = \frac{\varepsilon}{\varepsilon + \chi(1-\varepsilon)} \tag{3.34}$$

where χ is particle shape factor. For spherical particles, χ=1.5 and for ellipsoidal particles with dimensions of a=b=dc, χ=2.1 for d=5 and χ=3.1 for d=10. For χ=1, δ=ε and Equation (3.34) becomes:

$$D_L = \varepsilon D_m + (1-\varepsilon) D_e \tag{3.35}$$

corresponding to a parallel diffusion model (tortuosity factor=1). The experimentally determined η values were found to be in agreement with the δ values for the spherical nonporous particles, but not for the porous catalyst particles. The high D_L values for porous particles at low velocities were explained by including a contribution from the intraparticle diffusion. It was suggested that Equations (3.33) and (3.34) could be used to predict D_L at low flow velocities if the experimental data was not available.

In high velocity region, the limiting *Pe* approached to its theoretical value of 2 for large particles as shown in Figure 3.7. On the other hand, for small particles, *Pe* approached a constant value lower than 2 as shown in The x-axis represents the Péclet number based on the molecular diffusion (Pe_m) and y-axis is for the Péclet number based on the axial dispersion ($Pe=d_p v/D_L$). The limiting *Pe* was found to be proportional to particle size according to the expression (Suzuki and Smith, 1972):

$$Pe_\infty = 1.2 d_p \tag{3.36}$$

In the high velocity region, D_L was found to be proportional to the flow velocity as expressed by:

$$\frac{D_L}{v\varepsilon} = 0.83 \quad \text{mm} \tag{3.37}$$

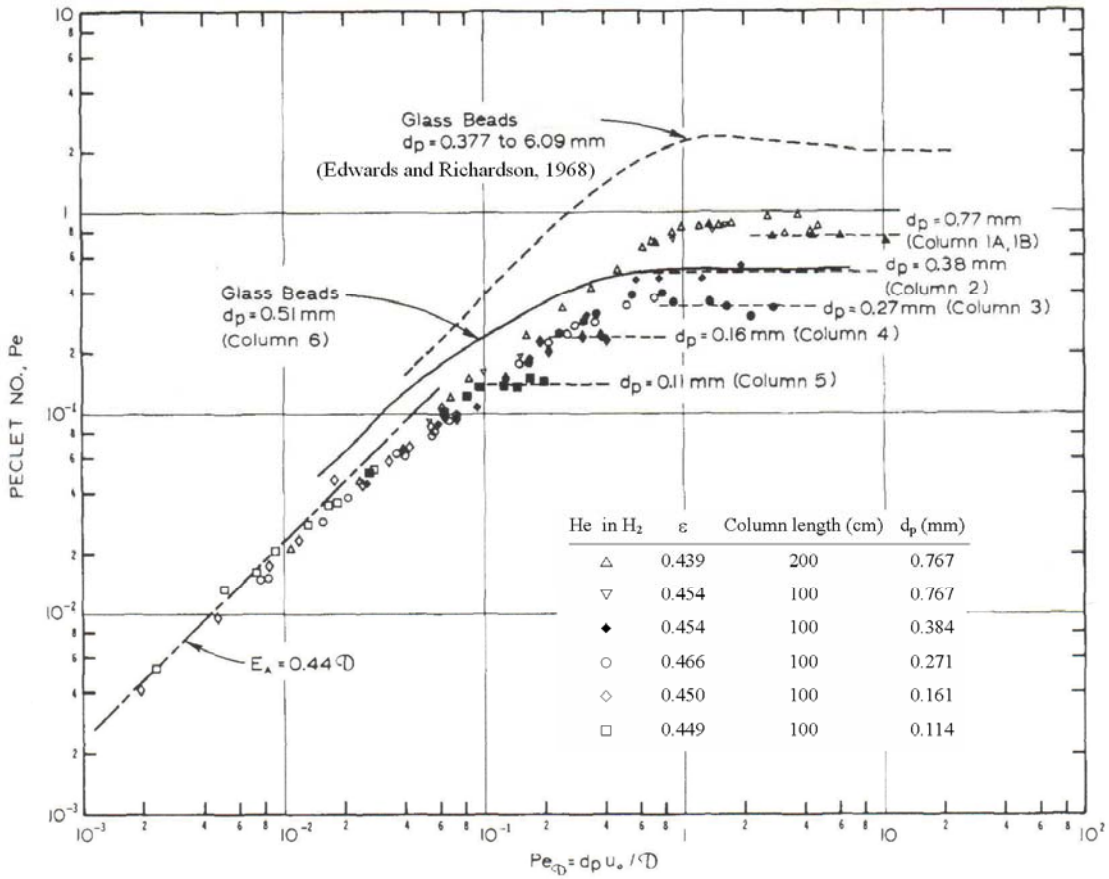

Figure 3.7. Effect of velocity on Péclet number.
(Source: Suzuki and Smith, 1972)

An expression was proposed for approximate estimation of the axial dispersion coefficient for beds of small particles over the entire range of velocities as follows:

$$D_L = \eta D_m + \ell v\varepsilon \tag{3.38}$$

where ℓ is the scale of dispersion and reported as 0.83 mm for 0.11 mm<d_p<0.77 mm and η=0.44 for porous catalyst particles. At high velocities, the contribution of intraparticle diffusion to the axial dispersion was found to be negligible (Suzuki and Smith, 1972).

Furthermore, Wakao showed that the axial dispersion was significant for experimental systems with rectangular adsorption isotherm for columns packed with porous particles especially at low Reynolds numbers. Diffusion in the intraparticle voids, which results in concentration gradient through the particle, contributes to the axial dispersion. The following correlation was given for the estimation of the axial dispersion coefficient (Wakao, 1976):

$$\frac{D_L}{vd_p} = \frac{20}{\varepsilon}\frac{D_m}{vd_p} + 0.5 = \frac{20}{ReSc} + 0.5 \tag{3.39}$$

For a typical bed voidage of 0.4, the value of $\gamma_1=20/\varepsilon$ gives 50 which is significantly higher than that for nonporous particles. Therefore, the axial dispersion is enhanced as compared to that for nonporous particles.

Another correlation for the estimation of the axial dispersion coefficient was given as follows:

$$\frac{1}{Pe} = \frac{D_L}{vd_p} = \frac{0.328}{ReSc} + \frac{3.33}{1+\dfrac{0.59}{ReSc}} \tag{3.40}$$

which is valid for 0.08<$ReSc$<1 (Hsu and Haynes, 1981).

In another criterion it was stated that the axial dispersion can be neglected only if the axial Péclet number of the bed is greater than about 100 (Levenspiel, 1972). The Péclet number for the fixed bed (Pe_{bed}) is expressed in terms of the particle-based Péclet number as follows (Inglezakis and Poulopoulos, 2006):

$$Pe_{bed} = \frac{L}{d_p} Pe \tag{3.41}$$

Another criterion states that, *Pe* should be high and the bed should be deep, i.e. high L/d_p in order to have ideal (plug) flow (Carberry, 1976). Furthermore, the following limits were given to avoid large-scale maldistribution of the flow (Treybal, 1980; Gunn, 1968, Carberry 1976; Chen et al., 1968):

$$\frac{L}{d_{column}} \geq 5 \tag{3.42}$$

$$\frac{d_{column}}{d_p} \geq 12 - 30 \tag{3.43}$$

$$\frac{L}{d_p} \geq 50 - 150 \tag{3.44}$$

where d_{column} is the column diameter.

If the aim of the packed column experiments to determine the micropore diffusion coefficient, contribution from the axial dispersion to the broadening of the response curve must be minimized and the dispersion of the response curve is dominated by micropore resistance. In order to minimize the axial dispersion, the column must be well packed. This is particularly important if the particle size is very small. Relatively large particles and high flow rates are preferred in order to minimize the axial dispersion effect (Ruthven, 1984). It is important to determine the axial dispersion coefficient directly under conditions as close possible to the conditions of the experimental measurements (Kärger and Ruthven, 1992).

3.5. Pressure Drop

The pressure drop through a packed column is dependent on the particle size, fluid velocity and bed dimensions. The experimental data show considerable scatter due to differences in bed voidage and/or wall effects and may be correlated in terms of a dimensionless friction factor (*f*):

$$f = \frac{d_p}{L}\frac{\Delta p}{\rho(\varepsilon v)^2} \tag{3.45}$$

where Δp is the pressure drop across the length of the column and εv is the superficial fluid velocity (u). There are commonly used two correlations for determination of the friction factor that is given by Chilton-Colburn (1931):

$$f = \frac{805}{Re} \qquad \text{for } Re < 40 \tag{3.46}$$

$$f = \frac{38}{Re^{0.15}} \qquad \text{for } Re > 40 \tag{3.47}$$

and given by Ergun (1952):

$$f = \left(\frac{1-\varepsilon}{\varepsilon^3}\right)\left[\frac{150(1-\varepsilon)}{Re} + 1.75\right] \tag{3.48}$$

The Ergun's equation including the particle sphericity factor (Φ_s) is also given in a differential form as follows (Inglezakis and Poulopoulos, 2006):

$$\frac{dP}{dz} = -\left[\frac{150\mu u}{\Phi_s^2 d_p^2}\right]\frac{(1-\varepsilon)^2}{\varepsilon^3} + \frac{1.75\rho u^2}{\Phi_s d_p}\frac{(1-\varepsilon)}{\varepsilon^3} \tag{3.49}$$

CHAPTER 4

MATERIALS AND METHODS

4.1. Preparation of Adsorbents

The zeolite particles after several treatment processes were used as an adsorbent in the NO adsorption studies. This chapter includes the preparation and characterization of the prepared zeolites as well as the experimental details for the adsorption studies.

4.1.1. Preparation of Zeolite with High Clinoptilolite Content

The zeolitic tuff mined from Gördes, Western Anatolia was crushed, ground and wet sieved to different size fractions. The mineral composition of the zeolite was determined by qualitative X-ray diffraction analysis. The separation of clinoptilolite from the parent rock by enrichment processes is based on the greater friability (based on the hardness values of the constituent mineral phase, namely 2.5-3 for biotite, 7 for quartz, 6 for sanidine and microcline, 3.5-4 for clinoptilolite in Mohr scale) and lower density of the zeolite relative to other rock constituents (http://webmineral.com). 50 grams of the fraction below 75 μm was dispersed in 500 ml deionized water in ultrasonic bath for 30 minutes. The suspended part and sediment were separated and dried. The sediment part was dry ground in a planetary mill (PM-100, Retch) using an alumina sample cup and 30 alumina grinding balls, at 300 rpm for 4 minutes and dispersed in 500 ml deionized water in ultrasonic bath for 30 minutes. After separation and drying of the sediment and suspended portion, the heavier portions were further ground as done before for three more times. At the end all the dried suspended part and sediment were mixed and the particle size distribution analysis was performed using

(Sedigraph 5100, Micromeritics Instrument Corporation) dispersing the powder in Calgon solution (% 0.7 by volume). It was found that the particle size ranged below 30 μm. This powder was dispersed in 500 ml deionized water in an ultrasonic bath for 15 minutes. The suspension was left to settle down for 15 minutes in 500 ml graduated cylinder, the sediment was separated and labeled as "Heavy". The suspended portion was taken to another cylinder and left to settle down for 3 hours 48 minutes. At the end of the settling time, the suspended portion was removed using a peristaltic pump and the remaining sediment was kept in a static oven at 65 ^{o}C for 24 hours. The powder obtained in this manner was labeled as "ClinRich". The suspended portion was left to further settle in another graduated cylinder for 24 hours and at the end of the settling period the sediment was separated from the suspended portion and dried under the same conditions. The zeolite powder obtained was labeled as "ClinRich-B". The remaining portion was dried and kept. The settling times were calculated on the Stokes' Law of Settling of Particles. It was assumed that all the mineral phases have the same particle size initially. Therefore, the separation by sedimentation will occur based only on the specific gravity differences between the mineral phases constituting the zeolitic tuff.

The clinoptilolite purity of ClinRich was confirmed by qualitative and quantitative X-ray powder diffraction analysis. The details of the analysis will be mentioned in Section 4.2.3. The concentration of the clinoptilolite phase in ClinRich was also confirmed thermally by heating the sample at 450 ^{o}C for 16 hours and by comparing the X-ray diffraction patterns before and after the thermal treatment (Mumpton, 1988). The thermal stabilities of ClinRich was also testes by gravimetrically on a thermal gravimetric analyzer (TGA-51, Shimadzu) and a differential thermal analyzer (DTA-50, Shimadzu) up to 1000 ^{o}C at a heating rate of 10 ^{o}C/min, under 40 ml/min N_2 flow.

After the confirmation of efficiency of the purification process that is the phase with high purity in clinoptilolite could have been achieved, ClinRich powder was tried to be packed into column for NO adsorption in order to elucidate the effect of clinoptilolite content of the zeolite on its adsorption properties. However some problems were encountered during packing as well as during the adsorption such as high pressure drop across the column related with the size of the powder. Thus it was decided to aggregate the fine powder in pellet form to get particles of manageable size. Generally a clay binder is mixed with small zeolite crystals together in order to obtain particles with satisfactory physical strength and size. But, some problems such as

blinding of the crystal surface leading to decrease in mass transfer rates and coking due to the catalytic activity of the binder during pelletization were reported in the literature. The proportion of the clay binder commonly amounts to 10-20 % by weight in the final pellet (Ruthven, 1984). For this purpose, ClinRich was mixed with kaolin in proportion of 9:1 by weight and the mixture was pelletized under 5 tons for 1 minute using a hydraulic press. The particle size of Washed sample was reduced to the same range as ClinRich after successive grinding and settling cycles. This powder was labeled as "WGround". After the confirmation of the particle size distribution, the powder was also aggregated into the pellets in the same manner as done for ClinRich. Both prepared cylindrical pellets with diameter of 10 mm and height of 6 mm were crushed and sieved to the particle diameter range of 75-150 μm and calcined at 400 ^{o}C for 12 hours in a static oven. The temperature was gradually increased to this temperature at a heating rate of 1 ^{o}C/min. The particles obtained after grinding, pelletization and calcination of Washed sample were labeled as "WGround-Kaolin" while those prepared from ClinRich as "ClinRich-Kaolin". Pure kaolin pellets were also prepared, crushed to the same particle size range and calcined in the same manner. Prior to the NO adsorption, desorption and temperature-programmed desorption studies, the prepared particles were packed into the column and activated *insitu* in the gas chromatograph oven according to the activation process applied to the other zeolites.

4.1.2. Preparation of the Metal-Sorbed Zeolites

The wet-sieved zeolitic material of 75-150 μm fraction was washed with deionized water in solid/liquid ratio (*S/L* ratio: g zeolite/ml solution) of 1/20 on a hot plate while being stirred mechanically. The temperature of the slurry was increased to about 90 ^{o}C, then the slurry was left to settle and the clear supernatant was discarded. This washing step was repeated once more and the remaining solid was kept in an oven at 65 ^{o}C for 24 hours to dry. This sample was labeled as "Washed".

50 grams of Washed zeolite was exchanged with sodium chloride (Riedel) in *S/L* ratio of 1/10 in order to obtain a material in homoionic form. The NaCl treatment was performed in a water bath at 80 ^{o}C, at 170 rpm, for 9 days. The NaCl solution was

renewed each three days. At the end of the treatment period, the supernatant was separated from the slurry using a peristaltic pump, the remained particles were washed with excess amount of deionized water to remove the chlorine and dried in a static oven at 65 ^{o}C for 24 hours. The zeolite particles obtained in this manner was labeled as "Na-Clin".

Na-Clin zeolite was contacted with nitrate salts of silver, cupper, iron and cobalt with initial concentration of 0.05 M in *S/L* ratio of 1/100 in a water bath at 60 ^{o}C, at 170 rpm for 24 hours. The metal sorption was also performed using nitrate salts of silver, cupper and iron with initial concentration of 0.01 M in *S/L* ratio of 1/20 under the same conditions for 1 hour. Silver sorption was carried out in the darkness. The initial pH values of the metal nitrate solutions before and after the addition of the zeolite were measured. The pH values of the slurries at the end of the sorption were also measured. After contacting Na-Clin with the metal salt solutions, the supernatant was decanted carefully using a peristaltic pump and the solid was washed with excess amount of deionized water repeatedly to remove the excess metal nitrate salts. The exchanged zeolite samples were dried in an oven at 65 ^{o}C for 24 hours and stored under room conditions in closed polyethylene bottles. The samples treated with metal salts with 0.05 M and 0.01 M initial concentrations are labeled as "0.05 M Metal" and "0.01 M Metal-1h", respectively. In order to elucidate the effect of cobalt content of the zeolites on the NO adsorption capacity, Na-Clin was also treated with aqueous cobalt nitrate solutions with initial concentrations of 0.01 M and 0.1 M in S/L ratio of 1/100 for 24 hours under the same conditions. These samples were labeled as "0.01 M Co-24h" and "0.1 M Co-24h", respectively. The coding of the samples is summarized in Table 4.1.

Table 4.1. Coding of the samples.

Sample ID	Parent zeolite	Treatment conditions				
		Treatment solution	Initial concentration of the treatment solution (M)	*S/L* (g zeolite/ml solution)	Temperature (^{o}C)	Treatment period
Washed	tuff	Deionized water	-	1/20	90	3 hours
Na-Clin	Washed	NaCl	1	1/10	80	9 days
0.05 M Co	Na-Clin	$Co(NO_3)_2 \cdot 6H_2O$	0.05	1/100	60	24 hours
0.05 M Ag		$AgNO_3$				
0.05 M Fe		$Fe(NO_3)_3 \cdot 9H_2O$				
0.05 M Cu		$Cu(NO_3)_2 \cdot 6H_2O$				
0.01 M Co-1h		$Co(NO_3)_2 \cdot 6H_2O$	0.01	1/20	60	1 hour
0.01 M Ag-1h		$AgNO_3$				
0.01 M Fe-1h		$Fe(NO_3)_3 \cdot 9H_2O$				

4.2. Characterization of Adsorbents

4.2.1. Particle Size Distribution

Particle size distributions of the Washed samples of both size intervals used in the NO adsorption studies (75-150 μm and 150-250 μm) were measured using a particle size analysis instrument (Mastersizer 2000, Malvern Instruments) after dispersing the powders in Calgon solution (0.1 % by volume) in an ultrasonic bath for 30 minutes. The particle size distribution of the purified clinoptilolite fraction (ClinRich) was also determined in the same manner. In order to examine the effect of clinoptilolite content of the mineral on the NO adsorption capacity, the 75-150 μm fraction was ground in the planetary ball mill (PM-100, Retch) and its particle size distribution was also determined.

4.2.2. Determination of Density, Volume and Porosity

The volume of zeolite particle is composed of volume of the skeleton (solid volume and closed pore volume) and volume of the open pores.

The density of a solid can be determined by comparing the weight of the sample in air to that immersed in a liquid of known density. Using the density measurement apparatus (YDK01, Sartorius) operated based on the Archimedes principle, the density of a solid is given by,

$$\rho = \frac{m_{dryinair}\left(\rho_{water} - \rho_{air}\right)}{0.99983\left(m_{dryinair} - m_{wetinwater}\right)} + \rho_{air} \qquad (4.1)$$

where $m_{dryinair}$ is the mass of dry (dehydrated) solid in air, $m_{wetinair}$ is the mass of completely hydrated solid in water, ρ_{water} is the density of water at the measurement temperature and ρ_{air} is the density of air at 25 ^{o}C, 1 atm (0.0012 g/cm^3). The density measured in this manner in this study excludes the open pore volume, so it is the true solid density (ρ_{true}).

The particle density ($\rho_{particle}$) can also be measured and calculated by:

$$\rho_{particle} = \frac{m_{dryinair}\rho_{water}}{m_{wetinair} \quad m_{wetinwater}} \tag{4.2}$$

where $m_{wetinwater}$ is the mass of completely hydrated solid in air.

The true solid densities were also directly measured by a helium pynometer (Ultrapycnometer 1000, Quantachrome).

The bulk density of a particle (ρ_{bulk}) is defined as:

$$\rho_{bulk} = \frac{m_{dryinair}}{V_{bulk}} \tag{4.3}$$

where V_{bulk} is the bulk volume of the particle. The total, open and closed pore volumes were also measured using the density measurement apparatus. The following volumes are calculated from the measured weights and the densities:

$$V_1 = \frac{m_{dryinair}}{\rho_{particle}} \tag{4.4}$$

$$V_2 = \frac{m_{dryinair}}{\rho_{true}} \tag{4.5}$$

where ρ_{true} is the true (skeletal) density and $\rho_{particle}$ is the particle density of the solid. Then the total pore volume (V_{total}) is determined from,

$$V_{total} = V_1 - V_2 \tag{4.6}$$

and the open pore volume (V_{open}) from,

$$V_{open} = \frac{m_{wetinair} - m_{dryinair}}{\rho_{water}} \tag{4.7}$$

Then the closed pore volume (V_{closed}) can be found as,

$$V_{closed} = V_{total} - V_{open} \tag{4.8}$$

The skeletal (true) volume of a solid ($V_{skeletal}$) includes the volumes of the solid and the closed pores so it can be expressed as:

$$V_{skeletal} = V_{bulk} - V_{open} \tag{4.9}$$

The skeletal (true) volume can also be measured directly by the helium pycnometer. In these measurements helium is used as a displacement medium. The assumption is that helium is capable of entering the whole pore space (except the closed pores) and it is not adsorbed by the solid.

The total pore volume per gram of dehydrated zeolite (V_p) can be calculated from the water content of the zeolite when fully hydrated. The amount adsorbed at

saturation can be determined from the plateau in the adsorption isotherm of Type I. At the saturation, it is assumed that the micropores of the adsorbent are filled with the water with the average density equals to the normal liquid density at the adsorption temperature (Breck, 1974). Then the total pore volume per gram of dehydrated zeolite can be calculated as,

$$V_P = \frac{V_{total}}{m_{dryinair}} \tag{4.10}$$

The total pore volume per gram of dehydrated zeolite can also be calculated from the skeletal (true) density of the solid material (excluding the volume in the open pores) (ρ_{true}) and with the density of the total particle (including the volume of pores) ($\rho_{particle}$) as:

$$V_p = \frac{1}{\rho_{particle}} - \frac{1}{\rho_{true}} \tag{4.11}$$

which gives the same value that calculated from Equation (4.10) .

It is possible to calculate the total pore volume of zeolites theoretically from the known structure. The total pore can be calculated as:

$$V_p' = V_f \frac{1}{\rho_f} \tag{4.12}$$

where V_f is the total void fraction in the crystal and ρ_f is the framework density (Breck, 1974).

The total pore volumes of the zeolites used as adsorbent in this study were determined from the data collected in thermal gravimetric analysis, and adsorption of CO_2 and N_2, at 30 ^oC and -196 ^oC, respectively by the application of the Gurvitsch Rule.

According to the Gurvitsch rule, the adsorption uptake at relative pressure of $P/P_o \approx 1$, when expressed as a volume of liquid should be the same for all adsorptives on a given adsorbent (Gurvitsch, 1915). The amount adsorbed at relative pressure of $P/P_o \approx 1$ can be expressed as a liquid volume according to:

$$V_p = \frac{VM}{22414\rho^*} \tag{4.13}$$

where V_P is the total pore volume, V is the amount of adsorbate adsorbed at saturation ($P/P_o \approx 1$), M is the molecular weight of the adsorbate and ρ^* is the liquid density of the adsorbate adsorbed in the pores at the measurement temperature (corrected density) which is given by:

$$\rho^* = \rho_b - \alpha(T - T_b) \tag{4.14}$$

where ρ_b is the density of liquid at normal boiling point and α is the thermal coefficient given as:

$$\alpha = \frac{\rho_b - \rho_c}{T_c - T_b} \tag{4.15}$$

where ρ_c is the critical density ($\rho_c = M/b$), b is the van der Waals co-volume ($b = RT_c 8P_c$), R is the gas constant, T_c and P_c are the critical temperature and critical pressure of the adsorbate, respectively.

For adsorption at temperatures above the critical temperature of the adsorbate, Suzuki recommended applying the Dubinin-Nikolaev equation in order to estimate the hypothetical density of the adsorbed phase as given by Equation (4.15) (Suzuki, 1990).

Particle porosity of the adsorbents can be determined by several alternative methods. The particle porosity (including open and closed pores) is calculated from:

$$\varepsilon_p = \frac{V_{total}}{V_{bulk}} \tag{4.16}$$

where ε_p is the particle porosity. V_{total} is determined from Equation (4.6) and V_{bulk} is calculated from the known dimensions of the specimen. If the closed pores are not excluded, the particle porosity becomes:

$$\varepsilon'_p = \frac{V_{open}}{V_{bulk}} \tag{4.17}$$

4.2.3. X-Ray Powder Diffraction

The powder X-ray diffraction patterns of the zeolite samples were recorded on a powder diffractometer (X'Pert Pro, Philips) equipped with Ni filtered CuKα radiation source (λ=1.540560 Å) over 2θ range of 5° to 50° at a 10.15 s measurement time per step and a step size of 0.01671°. The X-ray source was operated at 40 mA and 45 kV. Sample preparation for the X-ray analysis involved gentle grinding of the particles into a fine powder and packing of the powder into an aluminum sample holder with light compression to make it flat and tight.

For quantitative phase purity analysis, the clinoptilolite references with >90 % clinoptilolite content (27031, Castle Creek, Idaho and 27023, Hector, California; referred as Idaho and California in this thesis, respectively) obtained from Mineral

Research, Clarkson, New York supplied kindly by F. Mumpton in powder form were used. The reference from Idaho has >95% clinoptilolite content with only about 5% of impurities.

The quantitative mineralogical analysis was carried out using the Reference Intensity Ratio (RIR) technique (Bish and Chipera, 1988). RIR standard mixtures were prepared by mixing 1.0 μm metallurgical grade α-alumina powder (corundum) to each mineral standard in a 50:50 ratio by weight. To determine RIR values for each mineral phase, six replicate XRD scans were conducted on each RIR standard. Before each replicate analysis, the standard was removed from the sample mount, remixed with the standard remaining in the sample bottle, and the sample was repacked to the mount. The sum of three reflections from 21.0^o to 23.0^o 2θ region for clinoptilolite (2θ= 22.39^o, 22.71^o and 23.05^o) rather than individual reflections were used in order to normalize effects of both preferred orientation (i. e., crystallites of the sample all tend to lie in one direction because of their shape) and chemical variation.

The quantitative analysis method including the application of multiple analytical XRD lines proposed by Nakamura et al. was also employed (Nakamura et al., 1992). This method is based on the ratio of the summation of intensities of the seven characteristic peaks belong to clinoptilolite in the 2θ range of 9.82^o–19.02^o (2θ = 9.82^o, 11.15^o, 13.07^o, 14.89^o, 16.91^o, 17.28^o, and 19.02^o) for the sample to that for the mineral reference. The calibration curves were made by plotting the sum of the diffraction intensities of these lines against the mass fractions of standard materials in the calibrating mixtures. The mixtures prepared for the construction of the RIR calibration curve were also used to prepare the calibration curve for this method.

X-ray diffractograms were used to determine whether different treatments (washing, metal sorption, activation etc.) produced variations in the zeolite structures. The formation of new crystalline phases during metal sorption or activation was also checked. The databases the joint committee on powder diffraction standards in the International Centre for Diffraction Data (JCPDS-ICDD, PDF-1 database) were used to interpret the mineralogical compositions and crystalline phases in the zeolites.

4.2.4. Elemental Analysis

The solid phase elemental analyses were carried out to determine the chemical composition of the zeolite samples after different treatment procedures by an inductively coupled plasma atomic emission spectrometer with axial plasma Liberty Series II ICP-AES, Varian). The zeolite samples were treated with an alkali borate fusion flux (anhydrous lithium tetraborate) and dissolved in 1.6 M HNO_3 prior to the chemical analysis. The clinoptilolite reference minerals (Idaho and California) and the purified zeolite (ClinRich) were also analyzed in the same manner.

Elemental compositions of the zeolites were also determined using energy dispersive X-ray spectroscopy (EDX) on the particles. An average elemental composition of the sample was obtained by a data collection at 6 different regions of about 100 μm×50 μm area on the particle surface. The energy of the beam was 10 kV. EDX is used in conjunction with SEM. The technique detects X-rays emitted from the sample during bombardment by an electron beam to characterize the elemental composition of the analyzed volume. The energy of the X-rays is characteristic of the element from which it was emitted and depends on the sample under examination. The X-rays are generated in a region about 2 μm in depth and regarding the size of the particles, EDX can be considered as a surface characterization technique (http://www.uksaf.org/tech/edx.html). The spectrum of peaks identifying elements detected within the area analyzed is evaluated to determine the elemental composition of the area. The intensity of peaks (peak height) is related to the elemental concentration.

In order to investigate the reactions prevail during the metal sorption (ion exchange, adsorption, dissolution, proton binding etc.), NaCl was contacted with metal-free deionized water under the conditions in the metal sorption experiments. The initial pH values of the water were adjusted to the corresponding values which were measured just after the addition of Na-Clin to the metal salt solutions in the metal sorption experiments using 0.1 M HNO_3 or 0.1 M NaOH. At the end of the treatment periods, the aqueous phases were centrifuged and the concentrations of Al, Ca, Fe, K, Mg, Mn, Na and Si in the aqueous phase were determined by an inductively coupled plasma atomic emission spectrometer with axial plasma (Liberty Series II ICP-AES, Varian).

These experiments are not expected to simulate the interactions between heavy metal solution and Na-Clin, but the results provide some evidence relating to the possible mechanisms existing in the metal salt solutions including protonation, OH^- binding and ion exchange.

The aqueous phases at the beginning and at the end of the metal sorption and Na-Clin-water interaction experiments were also analyzed by the same method.

4.2.5. Zeta-potential Measurements

The zeta potential of Na-Clin was measured by a zeta potential measurement instrument (Zetasizer 3000 HAS, Malvern Instruments). The zeta potential measurements were carried out as a function of pH of the deionized water. 0.1 g of Na-Clin was were dispersed in 20 ml deionized water in an ultrasonic bath for 30 minutes. 0.2 ml of the suspension was diluted to 20 ml using deionized water and the pH was adjusted to 2, 4, 6, 8 and 10 using 0.1 M NaOH and 0.1 M HNO_3. These suspensions were stirred on a magnetic stirrer for 90 minutes in order to achieve the equilibria. The average of ten measurements was taken to represent the measured potential.

4.2.6. Scanning Electron Microscopy–Back Scattered Electron-Energy Dispersive X-Ray (SEM-BSE-EDX)

Scanning electron microscopy combined with energy dispersive X-ray (SEM-EDX) analyses was performed using Philips XL-30S FEG SEM. The morphology and crystal size of the materials were investigated using the scanning electron micrographs. The SEM spectra for the metal sorbed and subsequently activated zeolites were collected in both secondary electron (SE) mode and back scattered electron (BSE) mode. The BSE images (×800, 10.0 kV) were used in order to investigate the size and distribution of metal phases on the zeolite surface. Variations in the average atomic weight of the material are depicted as variations in the gray level of the image. The

zeolite particles were mounted directly on a carbon tape before the analysis. The bright spots observed on the surface of the zeolite particles in the BSE images were analyzed via energy dispersive X-ray spectroscopy (EDX) coupled to the scanning electron microscope in order to determine the elemental compositions.

4.2.7. Textural Properties

The surface areas, pore volumes and pore size distributions of the zeolites were obtained by the analysis of the nitrogen adsorption-desorption isotherms. A static volumetric adsorption instrument (ASAP 2000, Micromeritics Instrument Corporation), was used to measure the N_2 adsorption and desorption isotherms of the zeolite samples at the normal boiling temperature (-196 ^{o}C). The zeolite samples were also characterized by the CO_2 adsorption at 30 °C using the same equipment. Prior to the adsorption, the samples were degassed in vacuo (5×10^{-4} mbar) at 300 ^{o}C for 24 hours.

4.2.8. Thermogravimetric Analysis (TGA)

Thermogravimetric analyses of the zeolites were performed on a thermal gravimetric analyzer (Shimadzu TGA-51, Shimadzu) up to 1000 ^{o}C at a heating rate of 10 ^{o}C/min, under 40 ml/min N_2 flow.

4.2.9. Infrared Spectroscopy

The prepared zeolite samples were characterized using transmission Fourier transform infrared (FTIR) Spectroscopy. The samples were prepared using the standard potassium bromide (KBr) pellet method (sample/KBr:1/200 by weight). The sample-KBr mixtures were ground together in an alumina agate and pelletized under 4 tons/cm^2

pressure for 1 minute by a hydraulic press. The transmission infrared spectra were recorded in the region of 400–4000 cm^{-1} at room temperature after 256 scans at 2 cm^{-1} resolution using a spectrometer (FTIR-8400S, Shimadzu). For all the spectra, the baseline correction and normalization (with respect to the most intense band) were carried out.

The zeolites after loaded with NO were also inspected by infrared spectroscopy in order to determine the irreversibly adsorbed NO species. The infrared absorption measurements were carried out on a infrared spectrometer (FTS 3000MX, Excalibur Series, Digilab) at room temperature, in the wavenumber range from 400 to 4000 cm^{-1} after 256 scans at 2 cm^{-1} resolution. The spectrometer was equipped with a DTGS-TEC detector. The zeolites subjected to the temperature-programmed desorption process following the NO loading and those used in the release experiments were also tested. The samples were prepared in the same manner as for the metal-sorbed zeolites. The normalization has been performed on the each spectrum with respect to the zeolite amount in the pellet.

For the quantitative comparisons, the absorbance values were normalized with respect to the zeolite amount in the pellet and with respect to the absorbance of the most intense band in the spectrum.

4.3. NO Adsorption, Desorption and Temperature-Programmed Desorption (TPD)

4.3.1. Dynamic Adsorption Studies

The adsorption breakthrough profiles of the zeolites were obtained by passing NO gas at 20 ml/min flow rate through the column packed with the zeolite particles and recording the column effluent composition as a function of time using a thermal conductivity detector (TCD). The set-up shown in Figure 4.1 was constructed and employed in the NO adsorption, desorption and temperature-programmed desorption studies.

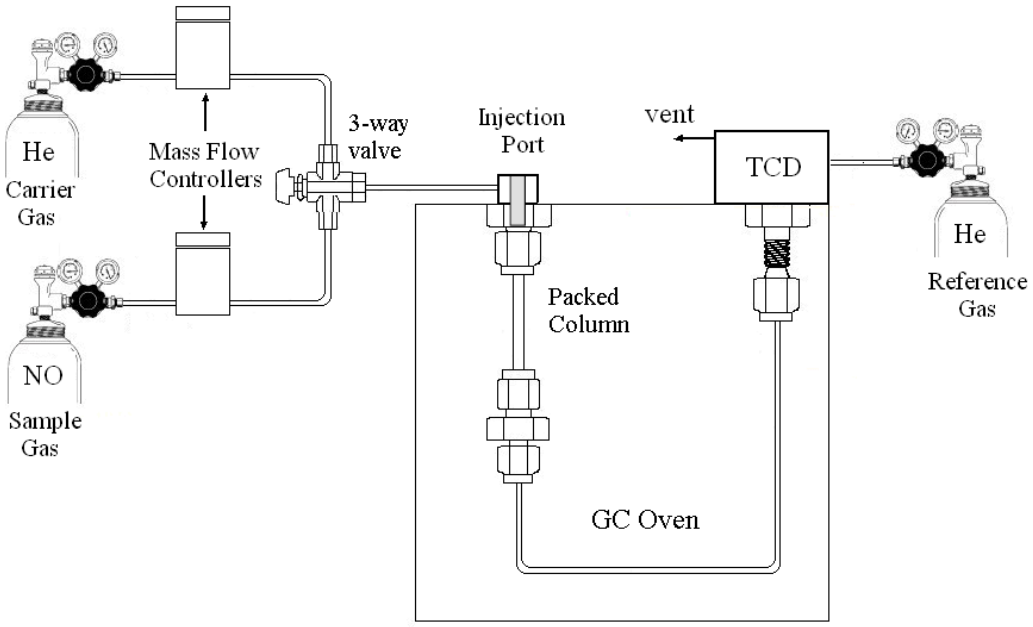

Figure 4.1. Experimental set-up used in the NO adsorption, desorption and temperature-programmed desorption studies.

To maximize the resolution and accuracy of the measurements, the dead volume containing both tube volume and inlet volume of column in the adsorption system were minimized. The "extra-column effects" arising from connecting tubing and detectors influence both the residence time and the band broadening of the breakthrough curve. Extra-column effects can be significant especially when the dead volume in the system is not negligible. This situation is occurred either when very short columns are used or when the time in the extra-column volume is non-negligible compared to the residence time in the adsorption column. For this purpose, tubing with outer diameter of 1/8 inch was used for the connections from the injection port to the column inlet and from the column outlet to the detector. The effect of dead volume was also accounted for in the treatment of the experimental data. For this purpose, the dead volume was estimated by passing NO through the empty column, "blank run". The total and reversibly adsorbed amounts determined from the profiles by integration were corrected for the dead volume effect. The percent contribution of the area above the breakthrough curve calculated from the empty column data to that calculated from the packed column data ranged between 12.5-21.6 %.

The column of 4.1 cm in length was made from type 316 stainless steel tubing with outer diameter of ¼ inches. The column was packed by tapping using a column vibrator. Commercially available pressed frits fabricated from Type 316 stainless steel with pore size of 20 μm (Alltech Associates Inc., Part No: 703325) were used at both end of the column. The mass of the zeolite packed into the column was determined from the difference in the mass of the column before and after the packing. The dehydrated masses of the zeolites in the column were determined based on the thermogravimetric analyses.

Table 4.2. Characteristics of the column and the adsorbents.

Particle diameter range (μm)	75-150 μm	150-250 μm
Average particle diameter, d_p (μm)	109	190
Column internal diameter, d_{column} (mm)	5.3	
Column length, L (cm)	4.1	
Column internal diameter/Average particle diameter	48.9	28.1
Bed voidage, ε	0.389	0.404
Particle porosity, ε_p	0.387	
Particle bulk density, ρ_{bulk} (g/cm^3)	1.246	
Interstitial velocity, v (cm/s)	2.635	5.993

The characteristics of the packed column were determined from the properties of the zeolites and from the dimensions of the system and are given in Table 4.2. The results of the dynamic analysis of the system were summarized in Appendix A.

The activation of the zeolites was performed *insitu*, in the oven of gas chromatograph first increasing the temperature of the oven to 100 ^oC where it was kept for 2 hours, then to 400 ^oC and kept at this temperature for 12 hours. The heating rate was constant at 1 ^oC/min. The activation was carried out under continuous helium flow of 50 ml/min. At the end of the activation process, the oven was cooled down to the adsorption temperature (30 ^oC). NO gas was passed through the column at 20 ml/min until the detector signal has reached a constant value. The flow rates of the gases were controlled by mass flow controllers calibrated for each gas (5850S, Brooks Instruments) and a processor (Read and Out Control Electronics 0152, Brooks Instruments). The flow was then switched to pure helium of 20 ml/min until the detector signal turned

back to the baseline. It took about 240 minutes of the detector signal to be stabilized at the baseline, so the desorption (purging) period was determined as 240 minutes. The purpose of this purging step was to remove the gas-phase and weakly (reversibly) adsorbed NO species. The experimental data were collected at time intervals of 0.017 minutes over a period of 120 minutes from the introduction of the step response, beyond which no notable change in the detector signal was detected. Therefore, there are about 7200 data points for each adsorption response curve and about 14400 data points for each desorption curve.

The temperature-programmed desorption (TPD) experiments were performed by ramping the oven temperature to 400 ^{o}C at a rate of 1 °C/min and keeping at this temperature for 180 minutes under the continuous helium flow of 20 ml/min. During the adsorption, purging and TPD runs, the column outlet gas was monitored continuously by a thermal conductivity detector (TCD) operating at 250 ^{o}C that is equipped with the gas chromatograph (6890N, Agilent Technologies).

Prior to the NO adsorption studies, in order to investigate whether the detector signal collected requires correction for the system properties, the carrier gas was passed through the empty column under the same temperature and flow conditions as in the packed column experiments. It was also confirmed that the carrier gas is not adsorbed by the zeolites under the experimental conditions of concern.

The irreversibility of the adsorption of NO was tested through successive adsorptions on the same adsorbent. The adsorption properties of the natural zeolite were compared with those of the synthetic ones (molecular sieves 3A, 4A and 5A, Sigma-Aldrich). The synthetic zeolites commercially available in shape of beads with the particle diameter range of 4-8 mesh were ground and sieved to the same particle size range of the zeolites. The activation, adsorption, purging and temperature-programmed desorption runs on the synthetic zeolites were performed under the same conditions as for the natural zeolites.

The sensitivity of the adsorption profiles to the adsorbate flow rate, adsorbent particle size, activation period, adsorption temperature and the mineral purity of the zeolite were tested. The non-porous (glass) particles obtained through grinding and sieving the commercially available glass beads with particle diameter in the 60-80 mesh range (Alltech Associates Inc., Part No: 5420) were also tested for their NO adsorption kinetics.

Typical adsorption and desorption breakthrough curves obtained are shown in Figure 3.1. The breakthrough curves were presented as normalized effluent concentration, i. e., the ratio of the concentration of NO in the column outlet stream to that in the feed. The x-axis was presented in terms of time or the amount of NO fed to the column per unit mass of zeolite packed in the column. The latter way of presentation is more convenient way of comparing the impact of process variables on the adsorption kinetics (Hand et al., 1984).

The equilibrium adsorption capacities of the zeolites for NO were determined from the breakthrough curves based on the overall mass balance on the column given in Equation (3.2). The integral term corresponds to the area above the adsorption breakthrough curve and was determined by a numerical integration method called the Trapezoidal Rule. The areas for the packed columns were corrected by subtracting the area above the empty column. The reversible adsorption capacities were similarly calculated from the area under the desorption profile. Accordingly, the irreversible adsorption capacities were determined by subtracting the reversible adsorption capacities from the corresponding total adsorption capacities.

4.3.2. Diffuse Reflectance Infrared Spectroscopy (DRIFTS)

In order to investigate the species formed during the course of NO adsorption, desorption and temperature-programmed desorption Fourier transform spectroscopy infrared (DRIFT) spectrum were collected on a spectrometer (FTS 3000MX, Digilab Excalibur Series), in the range of 1100-4000 cm^{-1}, by averaging 200 scans at a resolution of 2 cm^{-1}. The DRIFT spectra presented in this thesis were smoothed.

The experimental set-up shown in Figure 4.2 was constructed on the spectrometer. The set up includes a high-temperature, low-pressure reaction chamber (HVC-DRP, Harrick Scientific Products, Inc). The chamber is made up of chemically resistant 316 stainless steel and allows operation under high vacuum (10^{-6} torr) and at high temperatures (up to 600°C under vacuum). It has three inlet/outlet ports provided for evacuating the chamber and introducing gases. The dome has two CaF_2 windows and one glass window for observation. The chamber was installed in the Praying Mantis

(Harrick Scientific Products, Inc.). The temperature of the sample was measured by a K-type thermocouple and controlled by a low-voltage heating cartridge using a single-loop PID temperature controller (Series 989, Watlow). The vacuum in the chamber was created by a turbomolecular pump system (PT 50, Oerlikon Leybold Vacuum) including 2-stage rotary vane vacuum pump (Trivac D 2,5E, Oerlikon Leybold), Pirani vacuum gauge (stainless steel sensing cell with platinum filament and ceramics feed through, (measurement range: 5×10^{-4}–1000 mbar, Thermovac TR 216 S, Oerlikon Leybold,) and Penningvac vacuum gauge (measurement range: 10^{-9}–10^{-3} mbar, PTR 225, Oerlikon Leybold).

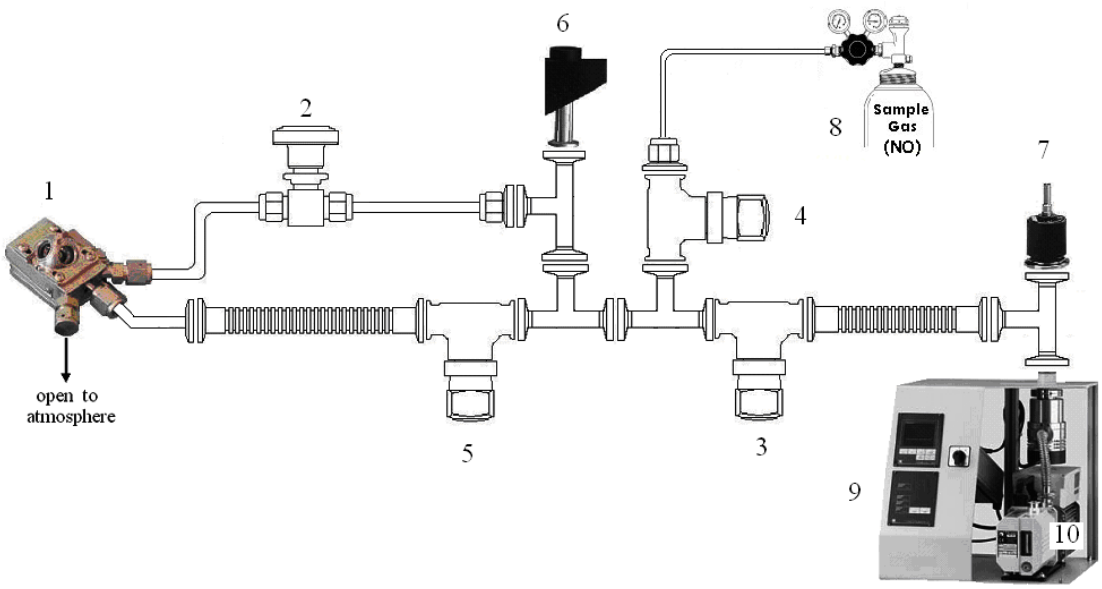

Figure 4.2. Experimental set-up for the diffuse reflectance infrared spectroscopy. 1, high temperature, low pressure reaction chamber; 2, high pressure needle valve; 3, 4, 5, vacuum valves; 6, Pirani vacuum gauge; 7, Penning vacuum gauge; 8, NO cylinder; 9, turbo molecular vacuum pump; 10, Rotary vane vacuum pump.

Prior to the NO adsorption, Washed sample was mixed with KBr in proportion of 1:9 by weight. The mixture was ground together in an alumina mortar. Then approximately 90 mg of the mixture was transferred to the sample cup of the reaction chamber and gas and vacuum lines were connected. The Washed zeolite-KBr mixture was then activated *insitu* at 400 ^{o}C for 12 hours under 2×10^{-4} mbar vacuum. The heating

rate was 1 ^{o}C/min. Then the sample was cooled to the adsorption temperature (30 ^{o}C). The adsorption procedure involved contacting the activated zeolite with NO at 30 ^{o}C for 15 minutes followed by outgassing with vacuum at 1×10^{-1} mbar to remove the weakly adsorbed species. The next IR spectra were then recorded by gradually increasing the pressure of NO. The NO pressure was adjusted using vacuum valve (shown as "4" in Figure 4.2) and measured by the Pirani vacuum gauge. After the adsorption of NO at 1000 mbar, the chamber was first evacuated at 1×10^{-1} mbar at 30 ^{o}C, then at 2×10^{-4} mbar for 30 minutes. Then the temperature of the chamber was increased to 400 ^{o}C at a heating rate of 1 ^{o}C/min and the spectra were recorded after 60 minutes. Following the cooling the chamber to the adsorption temperature under vacuum, the chamber was opened to the atmosphere and after 60 minutes the spectra was collected. The spectra of adsorbed NO species following each evacuation step were interpreted by comparing with those for the KBr which was treated under the same conditions in order to eliminate the changes in the KBr induced by adsorption, desorption and heating.

The level of DRIFTS signal is dependent on the scattering coefficient, which is strongly dependent of the particle size and the packing density of the sample. Prior to use, the as-received zeolite samples were ground into a powder to maximize spectral quality. The DRIFT spectra presented in this thesis were smoothed.

4.4. NO Loading

The zeolite powders were loaded with NO in the same manner as for the NO adsorption-desorption-TPD experiments. The difference was that after the NO loading, helium was purged overnight. The NO-loaded zeolite powders were depacked from the column, transferred immediately to 20-ml amber gas-tight glass vials with PTFE/silicone septa (Alltech) and stored in a molecular sieve 4A desiccator under ambient conditions. The zeolites loaded with NO in this manner were labeled as "Sample ID-NO". The zeolites which were loaded with NO then purged with helium for 240 minutes at 30 ^{o}C and subjected to the temperature-programmed desorption were labeled as "Sample ID-NO-Des".

4.5. NO Release

4.5.1. Antibacterial Properties of the NO-Loaded Zeolites

The antibacterial tests were performed using agar-well diffusion assay. The antibacterial activities of the zeolites after different treatments including the metal sorption, NO adsorption and purging, temperature-programmed desorption successive to the adsorption and purging were tested against the reference strain of *Escherichia coli* (NRLLB 3008) as representative for Gram-negative bacteria. The standardized cells were inoculated into nutrient broth and left to incubate overnight at 37 °C (~10^9 cfu/ml*) (cfu:* colony forming units). For the antibacterial activity tests, 19 ml of Mueller-Hinton agar was inoculated with 0.5 ml of the overnight-grown bacterial strains. The inoculated agar was then poured into petri dishes and allowed to set. Maximum four wells (5.5 mm diameter) were made in each plate with sterile cork borer and the agar was removed with sterile forceps. The wells were filled with approximately 40 mg of the NO-loaded zeolite particles. The agar plate was then covered with lid and incubated at 37 °C for 24 hours The antibacterial activities were tested in at least triplicate and expressed in terms of the average diameter of the growth zone inhibition. The zone of inhibition around each well was measured with a micrometer. The average diameters were normalized with respect to the zeolite mass filled to the well. The absence of growth inhibitory zone for the bacteria around the well was interpreted as the absence of antibacterial activity. Clear inhibition zone represents antibacterial properties and the diameter of inhibition indicates the strength of the antibacterial properties. The antibacterial properties of the zeolite before loaded with NO and after the thermal treatment following the NO loading were also tested.

The antibacterial activity of Washed-NO sample was also tested against the reference strain of Gram-positive bacteria *Bacillus subtilis* (NRLLB-4378) cells in the same manner. The standardized overnight-grown culture of *B. subtilis* contains ~10^7 cfu/ml. The stock *E. coli* and *B. subtilis* cultures viable cell concentrations were confirmed by plating the 1 ml from the appropriate dilutions according to the pour plate method.

The stability of the antibacterial activities of Washed-NO sample was examined in order to elucidate whether the antibacterial property has changed when NO-loaded zeolite is stored in a gas-tight vial for different time periods.

4.5.2. Bactericidal Properties of the NO-Loaded Zeolites

The effect of NO loading on the bactericidal activity of Washed zeolite was tested against *E. coli* and *B. subtilis*. Different amounts of the zeolite (500, 250, 100 and 5 mg) were contacted with 20 ml of phosphate buffer saline (5 mM PBS, pH 7.4) for 2 hours at 37 ^{o}C under 80 rpm stirring in a thermoshaker (Max-Q 4000, Lab-Line, Barnstead). 5 mM disodiumhydrogen phosphate (Na_2HPO_4) (Riedel-de Häen, 30427l), 5 mM sodiumhydrogen phosphate monohydrate ($NaH_2PO_4 \cdot H_2O$) (Sigma S071) and 150 mM NaCl (Riedel-de Häen, 31434) were used to prepare the PBS solution. The pH of the solution was confirmed using a pH meter (pH330i, WTW). The PBS was sterilized by filtering through a 0.45-μm sterile filter (Millipore) previously to use. The initial *E. coli* and *B. subtilis* bacterial loads in the PBS were adjusted to ~10^3 cfu/ml. At the end of the contact period, 1 ml samples were taken from the supernatants and poured on to the nutrient agar. After 48-hour incubation at 37 ^{o}C, the viable cells were counted. The bacterial concentrations of the *E. coli* and *B. subtilis* stock cultures were also determined in each experimental set by serial dilutions and found to be in the range of 7.2-13.9×10^8 cfu/ml and 2.8-3.7×10^7 cfu/ml, respectively.

The bactericidal activity of Washed zeolite against both bacteria was tested at the highest zeolite/PBS ratio as a control. Washed-NO-Des sample at the highest zeolite/PBS ratio was also tested in order to elucidate the effect of the loaded NO on the observed bactericidal activity.

4.5.3. NO Release in PBS

In order to determine whether there is a correlation between the amount of NO released and the bactericidal activity, different amounts of Washed-NO (0.25-25 mg/ml) were contacted with the PBS under the same conditions under which the bactericidal tests were performed. 50 µl samples were taken from the supernatants at 30 minutes time intervals and reacted with 50 µl Griess reagent (1% sulfanilamide in 5% phosphoric acid and 0.1% *N*-(1-naphthyl) ethylenediamine dihydrochloride in water) in a 96-well plate. Then, the solution was incubated for 10 minutes at room temperature, protected from light. A purple/magenta color formed immediately. The absorbance values at 525 nm were recorded using an UV-visible spectrometer (Multiskan Spectrum, Thermo Electron Corporation).

The total nitrite concentration in the buffer solution was taken to be equivalent to the NO released from the powders during each time period. The nitrite concentration was determined via the Griess spectrophotometric method (Schmidt and Kelm, 1996, Green et al., 1982; Privat et al., 1997). This method is an indirect measurement of NO. NO is first oxidized to nitrite by oxygen in aqueous solution. Sulfanilic acid is converted to a diazonium salt upon reaction with nitrite. Then, a coupling reaction between the diazonium salt and *N*-(1-naphthyl) ethylenediamine occurs, forming an azo dye that can be measured on a spectrophotometer. Nitrite is the product of NO oxidation in aerobic aqueous solution:

$$4NO + O_2 + 2H_2O \rightarrow 4H^+ + 4NO_2 \qquad (4.18)$$

The calibration was performed on nitrite standards prepared by dissolving $NaNO_2$ in the PBS and diluted to between 0 and 100 µM. The data were then collected over time and correlated with the calibration data, resulting in measurements of NO concentration in solution over time.

The NO release measurements in PBS were also performed on Washed and Washed-NO-Des samples at the highest zeolite/PBS ratios.

4.5.4. NO Release in Deionized Water

Approximately 50 mg of the NO-loaded zeolite samples were contacted with 100 ml deionized water in 100-ml closed Schott bottles at 37 ^{o}C without shaking. Following the addition of the NO-loaded powders into the deionized water, 50 μl samples were taken from the supernatants at time intervals. NO production was evaluated indirectly by measuring the accumulation of nitrite, the stable end product of NO oxidation, in the medium using the Griess reaction. The 50 μl samples taken from the supernatants were reacted with 50 μl of the Griess reagent in a 96-well plate for 10 minutes at room temperature in darkness. The absorbance was measured spectrophotometrically at 525 nm by using a microplate reader (Multiskan Spectrum, Thermo Electron Corporation). The nitrite concentration was determined from a sodium nitrite standard curve. Standards were prepared using sodium nitrite in the 0-100 μM range. To avoid interference by nitrites possibly present in the deionized water, the blank was also analyzed. Measurements were recorded at discrete intervals until the NO release was no longer detectable, i. e., the nitrite concentration in the samples was less than the detection limit (below 1 μM).

The zeolites that are used in the release experiments were labeled as “Sample ID-NO-Rel”.

CHAPTER 5

RESULTS AND DISCUSSION

5.1. Preparation of Zeolite with High Clinoptilolite Content

The starting powder used in the mineral purification process was obtained after successive grinding and settling runs on the natural zeolite with particle diameter below 75 μm (<75 μm). The particle size of the starting powder was found to be below 30 μm. The X-Ray powder diffractograms of the starting powder and fractions separated through the purification study as well as that of the clinoptilolite reference mineral (Idaho) are shown in Figure 5.1.

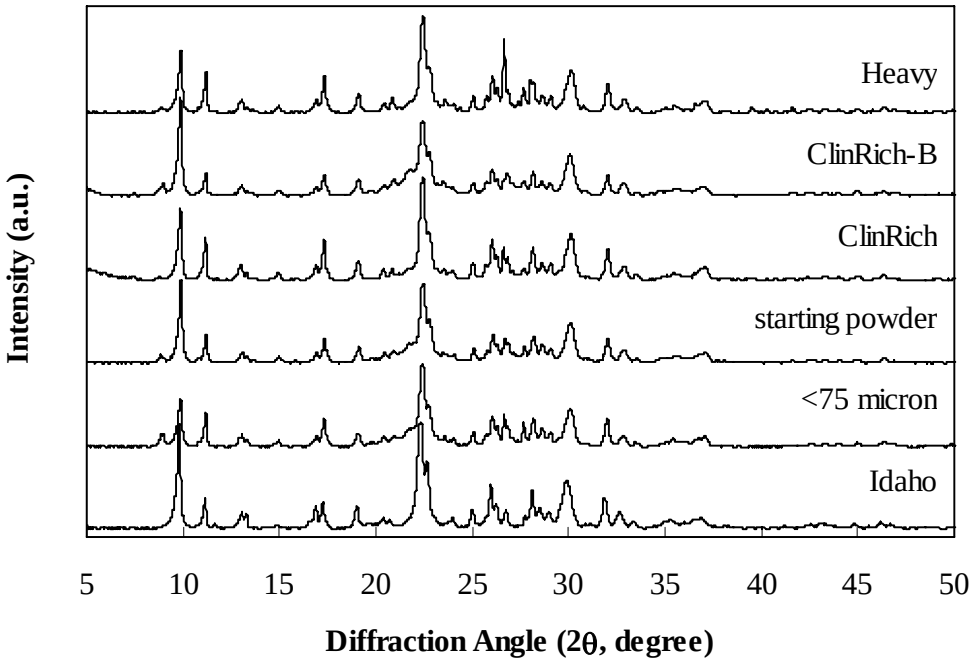

Figure 5.1. X-ray powder diffractograms of the clinoptilolite reference (Idaho) and the separated fractions through the purification study.

The calibration curves prepared for the quantitative analysis are shown in Figure 5.2. The calibration curves showed a good correlation between the clinoptilolite content of the zeolite and the relevant intensities. The regression coefficients (r^2) were found to be 0.977 and 0.925 for the RIR and the Nakamura's methods, respectively. The equation for the calibration curve obtained for the RIR method is:

$$RIR_{020} = 1.2098 \frac{I_{9.82}}{I_{22.39} + I_{22.71} + I_{23.05}} - 0.2814 \qquad (5.1)$$

and for the Nakamura's method:

$$SumI = I_{9.82} + I_{11.15} + I_{13.07} + I_{14.89} + I_{16.91} + I_{17.28} + I_{19.02} = 8307.2 \times CC \qquad (5.2)$$

where *CC* stands for the clinoptilolite content. The clinoptilolite contents of the different fractions determined by the quantitative analysis methods are compared in Table 5.1.

Table 5.1. Comparison of the methods applied for the determination of the clinoptilolite contents of the phases separated during purification study.

Method applied	Clinoptilolite content, *CC* (% weight)			
	<75 μm	Heavy	ClinRich	ClinRich-B
Nakamura's method	66	70	107	90
RIR method	37	50	95	94

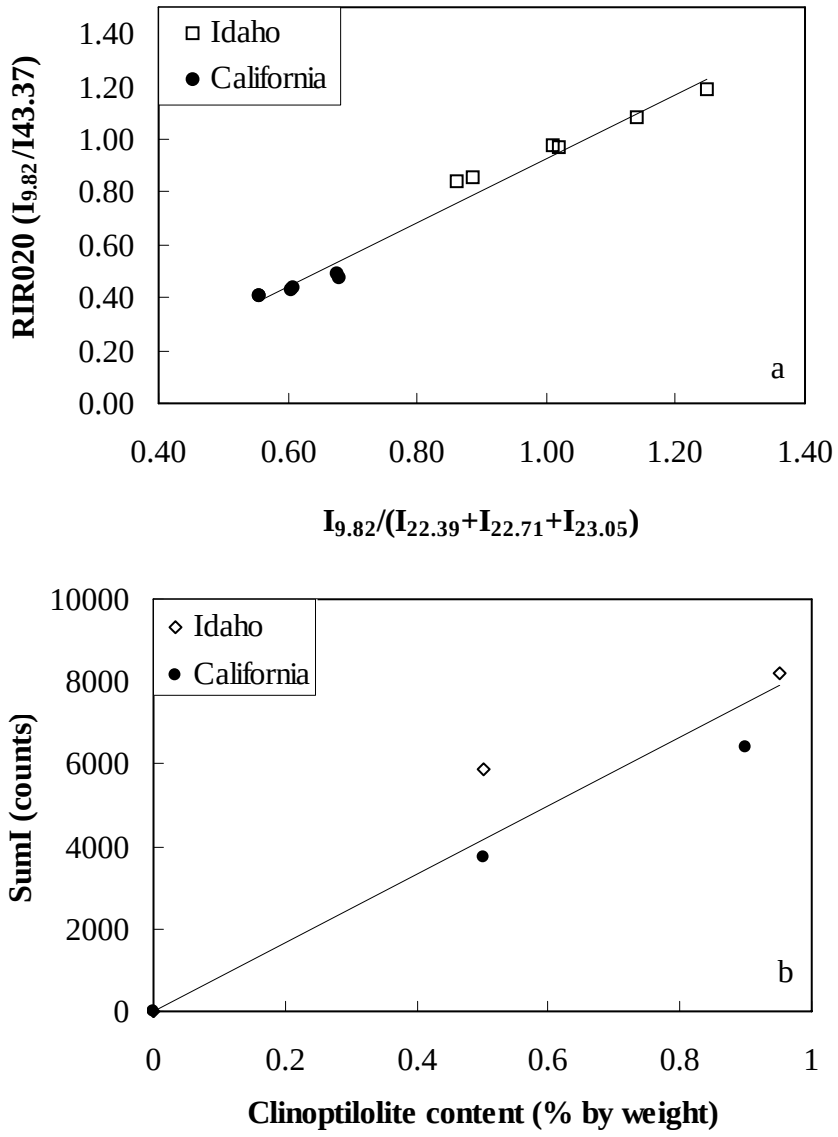

Figure 5.2. Calibration curves prepared for the quantitative mineralogical analysis: a, for the RIR method; b, for the Nakamura's method.

The presence of amorphous materials that are inherent in the <75 μm sample, the starting powder and ClinRich-B was indicated by the broad hump registered 2θ range between 20^o and 30^o. Thus, ClinRich-B was discarded from the study. Qualitative mineralogical analysis revealed that the starting zeolite powder contained predominantly clinoptilolite, and feldspars, quartz, biotite as mineral impurities. It was also revealed that the purified fraction (ClinRich) is a heulandite-group natural zeolite. The absence or weakness of the peaks related to the mineral impurities in the XRD pattern of ClinRich indicated highly pure and crystalline nature of the clinoptilolite

phase. The concentration of heavy mineral phases (feldspar, quartz at 2θ=27.7^{o} and 26.7^{o}, respectively) in Heavy fraction was detected in the XRD diffractogram.

The SEM micrographs for Heavy and ClinRich fractions are shown in Figure 5.3. Broken clinoptiolite crystals with clean surfaces were observed in the micrograph of ClinRich fraction whereas large crystals with diameters around 50 μm and with morphology other than clinoptilolite crystals were observed in the micrographs of Heavy fraction. These large crystals probably belong to a mineral phase with higher hardness and density with respect to clinoptilolite. The particles became smaller and had more uniform size distribution as going further through the purification steps.

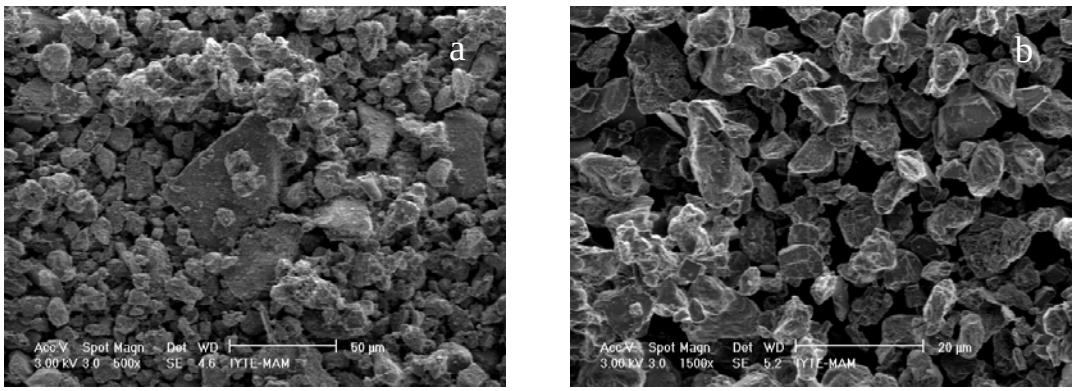

Figure 5.3. SEM micrographs of the mineral phases separated during the purification process, a, Heavy (×500); and b, ClinRich (×1500).

In order to test the thermal stability of the purified clinoptilolite fraction (ClinRich), the powder X-ray diffraction patterns of ClinRich before and after the thermal treatment at 450 ^{o}C for 16 hours were compared in Figure 5.4. Regarding the negligible changes in the intensity of the characteristic peaks belong to the clinoptilolite phase, it was confirmed that the purified phase was rich in clinoptilolite.

The elemental analyses showed that ClinRich has SiO_2/Al_2O_3 ratio of 5.73 and $(Na^{+}+K^{+})/(Ca^{2+}+Mg^{2+})$ ratio of 3.87 confirming that ClinRich is rich in clinoptilolite (Mumpton, 1960). It was also revealed that the purification process led to lower Fe_2O_3 content in ClinRich without significant changes in the concentrations of other cations.

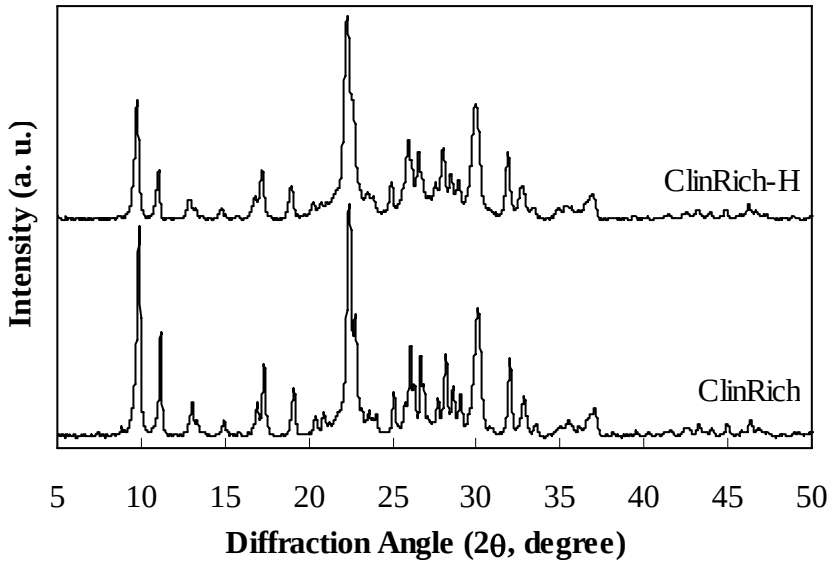

Figure 5.4. X-ray powder diffractograms of the purified clinoptilolite before and after thermal treatment at 450 ^{o}C for 16 hours (*H* stands for the thermally treated sample).

The TGA and DTA curves for ClinRich are given in Figure 5.5. The continuous TGA curve and the exothermic peak observed at very high temperatures (974 ^{o}C) confirmed that the major constituent of ClinRich is clinoptilolite (Gotardi and Galli, 1985). From the course of the D-TG curve, temperature of minimum corresponding to the maximum rate of weight loss was detected at 70 ^{o}C.

As follows from the DTA curve, the broad low-temperature endothermic peak at 63 ^{o}C represented loss of physically adsorbed water in the clinoptilolite and the high-temperature exothermic peak indicated the conversion of the clinoptilolite to another amorphous or crystalline phase at 974 ^{o}C. The temperature of the endothermic peak was lower than those reported in the literature as 140–160 ^{o}C (Tsitsishvili et al., 1992). The exothermic peak was observed at higher temperature than that in the literature as 750 ^{o}C (Tsitsishvili et al., 1992). These discrepancies can be explained by the differences in the type of the cations and the Si/Al ratio of the zeolite that influence the intensities and the temperature of the maxima of peaks in DTA curves (Sheppard and Starkey, 1966; Alietti et al, 1974). The lack of a peak around 250 ^{o}C indicated that the zeolite does not contain heulandite. Heulandite transforms into a heulandite-B phase around this temperature and becomes amorphous to X-rays around 350 ^{o}C (Mumpton, 1998).

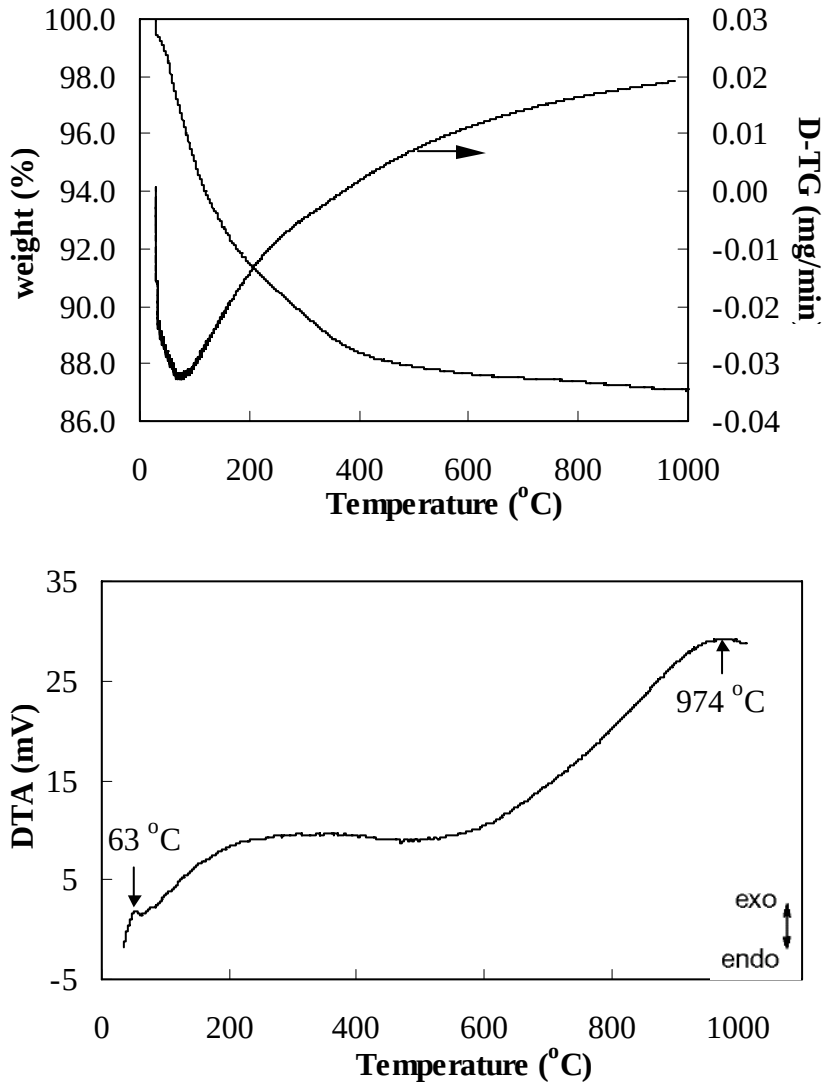

Figure 5.5. a, TG and D-TG curves; b, DTA curves for ClinRich.

5.2. Characterization of the Zeolites

5.2.1. Particle Size Distribution

The particle size distribution analysis revealed that the average particle diameters for the 75-150 μm and 150-250 μm fractions were 108.6±0.3 μm and 190.1±5.07 μm, respectively. The particle sizes of the microparticles used for the

preparation of the pellets (ClinRich and WGround) using a clay binder were also analyzed. From the particle size distributions for the purified zeolite (ClinRich) and for the ground fraction (WGround) shown in Figure 5.6, the average particle diameters were determined as 8.6±0.1 μm and 4.1±0.1 μm, respectively.

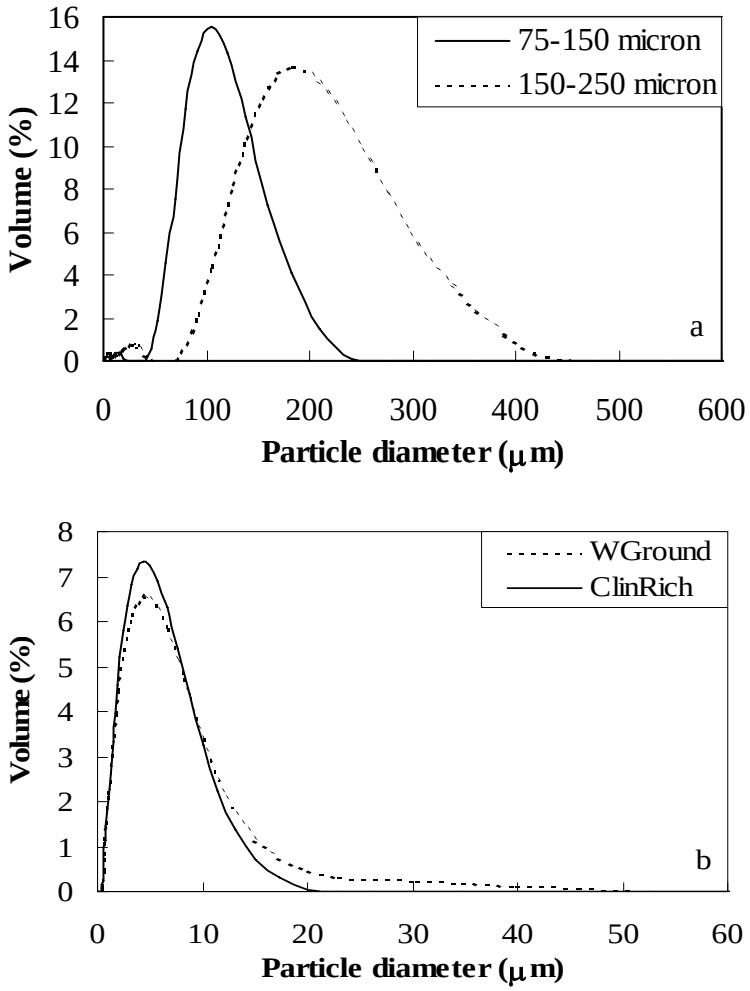

Figure 5.6. Particle size distributions of the zeolites: a, particles used as adsorbent in the NO adsorption studies; b, powders used in the preparation of the pellets.

5.2.2. Determination of Density, Volume and Porosity

A zeolite specimen of rectangular prism with bulk volume of 1.3590 cm^3 was cut from the zeolitic tuff and washed in the same manner as in the preparation of the zeolite particles. The dry weight of the specimen in air ($m_{dryinair}$) was measured immediately after dehydration at 400 ^oC for 24 hours in a static oven. The weight of the specimen in the liquid ($m_{wetinwater}$) was measured after the specimen was completely saturated with the liquid. The complete saturation of the specimen with water was achieved by boiling and vacuuming it in water. The density of the zeolite was calculated as 2.2664 g/cm^3 from Equation (4.1). The density measured in this manner excluded the open pores, so it corresponds to the true density of the zeolite (ρ_{true}).

The true solid density was also measured by the helium pycnometer as 2.3301 g/cm^3. The difference in the true densities measured by different methods was negligible and can be explained by the differences in size of the molecules used as displacement medium and interactions of these molecules with the zeolite.

The true density of bulk of the zeolite particles (75-150 μm) was also measured with the helium pycnometer and was found as 2.3196 g/cm^3. The different true densities measured by using the specimen and particles can be attributed to changes occurred in the structure of the crystals near the particle surface during grinding. Furthermore the bulk of powder contains also interparticle voids. The total volume of these interparticle voids depends on the size and shape of the individual particles and how well the particles are packed. The true solid densities of the pellets prepared from the ground Washed sample and ClinRich using kaolin as a binder measured by the helium pycnometer were 2.6242 and 2.6252 g/cm^3, respectively. The true solid density of the pure kaolin pellet was also measured in the same manner and was found as 2.9095 g/cm^3. The true solid densities determined in this thesis were a bit higher than the value given for clinoptilolite in the literature as 2.16 g/cm^3 (Breck, 1974). The true solid density of the clinoptilolite-rich mineral from Bigadiç region (Western Anatolia) was reported as 2.0006 g/cm^3 (Abusafa and Yücel, 2002). The differences might be related to the mineral composition of the zeolitic tuffs.

The particle density of the zeolite was determined as 1.5866 g/cm^3 from Equation (4.2). The bulk density of the specimen was calculated as 1.2977 g/cm^3 from Equation (4.3). The pellet (particle) bulk densities using the dry weight (measured immediately after calcination of the pellets at 400 ^{o}C for 12 hours in a static oven) and the bulk volume of the pellets were calculated as 1.550, 1.601 and 1.618 g/cm^3 for Washed, ClinRich and Pure kaolin pellets, respectively.

The total, open and closed pore volumes were also measured using the density measurement apparatus and the zeolite specimen. The $\rho_{particle}$ determined as 1.5886 g/cm^3 from Equation (4.2). Then the volumes V_1 and V_2 were calculated as 1.1116 cm^3 and 0.7569 cm^3 from Equation (4.4) and (4.5), respectively. Then the total pore volume was calculated from Equation (4.6) as 0.3547 cm^3. The open and closed pore volumes were computed from Equations (4.7) and (4.8) as 0.3324 cm^3 and 0.0223 cm^3, respectively.

The skeletal (true) volume of a solid defined in Equation (4.9) as 1.0266 cm^3. This volume was directly measured by a helium pycnometer as 0.8331 cm^3. The difference can be due to use of different probe molecules as displacement medium in the measurements.

The total pore volume per gram of dehydrated zeolite calculated as 0.2011 cm^3/g using Equation (4.11). Using the V_f and ρ_f values given as 0.34 cm^3/cm^3 and 1.71 g/cm^3, respectively (Breck, 1974), the theoretical total pore volume of the zeolite was calculated as 0.1988 cm^3/g from Equation (4.12). The thermal gravimetric (TG) data, N_2 adsorption data obtained at -196 ^{o}C and CO_2 adsorption data obtained 30 ^{o}C were used for calculation of the total pore volume by the application of the Gurvitsch Rule. The liquid densities of the adsorbates adsorbed in the pores at the measurement temperature (ρ*) were calculated from Equation (4.14) (Reid et al., 1987) and are given in Table 5.2.

Table 5.2. Properties of the adsorbates.

Property	N_2	CO_2	NO
Normal boiling temperature, T_b (K)	77.4	216.6	121.4
Critical temperature, T_c (K)	126.2	304.1	180.0
Critical pressure, P_c (bar)	33.9	73.8	64.8
Molecular weight, M (g/mol)	28.01	44.01	30.01
Adsorption temperature, T (K)	77.4	303	303
Density at normal boiling point, ρ_b (g/cm^3)	0.808	1.300	1.280
van der Waals co-volume, b (cm^3/mol)	38.69	42.83	28.87
Critical density, ρ_c (g/cm^3)	0.72	1.03	1.04
Corrected density, ρ^* (g/cm^3)	0.808	1.031	0.543

The total pore volumes calculated are presented in Table 5.3. The discrepancies between the total pore volumes calculated using different adsorbate (probe) molecules might arise from the properties of the probe molecules given in Table 5.4 as well as packing of the probe molecules differently in the pores. For a given adsorbent, the relative strength of adsorption of different adsorbates depends on the dipole and quadrupole moments and also on the polarizability of the adsorbate molecules. The lower total pore volumes estimated based on the N_2 adsorption data are related also with the steric effects since it has the largest kinetic diameter. The size of the channels of the zeolite limits the accessibility of adsorbate molecules with compatible size to a part of the porous structure. An exception of water to the Gurvitsch Rule was reported in the literature since water molecules cannot hydrogen bond effectively in the narrow micropores effectively reducing the density of the adsorbed phase hence the pore volume is underestimated (Gregg and Sing, 1982). In the literature, the total pore volume of the clinoptilolite-rich mineral from Bigadiç region (Western Anatolia) was reported as 0.2216 cm^3/g by mercury porosimeter (Abusafa and Yücel, 2002).

Table 5.3. Total pore volumes of the zeolites calculated based on the Gurvitsch Rule (cm^3/g).

Sample						
	TG data	Water content at the fully hydrated sate	Theoretical	N_2 adsorption	CO_2 adsorption	NO adsorption
Washed	0.083	0.201	0.199	0.056	0.107	0.447
Na-Clin	0.077			0.071	0.077	0.317
0.05 M Co	0.111			0.069	0.080	0.429
0.05 M Fe	0.082			0.134	0.086	0.359
0.05 M Ag	0.102			0.050	0.059	0.354
0.05 M Cu	0.099			0.071	0.082	0.472
0.01 M Co-1h	0.086			0.066	0.075	0.439
0.01 M Fe-1h	0.098			0.064	0.082	0.305
0.01 M Ag-1h	0.096			0.059	0.077	0.371
0.1 M Co-24h	0.104			0.070		0.413
0.01 M Co-24 h	0.105			0.060		0.462

Table 5.4. Properties of adsorbate molecules used for calculation of the total pore volume.

Gas	Polarizability (α) (10^{-24} cm^3)	Dipole moment (μ) ($e\times10^{-8}$ cm)	Quadrupole moment (Q) ($e\times10^{-16}$ cm^2)	Kinetic diameter (Å)
N_2	1.76[a], 1.4[g]	0[a]	0.27[a]	3.64[c]
NO	1.72[a]	0.16[a]	0.28[a]	3.17[f]
CO_2	3.01[b], 1.9[g]	0[b]	0.65[b]	3.30[c]
H_2O	1.48[h]	1.85[e]		2.65[d]

e is the electric charge of the proton, 1.602×10^{-19} C.

[a] Furuyama et al., 1984.

[b] Furuyama and Morimoto, 1978.

[c] Golden and Sircar, 1994.

[d] Hirschfelder et al., 1954.

[e] Lide, 1991.

[f] Stuart, 1952.

[g] Breck, 1974.

[h] Prausnitz et al., 1999.

The total pore volumes estimated from the reversibly and irreversibly adsorbed amounts of NO were also presented in Table 5.5. The total pore volumes estimated based on the reversibly adsorbed amount of NO were found to be close to the volumes estimated by other probe molecules, while those calculated from the irreversible adsorption were notably higher.

Table 5.5. Total pore volumes of the zeolites calculated based on the Gurvitsch Rule (cm^3/g).

Sample	Reversibly adsorbed NO amount	Irreversibly adsorbed NO amount
Washed	0.094	0.353
Na-Clin	0.119	0.198
0.05 M Co	0.130	0.300
0.05 M Fe	0.124	0.235
0.05 M Ag	0.080	0.274
0.05 M Cu	0.105	0.366
0.01 M Co-1h	0.132	0.307
0.01 M Fe-1h	0.106	0.199
0.01 M Ag-1h	0.103	0.267
0.1 M Co-24h	0.148	0.265
0.01 M Co-24 h	0.161	0.301

The particle porosity (including open and closed pores) was calculated from Equation (4.16) as 0.387. If the closed pores are not excluded, the particle porosity has become 0.245 as calculated from Equation (4.17). The pellet porosities were calculated as 0.379, 0.368 and 0.307 for WGround-Kaolin, ClinRich-Kaolin and pure Kaolin pellets, respectively. When compared with the ε_p values obtained by different methods, the discrepancies can be value attributed to error caused by externally adsorbed water when water is used as displacement medium, the differences in the size of the probe molecules and also the degassing procedures applied. The particle porosity value of 0.387 was used in the calculations of the bed voidages.

5.2.3. X-Ray Powder Diffraction

The X-Ray powder diffractograms of Washed sample and the reference clinoptilolite are shown in Figure 5.7. The qualitative mineralogical analysis revealed that Washed sample contained predominantly clinoptilolite (JCPDS 25-1349) as well as quartz (JCPDS 83-2465) ($2\theta=20.9^o$, 21.9^o, 26.7^o), feldspars (microcline JCPDS 83-1604, sanidine JCPDS 86-0683) ($2\theta=27.1^o$, 27.7^o) and biotite (JCPDS 76-0885) ($2\theta=8.9^o$).

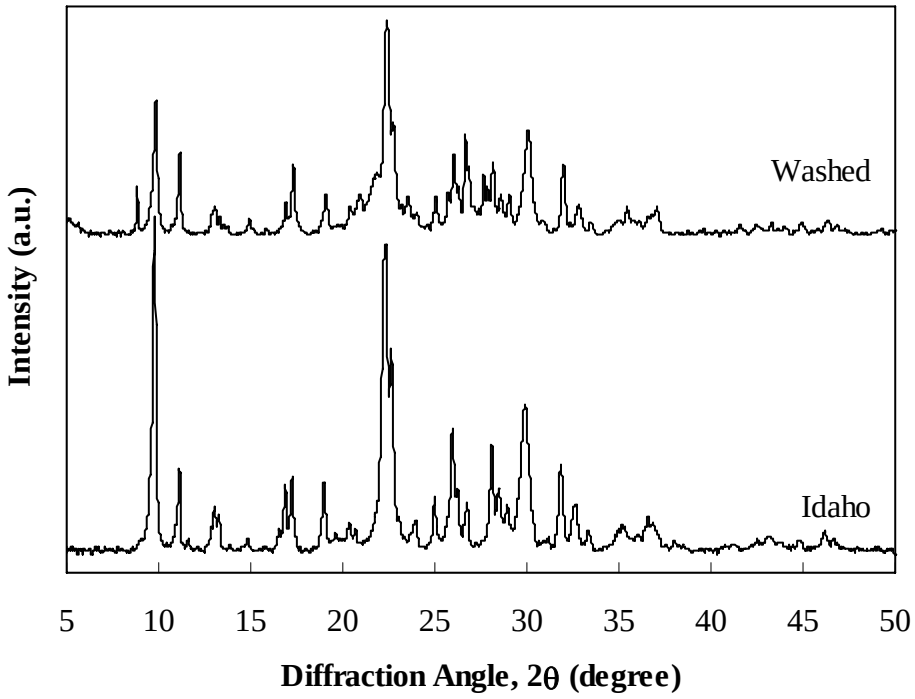

Figure 5.7. XRD diffractograms of the reference clinoptilolite (Idaho) and Washed.

From the calibration curves given in Figure 5.2, the clinoptilolite content of Washed zeolite was calculated as 34 % and 67 % by weight by the application of the RIR method and Nakamura's method, respectively. The low clinoptilolite content calculated by the RIR method could be attributed to the dependence of the intensity of

the 9.82^{o} band to the cation content of the zeolite. The intensity of this peak corresponding to (020) plane of clinoptilolite is mainly associated with differences in the nature, amount and position of the extraframework cations in clinoptilolite channels affecting the size and shape of the unit cell (Rodriguez-Iznaga et al., 2002; Petrov, 1995). The reference clinoptilolite minerals, Idaho and California, were found to be rich in sodium with 7.93 and 10.66 %, respectively, while Washed is rich in potassium with 8.38 % by weight. Hence, the clinoptilolite content of Washed zeolite was accepted as 67 % by weight.

The XRD diffractograms of the zeolites used as adsorbent in this thesis are compared in Figure 5.8. Inspection of these diffractograms revealed that the characteristic clinoptilolite peaks (2θ= 9.82^{o}, 11.15^{o}, 22.39^{o} and 30.10^{o}) did not shift, but their intensities were increased after NaCl treatment. The intensity of the peak at 2θ=8.9^{o} which belongs to biotite decreased significantly indicating the removal of nonzeolitic phases during the rigorous NaCl treatment. This also caused the characteristic clinoptilolite peaks to become sharper designating increased crystallinity in Na-Clin sample.

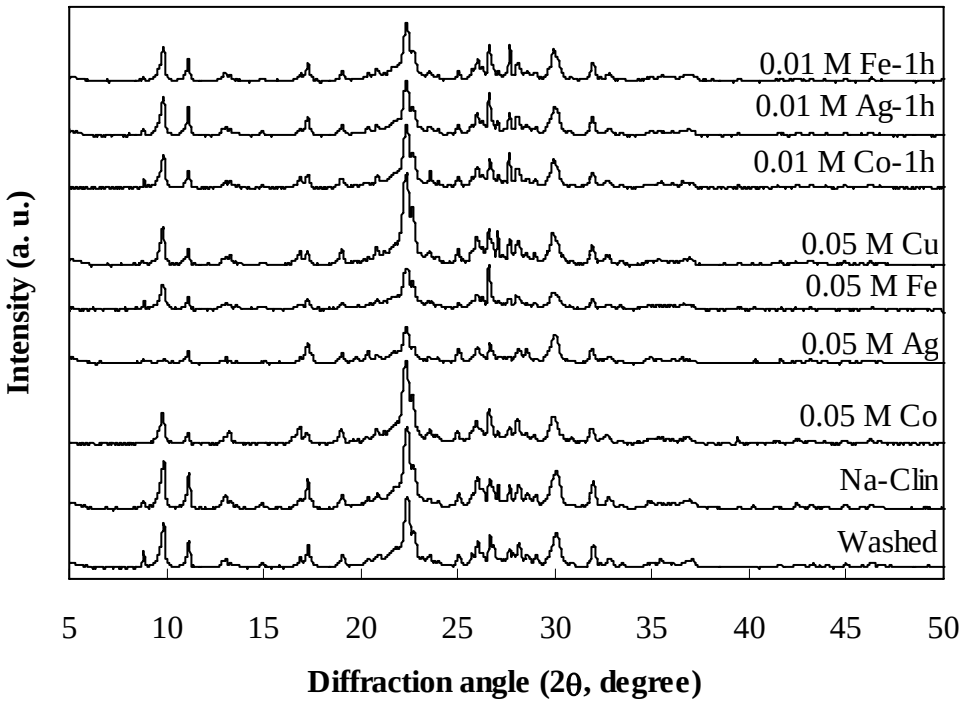

Figure 5.8. X-ray diffractograms of the zeolite samples.

The reflections attributed to the clinoptilolite were less intense in the diffractograms of 0.05 M Fe and 0.05 M Ag zeolites with respect to those for Na-Clin indicating a clear decrease in crystallinity as a result of distortion of the framework in response to the size of the cations and the number of cations per unit cell. Any such distortion was observed for 0.01 M samples. Thus, the degree of framework distortion can be related to the amount of metal cations in the zeolite.

It was observed that the main differences between the peaks are in their intensity in the XRD diffractograms of the metal-sorbed zeolites. The peak corresponding to (020) plane of clinoptilolite ($2\theta=9.82^{o}$) exhibited the highest intensity variation upon metal sorption. This was explained by the nature, amount and position of the extra-framework species in clinoptilolite channels affecting the size and shape of the unit cell (Rodriguez-Iznaga et al., 2002; Petrov, 1995).

None of the zeolites exhibited sharp peaks in the X-ray diffractograms indicating the presence of the metal oxides. This might be due to either high dispersion and/or low crystalline (amorphous) nature of the metal oxides formed on the zeolites. Furthermore, crystallites of small size and/or in concentrations below approximately 5% by weight cannot be detected by XRD (Jentys and Lercher, 2001).

The crystallinity of the zeolites was also examined after the activation process employed prior to the adsorption of NO. The XRD diffractograms of the zeolites before and after the activation are compared in Figures 5.9. No significant changes were detected in the diffractograms regarding the intensity and position of the reflections. The appearance of peaks in the 2θ range of $26–28^{o}$ belonging to quartz and feldspars in some diffractograms can be also explained by the mineral heterogeneity or by the preferred orientation of the large crystals of these phases or by concentration of quartz and feldspars in the zeolite due to dissolution of the clinoptilolite phase.

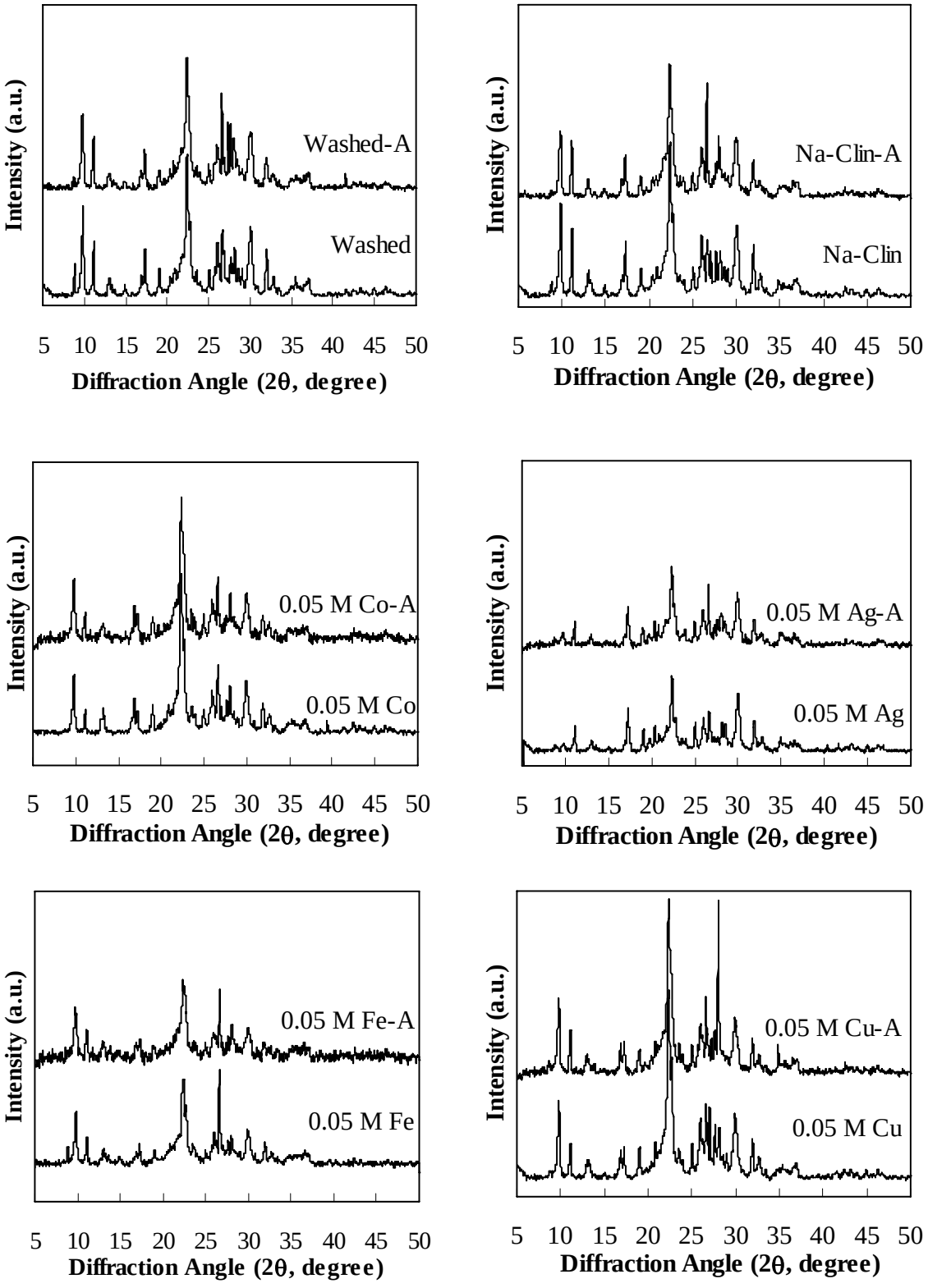

Figure 5.9. XRD diffractograms for the metal sorbed zeolites before and after the activation.

(cont. on next page)

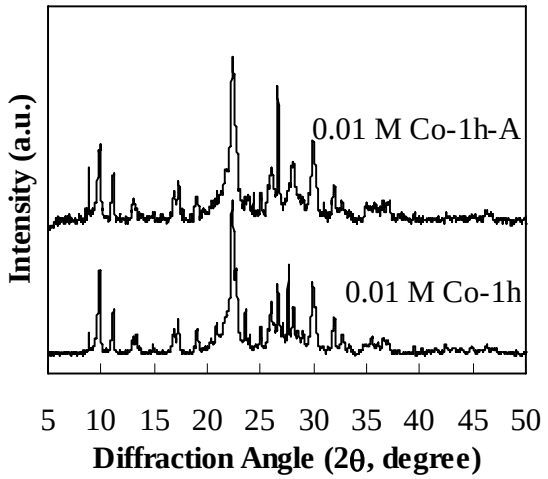

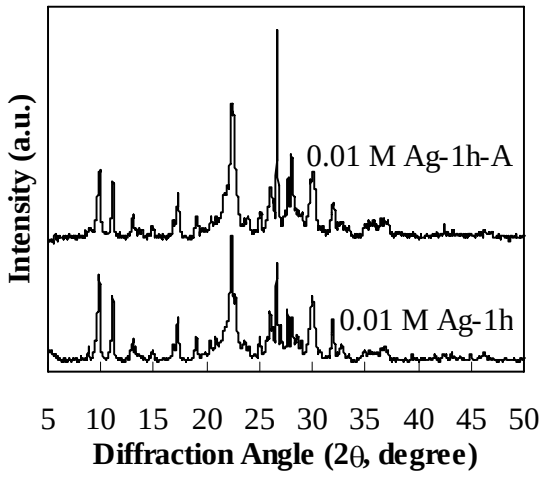

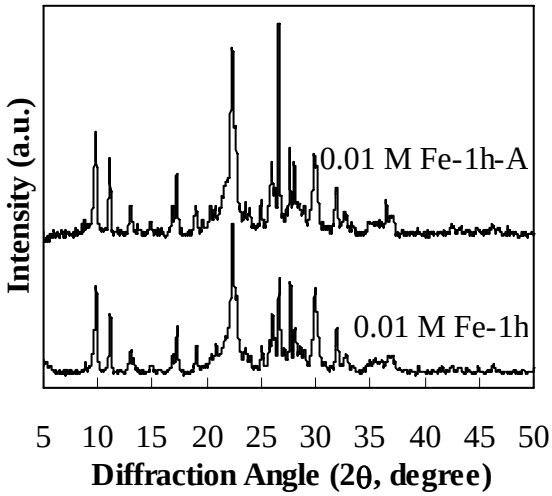

Figure 5.9. (cont.) XRD diffractograms for the metal sorbed zeolites before and after the activation.

The particles that were prepared from the pellets gave the X-ray diffractograms shown in Figure 5.10. In the diffractograms of WGround-Kaolin and ClinRich-Kaolin, the characteristic peaks for the clinoptilolite as well as peaks belong to the kaolin were detected.

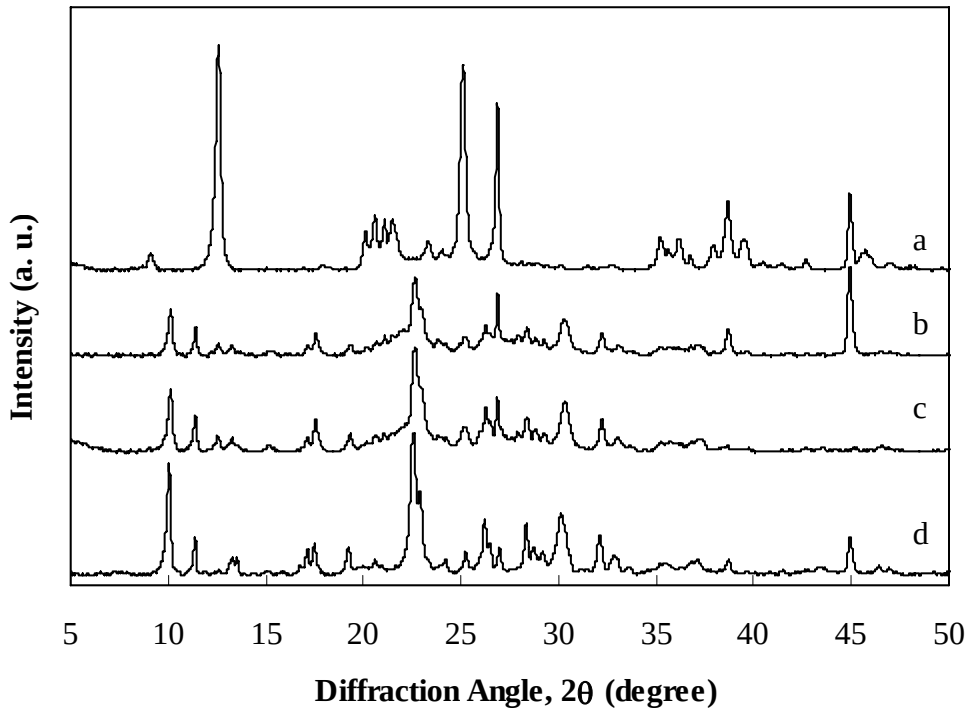

Figure 5.10. X-ray diffractograms of the particles prepared by pelletization. a, pure kaolin; b, WGround-Kaolin; c, ClinRich-Kaolin; d, Idaho.

5.2.4. Elemental Analysis

The aim of the NaCl treatment process is to remove specific ions from the structure of the material and locate more easily removable ones. In practice, the result of any pretreatment is the increase of the zeolite content in a single cation, bringing the material close to homoionic form. The final homoionic or close to homoionic form of the zeolite was found to improve its effectiveness and performance in ion-exchange applications (Semmens and Martin, 1988; Kesraoui-Ouki et al., 1993; Kurkovic et al.,

1997; Chmielewska-Horvathova and Lesny, 1995; Bremmer and Schultze, 1995; Gradev et al., 1988; Panayotova and Velikov, 2003). Sodium is preferred against other alkali and alkaline earth cations, as its homoionic forms are produced much more easily. Also, sodium is the weakliest bonded cation in clinoptilolite and thus it can be easily exchanged with cations from the solution (Rozic et al., 2002, Zamzow et al., 1990). Yang et al. measured the diffusion coefficients and concluded that sodium is exchanged out of the heulandite group zeolites faster than calcium or magnesium. The results were explained by the structural location of sodium and calcium in the zeolite and the difference in the hydration spheres associated with each cation (Yang et al., 1997).

The results of chemical analyses of the zeolite samples are summarized in Table 5.6. The zeolitic material was found to be rich in potassium ions. The elemental composition before and after the NaCl treatment revealed that 82 % of Ca^{2+}, 59 % of Mg^{2+}, 33 % of K^{+} and 15 % Fe^{3+} cations were exchanged with Na^{+}, but it was not possible to obtain a zeolite in homoionic form. Potassium is known to be more difficult to remove than the other cations in the clinoptilolite structure (Ackley and Yang, 1992). The chemical analysis revealed the SiO_2/Al_2O_3 ratio of 5.90 that is typical for the clinoptilolite-rich material (Breck, 1974; Tsitsishvili et al., 1992; Langella et al., 2000). The SiO_2/Al_2O_3 ratio was found as 5.84 for the mineral with the same geographic origin (Top, 2001; Top and Ülkü, 2004). Insignificant changes were observed in the SiO_2 and Al_2O_3 contents of the zeolite during NaCl treatment, 0.5 % and 1.2 %, respectively, suggesting that the zeolite structure retained its integrity as also confirmed by the X-ray diffraction and infrared spectroscopy analysis.

ClinRich was compared with the reference minerals in terms of the chemical composition in Table 5.7. The reference mineral Idaho contains remarkably higher iron and magnesium than the other reference. ClinRich is rich in potassium as compared to the references, which are rich in sodium. Its calcium content is higher than those of the references. The magnesium and iron contents of ClinRich are at almost the same level with California reference. The SiO_2/Al_2O_3 ratio of ClinRich fell in the range of those of the references. During the purification process, SiO_2/Al_2O_3 ratio of the zeolite slightly decreased. The most significant change was observed in the iron content of the zeolite, half of its iron oxide was removed during the purification process.

Table 5.6. Elemental compositions of the zeolites (oxide weight %).

Element in oxide form	Washed	Na-Clin	0.05 M				0.01 M-1h			0.1 M Co-24h	0.01 M Co-24h
			Co	Fe	Ag	Cu	Fe	Co	Ag		
Ag_2O	0	0	0	0	13.43	0	0	0	1.98	0	0
Al_2O_3	12.99	12.84	12.75	10.81	11.45	12.35	12.31	12.31	12.28	12.63	12.91
CaO	1.49	0.27	0.27	0.23	0.27	0.23	0.10	0.15	0.23	0.26	0.27
CoO	0	0	3.77	0	0	0	0	1.53	0	3.88	3.30
CuO	0	0	0	0	0	4.74	0	0	0	0	0
Fe_2O_3	1.49	1.27	1.14	13.87	1.00	1.18	2.86	1.23	1.27	1.20	1.18
K_2O	5.12	3.41	3.34	2.63	2.77	3.08	3.41	3.29	3.41	3.24	3.19
MgO	0.44	0.18	0.15	0.15	0.18	0.15	0.18	0.17	0.18	0.14	0.16
Na_2O	1.85	4.95	2.09	1.18	1.38	1.27	3.28	3.96	4.02	2.09	2.16
SiO_2	76.62	77.08	76.50	71.13	69.53	77.01	77.86	77.35	76.63	76.56	76.83

The theoretical cation exchange capacity (*TCEC*) of Washed zeolite was calculated from the chemical composition as sum of the exchangeable cations (Ca^{2+}, Mg^{2+}, Na^{+}, and K^{+}) (Tsitsishvili et al., 1992; Çulfaz and Yağız, 2004) as 2.08 meq/g. This value is in consistence with the values reported in the literature (1.49–2.81 meq/g) (Milan et al., 1997; Langella et al., 2000; Panayotova and Velikov, 2003; Semmens and Martin, 1988; Castaldi et al., 2005; Mozgawa and Bajda, 2005; Englert and Rubio, 2005; Du et al., 2005; Sprynskyy et al., 2006; Çağın, 2006; Stylianou et al., 2007).

Table 5.7. Elemental compositions of the clinoptilolite reference minerals and ClinRich (oxide weight %).

Element in oxide form	Idaho	California	ClinRich
Al_2O_3	13.98	12.91	13.42
CaO	0.23	0.59	1.66
Fe_2O_3	2.51	0.86	0.78
K_2O	1.89	1.49	5.39
MgO	2.48	0.49	0.40
Na_2O	5.43	7.26	1.41
SiO_2	73.48	76.40	76.94
SiO_2/Al_2O_3	5.26	5.92	5.73

It has been suggested in the literature that there is a linear correlation between the zeolite content and the real exchange capacity (*REC*) of the tuff assuming that some minerals or impurities contained in the zeolite tuff are inactive regarding ion exchange (such as quartz) (Ming and Dixon, 1987; Ming et al., 1993). Thus, the real exchange capacity is related to the ideal exchange capacity as *REC=p(IEC)*, where *p* is the fraction of the zeolite in the tuff. The ideal exchange capacity (*IEC*) is calculated from the chemical formula of pure clinoptilolite samples as 2.16 meq/g. Inglezakis presented the real exchange capacity values versus purity of clinoptilolite samples derived from the related literature and obtained the graph presented in Figure 5.11 (Inglezakis, 2005). Regarding the calculated theoretical exchange capacity of 2.08 meq/g and the clinoptilolite content of 67 % (by weight) Washed zeolite, the point fell above the ideal line. This case was explained by the presence of active mineral phases in the zeolite

having ion exchange capacities (Inglezakis, 2005). Using the clinoptilolite content determined as 95 % (by weight) by the RIR method and the *TCEC* values calculated as 2.06 meq/g, the point of ClinRich was found to be on the ideal line.

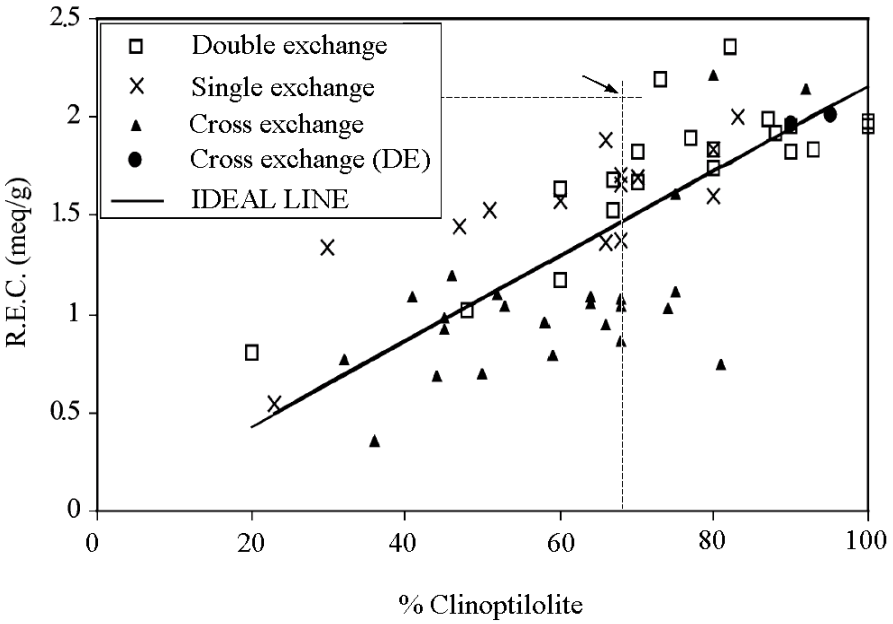

Figure 5.11. Relationship between the real exchange capacity and clinoptilolite content of clinoptilolite-containing zeolites (DE refers to double exchange, a cross-exchange method followed by a second exchange step, again under dynamic conditions) (Source: Inglezakis, 2005).

After NaCl treatment, the TCEC was increased to 2.20 meq/g. While 25 % of the total exchangeable cation in Washed zeolite was sodium, this proportion was increased to about 64 % after NaCl treatment. The sodium cations in the solution were mainly exchanged with the calcium and magnesium cations in Washed zeolite. It was not possible to achieve complete exchange of the cations. The potassium and iron present in Washed zeolite could not be exchanged significantly due to the location occupied by these cations. This situation was also reported in literature by researchers working with clinoptilolites of different origins (Semmens and Seyfarth, 1978; Jama and Yücel, 1990; Faghihian et al., 1999; Langella et al., 2000). Potassium cation is located at the M3 site in the channel c as shown in Figure 1.4 and has the highest coordination to the framework oxygens and water molecules leading to strong bonding

at the M3 site (Koyama and Takeuchi, 1977; Jama and Yücel, 1990). The difference between the theoretical and experimental cation exchange capacities is associated with the availability of the exchangeable cations for ion exchange and the conditions under which the ion exchange process is performed. The exchangeable cations may be either located at inaccessible sites of the clinoptilolite structure and/or components of other mineral phases present in the zeolite (such as feldspar, biotite and quartz) (Inglezakis et al., 2002; Concepción-Rosabal et al., 2005; Kesraoui-Ouki and Kavannagh, 1997).

5.2.4.1. Interaction of Na-Clin with Deionized Water

The ion exchange processes in zeolites are affected by several factors such as concentration and nature of cations and anions, temperature, acidity of the solution and crystal structure of the zeolite (aluminium content, pore size, type and exchangeability of cations). Additionally, the zeolite mineral stability and its structural changes under hydrothermal treatment in various environments play an important role in its potential applications as an ion exchanger.

The changes in aqueous phase proton, exchangeable and framework (Si^{4+}, Al^{3+}) cation concentrations during the interaction of Na-Clin with deionized water under different conditions are summarized in Table 5.8 and shown graphically in Figure 5.12.

The interaction of Na-Clin with deionized water caused the pH of the water to increase. This increase in the solution pH can be consequence of the following reactions:

$$\equiv Al - OH + H^+ \leftrightarrow \equiv Al - OH_2^+ \tag{5.3}$$

$$\equiv Si - O^- + H^+ \leftrightarrow \equiv Si - OH \tag{5.4}$$

These reaction shows the adsorption of protons in the solution to the neutral and negative surface hydroxyl groups and thereby protonation of them (proton binding). These reactions occur in acidic to neutral solutions.

In the same pH range, the protons in the solution may also exchange with the cations in the zeolite structure (proton exchange) which also leads to increase in solution pH. In this case, the concentrations of the cations in the solution are expected to increase.

Table 5.8. Change in the aqueous phase cation concentrations during interaction of Na-Clin with deionized water (meq/g).

S/L, treatment period	1/20, 1 hour			1/100, 24 hours			
Initial pH	2.54	5.57	5.26	1.92	5.08	5.14	4.36
Final pH	2.63	7.78	6.57	2.06	7.62	6.17	7.79
H^+	-0.01	0	0	-0.33	0	0	0
Ca^{2+}	0	0	0	0	0	0	0
K^+	0	0	0	0.02	0	0	0
Mg^{2+}	0	0	0	0	0	0	0
Na^+	0.22	0.09	0.10	0.08	0.09	0.13	0.08
Fe^{3+}	0	0.06	0	0	0.01	0.01	0.01
Total cations released (Na+K+Ca+Mg)	0.22	0.09	0.10	0.11	0.09	0.13	0.08
Contribution of Na^+ to exchange (%)	98.2	97.6	97.8	77.4	99.0	98.2	98.9
Si^{4+}	0.10	0.06	0.05	0.43	0.14	0.18	0.19
Al^{3+}	0.03	0	0	0.08	0.01	0.01	0.01

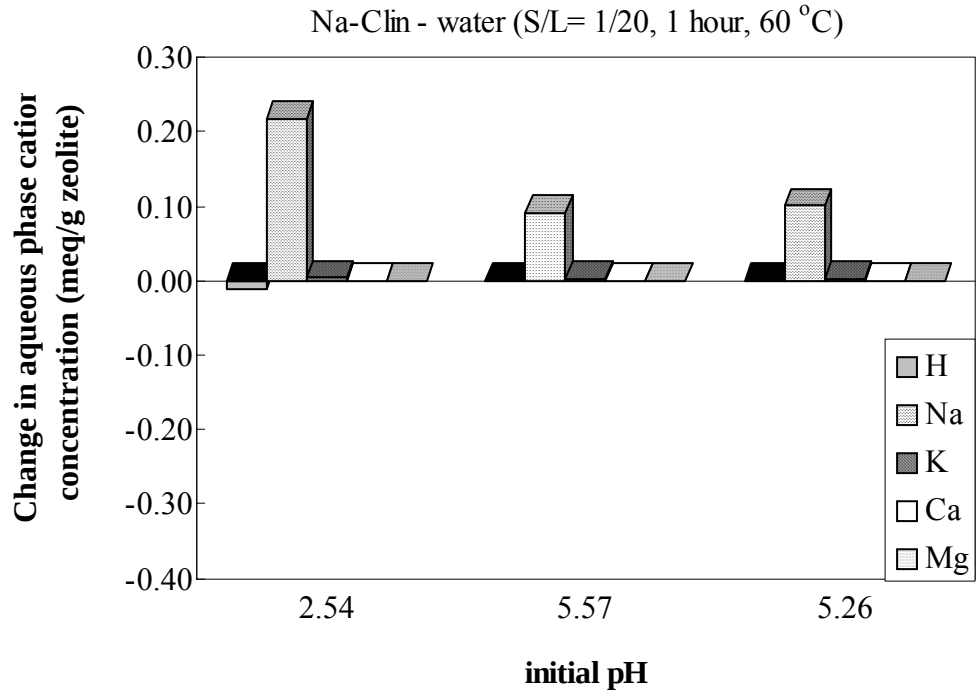

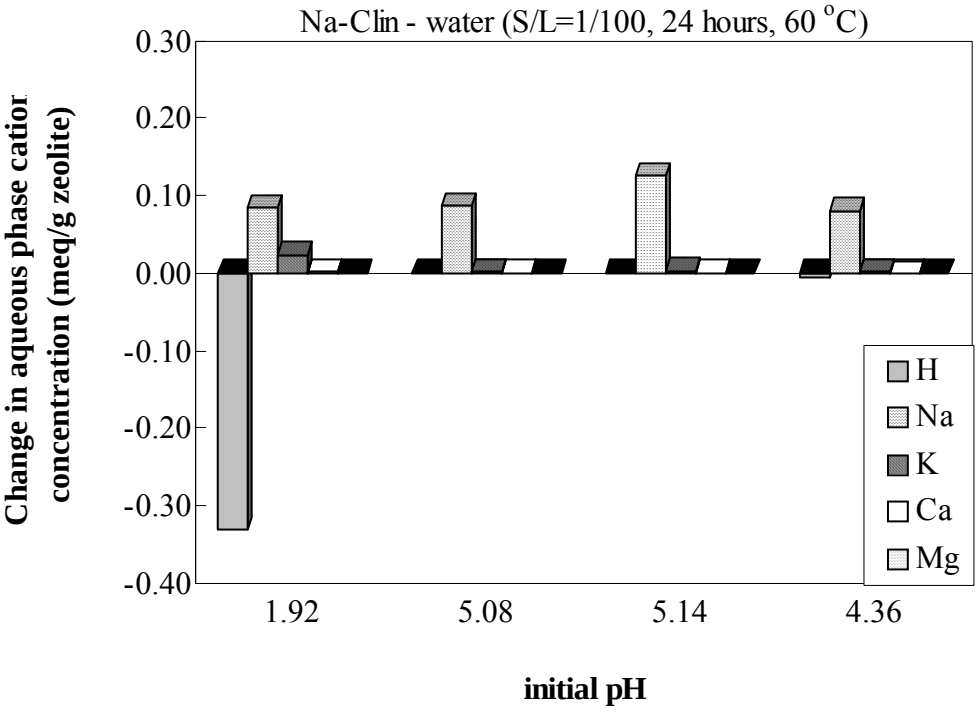

Figure 5.12. Change in concentrations of H^+ and exchangeable cations in the aqueous phase during interaction of Na-Clin with water.

The amount of proton uptake was at the highest level for the case where less amount of Na-Clin was contacted with water with the highest initial acidity for 24 hours. When higher amount of Na-Clin was interacted with water with a slightly lower acidity for shorter period, negligible amount of proton uptake occurred. The amount of proton uptake under other conditions was also under the detection limit.

The exchangeable cations were released in insignificant amount, except for Na^+. The amount of Na^+ released was at almost the same level in all solutions, except for that under the conditions of the highest acidity, higher *S/L* ratio, and shorter period of contact. The amount of Na^+ released in this run was almost two times of those released under other conditions. When Na-Clin was contacted with water of higher acidity, less Na^+ was released. The lower Na^+ release under the conditions of higher acidity, in lower *S/L* ratio and longer periods exhibited that the amount of Na^+ released is not only related with the acidity of the solution but also the *S/L* ratio and the contact period.

The total amount of exchangeable cations released was considerably higher than the amount of proton uptake in all cases, except for the case where the initial pH of 1.92, in lower *S/L* ratio as seen in Figure 5.12. For this run, the amount of proton uptake was significantly higher than the amount of total cations released. This implied that the uptake of protons was not solely due to proton exchange, but also due to proton binding leading to protonation of the surface groups as given by Reactions (5.3) and (5.4). For the other cases where the amount of cation released was higher than the proton uptake, decationization and partial dissolution might be the prevailing mechanism.

Both Si^{4+} and Al^{3+} were released at the highest level when Na-Clin was contacted with water of highest acidity, in low *S/L* ratio and for longer period.

The dissolution of natural zeolites is the result of acidic and basic behavior of aluminosilicate structure in the presence of H^+ or OH^- in the solutions according to the Brønsted and Lewis theory.

Dissolution of aluminium is partially due to proton action. The formation of the surface complexes ($\equiv$Al-OH_2^+) according to Reaction (5.4) increases aluminium dissolution and consequently increases Al^{3+} hydrolysis, which takes place when Al^{3+} species come into the solution:

$$\equiv Al-OH + H^+ \leftrightarrow \equiv Al-OH_2^+ \leftrightarrow Al^{3+} + H_2O$$

$$Al^{3+} + H_2O \leftrightarrow Al(OH)^{2+} + H^+$$

$$Al(OH)^{2+} + H_2O \leftrightarrow Al(OH)_2^+ + H^+ \qquad (5.5)$$

$$Al(OH)_2^+ + H_2O \leftrightarrow Al(OH)_{3(aq)} + H^+$$

$$Al(OH)_{3(aq)} + H_2O \leftrightarrow Al(OH)_4^- + H^+$$

These reactions produce protons causing the solution pH to decrease.

Regarding the increases in the solution pH values during the treatment for all cases in this study, it can be suggested that the neutral and negative surface hydroxyl groups of Na-Clin were protonated due to proton binding (Reactions 5.3 and 5.4). Furthermore regarding the increase in the concentrations of the cations in the solution phase, prevalence of the cation exchange can be suggested.

When the participation of each ion to the total amount of exchangeable cations is considered, it is clear that Na^+ has the greatest contribution to the total amount of cations released (77-99 %). Trace amounts of K^+ and almost no Ca^{2+} and Mg^{2+} were released from Na-Clin during the treatments. Detection of these cations in trace amounts in the water may also be interpreted as an indication of partial dissolution or decationization. Furthermore, the strength of bond between these cations and the framework oxygens may be effective in the limited release. The exception here again is for the lower ratio with initial pH of 1.92. In this run, relatively significant increase in the K^+ concentration in the water was observed besides Na^+. This can be explained by the dissolution of impurities containing K^+ regarding the long treatment period and the low S/L ratio.

Removal of a variety of impurities that occupy micropores and macropores of clinoptilolite such as calcium carbonate, unaltered glass by the protons in acidic solutions was reported in the literature (Haggerty and Bowman, 1994). Considerable reduction of feldspar and illite in the Slovakian clinoptilolite after acid treatment was confirmed based on the X-ray diffractograms (Wingenfelder et al., 2005).

The qualitative X-ray diffraction analysis revealed that Na-Clin does not contain only clinoptilolite, but also quartz, feldspars (microcline and sanidine) and biotite. Among these impurities biotite and feldspars contains significant amount of potassium

(http://webmineral.com). However, it is not possible to specify which of the phases dissolved to what extent. Wingenfelder and coworkers decided on which phases are dissolved based on the X-ray diffractograms of the samples (Wingenfelder et al., 2005). In the present study, the X-ray diffractograms shown in Figure 5.13 showed that the intensity of the peaks belong to feldspars and biotite decreased after Na-Clin was treated in highly acidic solutions, whereas the clinoptilolite peaks remained almost unchanged. The changes were summarized in Table 5.9.

Table 5.9. Qualitative mineralogical analysis of Na-Clin and its acid-treated forms.

Diffraction angle (2θ), mineral phase	Intensity (counts)		
	a	b	c
8.9°, biotite	261	219	0
20.9°, quartz	392	372	296
26.7°, quartz low	674	1006	835
27.1°, sanidine	552	379	0
27.7°, microcline	563	670	780

a, Na-Clin before any treatment
b, Na-Clin after interaction with water with initial pH=1.92, *S/L*=1/100, 24 hours
c, Na-Clin after interaction with water with initial pH=2.54, *S/L*=1/20, 1 hour.

The intensity and position of the characteristic peaks of clinoptilolite phase in Na-Clin did not change significantly after the acid treatment. The remarkable change was observed in the intensity of the 2θ=9.82° peak, the intensity increased by 40% after contact with water with initial pH of 2.54 and in the higher *S/L* ratio. This change is mainly associated with the nature, amount and position of the cations in clinoptilolite channels determining the unit cell size to change. (Rodriguez-Iznaga et al., 2002; Petrov, 1995). The total amount of cations released was found to be at the highest level for this case as stated previously.

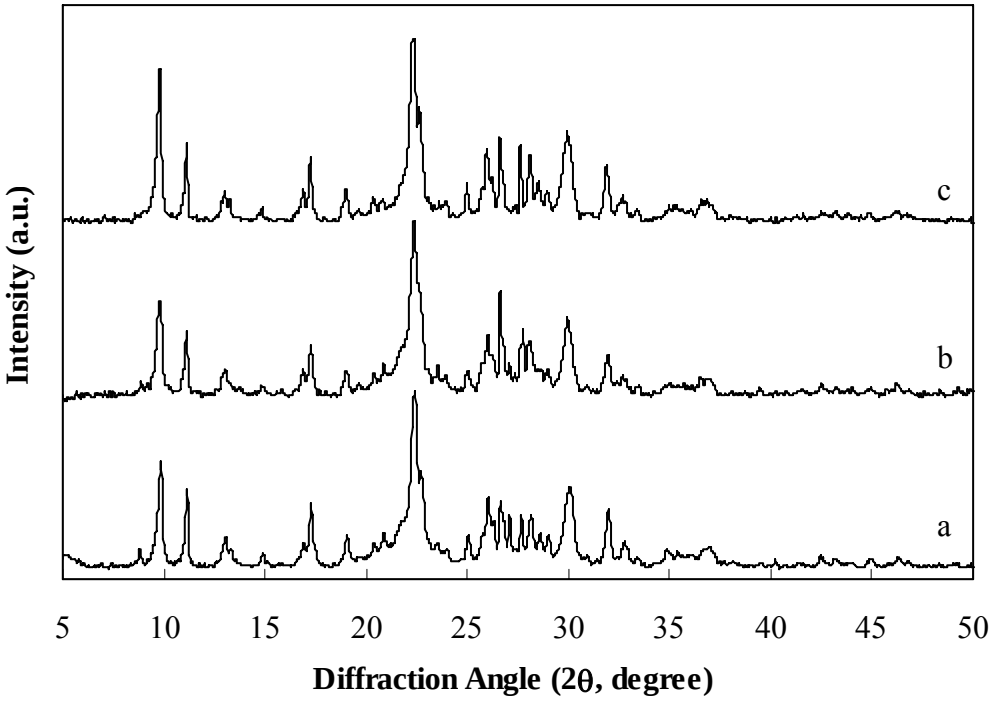

Figure 5.13. X-ray powder diffractograms of Na-Clin, a, before any treatment; b, after interaction with water with initial pH of 1.92, *S/L*=1/100, 24 hours; and c, after interaction with water with initial pH of 2.54, *S/L*=1/20, 1 hour.

5.2.4.2. Metal Sorption - Solid Phase

The elemental compositions of the zeolites are given in Table 5.10. The amount of iron sorbed by Na-Clin was higher than the total cation exchange capacity of Na-Clin in 0.05 M Fe zeolite. This led to the conclusion that besides ion exchange, other processes took place, such as precipitation of iron in the form of a low-solubility phase and/or salt adsorption that increase the amount of iron uptake. The electron micrographs of 0.05 M Fe sample depicted the excess precipitate formed on the surface. The absence of sharp peaks in the X-ray diffractogram revealed that either the species formed are not crystalline or the concentration of those species formed are below the detection limit (5 % by weight) (Jentys and Lercher, 2001). Considering the highly acidic conditions under the iron sorption experiments were performed, limited metal sorption is expected due to competition of protons with the iron cations in the solution for the same

exchange sites (Inglezakis et al., 2001; Haggerty and Bowman, 1994; Wingenfelder et al., 2005). The low iron sorption was expected also due to the increased electrostatic repulsion between the iron cations and the protonated clinoptilolite surface (Cabrera et al., 2005).

Figure 5.14 shows the changes in solid-phase cation concentrations due to the metal sorption. It is obvious that mainly Na^+ was released from Na-Clin, besides small amounts of Ca^{2+}, Mg^{2+} and K^+. The released amounts of potassium were found to be slightly higher for 0.05 M Fe and 0.05 M Ag. Examination of the changes in the total cation and metal concentrations in 0.05 M zeolites, it was revealed that there is a stoichiometry between the amount of metal uptake and that of total cations released. This indicated the exchange of cations in the zeolite with the metal ions in the solution. However, for 0.05 M Fe zeolite, the amount of metal sorbed was found to be drastically higher than the total amount of cations released. A small difference between the total amount of cations released and the amount of the metal sorbed was observed for 0.01 M Ag-1h sample. This non-stoichiometry is mainly attributed to the prevalence of adsorption and dissolution possibly accompanying the silver exchange. For the other 0.01 M Metal-1h samples, there is stoichiometry between the incoming and outgoing ions designating that the ion exchange prevailed for these samples.

Table 5.10. Elemental compositions of the zeolites (meq/g zeolite).

Element	Washed	Na-Clin	0.05 M				0.01 M-1h		
			Co	Fe	Ag	Cu	Fe	Co	Ag
Ag	0	0	0	0	1.03	0	0	0	0.15
Al	6.55	6.64	6.42	5.61	5.96	6.97	6.98	6.46	6.31
Ca	0.45	0.08	0.08	0.07	0.09	0.08	0.04	0.05	0.07
Co	0	0	0.86	0	0	0	0	0.36	0
Cu	0	0	0	0	0	1.30	0	0	0
Fe	0.48	0.42	0.37	4.60	0.33	0.38	1.03	0.41	0.42
K	0.93	0.64	0.61	0.49	0.52	0.63	0.70	0.62	0.64
Mg	0.19	0.08	0.06	0.06	0.08	0.07	0.08	0.08	0.08
Na	0.51	1.40	0.58	0.34	0.39	0.39	1.02	1.14	1.13
Si	43.71	45.08	43.59	41.78	40.98	49.20	49.93	45.91	44.52

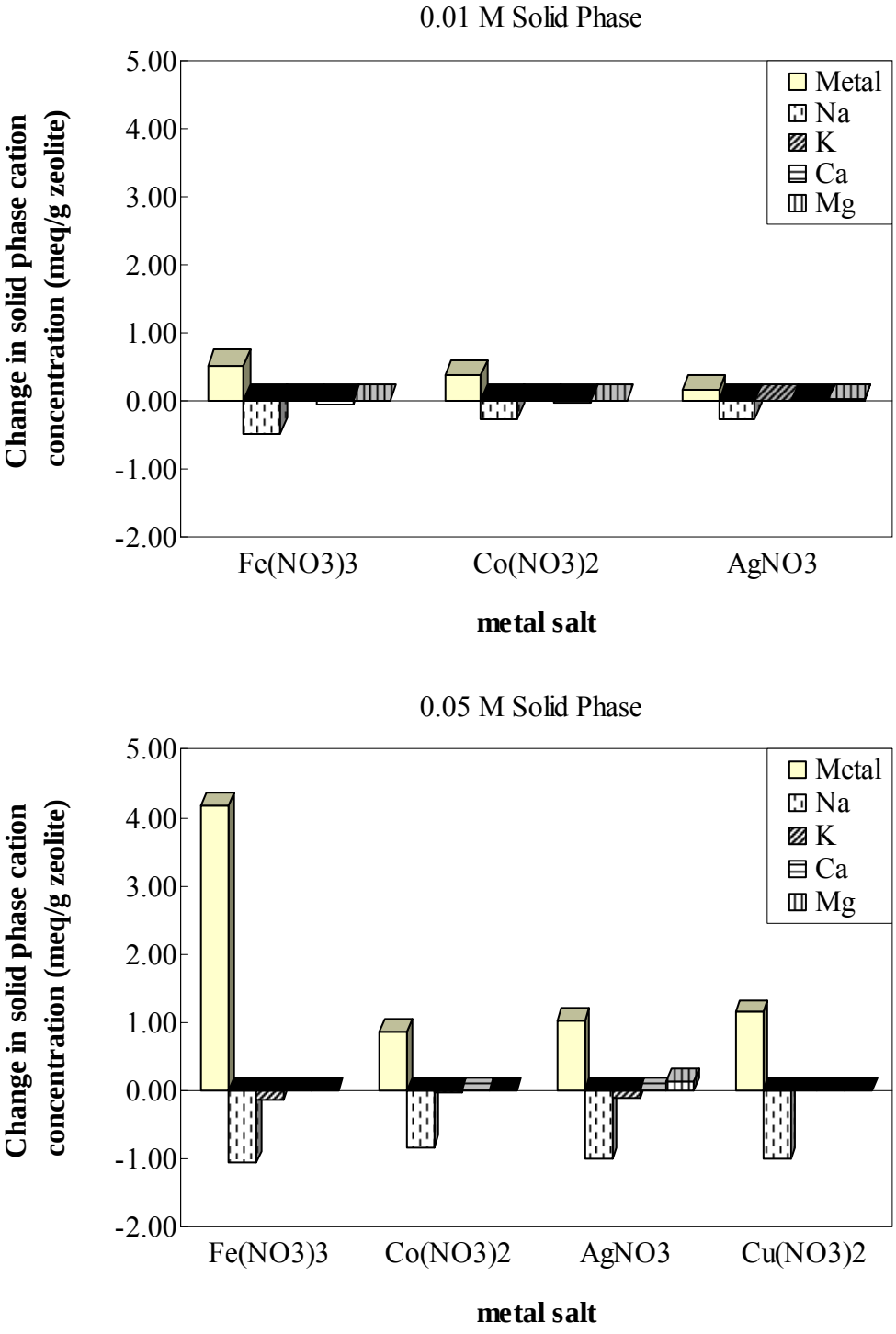

Figure 5.14. Change in concentrations of exchangeable and metal cations in the solid phase during interaction of Na-Clin with metal salt solutions.

The different exchange degrees of the metal cations can be explained by the hydrated radius, valence and hydration energy of the cation, as well as by the experimental conditions under which the ion exchange was performed (*S/L*, temperature, initial metal cation concentration, and shaking speed). If the hydrated radius of the cation is comparable to the size of the zeolite channel dimensions, then the exchange becomes difficult. Also, the cations with high hydrated radius cannot be removed readily from the structure. It was reported that some transition metal cations are strongly solvated and their hydration shells prevent them from penetrating into the narrow channels or cavities of the zeolite structure (Breck, 1974; Barrer, 1978). High selectivity of clinoptilolite to silver was attributed to the low charge (Langella et al., 2000), higher polarizability, high ionic radius (Barrer, 1978) and low hydration energy (Semmens and Seyfard, 1978). The properties of the cations of interest that affect their exchangeability are given in Table 5.11.

Table 5.11. Ionic and hydrated radii, hydration enthalpy of the cations.

Cation	Pauling ionic radius (Å)	Hydrated radii (Å)	Hydration Entalphy (kcal/mol)
Na^{+}	0.95[a]	3.58[a]	-98.2 (-97[b])
K^{+}	1.33[a]	3.31[a]	-79[b]
Mg^{2+}	0.65[a]	4.28[a]	-450[b]
Ca^{2+}	0.99[a]	4.12[a]	-373[b]
Fe^{3+}	0.60[c]	4.57[c]	-1053.8[h]
Co^{2+}	0.72[d]	4.23[a,d]	-479.5[a,f]
Cu^{2+}	0.72[d]	4.19[a,d]	-498.7[a] (-502[b,e]) (-507[g])
Ag^{+}	1.26[d]	3.41[d]	-112.92[h]

[a] Semmens and Seyfarth, 1978.
[b] Woods and Gunter, 2001.
[c] http://www.chem.ox.ac.uk/teaching/Exams2005/PartIBGenIn.org.pdf
[d] Nightingale, 1959.
[e] Inglezakis et al., 2004.
[f] Inglezakis and Grigoropoulou, 2001.
[g] Lide, 1991.
[h] Mishchenko and Poltoratskii, 1972.

5.2.4.3. Metal Sorption - Aqueous Phase

The results of the elemental analysis of the aqueous phases at the beginning and end of the metal sorption are summarized in Table 5.12 together with the changes in the solution pH. The results are also represented graphically in Figure 5.15.

Table 5.12. Changes in the aqueous phase cation concentrations during the metal sorption (meq/g).

	0.01 M-1h			0.05 M			
	Fe	Co	Ag	Fe	Co	Ag	Cu
Initial pH	2.54	5.57	5.26	1.92	5.65	5.19	4.36
Final pH	2.20	5.54	5.87	1.34	4.79	5.07	4.28
Ca^{2+}	0	0	0	0	0	0.02	0
K^{+}	0	0	0	0.06	0.03	0.07	0.04
Mg^{2+}	0	0	0	0	0.01	0.01	0
Na^{+}	0.27	0.24	0.12	0.70	0.52	0.90	0.67
Fe^{3+}	-0.57	0	0	0	0	0	0
Metal	-0.57	-0.38	-0.20	-4.31	-0.37	-1.36	-1.26
Total cations released (Na+K+Ca+Mg)	0.27	0.24	0.12	0.77	0.55	0.99	0.71
Contribution of Na^{+} to exchange (%)	99.6	99.5	99.9	91.3	94.4	90.7	94.4
Si^{4+}	0	0	0	0.77	0	0	0
Al^{3+}	0.07	0	0	0.74	0	0	0

During the metal sorption processes, mainly Na^{+} was released from Na-Clin (percent contribution to the total amount of exchangeable cations: 90.7–99.9 %). No K^{+}, Ca^{2+} and Mg^{2+} were detected in the solution at the end of 1-hour treatment period. More exchangeable cations were released form Na-Clin when present in lower *S/L* ratios.

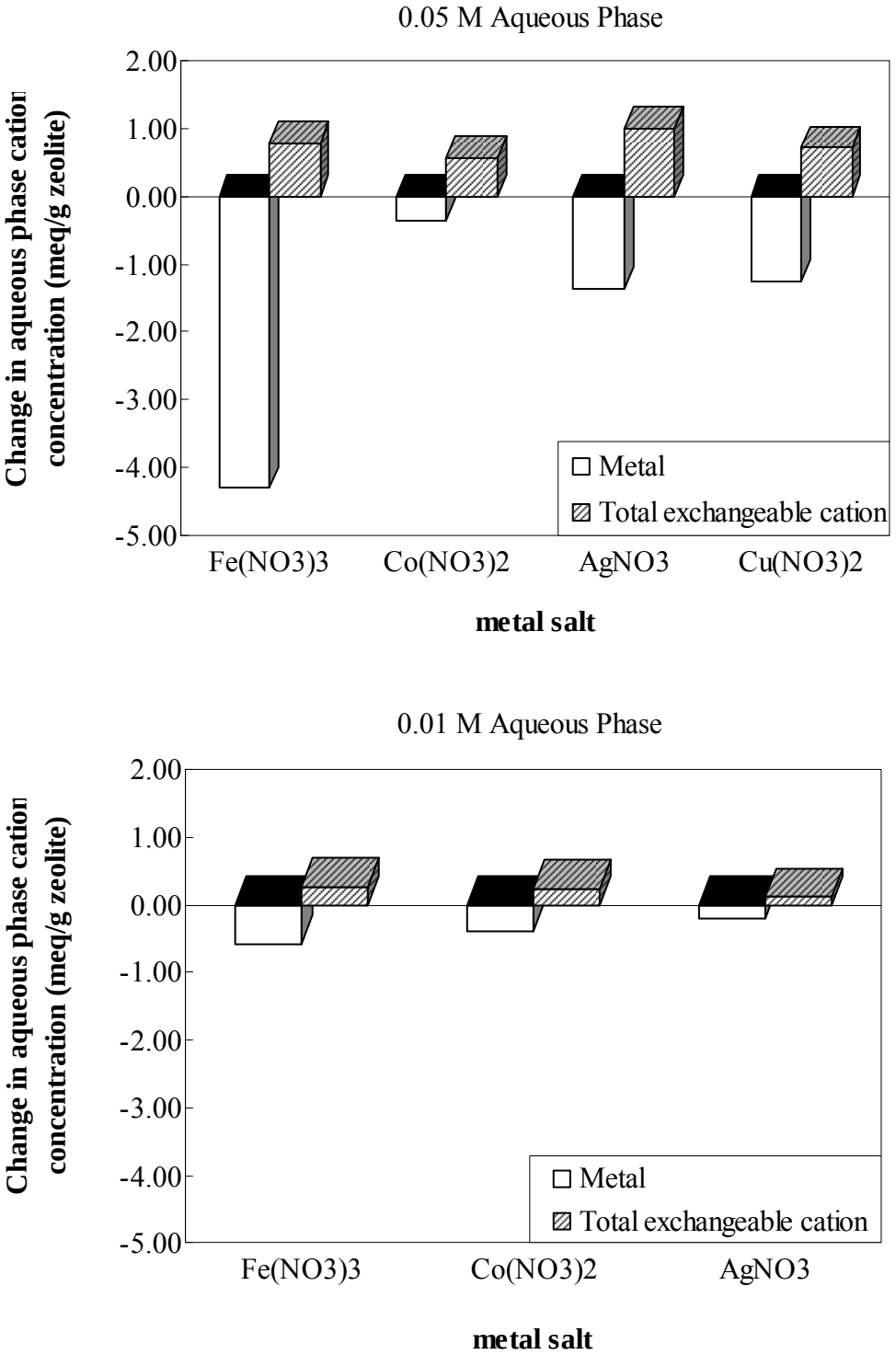

Figure 5.15. Change in concentrations of H^+, exchangeable and metal cations in the aqueous phase during interaction of Na-Clin with metal salt solutions.

It was found that there is a nonstoichiometry between the amount of exchangeable cations released and the amount of metal sorbed. For all cases, the amount of metal sorbed was higher than the total amount of released exchangeable cations, except for 0.05 M Co zeolite. For this sample the total amount of cations released were higher than the amount of cobalt sorbed. This might be related with the dissolution and/or adsorption accompanying the cobalt exchange. Si^{4+} was not detected in the solutions, except for the iron sorption from the solution with 0.05 M initial concentration. The Al^{3+} release was also noticeable for this run. The amount of Al^{3+} detected in the other solutions was at the insignificant level.

The pH of the solutions decreased during the course of metal sorption, except for that of 0.05 M Ag sample. The importance of solution acidity as a controlling parameter in the sorption process comes from its influence on the metal speciation and on the surface properties of the sorbent (Elliott and Huang, 1981; Lin and Yang, 2002).

The metal cations in aqueous solution are solvated or hydrated with water molecules, forming complex cations. Several reports on the existence and behavior of these hexaaqua complex cations in aqueous solution are available in the literature. It is well established that there exists equilibrium between metal cations (M^{2+}) and their complex forms. The formation of hydroxyl-complexes of metal ions is a function of solution pH and initial metal ion concentration. The concentration of metal in the solution is the sum of concentrations of metal cation and metal–hydroxy species according to:

$$[M]_{total} = [M^{n+}] + [M(OH)_{n-1}^{n-1}] + [M(OH)_{n}^{n-2}] + [M(OH)_{n+1}^{n-3}] + [M(OH)_{n+2}^{n-4}] \qquad (5.6)$$

The concentrations of the metal species found in the solution during the metal sorption were determined using Visual MINTEQ version 2.12 Software and are presented in Table 5.13. The software is a version of MINTEQA2 which is a chemical equilibrium model for the calculation of metal speciation, solubility equilibria etc. for natural waters released by USEPA (United States Environmental Protection Agency) in 1999.

Table 5.13. Metal species present in the solution during metal sorption experiments.

Metal Salt	Metal species in the solution
0.01 M $Fe(NO_3)_3$	Fe^{3+}, $FeOH^{2+}$, $Fe(OH)_2^{+}$, $Fe_2(OH)_2^{4+}$, $Fe_3(OH)_4^{5+}$
0.05 M $Fe(NO_3)_3$	Fe^{3+}, $FeOH^{2+}$, $Fe(OH)_2^{+}$ $Fe_2(OH)_2^{4+}$, $FeNO_3^{2+}$
0.01 M $Co(NO_3)_2$	Co^{2+}, $CoNO_3^{+}$
0.05 M $Co(NO_3)_2$	Co^{2+}, $Co(NO_3)_2$(aq), $CoNO_3^{+}$
0.01 M, 0.05 M $AgNO_3$	Ag^{+}, $AgNO_3$ (aq)
0.05 M $Cu(NO_3)_2$	Cu^{2+}, $CuOH^{+}$, $Cu_2(OH)_2^{2+}$, $CuNO_3^{+}$, $Cu(NO_3)_2$ (aq)

The formation of such species reduces participation of the metal cation in ion exchange and strongly influences the mechanisms of their incorporation into the zeolite structure. Many studies are available in the literature on the occurrence of hydrolysis processes and precipitation of low-solubility substances (metal hydroxides etc.) during the ion exchange in zeolites (Keane, 1995; Inglezakis et al., 2004; Schoonheydt et al., 1976; Wark et al., 1993). It was reported that precipitation of atacamite, $CuCl_2 \cdot 2Cu(OH)_2$, on the surface of the clinoptilolite may clog part of the pores and thus it may decrease the further uptake of the copper ions (Blanchard et al., 1984). Adsorption or fixation of metal species as hydroxy complexes on zeolite surface may also lead to reduction or reversion of surface negative charge, and thus to reduce the uptake of metal (Ersoy and Çelik, 2002).

The adsorption behavior of zeolitic minerals is based on the Brønsted and Lewis theory of acidic and basic sites existing in the microporous structure. Namely, the oxygen atom in the Si–O–Al species bears a negative charge of the lattice and represents the structural basic site as a potential adsorption location. Therefore, not only does isomorphous Si/Al substitution account for a negative charge, but the oxygen from the lattice also behaves as a proton acceptor. This effect is often named in the literature as oxygen alkalinity (Trgo and Perić, 2003; Shahwan et al., 2005). This can be responsible for the adsorption of positively charged metal species.

The possible mechanisms taking place during metal sorption are summarized below (Stumm and Morgan, 1996). In acidic and neutral pH range, the neutral and negative surface hydroxyl groups are protonated as given by Equations (5.3) and (5.4). These protonation reactions consume H^+ ions and result in the solution pH to increase. Again in the same pH range, protons in the surface hydroxyl groups of Si-OH and Al-

OH behaves as an exchangeable cation. As metal concentration increases, metal ions are forced into internal surface sites and also form inner-sphere complexes. This kind of complexation leads to more stable surface groups due to the formation of covalent bonds:

$$\begin{aligned} \equiv S-OH + M^{2+} &\leftrightarrow \equiv S-OM^{+} + H^{+} \\ \equiv 2S-OH + M^{2+} &\leftrightarrow \equiv (S-O)_2 M + 2H^{+} \end{aligned} \tag{5.7}$$

During these reactions take place, protons are released from the surface, therefore the solution pH decreases.

In the basic pH range, OH^- ions may react with clinoptilolite surface and caused the surface to be deprotonated:

$$S-OH + OH^{-} \leftrightarrow S-O^{-} + H_2O \tag{5.8}$$

Those deprotonated surface groups (S-O$^-$) behave as Lewis bases and the sorption of metal ions (and protons) can be understood as competitive complex formation:

$$\equiv Si-O^{-} + M^{2+} \leftrightarrow \equiv Si-OM \tag{5.9}$$

Formation of metal-hydroxyl complexes (hydrolysis of metal ions):

$$\begin{aligned} M^{2+} + H_2O &\leftrightarrow MOH^{+} + H^{+} \\ MOH^{+} + H_2O &\leftrightarrow M(OH)_2 + H^{+} \end{aligned} \tag{5.10}$$

As a result of hydrolysis of metal ions, the pH of the solution decreased. Hydrolysis of metals caused the metal uptake to increase up to a level due to formation of charged metal hydroxyl species and adsorption or ion exchange of these species on the active sites of clinoptilolite surface. But on the other hand it leads to decrease in the metal uptake due to formation of neutral metal-hydroxyl species due not only to the clogging of clinoptilolite pores via surface precipitation but also to the loss of electrostatic attraction.

When the concentration changes in the solid phase and in the aqueous phase are compared, it was revealed that the metal cation mass balance was established. In the case of the total amount of exchangeable cations, it was observed that the amounts of exchangeable cations uptake were generally higher than those released.

For 0.01 M samples, the concentrations of Si^{4+} and Al^{3+} in the aqueous phase did not change during the course of metal sorption, except slight increase in the Al^{3+} concentration during the iron sorption. On the other hand, the solid phase analyses of the zeolites after the metal sorption showed remarkable changes in the Si^{4+} and Al^{3+} concentrations. Interestingly, the higher amount of Si^{4+} was detected in 0.01 M Fe-1h and 0.01 M-Co-1h samples at the end of the metal sorption than that present in Na-Clin. In the case of silver, cobalt and copper sorption from solution with 0.05 M initial concentration, although no Si^{4+} and Al^{3+} were detected in the aqueous phase, the solid phase concentrations have changed. During the iron sorption, the Si^{4+} and Al^{3+} concentrations in the aqueous phase increased. The solid phase concentrations Si^{4+} and Al^{3+} decreased in all 0.05 M samples, except for 0.05 M Cu zeolite. The Si^{4+} and Al^{3+} content of this sample increased during the course of copper sorption.

5.2.5. Zeta-potential Measurements

Figure 5.16 shows the change of the zeta potential of Na-Clin as a function of pH. The zeta potential of Na-Clin was strongly affected by the solution acidity. As the solution acidity increased, the negativity of the surface decreased due to adsorption of H^+ on the negative charge centers on the surface. The surface of Na-Clin maintained its negative character within the pH range of 2-10.

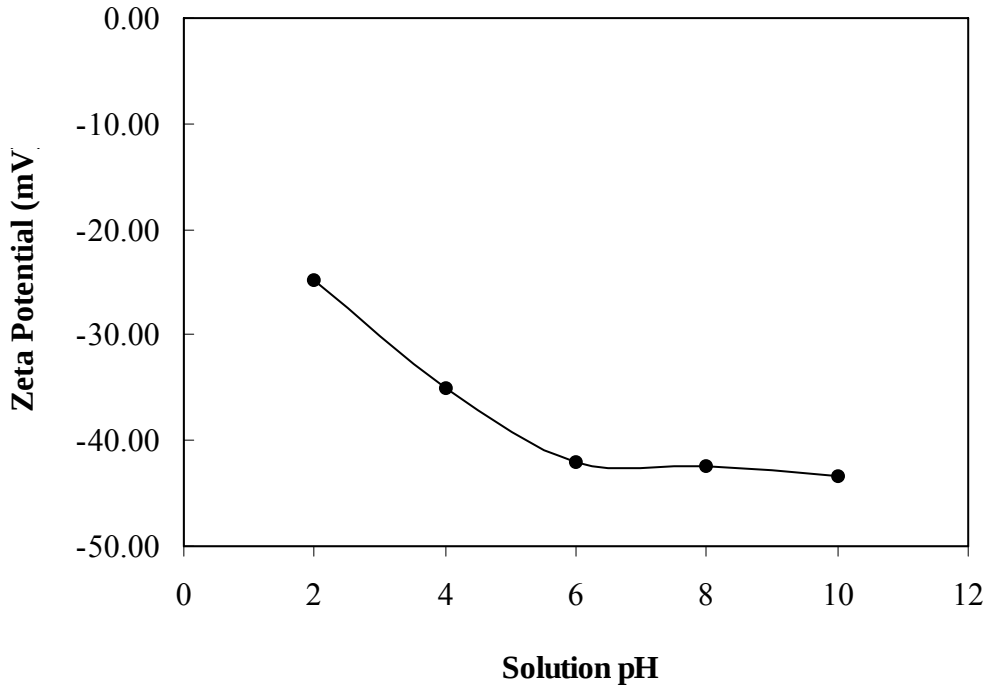

Figure 5.16. Dependence of the zeta potential of Na-Clin on the solution acidity.

5.2.6. Scanning Electron Microscopy–Back Scattered Electron-Energy Dispersive X-Ray (SEM-BSE-EDX)

The scanning electron micrographs of Washed and Na-Clin particles were shown in Figure 5.17. In the micrographs, the well-defined clinoptilolite crystals of tabular/platy morphology were observed on the surface of the particles. The clinoptilolite crystals were also detected grown in the inner parts of the particles (Ackley and Yang, 1991a). From these micrographs, the average size of the clinoptilolite crystals was determined visually as around 5 μm.

The scanning electron micrographs of ClinRich-Kaolin and WGround-Kaolin particles revealed the presence of clinoptilolite crystals on the surface of the particles as seen in Figure 5.18. The surface morphology (cleavages, macrosteps, small fractures, cracks which are actually mesopores and macropores), and the surface microtopography (microsteps, kinks, terrace vacancies) play an important role in metal sorption since the

metal sorption mechanisms are related to processes taking place on the surface, (Godelitsas and Armbruster, 2003).

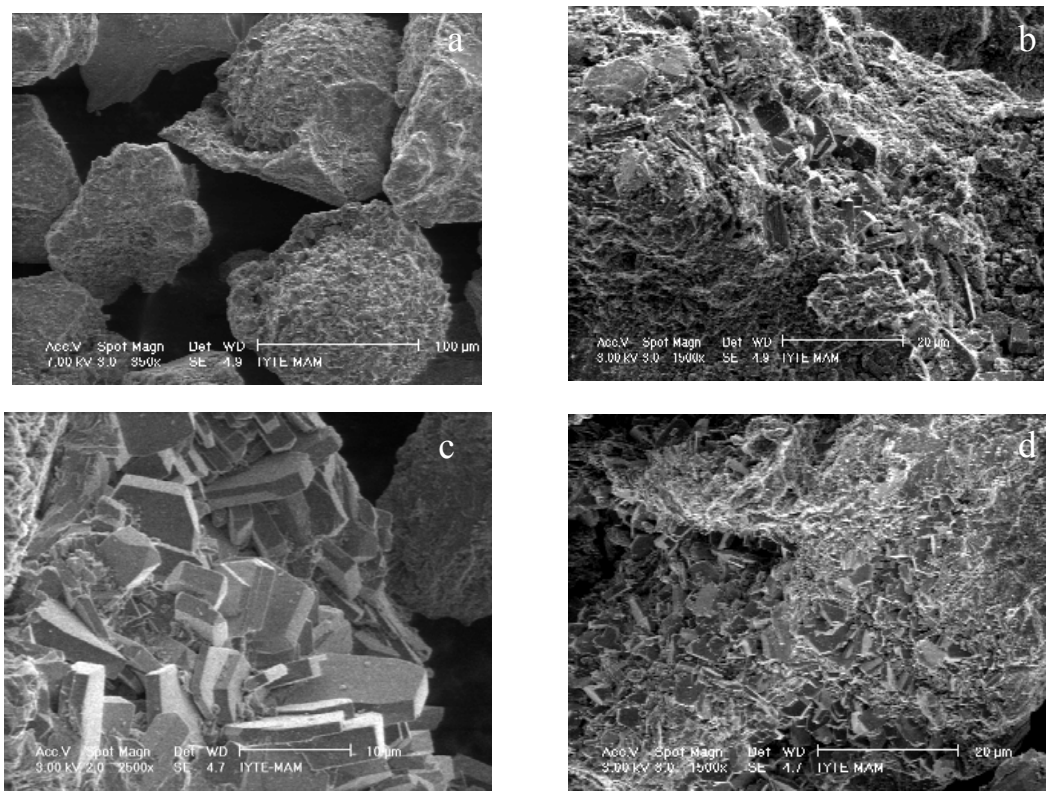

Figure 5.17. Scanning electron micrographs of Washed (a, ×850; b, ×1500) and Na-Clin (c, ×2500; d, ×1500) particles.

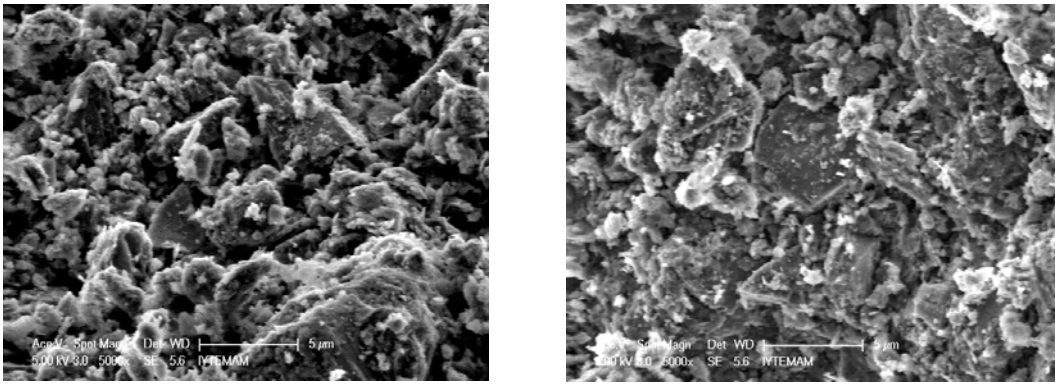

a b

Figure 5.18. SEM micrographs of ClinRich-Kaolin (a, ×5000) and WGround-Kaolin (b, ×5000) particles.

To check the distribution of cations on the surface of the zeolite after the sorption of metals, the surfaces were mapped with X-ray energy dispersive spectroscopy. The representative backscattering electron images in negative form were given in Figure 5.19. Dark spots and regions designating the presence of metals sorbed can be observed on the surface of the grains. The darker spots observed on the surface of Na-Clin have high Fe content. The SEM images for 0.05 M Co sample and its activated form showed the clinoptilolite crystals with clean surfaces. No indication of surface precipitation was observed. In the BSE images, very few dark spots with diameter ~1 μm were detected on the surface. The EDX analysis showed that those dark spots contain approximately 6 % (by weight) Co besides O, Si and Al. More spots which are homogenously distributed throughout the surface were detected on the surface of 0.01 M Co-1h zeolite. Those spots have narrow size distribution around 1 μm and the elemental analysis revealed they contain approximately 10 % (by weight) Co besides O, Si and Al. After activation, no change was detected in the size, distribution and elemental composition of the spots on the surface of the cobalt-sorbed zeolites.

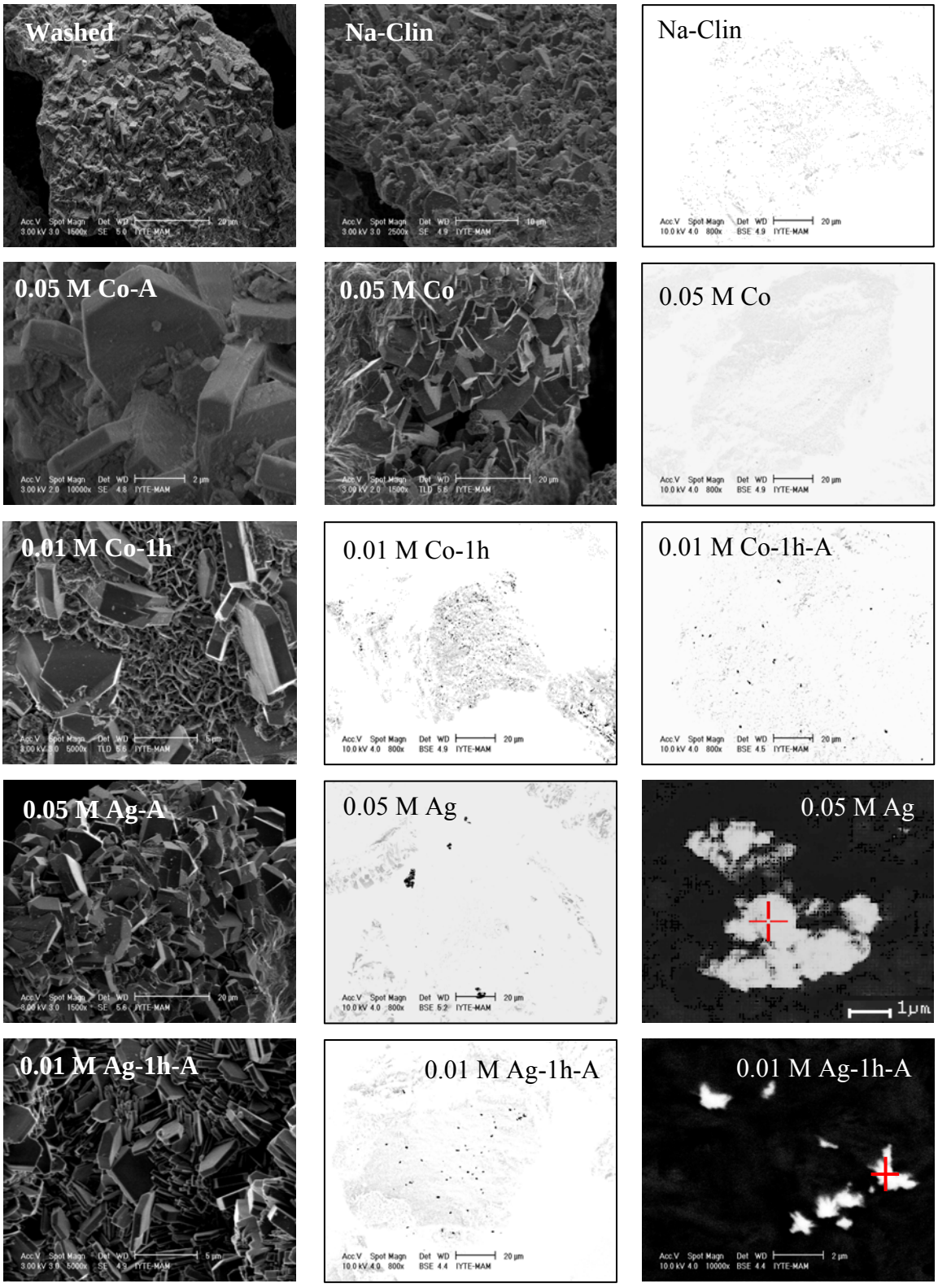

Figure 5.19. SEM and BSE micrographs (negative) of the zeolite samples.

(cont. on next page)

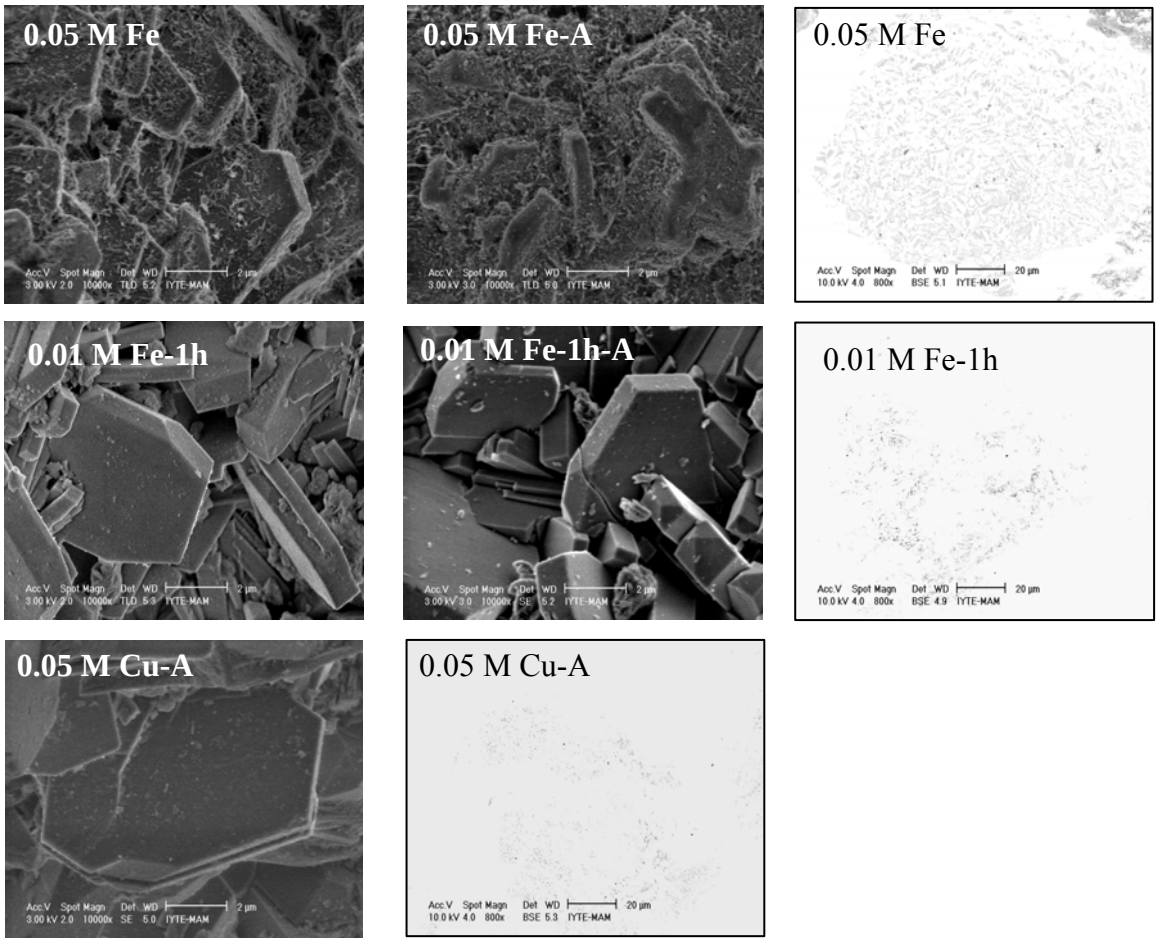

Figure 5.19. (cont.) SEM and BSE micrographs (negative) of the zeolite samples.

The SEM images of the silver-sorbed samples illustrated presence of any new phases on the clinoptilolite crystals. However, in the BSE image of 0.05 M Ag sample, relatively large (~5 μm) spots were detected. The EDX analysis on those spots indicated that they have about 85 % (by weight) Ag content together with very small amounts of O, Si and Al. On the surface of 0.01 M-Ag-1h, dark spots of smaller size and homogenous distribution were detected. The elemental composition analysis revealed approximately Ag of 10 %, Si of 40 %, Al of 8 % and O content of 25 % (by weight). In the SEM micrographs of 0.05 M Fe sample, drastic precipitation of needle-like phase on the surface of clinoptilolite crystals was observed. The BSE images showed homogenous distribution of a phase on the surface. The spots have size distribution within the range of ~1-3 μm. The EDX analysis on the spots depicted highly variable Fe content of 25-60 % (by weight). Si, Al and O were also detected in the spots. There was no such a drastic precipitation on the clinoptilolite crystal surface present on 0.01 M Fe-

1h sample. Besides very few distributed dark spots, some regions of intense metal accumulation on one part of the grains were observed. The EDX analysis on these regions indicated the elemental composition of approximately 20 % Fe, 20 % Si, 7 % Al and 45 % O (by weight). In the SEM micrograph of 0.05 M Cu, no precipitation was detected on the surface. Very few, homogenously distributed dark spots seen on the surface have Cu content of approximately 5-35 % (by weight) besides Si, Al and O.

The results of EDX analyses performed on the surface of the particles are given in Table 5.14 together with the bulk chemical compositions. The EDX analyses were carried out on six different areas on the surface and the average values were reported with the standard deviation. For 0.05 M Ag, 0.05 M Fe, 0.01 M Co-1h and 0.01 M Ag-1h samples, the surface concentrations of the metal was found to be significantly higher than the bulk concentration. The SEM, BSE and EDX analysis on 0.05 M Fe zeolite revealed possible precipitation of insoluble solid phases on the surface during the iron sorption. The zeolites with higher metal contents on the surface as compared to that in their bulk structure might indicate that different mechanisms prevailed during the metal sorption process including adsorption, precipitation of the metal hydroxides on the surface accompanying to the ion exchange. Those phases can be detected by X-ray diffraction technique if they are crystalline and present in high concentrations (more than 5% by weight) (Jentys and Lencher, 2001).

It is known from the literature that different shape of surface crystal faces and their imperfections, such as corners, broken bonds, and edge sites, as well as amphoteric nature of hydroxyl surface groups [≡(Al or Si)–OH], leads to formation of sites with different energy. The range of site energies with different sorption affinities on the surface of the zeolitic grain results in nonhomogeneous distribution of different metal species adsorbed (Baeyens and Bradbury, 1997; Godelitsas et al., 2001)

Table 5.14. Comparison of the bulk and surface elemental composition of the zeolites (by weight).

	Washed		0.05 M Co		0.05 M Ag		0.05 M Fe		0.05 M Cu	
Element	EDX	ICP	EDX	ICP	EDX	ICP	EDX	ICP	EDX	ICP
Na	2.51±0.34	2.71	2.71±0.90	3.04	1.56±0.33	1.84	1.62±0.47	1.69	2.07±0.61	1.83
Mg	0.95±0.41	0.52	0	0.17	0	0.54	0	0.17	0.92±0.21	0.18
Al	13.98±1.00	13.57	12.18±1.23	13.26	9.78±0.51	10.90	10.32±2.96	11.01	13.40±0.44	13.52
Si	64.93±1.04	70.67	65.15±1.51	70.28	46.40±2.66	58.47	54.86±3.35	63.96	64.70±2.17	70.18
K	8.99±1.07	8.38	6.66±1.95	5.46	3.48±0.80	4.14	3.91±1.00	4.19	5.85±1.23	4.98
Ca	4.80±1.46	2.10	1.98±0.68	0.40	1.35±0.35	0.36	1.18±1.46	0.32	1.58±0.49	0.32
Fe	3.84±1.63	2.05	4.88±2.05	1.57	4.72±1.83	1.26	28.10±2.23	18.66	3.38±1.05	1.62
Co	0	0	6.43±1.48	5.83	0.	0	0	0	0	0
Ag	0	0	0	0	32.72±2.62	22.49	0	0	0	0
Cu	0	0	0	0	0	0	0	0	8.10±1.57	7.38

(cont. on next page)

Table 5.14. (cont) Comparison of the bulk and surface elemental composition of the zeolites (by weight).

	Na-Clin		0.01 M Co-1h		0.01 M Fe-1h		0.01 M Ag-1h	
Element	EDX	ICP	EDX	ICP	EDX	ICP	EDX	ICP
Na	8.50±2.15	7.26	6.49±0.46	5.81	6.38±0.56	4.83	6.03±1.04	5.83
Mg	1.25±0.20	0.21	1.22±0.07	0.22	0	0.23	1.15±0.19	0.25
Al	15.61±1.15	13.44	14.80±0.46	12.87	14.40±0.72	12.91	13.75±1.05	12.69
Si	66.48±2.14	71.26	65.65±1.05	71.41	67.74±1.81	72.14	63.47±2.80	69.96
K	4.48±1.48	5.60	5.58±0.61	5.40	5.84±1.09	5.63	5.96±0.73	5.60
Ca	0.84±0.62	0.38	0.56±0.07	0.21	1.35±0.23	0.15	1.27±0.52	0.33
Fe	2.84±0.74	1.76	1.94±0.80	1.70	4.28±1.36	3.96	3.00±1.40	1.74
Co	0	0	3.76±0.63	2.38	0	0.00	0	0.00
Ag	0	0	0	0.00	0	0.00	6.71±1.26	3.60
Cu	0	0.08	0	0.00	0	0.14	0	0.00

5.2.7. Textural Properties

The textural characteristics of the zeolites were examined by analysis of nitrogen adsorption and desorption isotherms obtained at -196 ^{o}C and of carbon dioxide adsorption isotherms at 30 ^{o}C volumetrically.

The N_2 adsorption isotherms of the zeolites are presented in Figure 5.20. All the N_2 isotherms corresponded to Type IV according to IUPAC (the International Union of Pure and Applied Chemistry) classification (Gregg and Sing, 1982). The hysteresis loops appeared in the multilayer range of the isotherms that is usually associated with capillary condensation in mesopores (secondary porosity). The presence of mesopores is associated with the presence of the accompanying material (feldspar, quartz, and others). The hysteresis loop observed in the isotherm of 0.05 M Cu sample did not exhibit a closure indicating the irreversible adsorption of N_2 by this zeolite. For Washed, Na-Clin, 0.05 M Fe and 0.05 M Co samples, the increment in the adsorbed amount due to the multilayer adsorption and capillary condensation in the mesopores was observed at P/P_o~0.4, while for other samples at P/P_o~0.5.

From the adsorption branch, the specific surface areas of the zeolites were found to be in the range of 33.6-157.3 m^2/g from the linear portion of the BET (Brunauer-Emmett-Teller) plots (Brunauer et al., 1938). The linear regions extended from pressure range P/P_o=0.044-0.308 and correlation coefficients in the range of 0.987-0.999 (Figure 5.21). The parameters in the BET model (C and the monolayer capacity) calculated from the slope and intercept of these plots and reported in Table 5.15.

The parameter C in the BET model is related exponentially to the enthalpy of adsorption in the first adsorbed layer, i.e., $exp[-(\Delta H_d-\Delta H_v)/RT]$, ΔH_d is the enthalpy of adsorption in the first layer and H_v is the heat of vaporization (Jentys and Lercher, 2001). It is used to characterize the shape of the isotherm in the BET range. The large C value indicated the presence of a sharp knee in the BET region of the adsorption isotherm so the presence of microporosity (Gregg and Sing, 1982). The negative C values indicated that the enthalpy of first adsorbed layer was lower than the latent heat of nitrogen.

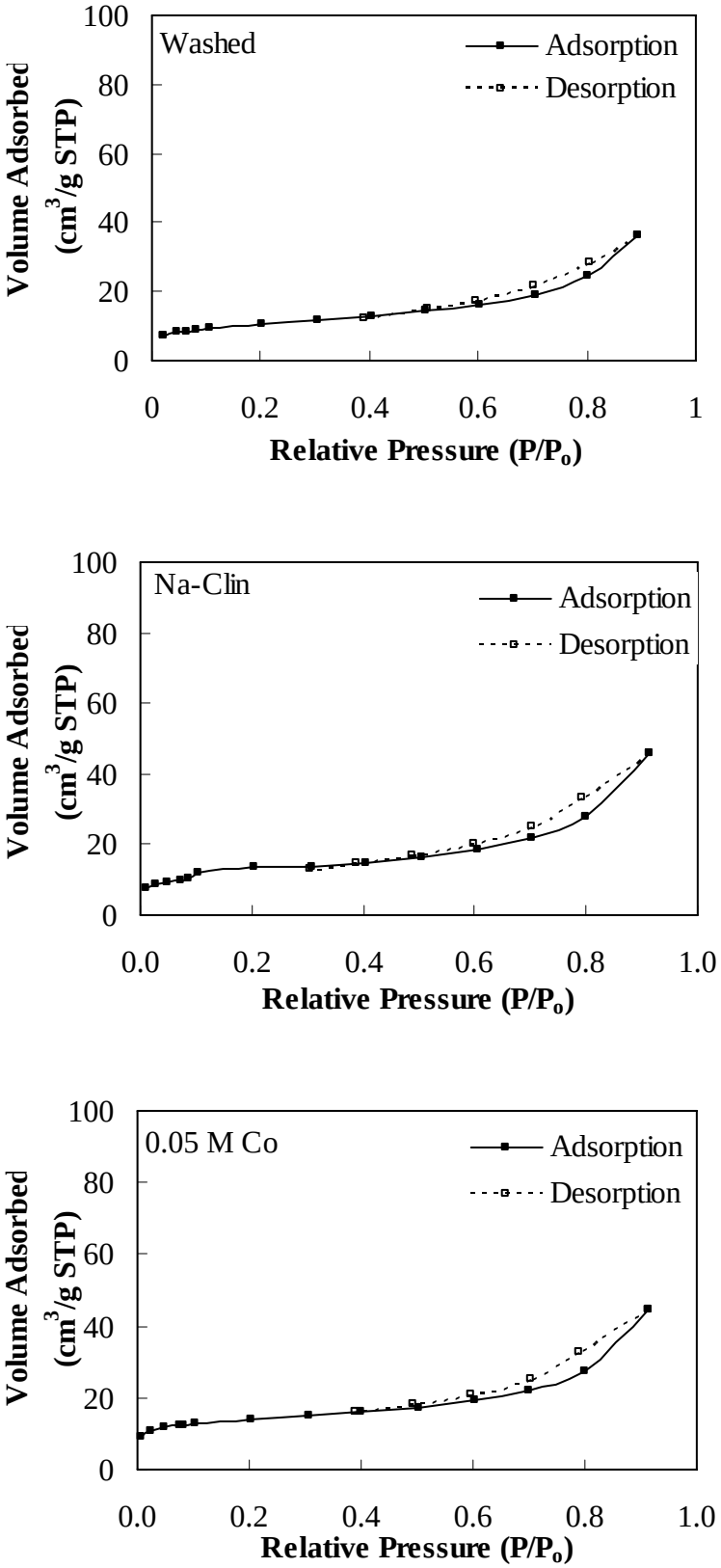

Figure 5.20. N_2 adsorption and desorption isotherms of the zeolites (-196 ^{o}C).

(cont. on next page)

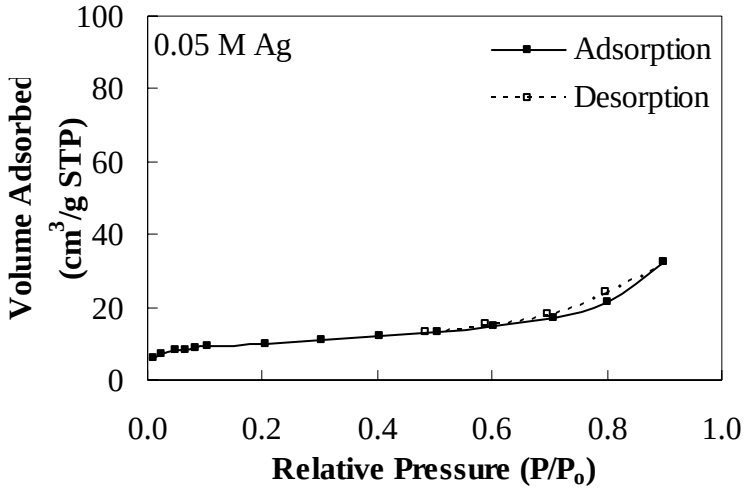

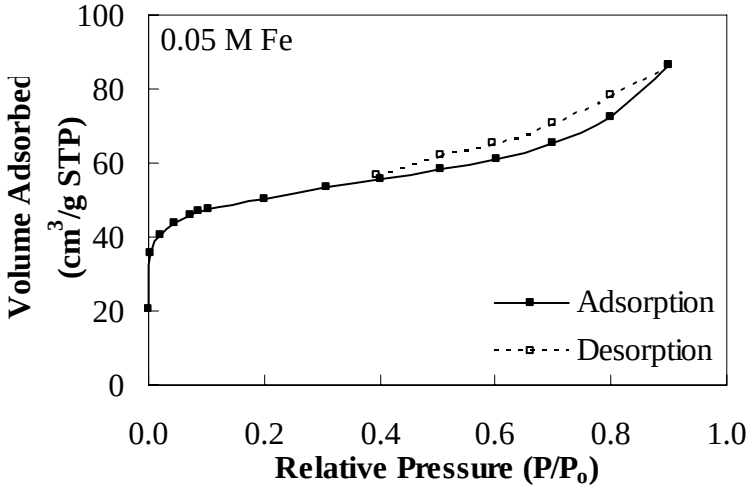

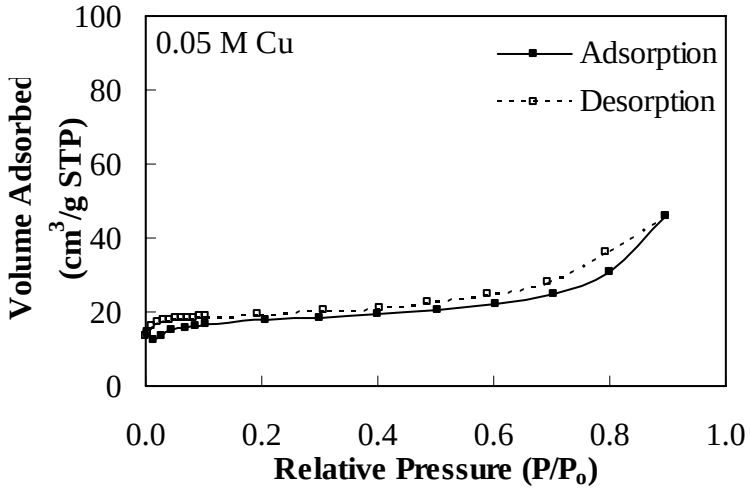

Figure 5.20. (cont.) N_2 adsorption and desorption isotherms of the zeolites (-196 ^{o}C).

(cont. on next page)

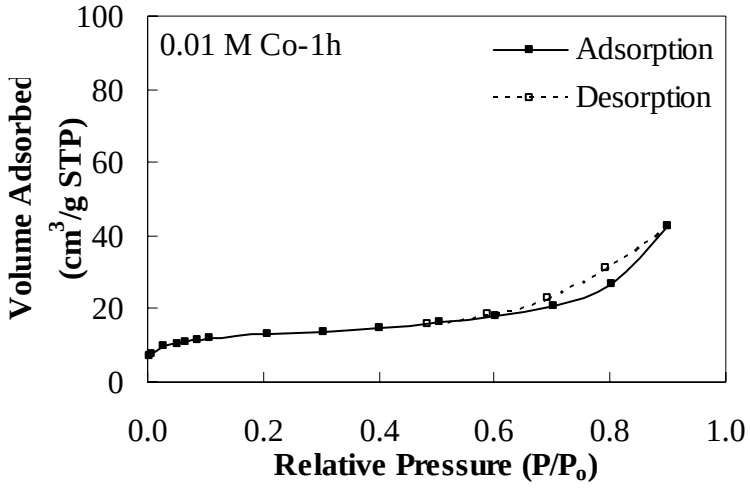

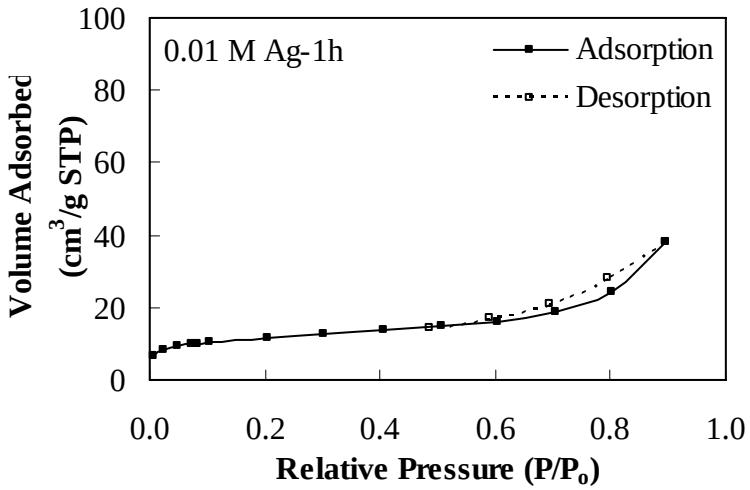

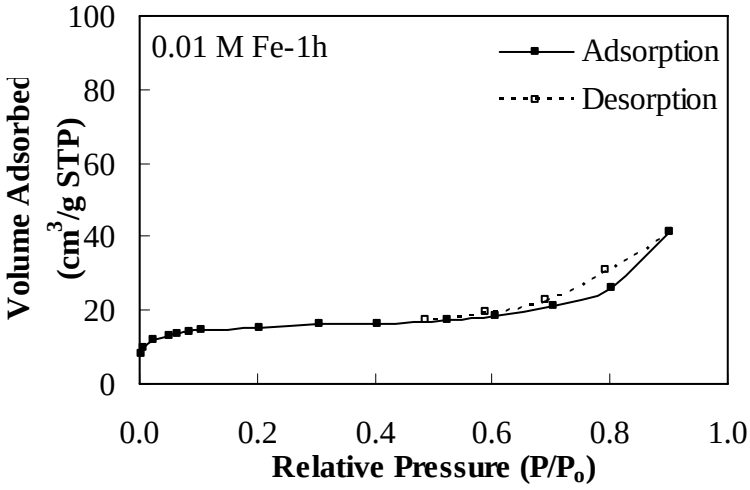

Figure 5.20. (cont.) N_2 adsorption and desorption isotherms of the zeolites (-196 ^{o}C).

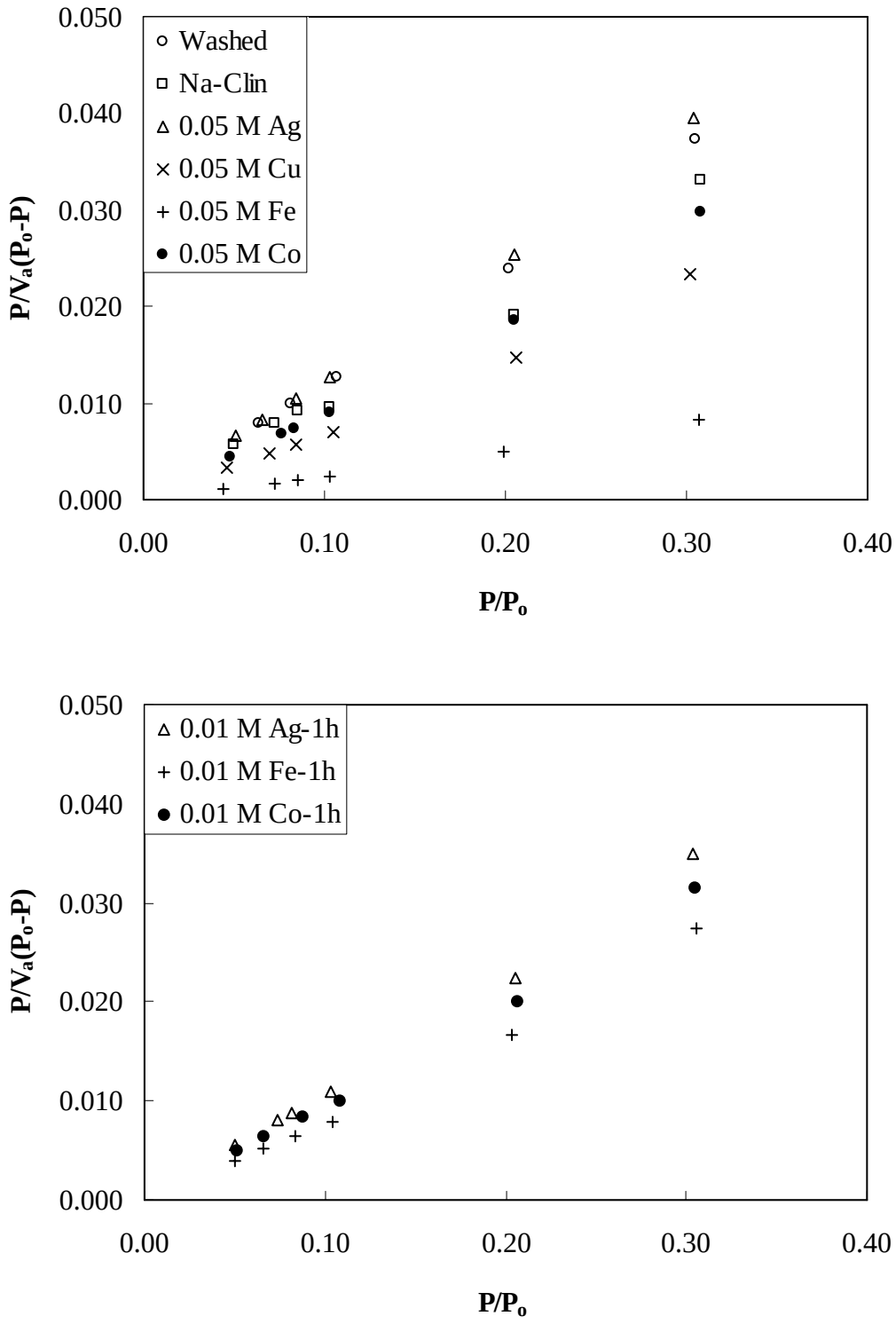

Figure 5.21. BET plots from the N_2 adsorption data.

Table 5.15. BET model parameters from the N_2 adsorption data.

Sample	Monolayer capacity, V_m (cm^3/g)	C	BET surface area (m^2/g)
Washed	8.26	4654.8	35.96
Na-Clin	9.63	-508.3	41.93
0.05 M Ag	7.72	-295.8	33.59
0.05 M Cu	12.80	-89.6	55.71
0.05 M Fe	36.14	-83.3	157.31
0.05 M Co	10.29	-120.1	44.78
0.01 M Ag-1h	8.67	-184.3	37.73
0.01 M Fe-1h	11.12	-81.0	48.42
0.01 M Co-1h	9.68	-153.8	42.12

The BET model assumes that all adsorption sites on a surface are identically energetic and neglects adsorbate-adsorbate interactions in the same layer and does not account the possibility of micropore filling. Thus, the BET model does not govern the micropore adsorption. Therefore, the BET surface area was used for comparative purposes. The NaCl treatment caused an increase in the BET surface area due to the removal of mineral impurities from the surface of the zeolite. The BET area of the zeolite did not change notably after metal sorption, except for 0.05 M Fe sample. The BET area of this sample was found to be almost four times higher than the parent zeolite. The significant rise in the BET surface area of 0.05 M Fe sample was attributed to decationation and dealuminaton, and also by dissolution of amorphous silica blocking the channels in the clinoptiolite structure. Hernandez and co-workers reported that the cation blocking effect in the clinoptilolite was lowered by acid treatment, i.e. substituting large ions by protons. Furthermore, acid treatment for longer periods caused to leaching of aluminium from framework positions (Hernandez et al., 2000). The elemental analysis confirmed the significant degree of dealumination for 0.05 M Fe sample. In the case of 0.05 M Ag zeolite, the lower BET surface area might be explained by the presence of silver oxide species in the channels of the zeolite which might cause the blocking of some pores.

According to the Langmuir theory, the limiting adsorption at the plateau represents completion of the monolayer and can be converted into the specific surface area using the crossectional area of the adsorbate molecule. The Langmuir model is given by,

$$\frac{V}{V_m} = \frac{a(P/P_o)}{1 + a(P/P_o)} \tag{5.15}$$

where V_m is the monolayer capacity of the adsorbent and a is the affinity constant. The parameter a is a measure of how strong an adsorbate molecule is attracted onto a surface.

The experimental N_2 adsorption data fitted to the Langmuir model as shown in Figure 5.22. The Langmuir model was found capable of describing the N_2 adsorption isotherms for up to $P/P_o \leq 0.31$ ($r^2 \geq 0.993$). The parameters in the Langmuir model calculated from the linear relative pressure range are listed in Table 5.16.

Table 5.16. Langmuir model parameters from the N_2 adsorption data.

Sample	Monolayer capacity, V_m (cm^3/g)	a	Langmuir surface area (m^2/g)
Washed	12.23	43.51	53.21
Na-Clin	14.41	43.65	62.72
0.05 M Co	15.24	71.15	66.35
0.05 M Ag	11.42	53.09	49.69
0.05 M Fe	53.47	130.77	232.75
0.05 M Cu	18.98	80.95	82.59
0.01 M Co-1h	14.12	76.29	61.48
0.01 M Ag-1h	12.80	61.02	55.73
0.01 M Fe-1h	16.23	116.89	70.66
0.01 M Co-24h	14.64	52.54	63.73
0.1 M Co-24h	14.95	68.06	65.06

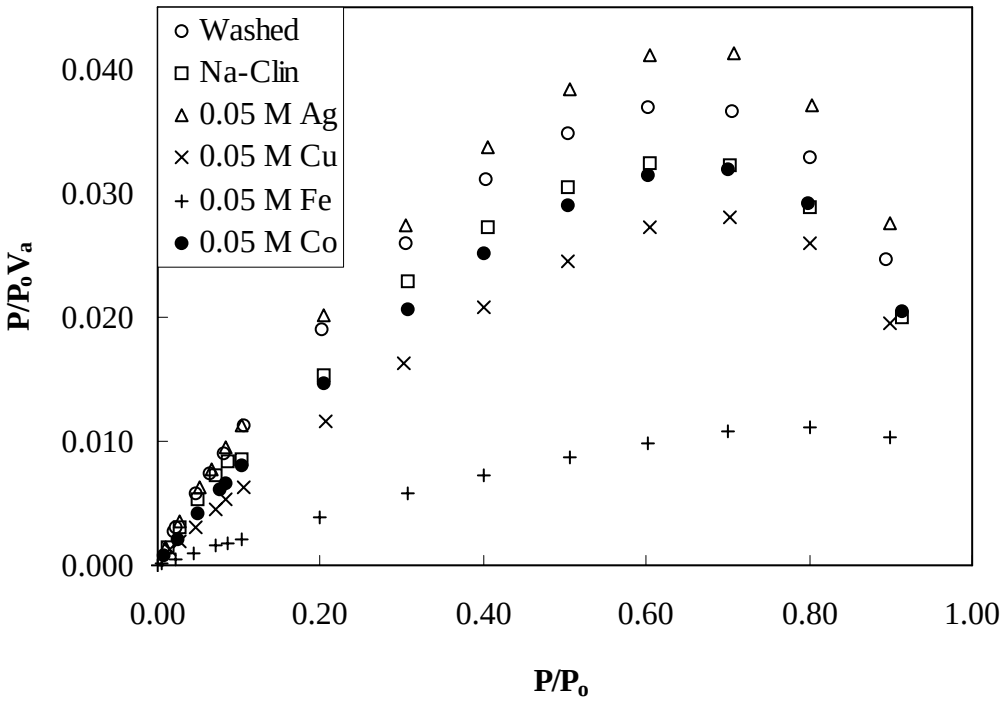

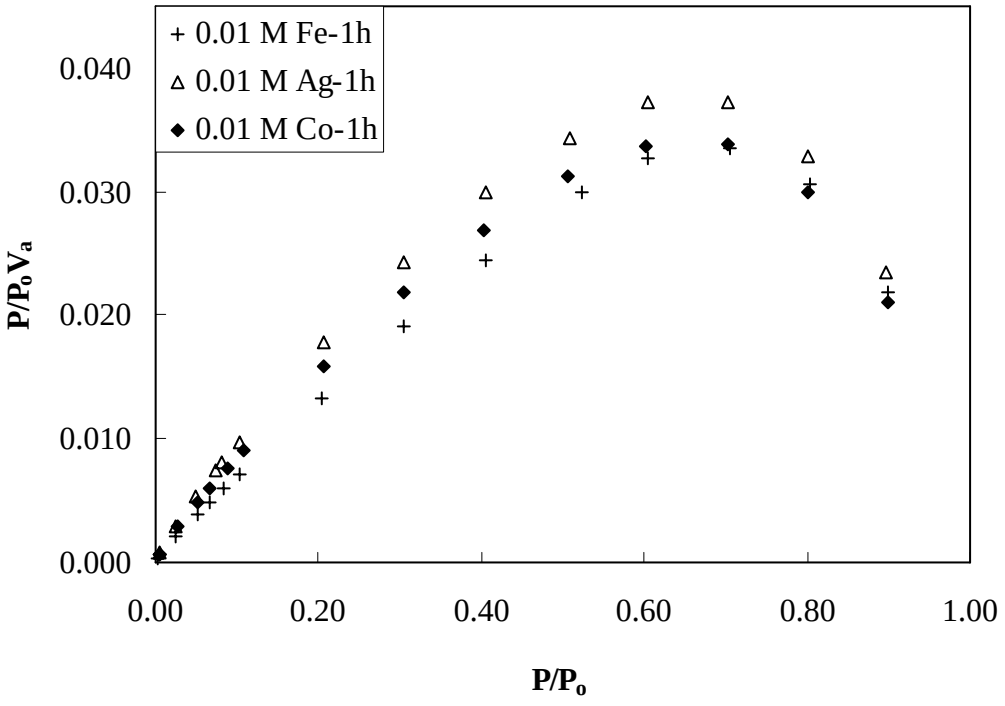

Figure 5.22. Langmuir plots for the N_2 adsorption data.

The CO_2 adsorption isotherms of the zeolites shown in Figure 5.23 were of Type I which is typical of predominantly microporous adsorbents having relatively small external surfaces. The Type I isotherms indicated that the CO_2 molecules could penetrate freely into the micropores. There was an abrupt increase of adsorption at low equilibrium pressures in all isotherms. The remarkable increase of CO_2 adsorption at low equilibrium pressures is attributed to the strong electrostatic interactions between quadrupole moments of the CO_2 molecules and the zeolite cations. At higher pressures, the CO_2 isotherms reached the plateau indicating the saturation of the adsorption sites. This limit exists because the pores are so narrow that they cannot accommodate more than a single molecular layer on their walls. The initial steep part of the Type I isotherm represents micropore filling (rather than surface coverage) and the low slope of the plateau is due to multilayer adsorption on the small external area. The limiting uptake is governed by the accessible micropore volume rather than by the internal surface area (Sing et al., 1985). The majority of pore filling occurs at $P/P_o < 0.1$ and the adsorbed amount increases gradually above relative pressure of 0.6. The textural properties of the zeolites determined based on the CO_2 adsorption data are presented in Table 5.17. Since CO_2 undergoes chemical adsorption (chemisorption) on the surface of zeolites, it was not possible to obtain the desorption isotherms due to the limitations of the instrument.

The CO_2 adsorption capacity of Washed sample was higher than those of other zeolites in the entire relative pressure range. This may be resulted from the decrease in the basic character of the framework oxygen acting as basic center upon substitution of K^+ by Na^+ (Aguilar-Armenta et al., 2001). In the low-pressure range ($P/P_o<0.1$), the CO_2 adsorption capacities of the zeolites were in the order of Washed>0.01 M Fe-1h> Na-Clin≈0.01 M Ag-1h>0.01 M Co-1h>0.05 M Co>0.05 M Cu>0.05 M Fe>0.05 M Ag. The differences in the CO_2 adsorption capacities of the zeolites in the low-pressure range can be related to the cationic densities of the zeolites. The cations represent the 'active specific center' for the adsorption of gas molecules and the amount of cations present depend on the Si/Al ratio of the zeolite. As the Si/Al ratio decreases, there are more Al atoms in the structure and therefore the zeolite has a greater cationic density (Breck, 1974). In other words, the chemical nature of the surface on the adsorption of CO_2 is important at low relative pressures, since there are specific interactions between the high quadrupole of the CO_2 molecule with the electric field created by the cations in the zeolite structure. At high relative pressures, the order of CO_2 adsorption capacity has become Washed>0.05 M Fe>0.01 M Fe-1h>0.05 M Cu>0.05 M Co>Na-Clin≈0.01 M

Ag-1h>0.01 M Co-1h>0.05 M Ag. The amount of gas adsorbed at high-pressure range (at high degrees of volume filling) depends on the micropore volume (Hernández-Huesca et al., 1999).

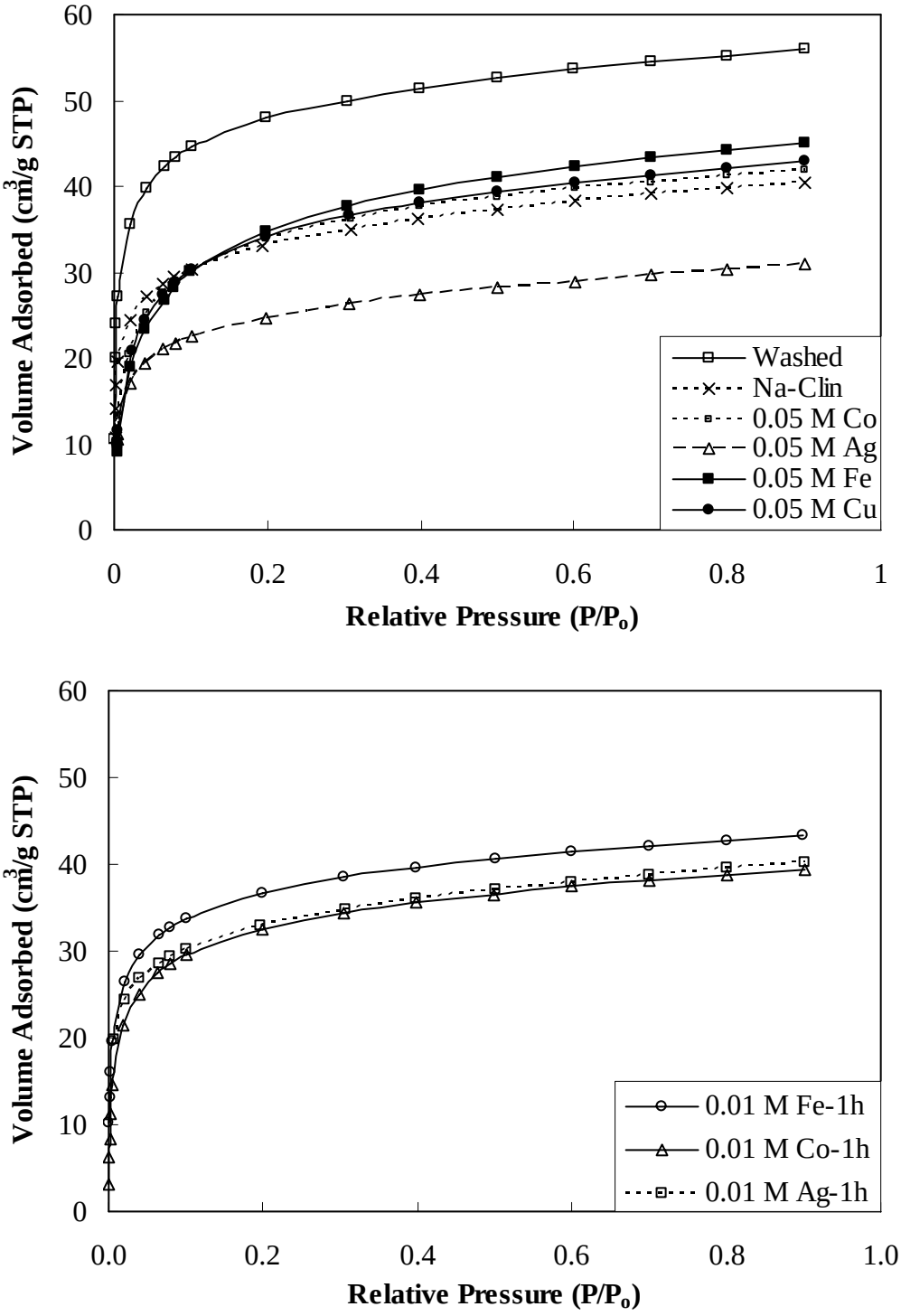

Figure 5.23. CO_2 adsorption isotherms of the zeolites (30 ^oC).

Table 5.17. Textural properties of the zeolites (CO_2 adsorption at 30 ^oC)

Textural property	Washed	Na-Clin	0.05 M				0.01 M-1h		
			Co	Fe	Ag	Cu	Co	Ag	Fe
Single Point Total Pore Volume (cm^3/g)	0.019	0.020	0.018	0.017	0.019	0.018	0.006	0.036	0.019
Micropore Volume (t-plot) (cm^3/g)	0.047	0.027	0.016	0.004	0.018	0.014	0.023	0.027	0.031
Average Pore Diameter (4V/A by BET) (Å)	4.88	7.06	6.36	5.43	9.23	6.09	2.07	3.40	6.12
Maximum Pore Volume (Saito-Foley Model) (cm^3/g)	0.08	0.06	0.06	0.06	0.04	0.06	0.05	0.06	0.06
Median Pore Diameter (Saito-Foley Model) (Å)	5.20	5.10	6.20	6.70	5.80	6.40	5.80	5.90	5.40
Micropore Surface Area (Dubinin-Astakhov Model) (m^2/g)	280.2	204.0	196.7	201.6	148.9	196.9	187.4	214.9	217.9

The CO_2 adsorption capacities obtained at 100 mmHg in the present study were compared with those of the clinoptilolites given in the literature in Table 5.18. The differences might be attributed to the zeolite purities as well as to the cation compositions of the clinoptilolites.

Table 5.18. CO_2 adsorption capacities of clinoptilolite-rich natural zeolites from different geographical origin at 100 mmHg.

Origin of the zeolite mineral	Temperature (^oC)	CO_2 adsorption capacity (mmol/g)	Reference
USA	25	1.43	Breck, 1974
Mexico	27	1.59	Hernandez-Huesca et al., 1999
Gördes, Turkey	30	1.29	Present study

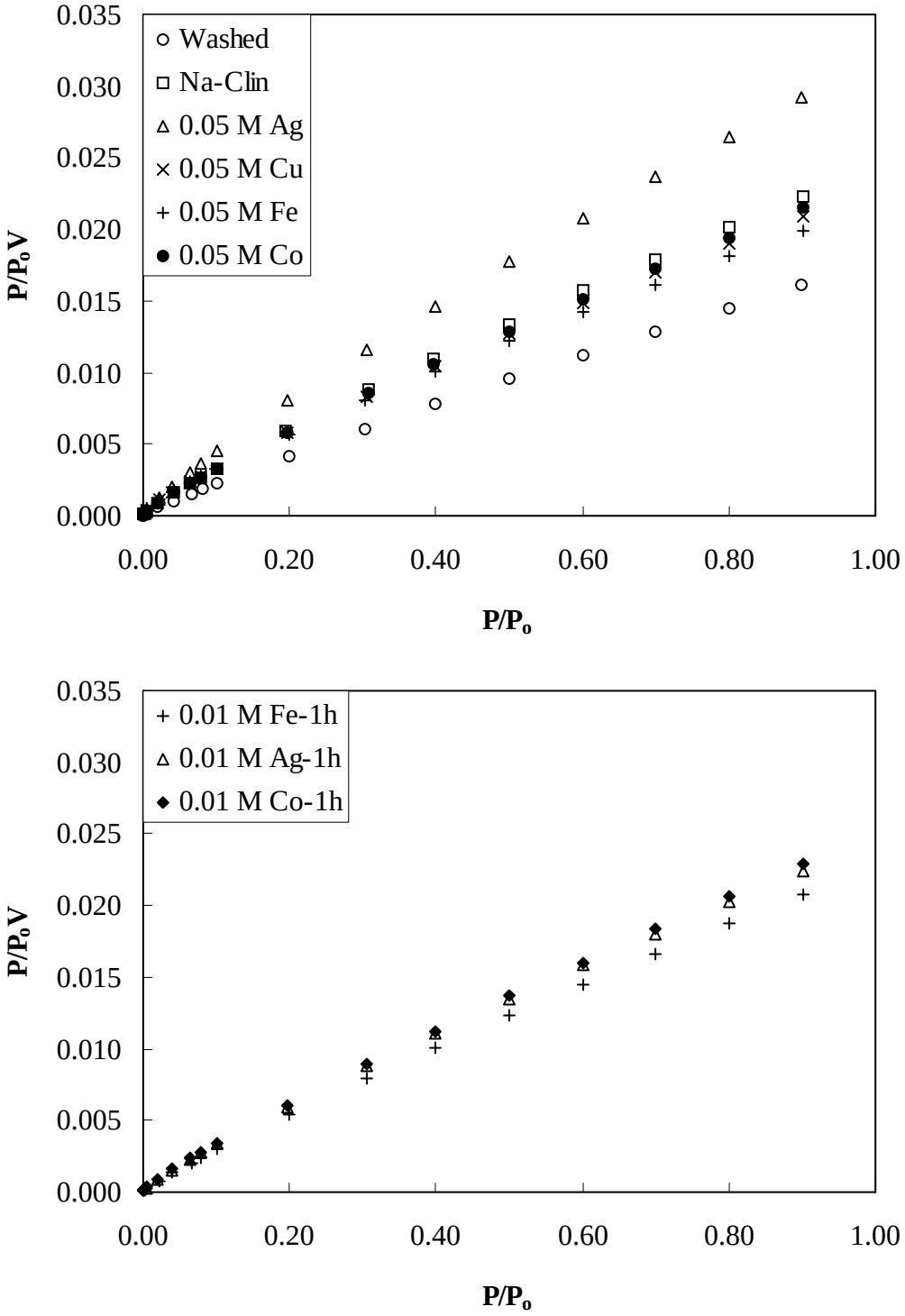

Figure 5.24. Langmuir model plots of the CO_2 adsorption data.

The CO_2 adsorption isotherms were fitted to the Langmuir model as shown in Figure 5.24. The Langmuir model was able to fit the CO_2 adsorption isotherms over the entire relative pressure range with regression coefficients, $r^2 \geq 0.997$. The model parameters (V_m and a) are given in Table 5.19.

Table 5.19. The Langmuir model constants for the CO_2 adsorption.

Sample	Monolayer capacity, V_m (cm^3/g)	a	Langmuir surface area (m^2/g)
Washed	55.87	59.67	232.67
Na-Clin	40.16	48.16	161.46
0.05 M Ag	30.96	32.89	122.28
0.05 M Cu	43.48	27.81	174.72
0.05 M Fe	46.08	23.04	183.75
0.05 M Co	42.19	31.73	172.47
0.01 M Ag-1h	40.49	33.70	160.54
0.01 M Fe-1h	43.10	55.37	179.27
0.01 M Co-1h	39.22	45.54	161.20

The BET model was also fitted to the CO_2 adsorption data and the plots are shown in Figure 5.25. The linear regions in the BET plots extended from P/P_o=0.05 to 0.309 with regression coefficients, $r^2 \geq 0.996$. The parameters obtained by the application of the BET model to the CO_2 adsorption data are listed in Table 5.20. The surface areas calculated from the BET model were lower than those obtained from the Langmuir model indicating that the formation of second adsorption layer may occur before the surface was covered completely by the adsorbate. The Langmuir surface area is more commonly reported for monolayer adsorption on microporous solids. The BET model gives information about the strength of interaction between the adsorbate molecules and zeolite surface.

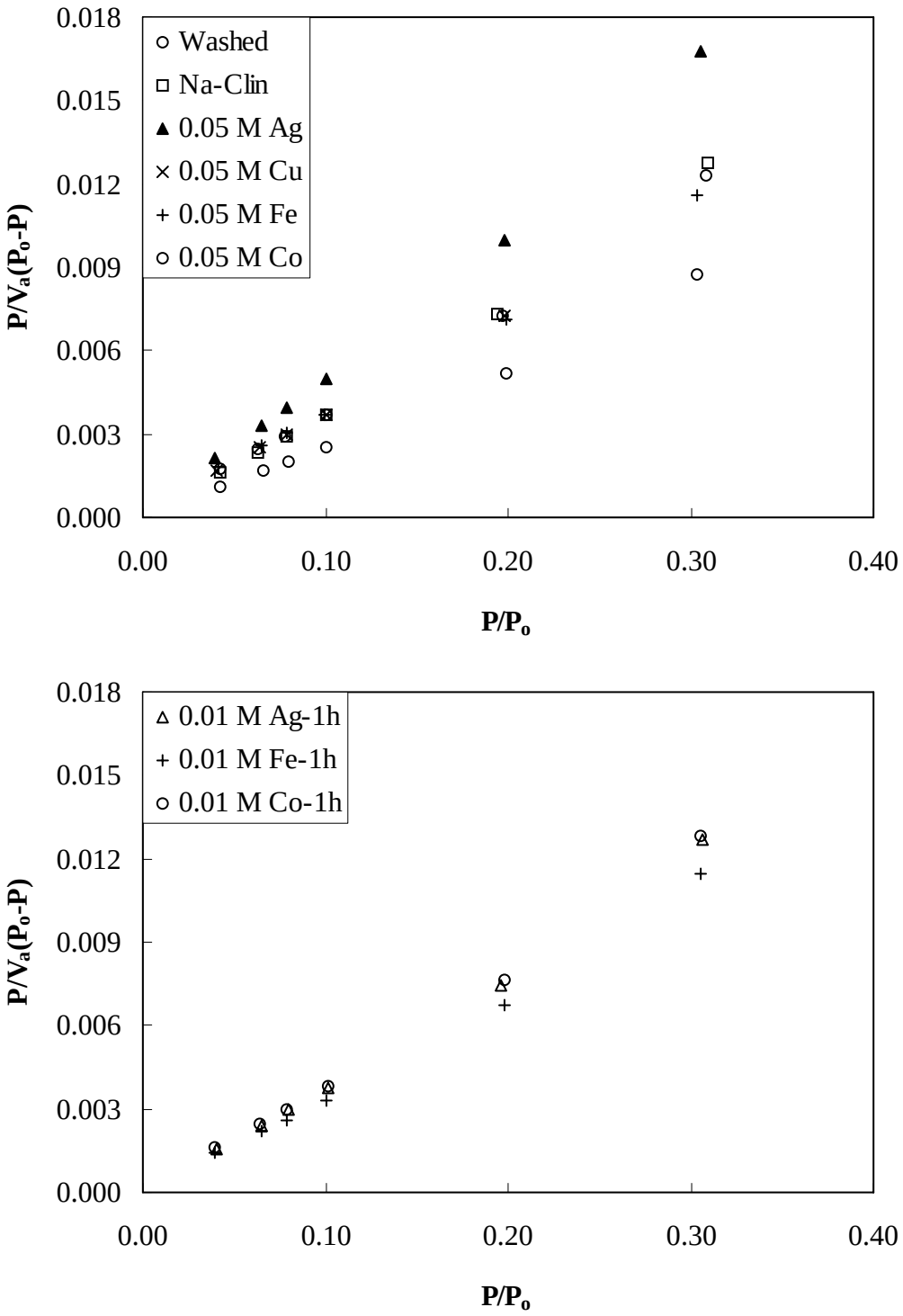

Figure 5.25. BET plots for the CO_2 adsorption.

Table 5.20. BET model parameters for the CO_2 adsorption.

Sample	Monolayer capacity, V_m (cm^3/g)	C	BET surface area (m^2/g)
Washed	36.05	-451.8	164.66
Na-Clin	24.92	-577.4	113.81
0.05 M Ag	18.78	-1060.8	85.77
0.05 M Cu	26.32	380.0	120.20
0.05 M Fe	27.74	-147.2	126.68
0.05 M Co	25.94	678.8	118.46
0.01 M Ag-1h	24.61	-252.4	112.39
0.01 M Fe-1h	27.59	-650.7	126.02
0.01 M Co-1h	24.75	3339.8	113.02

The adsorbed volume of CO_2 at STP was converted the liquid volume using the corrected density of CO_2 at the adsorption temperature. Then the CO_2 adsorption data was fitted to the Dubinin-Raduskevich (D-R) model given by Equation (2.3) and plotting in lnW against $ln^2(P_o/P)$ as shown in Figure 5.26. The straight lines over the relative pressure range of 0.001-0.1 were obtained. From the slope, the value of $-(RT/\beta E_o)^2$ and from the y-axis intercept lnW_L were determined. The W_L and βE_o values were reported in Table 5.21. Washed zeolite has the highest D-R micropore volume. Treatment of Na-Clin with the high-concentration silver nitrate solution led to decrease in the D-R micropore volume. This may be explained by the presence of silver oxide particles in the channels of the zeolite. The higher D-R micropore volumes of the iron-sorbed zeolites with respect to the parent zeolite (Na-Clin) can be attributed to the decationization and to the dissolution of amorphous silica blocking the channels in the clinoptiolite structure during the sorption under highly acidic conditions. Under the acidic conditions of interest substitution of the cations located in the channels by small protons is also possible (Hernandez et al., 2000). The X-ray, infrared spectroscopy and elemental analysis confirmed the significant degree of dissolution in 0.05 M Fe sample. The micropore volume of 0.05 M Cu zeolite was also higher than the other zeolites. The acidity of the metal salt solution in which the cupper sorption was carried out (initial and final pH values were 4.36 and 4.28, respectively) was not high as that for the iron sorption. Therefore, the dissolution or dealumination cannot be the reason for the high micropore volume as also confirmed by the elemental analysis.

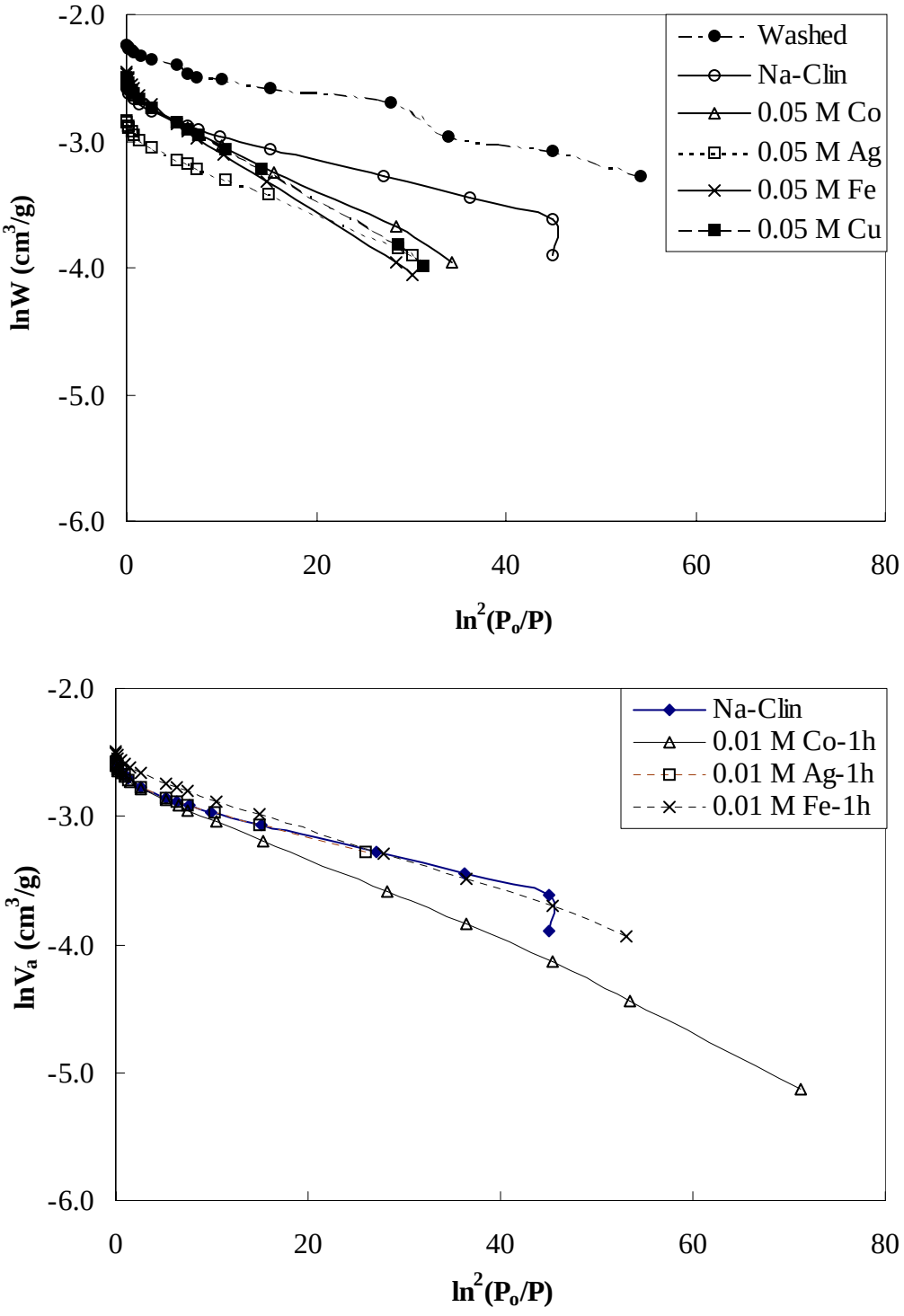

Figure 5.26. D-R plots for CO_2 adsorption.

Table 5.21. Dubinin-Radushkevich model parameters from CO_2 adsorption data.

Sample	βE_o	Limiting micropore volume, W_L (cm^3/g)
Washed	17.553	0.0937
Na-Clin	18.423	0.0626
0.05 M Co	13.097	0.0699
0.05 M Fe	11.584	0.0730
0.05 M Ag	14.497	0.0505
0.05 M Cu	12.220	0.0723
0.01 M Ag-1h	17.770	0.0634
0.01 M Co-1h	14.127	0.0668
0.01 M Fe-1h	16.161	0.0729

When the N_2 and CO_2 adsorption isotherms were compared, a sharp uptake in a very low relative pressure range was observed in the CO_2 adsorption isotherms, while the adsorbed amount increased gradually at the low relative pressures in the N_2 adsorption isotherm. At higher pressures, CO_2 isotherms reached a plateau upon saturation of adsorption sites, while N_2 isotherms continued to have substantial increase in uptakes. The experimental data show that the CO_2 adsorption saturation capacity of the zeolites is about the same that of nitrogen. For all cases CO_2 adsorption was higher than N_2 except for 0.05 M Fe sample. The higher adsorption capacity of 0.05 M Fe zeolite can be attributed to the adsorbate-adsorbent interactions and the steric effects. The strong interaction between 0.05 M Fe and N_2 was also reflected by the very high b value of the Langmuir model. The dissolution in 0.05 M Fe zeolite may have cause formation of larger pores in which N_2 molecules can penetrate without sterically limited. The gas adsorption rate, selectivity and capacity of zeolites depends on several factors; type, size, number and location of the charge-balancing cations, Si/Al ratio, size and shape of the pores, polarity and size of adsorbate molecules. Experimental conditions such as pressure and temperature also affect the adsorption capacity of zeolites.

The lower N_2 adsorption was probably due to steric factors, as a result, the micropores of the zeolites did not participate in the adsorption process. Considering that clinoptilolite adsorb molecules with kinetic diameter not exceeding 3.5 Å (Breck, 1974) and that the kinetic diameter of CO_2 molecule is 3.30 Å, it is obvious that CO_2

adsorption is not limited by the steric factor, i. e., the CO_2 molecules freely penetrate the entrance windows toward the micropores. N_2 molecules (kinetic diameter of N_2 is 3.64 Å) cannot penetrate freely into the micropores of the zeolites (Hernández-Huesca et al., 1999). At -196 ^oC N_2 molecules cannot diffuse freely into the micropores of clinoptilolite. In the case of CO_2 adsorption performed at 30 ^oC, the diffusion of adsorbate molecules in the micropores is enhanced (Hernández-Huesca et al., 1999; Rouquerol et al., 1999; Rodríguez-Reinoso and Molina-Sabio, 1998). Furthermore, CO_2 has high quadrupole moment so its adsorption isotherm is very sensitive to the presence of polar groups or ions on the surface of the solid. The micropore volumes determined from the CO_2 adsorption data were found to be higher than those calculated from the N_2 adsorption data, except for 0.05 M Fe zeolite.

Hernández-Huesca and coworkers proposed that the adsorption of CO_2 at temperatures close to room temperature could be used as a means that is much cheaper than the adsorption of N_2 at 77 K for the purpose of evaluating the microporous volume of natural zeolites. In addition, the adsorption of N_2 at 77 K is not applicable to ultramicroporous zeolites including clinoptilolite (Hernández-Huesca et al., 1999), since diffusion of N_2 into the channels of clinoptilolite is restricted, and diffusion is so slow at temperatures near the boiling point of N_2 that isotherm measurement is not practical (Ackley and Yang, 1991a,b). A drawback of CO_2 adsorption at ambient temperature is that in most commonly used equipments, which predominantly operate in the pressure range of vacuum to 1 bar, only a limited range of micropores can be measured, unless high-pressure CO_2 adsorption is used (Ravikovitch et al., 2000; Cazorla-Amorós et al., 1998).

The ClinRich-Kaolin, WGround-Kaolin and pure kaolin particles were also analyzed by the CO_2 adsorption at 30 ^oC. The isotherms are presented in Figure 5.27 and the textual properties were summarized in Table 5.22. The decrease in the BET surface area of Washed zeolite after pelletization can be explained by the blinding of the pores by binder. Average pore diameter changed significantly after grinding and pelletization of Washed zeolite. The micropore volumes of Washed and ClinRich-Kaolin samples calculated based on the D-R model were not different from each other, but after grinding Washed sample and forming into the pellet to obtain the WGround-Kaolin particles, the micropore volume decreased approximately by 25%. Kaolin did not adsorb CO_2 at 30 ^oC.

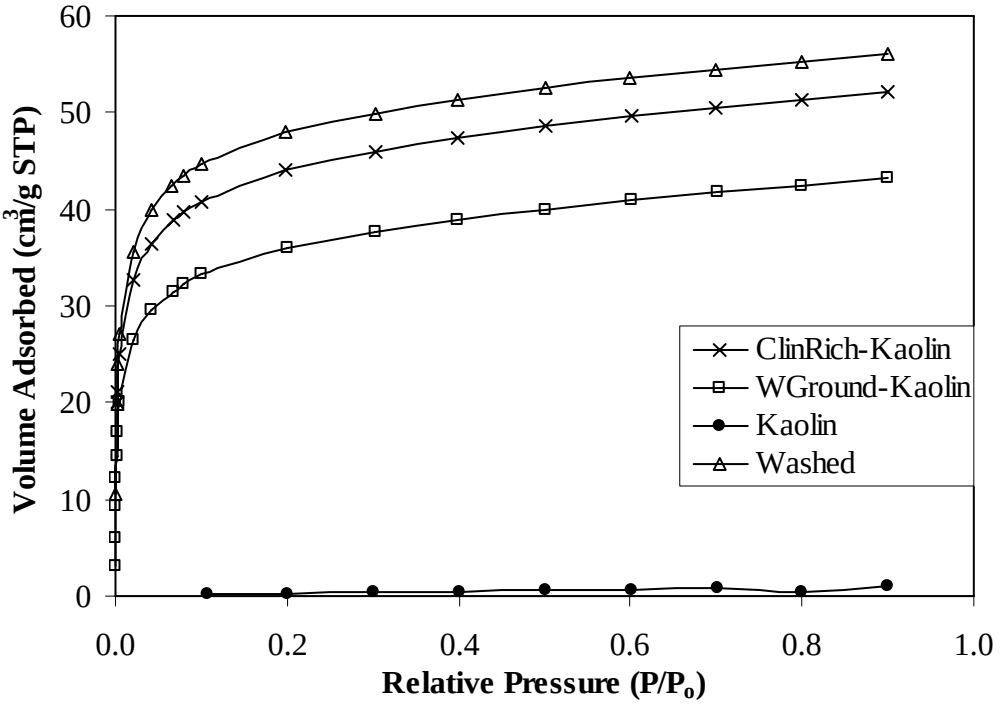

Figure 5.27. CO_2 adsorption isotherms of the ClinRich-Kaolin, WGround-Kaolin and pure kaolin (30 ^{o}C).

Table 5.22. Textural properties of the particles prepared by pelletization.

Textural property	Washed	ClinRich-Kaolin	WGround-Kaolin	Kaolin
Single Point BET Surface Area at P/P_o= 0.3 (m^2/g)	164.58	146.57	119.84	1.27
BET Surface Area (m^2/g)	164.66	146.52	119.90	1.49
Langmuir Surface Area	232.67	214.10	175.33	3.16
Single Point Total Pore Volume (cm^3/g)	0.0193	0.0366	0.0055	
Micropore Volume (t-plot) (cm^3/g)	0.0465	0.0413	0.0325	0.0004
Average Pore Diameter (4V/A by BET) (Å)	4.88	9.99	1.85	11.16
Maximum Pore Volume (Saito-Foley Model) (cm^3/g)	0.0817	0.0748	0.0609	-
Median Pore Diameter (Saito-Foley Model) (Å)	5.20	5.20	5.20	-
Micropore Surface Area D-R Model) (m^2/g)	280.16	270.32	211.66	-
Limiting Micropore Volume (D-R Model) (cm^3/g)	0.0937	0.0934	0.0710	-

Two types of porosity present in clinoptilolite: The primary porosity (microporosity) results from the crystalline structure of the zeolite. The secondary porosity is connected with the zeolite crystal size and other minerals in the rock as well as by structural features of the rock. The secondary porosity is presented usually by system of meso- and macropores (Tsitsishvili et al., 1992).

The mesopore size distributions of the zeolites were calculated from the desorption branch of the N_2 adsorption isotherm by the application of the pore size model developed by Barret, Joyner and Halenda (BJH) (Barret et al., 1951), which is based on the Kelvin equation and corrected for multilayer adsorption, for calculations of the PSD over the mesopore and part of the macropore range from the desorption branch and are shown in Figure 5.28. The desorption branch can provide more information about the degree of pore blocking than the adsorption branch.

All the zeolites exhibited bimodal mesopore size distribution at around 30 Å and 70 Å. The mesopore volume in the microporous solids is attributed to the pores between the crystals (intercrystalline pores). The iron sorbed samples showed a drastically high pore volumes around 40 Å which might be the indication of the increase of mesopore volumes due to removal of nonzeolitic phases considering the highly acidic conditions during the iron sorption. It was also seen that the size of the mesopores increased after iron sorption. As the iron content of the zeolite increased, the peaks in the PSD shifted to lower pore diameters, but still larger than the parent zeolite. The higher volume of mesopores in 0.05 M Fe and 0.01 M Fe-1h samples can be explained by the dissolution leading to formation of secondary (mesoporous) porosity.

The N_2 adsorption isotherms did not give meaningful data for the micropore size distribution. It is known from the literature that the use of N_2 cause problems, as the presence of a quadrupole moment in N_2 results in strong interactions with the heterogeneous surface of the zeolite framework. On the other hand, adsorption of N_2 is more favorable for mesoporosity measurements as its adsorption in micropores occurs at lower relative pressures (Storck et al., 1998; Venero and Chiou, 1988).

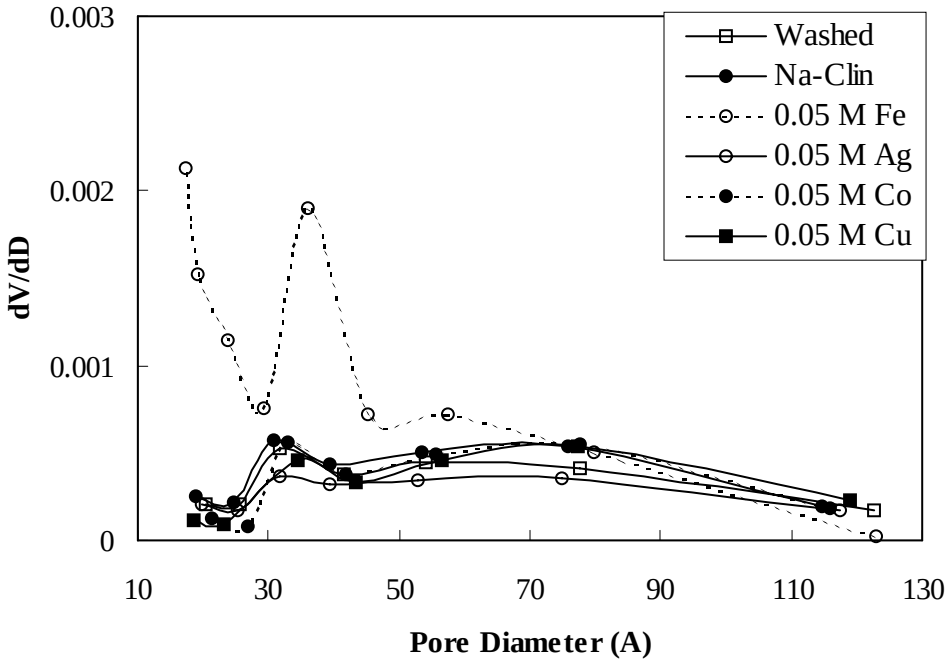

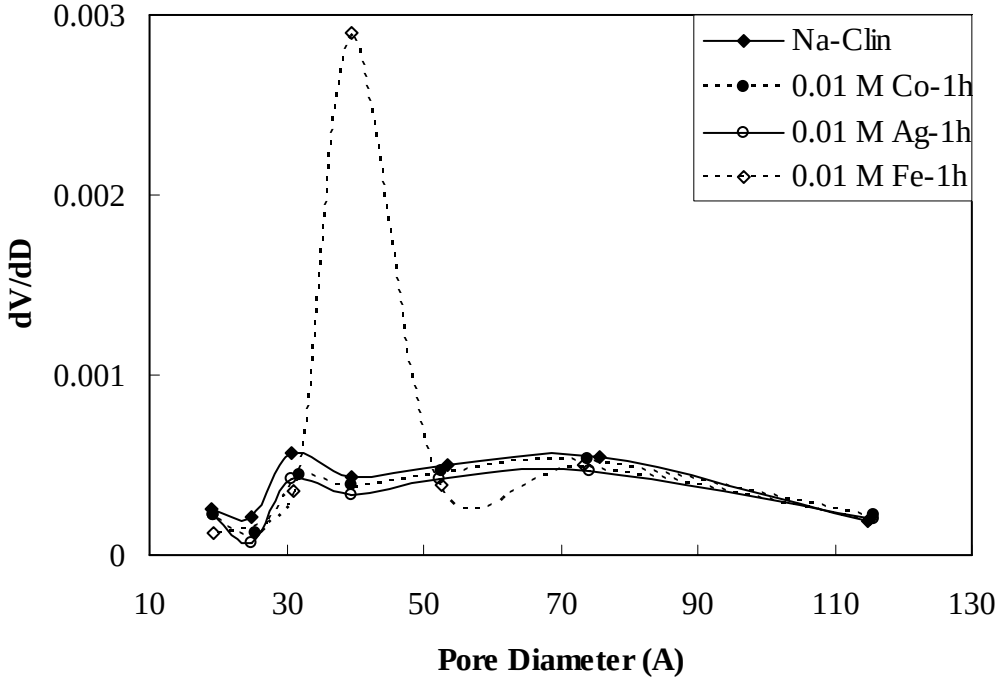

Figure 5.28. Mesopore size distributions of the zeolites.

Due to the presence of exchangeable cations in the channels of the clinoptilolite, diffusion of the N_2 molecules is prevented. Therefore contribution of narrow pores to PSD is insignificant (Korkuna et al., 2006) Moreover, high quadrupole moment of N_2 molecule can result in enhanced interaction with the heterogeneous surface of the zeolite framework, leading to a more difficult discrimination between zeolites of different pore sizes (Storck et al., 1998; Venero and Chiou, 1988). Hence the micropore size distributions of the zeolites were determined using CO_2 adsorption data at 30 ^{o}C. The conventional the Saito–Foley (S-F) model for cylindrical pore geometry (Saito and Foley, 1991) was applied for micropore size calculations and the pore size distributions were shown in Figure 5.29. For Washed and Na-Clin samples, the majority of the channels have a dimension of 7.2×4.4 Å (Ackley and Yang, 1991b) which agrees with the PSD shown (7.8×5.6 Å). The pore size distributions in the micropore region indicated that Washed, Na-Clin, 0.01 M Co-1h and 0.01 M Fe-1h samples showed trimodal while the others showed bimodal pore size distribution. No pore size distribution data were available for the metal sorbed zeolites for pore diameter less than about 5.7 Å, except for 0.01 M Co-1h and 0.01 M Fe-1h samples.

Washed, Na-Clin, 0.01 M Co-1h and 0.01 M Fe-1h samples have an accessible microporous structure to the adsorptive CO_2 molecules and for these zeolite samples, contribution of micropores to the total adsorption is important. The metal sorption changed the pore size distribution mainly in the micropore range. This implied that broader pores were less sensitive to the metal sorption, except for the iron sorption. The S-F model relates the free energy of adsorption to the interaction energy of the adsorbate molecule in the pore using the Lennard-Jones type of interactions. However, the electrostatic forces between the sorbate and sorbent are neglected in the S-F model. In the case of polar adsorbate-zeolite system, the polar molecule has strong electrostatic interactions with the oxide ions of the zeolite framework as well as the metal ions present in the zeolite framework (Rege et al., 2000).

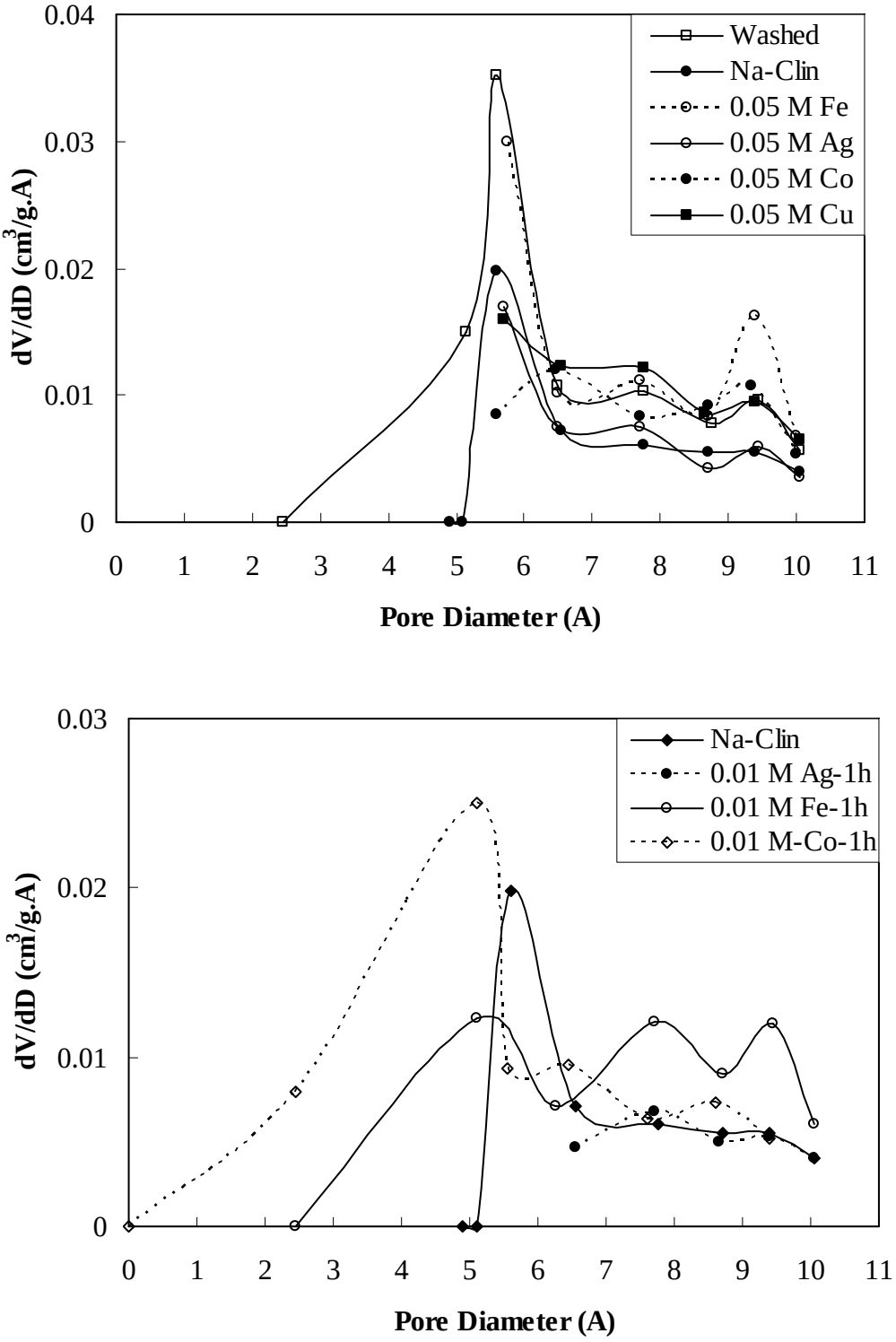

Figure 5.29. Pore size distributions of the zeolites in the micropore range (Saito-Foley model).

5.2.8. Thermogravimetric Analysis (TGA)

The thermal gravimetric (TG) curves of the zeolites are shown in Figure 5.30. The continuous and uninterrupted thermogravimetric curves showed that the dehydration is reversible and the framework did not destroyed by heating (Gottardi and Galli, 1985).

Water is adsorbed into zeolites by filling oxygen-lined channels and hydrating the cations present in the channels. Thus, equilibrium dehydration and hydration behavior of zeolites depends on external conditions (temperature, pressure) as well as on the specific topology of the aluminosilicate framework. At constant temperature, pressure, and Si/Al, the amount of water in clinoptilolite is a function of cation composition (Wilkin and Barnes, 1999). The water in clinoptilolite was classified in three groups as externally adsorbed water, loosely bound water and tightly bound water (Knowlton and White, 1981). Thus, the dehydration occurs in stepwise manner, mainly at three steps since water molecules contained in clinoptilolite are held with a range of energies dependent on the cation-water bond distances and on the exchangeable cation site (Bish, 1984).

In order to distinguish these steps, tangents lines were drawn to the linear portions of TG curves and vertical lines were dropped from their intersection points, so the boundaries between the linear portions were determined (Knowlton and White, 1981). The low temperature inflection point was observed at approximately 85 ^{o}C. The weight loss up to this temperature is due to desorption of externally adsorbed water. Other inflection point was detected at about 285 ^{o}C and assigned to desorption of loosely bound water. Above 285 ^{o}C, slow desorption of tightly bound water takes place. For the zeolites of interest in this study, the integrated and partial weight losses determined are given in Table 5.23.

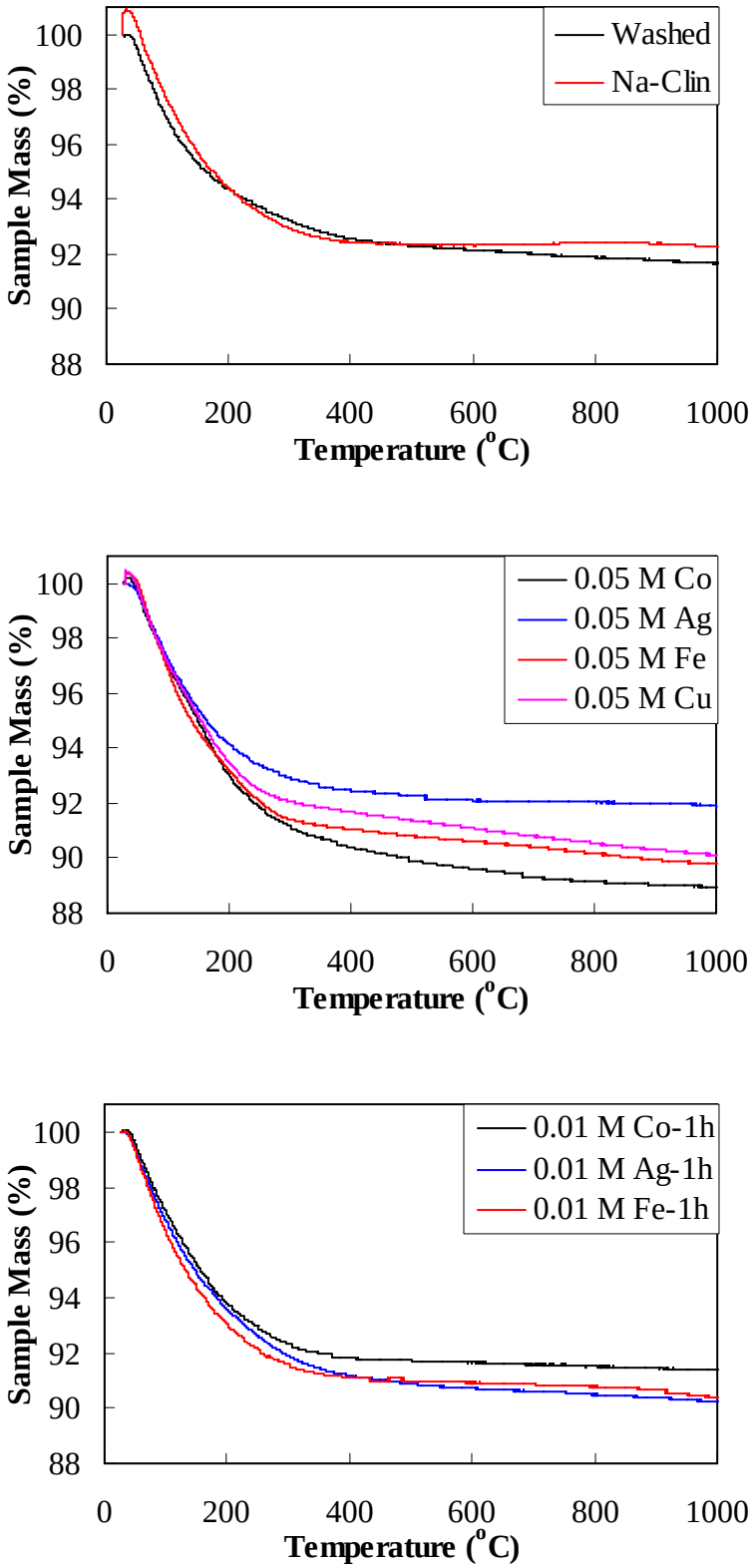

Figure 5.30. Thermal gravimetric curves of the zeolites.

Table 5.23. Partial and integrated weight losses for the zeolites.

Samples	Weight loss (%)			Integrated weight loss (%)
	25-85 °C	85-285 °C	285-1000 °C	
Washed	2.43	6.64	1.70	8.33
Na-Clin	1.69	6.91	0.83	7.73
0.05 M Co	2.25	8.67	2.42	11.08
0.05 M Ag	2.06	6.97	1.20	8.17
0.05 M Fe	2.26	8.47	1.72	10.18
0.05 M Cu	2.20	7.84	2.04	9.88
0.01 M Co-1h	2.20	7.51	1.09	8.60
0.01 M Ag-1h	2.54	7.92	1.86	9.77
0.01 M Fe-1h	2.81	8.33	1.28	9.61

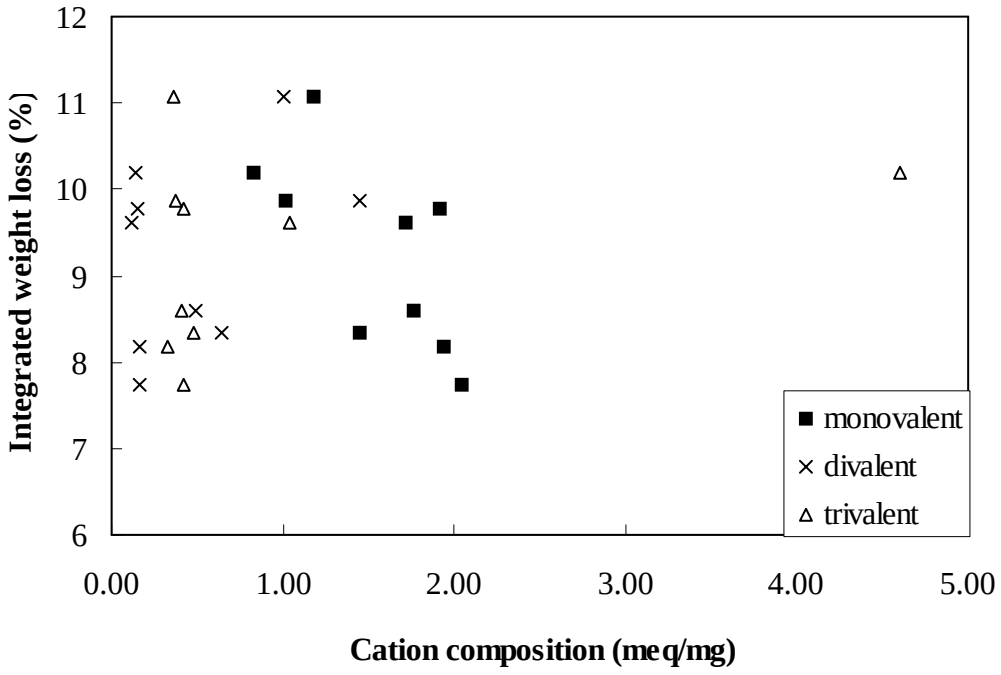

Figure 5.31. Relationship between the integrated weight loss and the cation content of the zeolites.

The integrated weight loss and weight loss above 285 ^{o}C exhibited poor correlation with the monovalent (K+Na+Ag) cation content of the zeolite as shown in Figure 5.31. The weight loss between 25-85 ^{o}C showed no correlation with the monovalent, divalent (Ca+Mg+Co+Cu) and trivalent (Fe) cation content of the zeolite (the graph was not shown).

The D-TG curves were obtained by differentiating the TGA curves with respect to time and shown in Figure 5.32. The minimum was observed at different temperatures for different zeolites. In the D-TG curves of 0.05 M Co and 0.05 M Fe zeolites, also a shoulder peak was detected at 103 ^{o}C and 45 ^{o}C, respectively. From the course of the D-TG curve, the temperatures of minima corresponding to the maximum rate of weight loss and the rate of weight losses determined directly from the peak heights are given in Table 5.24. The iron-sorbed zeolites gave the highest rate of weight losses.

Table 5.24. Temperatures corresponding to maximum rate of weight loss and the rate of weight losses for the zeolites.

Samples	D-TG peak minima (^{o}C)	D-TG peak height (rate of weight loss) (mg/min)
Washed	100	-0.380
Na-Clin	116	-0.328
0.05 M Co	103, 174	-0.386
0.05 M Ag	124	-0.372
0.05 M Fe	45, 105	-0.426
0.05 M Cu	125	-0.367
0.01 M Co-1h	136	-0.360
0.01 M Ag-1h	120	-0.393
0.01 M Fe-1h	120	-0.436

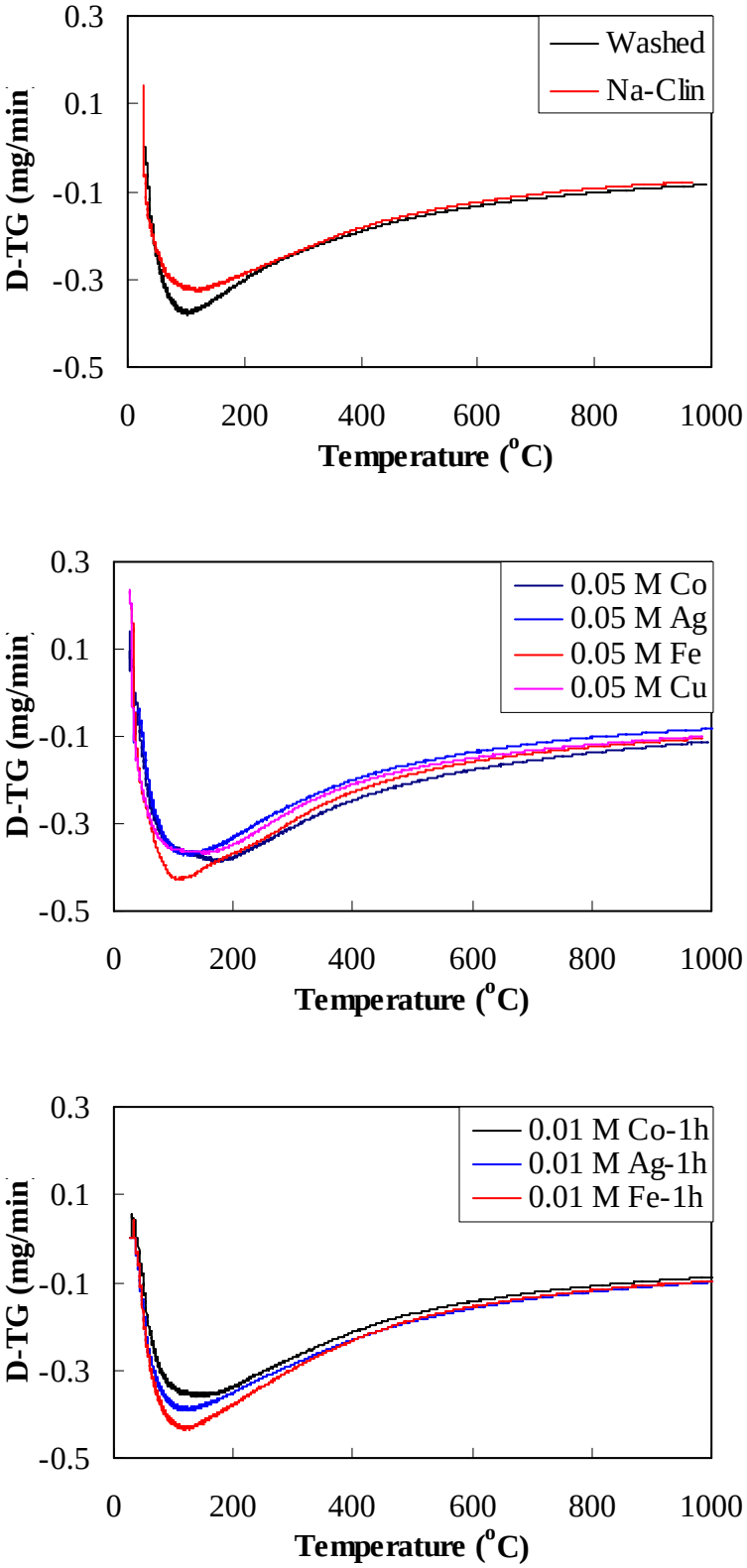

Figure 5.32. Derivative thermal gravimetric curves of the zeolites.

5.2.9. Infrared Spectroscopy

Infrared spectroscopy can be used to characterize various aspects of zeolites, including the vibrations of the framework, the nature of OH groups in the structure and how introducing different cations can affect the acid site strength, changes due to adsorption of molecules and effect of temperature and hydration. Infrared spectra can be very useful in obtaining information about the structure, channel size and the cation substitution in the tetrahedral sites of zeolite minerals. Furthermore inspection of the structure-sensitive bands provides information regarding framework properties, including Si/Al ratios (Karge, 1998).

The transmittance infrared spectra of the zeolites are shown in Figure 5.33 and the assignment of vibration bands in the spectra are summarized in Table 5.25.

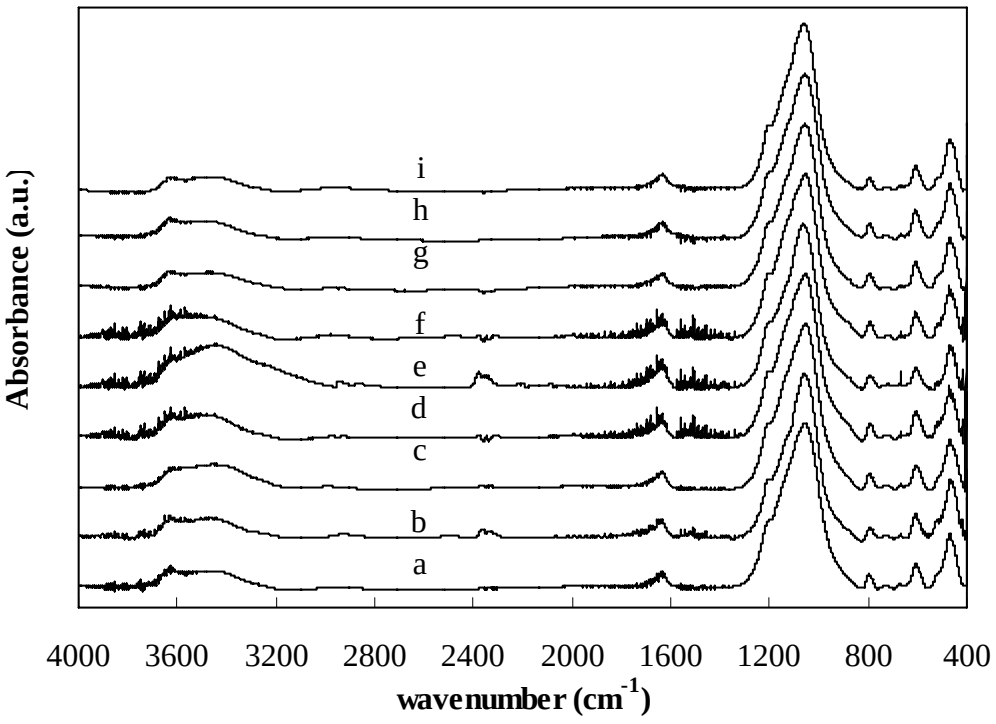

Figure 5.33. Transmittance spectra of the zeolites: a, Washed; b, Na-Clin; c, 0.05 M Co; d, 0.05 M Ag; e, 0.05 M Fe; f, 0.05 M Cu; g, 0.01 M Co-1h; h, 0.01 M Ag-1h, and i, 0.01 M Fe-1h.

Table 5.25. Assignment of vibration bands for the natural zeolitic mineral. (Source: Breck, 1974)

Vibration modes	Frequency (cm^{-1})	Intensity
Pore opening vibrations (motion of the tetrahedra rings forming the pore openings) (300-420 cm^{-1})*	418 .6	
Internal tetrahedra bending (T-O bending) (420-500 cm^{-1})	472.6	Strong
Double ring (500-650 cm^{-1}) *	521.8	Shoulder
External tetrahedra double ring	609.5	Medium
Internal tetrahedra symmetrical stretching (650-820 cm^{-1})*	727.2	Very weak
	669.3	
External tetrahedra linkage symmetric stretching (750 – 820 cm^{-1})*	796.6	Weak
External tetrahedra linkage asymmetric stretching (1050-1150 cm^{-1})*	1058	Strong
Internal tetrahedra asymmetric stretching	1204.6	Shoulder
O-H bending	1635.4	Wide
* structure sensitive vibrations		

The bands in the 300-420 cm^{-1} region are assigned to pore opening vibrations (Breck, 1974). No band was observed it the spectrum of Washed and 0.01 M samples. After the NaCl treatment, two bands appeared in this region at 412.8 and 418.6 cm^{-1}. The former disappeared in the spectrum of the metal-sorbed zeolites. The latter disappeared in the spectra of 0.05 M Co sample. No change either in the intensity or in the position of this band was observed for the other zeolites.

The position of the second strongest band in the spectrum observed at 472.6 cm^{-1} was not affected either by NaCl treatment or metal sorption, but its intensity decreased depending on the metal present. The position of this band strongly depends on the T-O-T angle and therefore is used to characterize the Al content of the lattice (Jentys and Lencher, 2001). After NaCl treatment, the intensity of this band slightly increased and after metal sorption decreased depending on the metal. The decrease was more remarkable for the 0.05 M samples, especially for 0.05 M Fe zeolite. The comparison of the intensity of this band with those pseudolattice bands (500–700 cm^{-1}) can be used to determine the degree of amorphization in zeolites (Mozgawa et al., 1999).

The bands in the 500-700 cm^{-1} region are due to pseudo-lattice vibrations of structural units. In this region, Washed zeolite exhibited three bands at 516.9 cm^{-1}, 669.3 cm^{-1} and at 609.5 cm^{-1}. The band at 516.9 cm^{-1} is related to pore opening vibrations. The intensity of this band in the spectrum of 0.05 M Fe sample drastically

declined. No changes were observed in the frequencies of the bands in this region upon the metal sorption, but in their intensities. It was reported in the literature for the Fe-over exchanged clinoptilolite that these vibrations shifted to lower wavenumber due to the presence of iron species in the internal channels and on the external surface of the zeolite (Doula, 2007). The changes in the intensities and positions of these vibrations upon metal sorption were attributed to the difficulty in these bonds to vibrate (Mozgawa, 2000; Castaldi et al., 2005).

The band at 609.5 cm^{-1} is due to stretching of the internal tetrahedral bonds and typical for ordered crystal structure (Mozgawa et al., 2002). This band is detected in the 600-610 cm^{-1} range for clinoptilolite and its position is related to the clinoptilolite content of the mineral. The degree of changes in the intensity of this band is related to the content, radius and charge of the cations causing ring deformations (Castaldi et al., 2005). No noticeable change in the intensity of this band upon either the NaCl treatment or the metal sorption was observed in the present study.

The intensity of the band at 669.3 cm^{-1} increased for all zeolites, except for 0.01 M iron- and cobalt-sorbed zeolites. For these samples the intensity decreased. The rise in intensity for 0.05 M Fe zeolite was significant. This band is due to ring vibrations and sensitive to changes in the type and amount of non-tetrahedral cations. It is connected with symmetrical stretching vibrations of Si–O bond existing in the 6-membered rings of the zeolite and sensitive to changes in the type and the amount of non-tetrahedral cations (Flanigen et al. 1971). Mozgawa and Bajda noticed systematic increase in the intensities of the bands in the 650-710 cm^{-1} range, specifically in those at 673 and 693 cm^{-1} with increasing cadmium, lead and nickel content of the clinoptilolite and attributed these changes to degree of ring deformation depending on the mass and radius of the cations (Mozgawa and Bajda, 2005; Mozgawa, 2000).

The bands observed at 796.6 and 727.2 cm^{-1} belong to the Si–O–Si and Al–O–Si bridges, respectively. The band at 796.6 cm^{-1} is assigned to external tetrahedral symmetric stretching vibration (Breck, 1974). The sorption of metal cations did not affect the frequency of this band, but caused an increase in the intensity. The order of intensity increase was found to be 0.05 M Cu>0.05 M Co~0.01 M Fe-1h~0.01 M Co-1h~0.01 M Ag-1h>0.05 M Fe>Washed>Na-Clin>0.05 M Ag.

The bands in the 400–1200 cm^{-1} range are assigned to the internal stretching vibrations of Si–O(Si) and Si–O(Al) in tetrahedra. In the spectrum of Washed zeolite, the strongest T–O stretching vibration appeared at 1058.0 cm^{-1} with a shoulder at

1204.6 cm^{-1}. The position of this band depends on the Si/Al ratio and is considered to be determinative for the aluminium content in the crystalline framework. Substitution of Al^{3+} for Si^{4+} decreases T–O–T angle, and the resulting frequency is lower, due to the weaker character and increased length of the Al–O bond. The force constant for the mode in an Al–O–Si bond is lower than the corresponding mode in a Si–O–Si linkage. The treatment of Na-Clin with different metal salts did not cause significant dealumination as indicated by the unchanged position of the main band at 1058.0 cm^{-1}, except for the iron-sorbed samples. The dealumination caused this band to shift to 1066 cm^{-1} and 1062 cm^{-1} for 0.05 M Fe and 0.01 M Fe-1h samples, respectively (Mozgawa, 2000; Mozgawa et al., 1999). The elemental analyses confirmed the dealumination in these samples.

The ratio of the intensity of the 1058 cm^{-1} band to that of the 472.6 cm^{-1} band was related to the nature and position of the cations in the zeolite structure (Rivera-Garza et al., 2000). In our case, the ratio for 0.05 M Fe was found to be significantly higher than that for Na-Clin.

The isolated band at 1635.4 cm^{-1} is due to bending vibration of sorbed water (H–O–H bending). For fully activated zeolite, this band disappears (Breck, 1974). In the OH stretching region (3000–3700 cm^{-1}), the spectrum of Washed sample mainly presented two bands with maxima at 3450.8 cm^{-1} and at 3630.2 cm^{-1}, and a shoulder at 3259.8 cm^{-1}. The band at 3630.2 cm^{-1} is due to isolated OH stretching and attributed to interaction between the water hydroxyl and the cations present. The other band at 3450.8 cm^{-1} is attributed to the hydrogen bonding of the water molecule to surface oxygen. Noticeable changes were detected in both positions and intensities of the bands in this region depending upon the radius, mass and charge of the cation (Tsitsishvili et al., 1992). It can be inferred from those results that since the cations introduced into the zeolite structure are coordinated with water molecules, the cations may modify the water adsorption capacity. The content and location of water molecules depends on many factors, such as the size and shape of the cavities and channels, the number and the nature of the cations in the structure (charge, ionic radius, hydration enthalpy) and the environmental situation of the zeolite (i.e. the relative humidity and temperature) (Breck, 1974). For 0.05 M Fe sample, the positions of the bands did not change but the intensities remarkably increased. These increases in the intensities can be attributed to the addition of hydrogen atoms on the ≡Al–OH–Si≡ and ≡Al (or Si)–OH groups during ion exchange and surface complexation reactions (Filippidis et al., 1996; Oelkers and

Schott, 1995). It was reported in the literature that the intensity of the bands at 3470 cm^{-1}, 3402 cm^{-1} and 3327 cm^{-1} decreased after contacting the clinoptilolite with iron salt in a strongly basic solution. The decreases were explained by the proton detachment from the zeolite due to reaction with the OH^- in the solutions (Doula, 2007). The 3450.8 cm^{-1} band became more pronounced which caused the band at 3630.2 cm^{-1} to become indistinguishable. On the other hand, the other iron-sorbed sample was obtained under the similarly acidic conditions, no significant changes were observed either in the position or intensity of the bands. Therefore, the changes were not only dependent on the acidity of the solution but also to other parameters including the zeolite/solution volume, treatment period and metal concentration. Furthermore, considering the strongly acidic conditions under which the iron sorption reactions were performed in this study, the neutral and negative surface hydroxyl groups are protonated according to the reactions in Equations (5.7) and (5.8). It is known from the metal speciation model that under these conditions, there exist positively charged iron species in the solution which may exchange with the protons in the protonated surface groups. The decrease of the solution pH during the iron sorption confirmed the release of the protons from the zeolite surface. As a result, monodendate and bidendate inner sphere complexes might be formed (Equation 5.10). This kind of complexation leads to stable surface groups due to the formation of covalent bonds.

The spectra for the NO-adsorbed zeolites are presented in Figure 5.34. A sharp band at 1384.9 cm^{-1} was observed in all spectra which did not appear in the spectra of the powders before NO loading. This band is close to the band at 1400 cm^{-1} which is assigned to NO_3^- species induced upon adsorption of NO on different zeolites (Chao and Lunsford, 1971).

No relationship between the intensity of this band and the amount of irreversibly adsorbed amount of NO could be found. This band either lost intensity or disappeared in the spectra of the NO-loaded zeolites after heated to 400 ^oC for 180 minutes (Figure 5.35) and after the NO-loaded zeolites were contacted with water as shown in Figure 5.36.

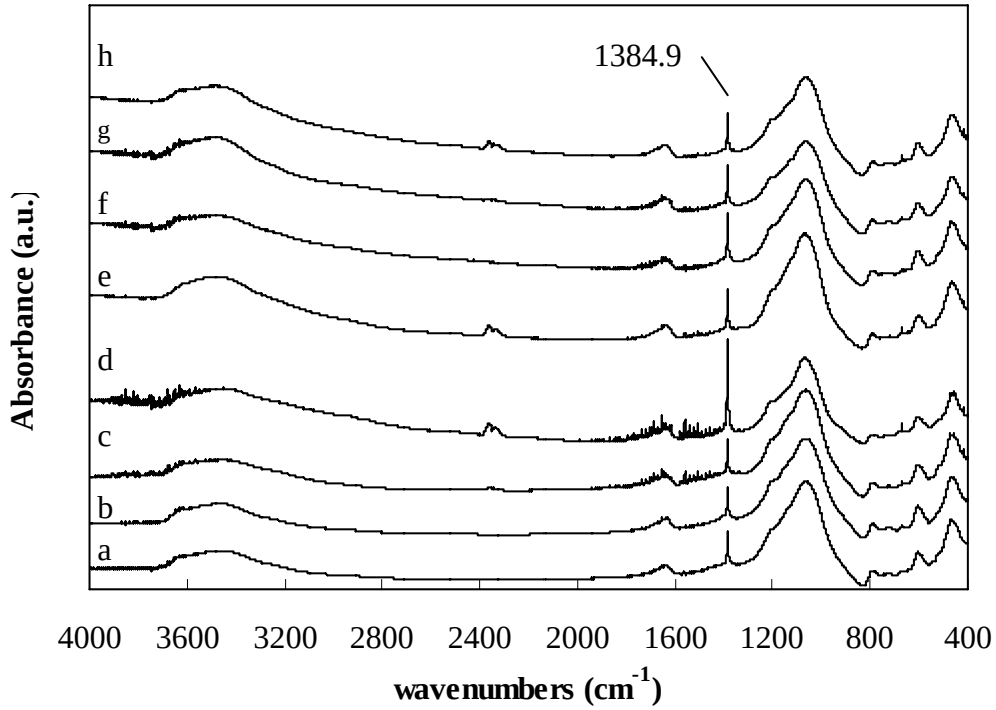

Figure 5.34. Transmittance spectra of the zeolites after NO adsorption and helium purging: a, Washed-NO; b, 0.05 M Ag-NO; c, 0.05 M Co-NO; d, 0.05 M Fe-NO; e, 0.05 M Cu-NO; f, 0.01 M Co-1h-NO; g, 0.01 M Ag-1h-NO; h, 0.01 M Fe-1h-NO.

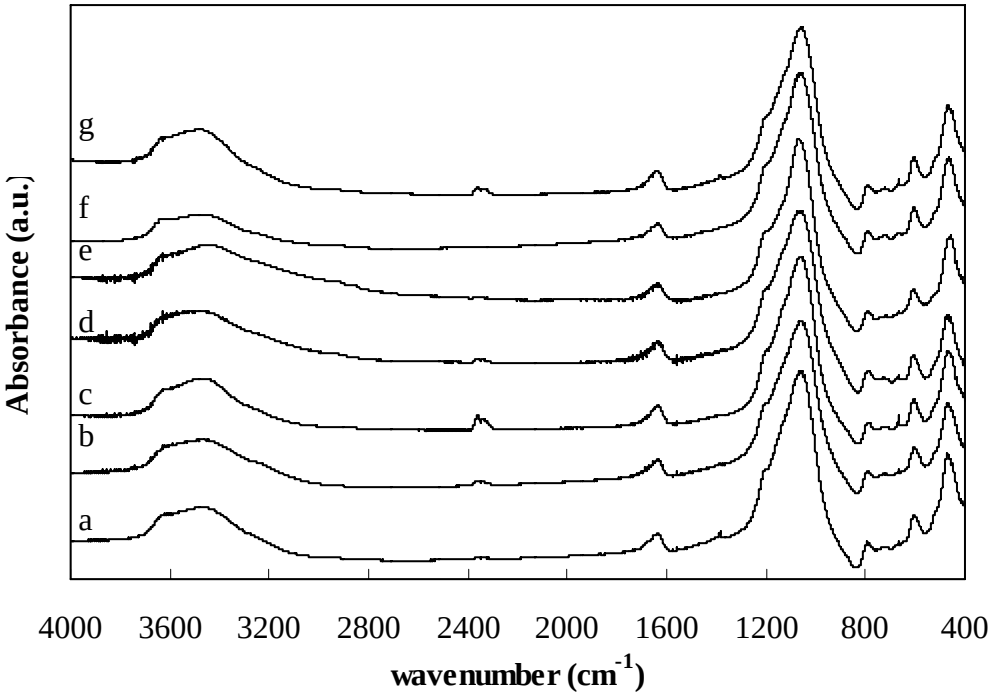

Figure 5.35. Transmittance spectra of the zeolites after thermal treatment successive to NO adsorption: a, Washed-NO-Des; b, 0.05 M Co-NO-Des; c, 0.05 M Ag-NO-Des; d, 0.05 M Cu-NO-Des; e, 0.05 M Fe-NO-Des; f, 0.01 M Fe-1h-NO-Des; g, 0.01 M Ag-1h-NO-Des.

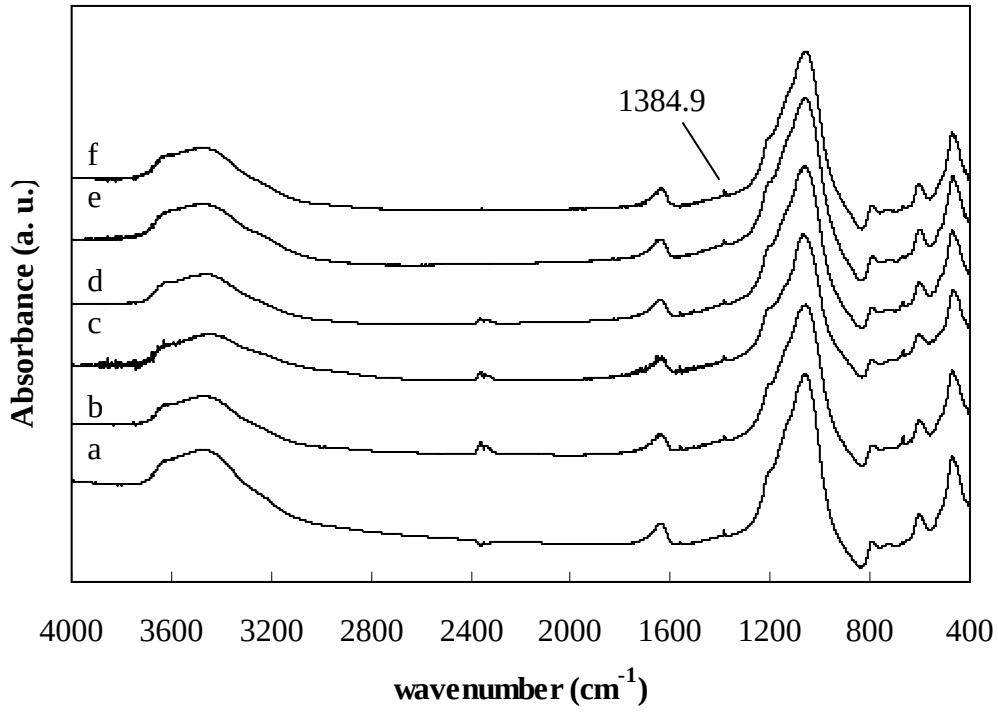

Figure 5.36. Transmittance spectra of the NO-loaded zeolites after contacted with water at 37 ^{o}C: a, Washed-NO-Rel; b, 0.05 M Ag-NO-Rel; c, 0.05 M Fe-NO-Rel; d, 0.05 M Cu-NO-Rel; e, 0.05 M Co-NO-Rel; f, 0.01 M Ag-1h-NO-Rel.

5.3. NO Adsorption-Desorption-Temperature Programmed Desorption

Helium was used as carrier gas in the NO adsorption, desorption and temperature-programmed desorption (TPD) experiments, so its adsorption by the column material affects the reliability of the data acquired. Thus, before the NO adsorption studies, the empty column was purged with constant helium flow of 20 ml/min at 30 ^{o}C for 360 minutes, then the column was heated to 400 ^{o}C at a heating rate of 1 ^{o}C/min where it was kept for 180 minutes in order to provide information about the hydrodynamics of the column. The profile obtained is shown in Figure 5.37. The level of the detector signal was significantly lower than that recorded during the packed column adsorption runs designating that there was no desorption from the column material, and from the connections between the inlet and column and also between the

column and the detector. Therefore, the data collected from the NO adsorption-desorption-TPD did not require correction for this factor.

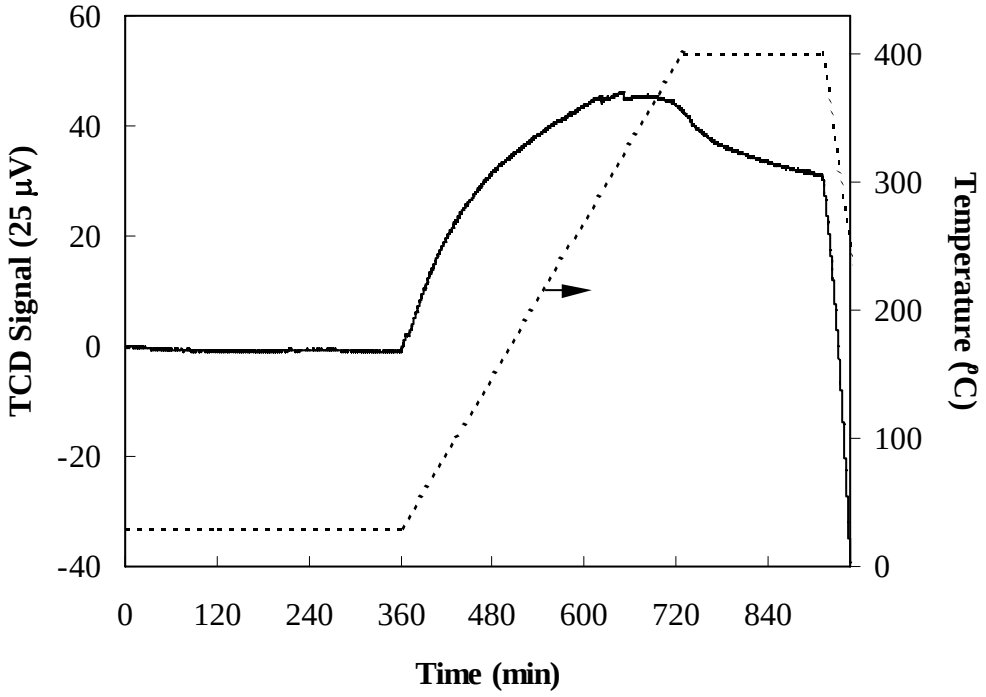

Figure 5.37. TCD signal change at the outlet of the empty column under helium flow and the temperature program.

In order to check whether the carrier gas is adsorbed by the zeolite under the experimental conditions of concern, the helium was passed through the column packed with Washed zeolite. For this run nitrogen was used as the carrier gas. Washed zeolite particles with diameter in the 75-150 μm range were packed into the column and activated under nitrogen flow under the same conditions as in the case when helium was used as carrier gas. After activation, the flow was switched from nitrogen to helium. The helium flow of 20 ml/min was passed through the column at 30 ^{o}C and when the signal leveled off at a constant value, the flow was switched to nitrogen again until the signal turned back to the baseline. Successively NO was started to pass through the column using helium as carrier gas. From the detector signal profile shown in Figure

5.38 no difference was noticed in the NO breakthrough capacity of the zeolite after and before the helium adsorption indicating that Washed zeolite did not adsorb helium.

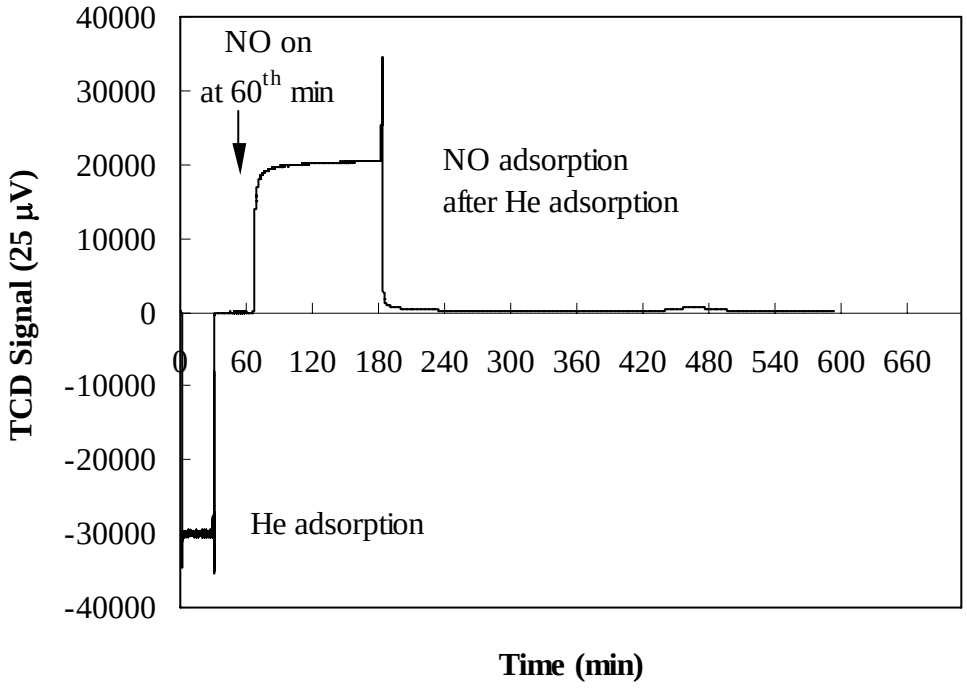

Figure 5.38. Breakthrough curves for the helium adsorption and the subsequent NO adsorption on Washed zeolite.

Washed zeolite was subjected to the temperature and flow program under the helium flow after the activation in order to confirm that there is no any species desorbed from the zeolite other than those associated with the NO adsorption and all the preadsorbed material was desorbed during the activation process. The profile is presented in Figure 5.39 depicted that the detector signal was at negligible level when compared to the signals detected during the adsorption-desorption-TPD runs and the activation process applied was effective in removing the preadsorbed material from the surface of the zeolite.

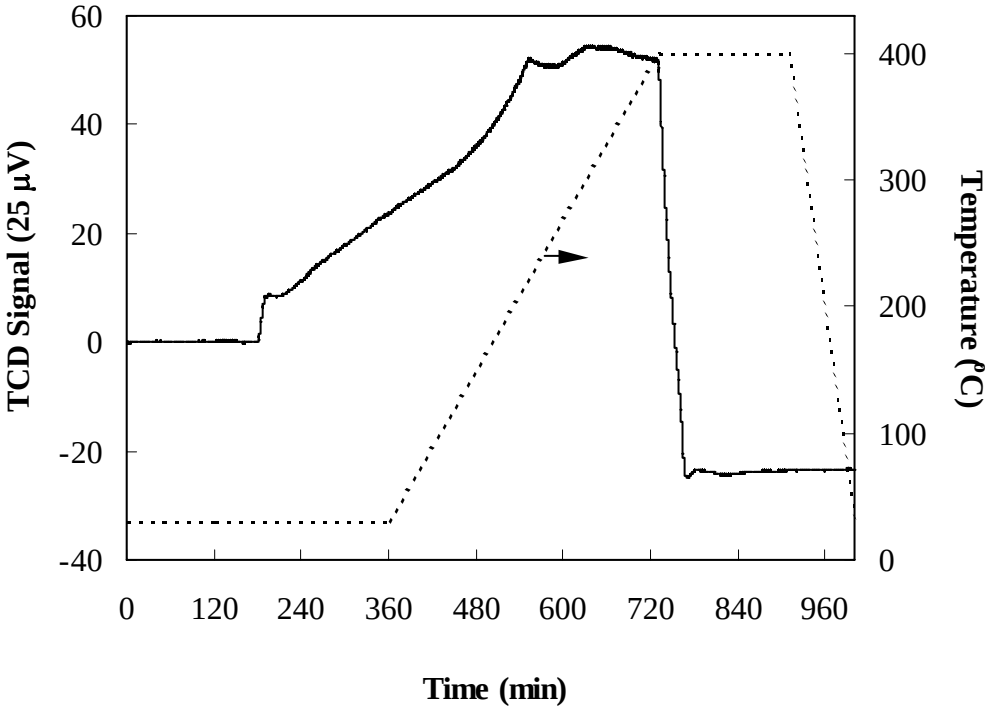

Figure 5.39. Breakthrough curve obtained for Washed zeolite under helium flow and the temperature program.

Kärger and Ruthven stated the importance of determination of the axial dispersion directly under conditions as close as possible to the conditions of the experimental measurements (Kärger and Ruthven 1992). For this purpose, the breakthrough curve for the column packed with nonporous glass particles of the identical size with the zeolites was obtained and illustrated in Figure 5.40. The breakthrough curve for the column of glass particles overlapped with that for the empty column. Comparison of the breakthrough curves obtained indicated that the delay of the response was due to adsorption, so that the axial dispersion was accepted negligible under the experimental conditions of concern in this thesis. On the other hand, this method of determination of axial dispersion has disadvantages due to possible differences in packing of the two columns (Kärger and Ruthven 1992). Furthermore, some contribution to axial dispersion may arise from the intraparticle diffusion in the porous particles as previously mentioned (Wakao, 1976). The column of the glass beads approached the equilibrium much faster as compared to the

column of the zeolite particles, but could not attain within the adsorption time of 120 minutes. The nonattainment of the equilibrium within the practical time period of 120 minutes was also the case for all the breakthrough curves obtained in this study. Therefore, the adsorption capacities of the adsorbents of interest in this study were determined from the breakthrough curves for the adsorption period of 120 minutes for practical purposes. This slow approach to equilibrium might be attributed to small intracrystalline diffusivities (Kärger and Ruthven 1992).

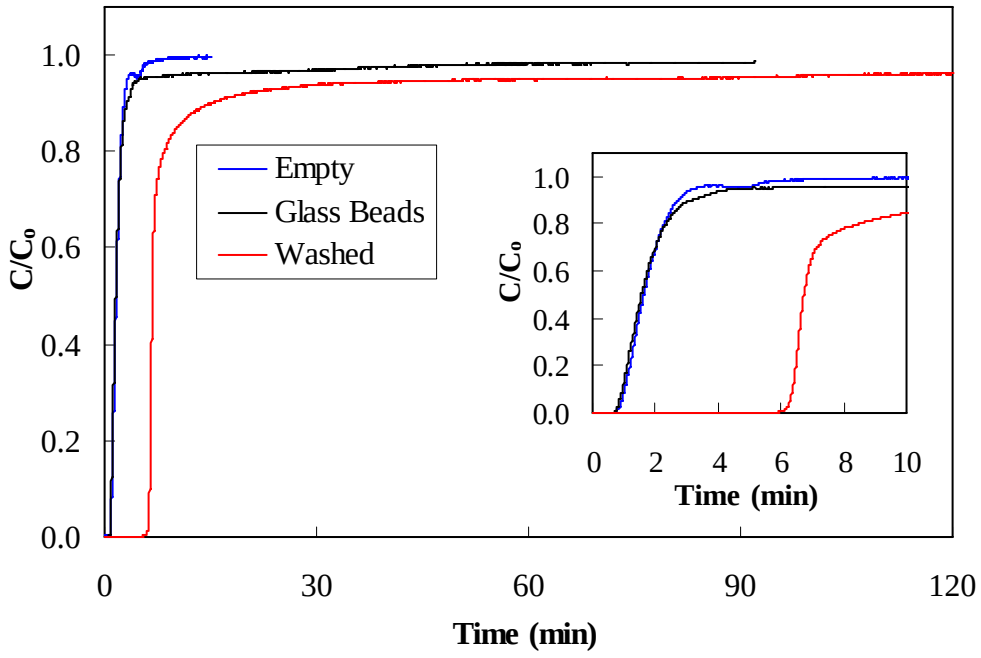

Figure 5.40. NO adsorption breakthrough curves for empty and packed columns of the nonporous glass particles and Washed zeolite particles (75-150 μm).

The irreversibility of the NO adsorption in Washed sample was examined through successive adsorption of NO on the zeolite. Between the successive adsorption runs, no thermal treatment was applied. The adsorption profiles obtained are presented in Figure 5.41. One cycle included the adsorption of NO adsorption at 30 ^{o}C under 20 ml/min NO flow for 120 minutes and subsequent purging of the column with helium at the same

temperature and flow rate for 240 minutes. The breakthrough time and the time required to saturate the bed declined remarkably for the 2nd cycle. The equilibrium adsorption capacity of Washed zeolite in the 2nd adsorption cycle was found to be 28 % of that in the 1st cycle. This indicated the formation of the species on the zeolite surface during the 1st adsorption cycle which could not have been removed by the helium-purging step applied. These species might prevent further adsorption of the NO molecules during the 2nd cycle. It is also probable that these species cause increase in mass transfer resistance leading to loss in the adsorption capacity (Misk et al., 2000).

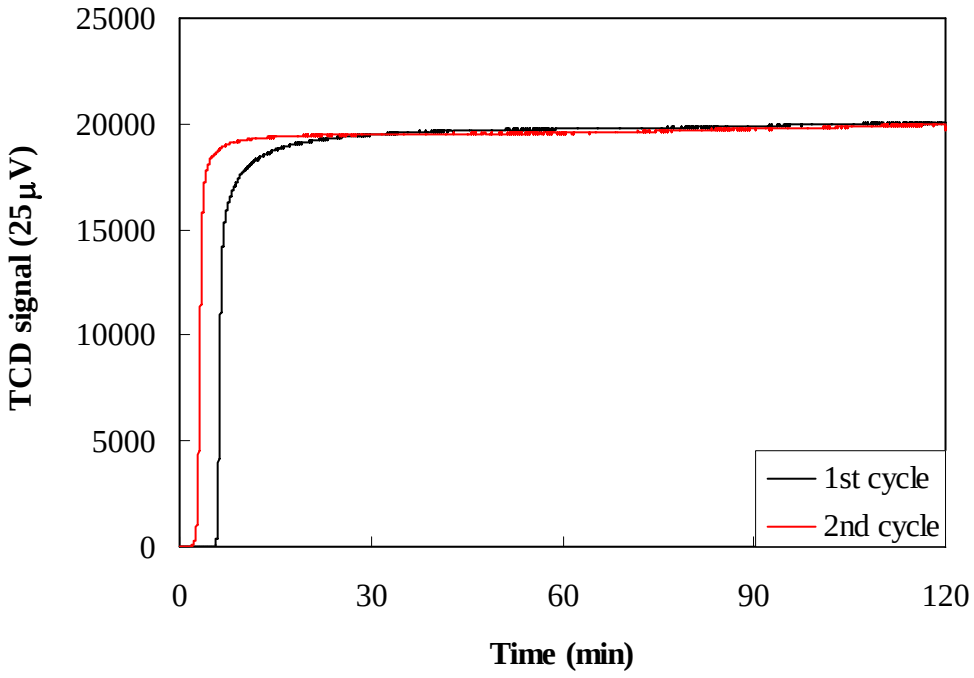

Figure 5.41. Breakthrough curves for the successive adsorption of NO on Washed zeolite.

After the 2nd cycle, the zeolite was heated to 400 °C at a rate of 1 °C/min under helium flow and the TPD profile obtained was compared with that obtained after the 1st cycle in Figure 5.42. The changes in the peak maxima and desorption temperatures were observed in these profiles. Desorption of the first peak was retarded after the 2nd cycle. The

desorption temperature of 235 ^{o}C of the second peak decreased to 210 ^{o}C after the 2nd cycle. A new shoulder peak appeared at 309 ^{o}C after the 2nd cycle implied the formation of new species on the zeolite during the 2nd cycle. The shoulder peak at 357 ^{o}C disappeared in the profile after the 2nd cycle. The intensity of the first peak was decreased, while that of the second peak was increased and both peaks became broader after the 2nd cycle.

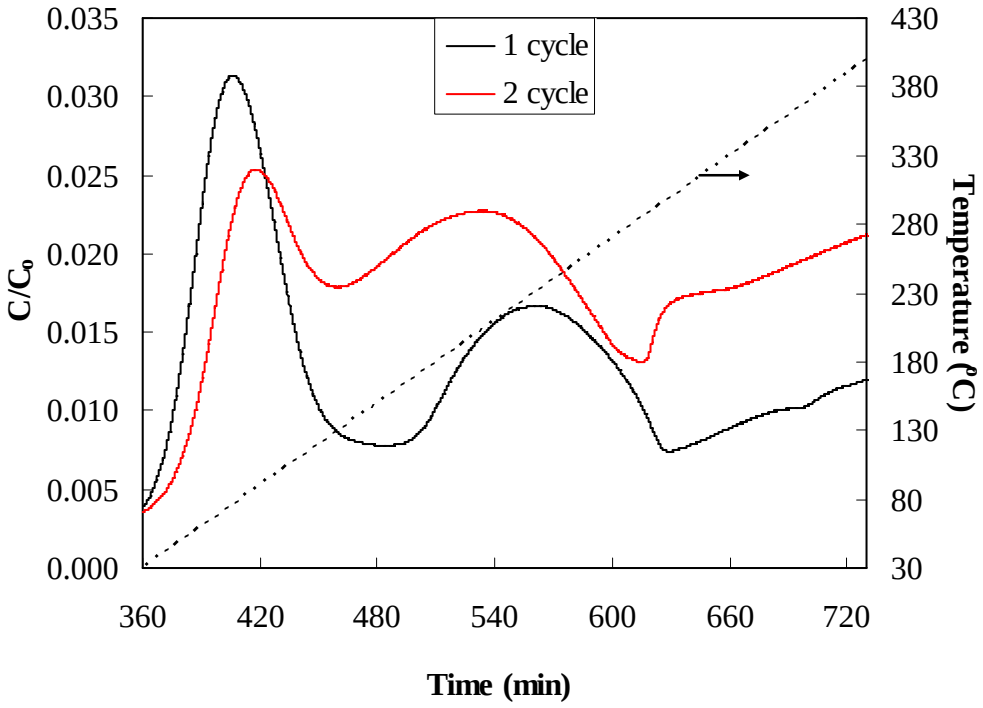

Figure 5.42. Temperature-programmed desorption profiles for the successive adsorption of NO on Washed zeolite.

The NO adsorption properties of Washed zeolite were compared with those of the synthetic zeolites in Figure 5.43. The total NO adsorption capacity of Washed zeolite was found to be higher than those of the synthetic zeolites. For a given adsorbate, the gas adsorption rate, selectivity and capacity of adsorbent depends on the type, size, amount and location of the cations residing in the microporous channels, Si/Al ratio, size and shape of the pores (Ackley and Yang, 1991a,b). The pore diameter of the 3A zeolite is smaller than

the kinetic diameter of a NO molecule, so the adsorption of NO in 3A is kinetically hindered. In the sodium form (4A), all windows are partially obstructed by sodium cations and the effective aperture of the sieve is reduced from about 4.4 to 3.8 Å. If the sodium cations are exchanged for Ca^{2+} and Mg^{2+} as in 5A, the number of cations per cell decreases. Since the diameter of the potassium ion is greater than that of sodium, the pore size of 3A is smaller than that of 4A (Ruthven, 1984; Breck, 1974). In addition to the molecular sieve effect based on the geometrical factors, zeolites also exhibit chemical selectivity. Cations present in the channels of a microporous adsorbent cause considerable electrostatic interaction between the surface and the negative charge of polar and polarizable adsorbates (Young and Crowell, 1962). The temperature-programmed desorption of the zeolites shown in Figure 5.44 confirmed the restriction of NO adsorption in zeolite 3A and 5A.

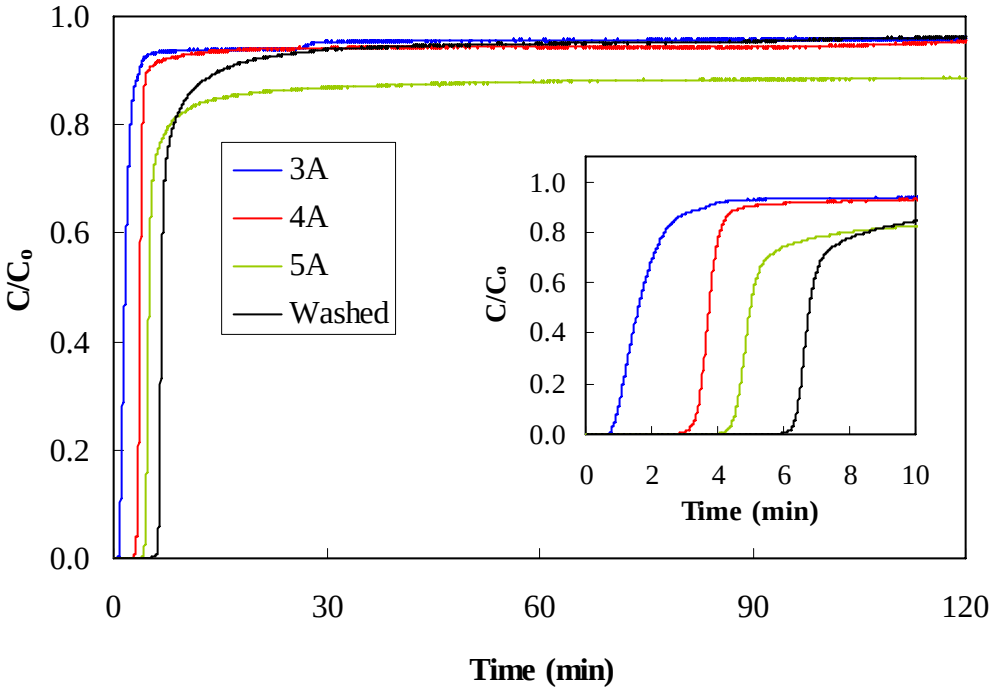

Figure 5.43. Adsorption profiles for Washed and synthetic zeolites.

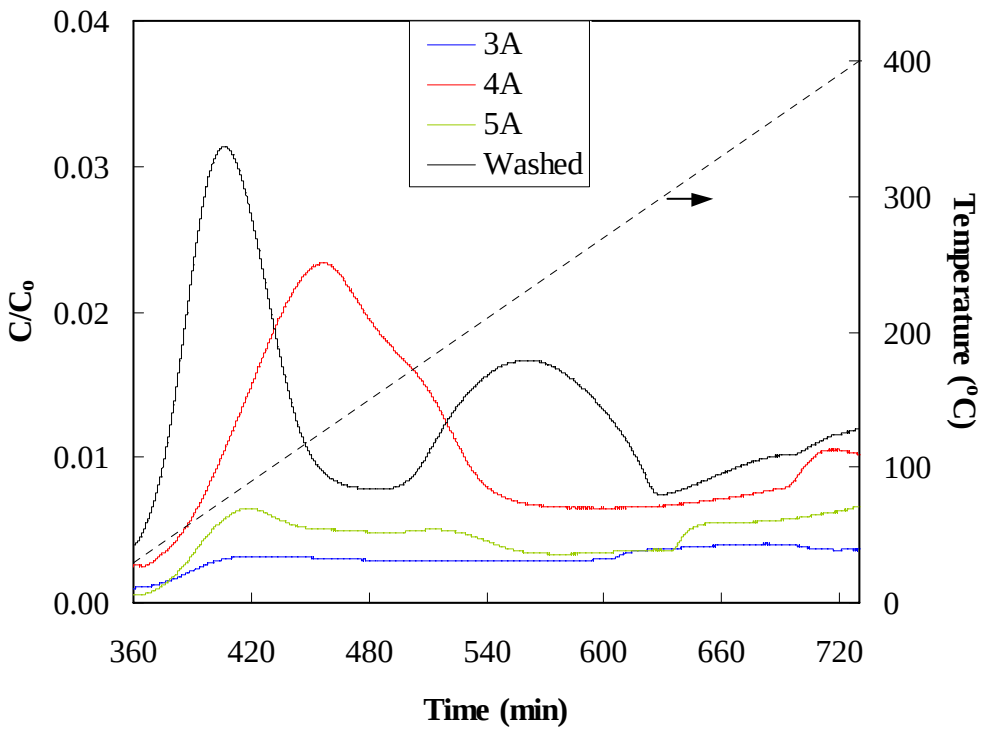

Figure 5.44. TPD profiles for Washed and synthetic zeolites.

5.3.1. Effect of NO Flow Rate on NO Adsorption

The effect of the NO feed flow rate on the adsorption breakthrough curve examined for Washed zeolite particles of 109 μm in diameter is shown in Figure 5.45. The breakthrough time decreased from 3.20 to 1.78 minutes as the flow rate increased from 20 to 50 ml/min. The breakthrough curve has become steeper and the time required for saturation of the adsorbent decreased at the higher flow rate.

The amount of NO adsorbed within the 120 minutes of adsorption decreased from 8.09 mmol/g to 7.59 mmol/g with the increase of the NO feed flow rate from 20 ml/min to 50 ml/min. This might be explained by the contact time between NO molecules and the zeolite for the case of that the adsorption rate is controlled by intraparticle diffusion. At higher flow rates, the residence time available for each NO molecule to diffuse within the

particle where it reacts with the adsorption sites gets shorter. Hence some of the NO molecules might escape from being adsorbed as the flow rate increases. At low flow rates, the NO molecules have more time to contact with the active sites within the zeolite particle, so more NO molecules can be adsorbed within a specified time period.

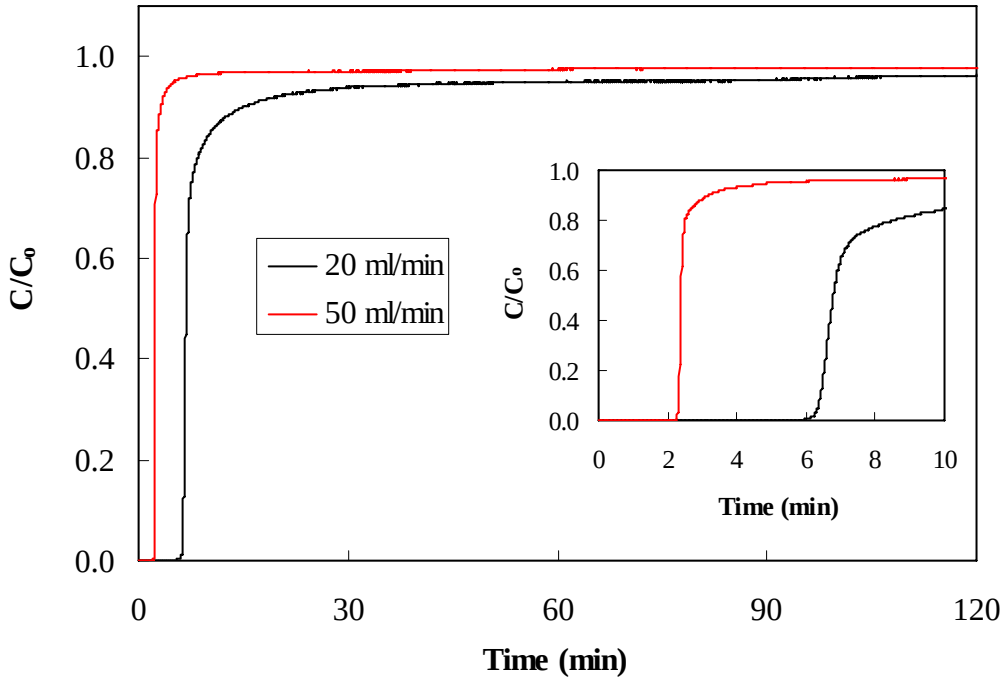

Figure 5.45. Effect of feed flow rate on the adsorption of NO in Washed zeolite.

The time axis was normalized with respect to the amount of NO introduced to the bed per unit mass of zeolite in order to compare the effect of the flow rate on the adsorption kinetics. The breakthrough curves for different NO feed flow rates almost overlapped at the initial part of the adsorption as shown in Figure 5.46. Transfer of NO molecules from the bulk fluid phase to the adsorption sites within the particle occurs through several steps as mentioned. First, the NO molecules diffuse through the external film surrounding the particle. The external film exists whenever there are more than one gas species in the fluid phase. Under the conditions of concern in this study, this is the case only at the very start

up of the adsorption. During this time period the NO molecules introduced to the bed diffuse through the helium molecules which are already present in the interparticle voids and intraparticle pores. Initially since the concentration of the adsorbate in the fluid phase is remarkably higher than that at the particle–fluid interface, i.e. the driving force for the external film mass transfer, diffusion of the NO molecules from the fluid phase to the particle surface occurs rapidly. As the adsorption proceeds the concentration of NO on the particle surface increases and the driving force for the external mass transfer decreases. After the certain time period, the external film mass transfer resistance becomes negligible. In addition, after this time period, since there is no helium molecules in the fluid phase the external film on the particle surface disappears. Thereafter self-diffusion of NO molecules starts and the adsorption occurs through other mass transfer mechanism(s).

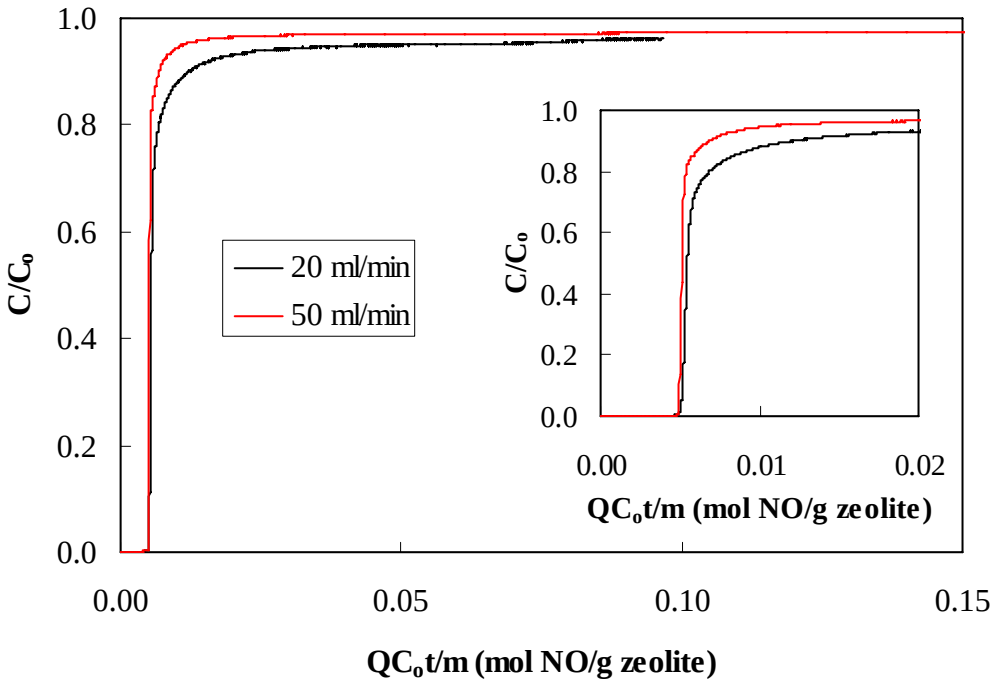

Figure 5.46. Effect of NO feed flow rate on the NO adsorption breakthrough curve for Washed zeolite normalized with respect to the total amount of NO fed to the column per unit mass of the zeolite.

5.3.2. Effect of Zeolite Particle Size on NO Adsorption

The effect of particle size of Washed zeolite on the adsorption breakthrough curve is shown in Figure 5.47. From the figure, it was revealed that as the average particle diameter increased from 109 μm to 190 μm, the breakthrough time decreased from 3.2 to 2.5 minutes. The particle size of the adsorbent did not affect the slope of the breakthrough curve and the saturation time remarkably. At the 18th minute, the curves coincided with each other where the adsorbent was almost saturated. The amount of NO adsorbed within 120 minutes was found to be almost independent of the particle size as expected since the adsorption equilibrium state is independent of the particle size.

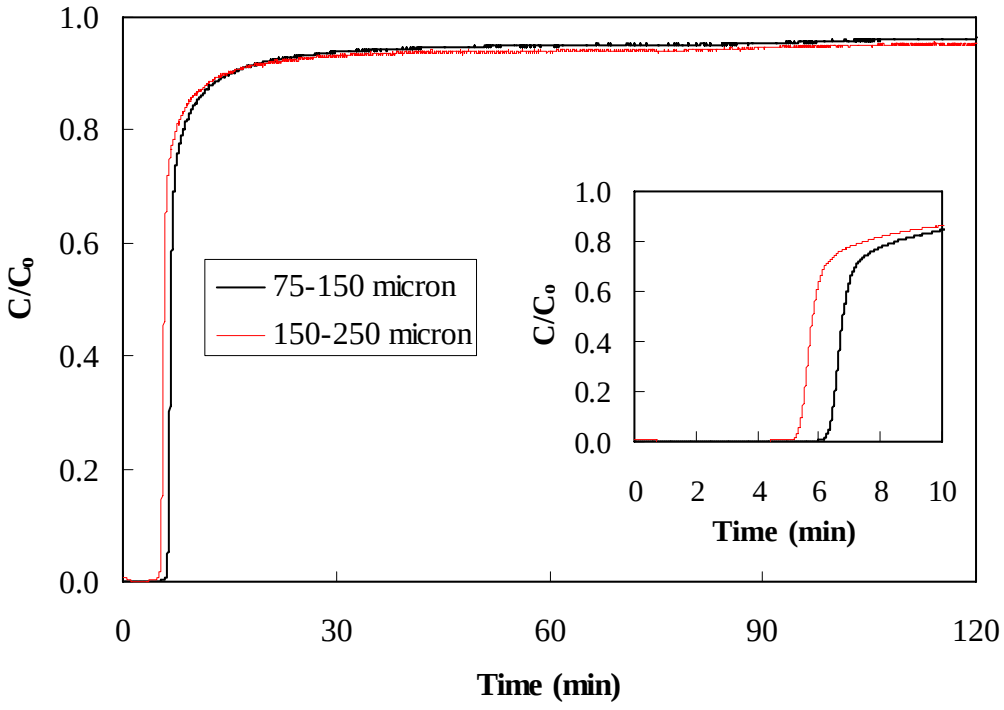

Figure 5.47. Effect of particle size of Washed zeolite on the NO adsorption.

The breakthrough curves obtained for the beds of zeolite particles with different sizes were also presented in terms of the amount of NO introduced to the bed per unit mass of zeolite in Figure 5.48. The slight sensitivity of the breakthrough curve on the particle size can be more clearly seen from this figure.

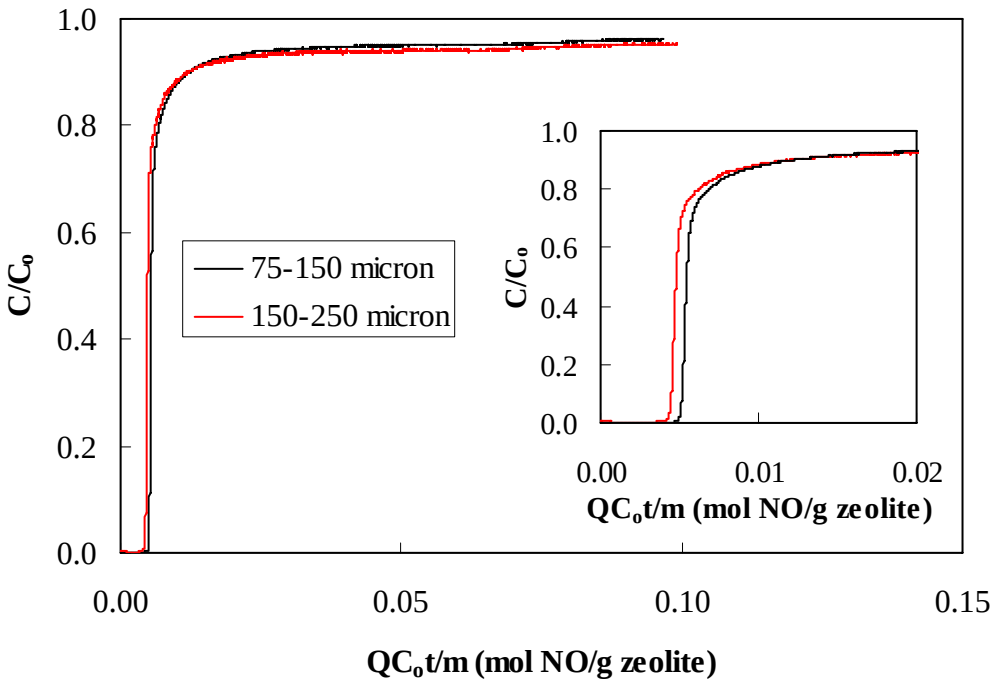

Figure 5.48. Effect of particle size of Washed zeolite on the NO adsorption breakthrough curve normalized with respect to the total amount of NO fed to the column per unit mass of the zeolite.

As the particle size increases, the total length of the diffusion path inside the particle increases, i. e., the time for an adsorbate molecule to reach the adsorption site becomes longer. If the adsorption rate is controlled by the intraparticle diffusion, the adsorption rate will be proportional to the ratio of diffusion coefficient over the square of the particle radius and lower adsorption rate will be observed for larger particles. Particle size dependence of the adsorption kinetics also reveals the relative importance of the micropore

or macropore diffusion resistances. The macropore diffusion rate is inversely proportional to the square of the particle radius, but the micropore diffusion rate is independent of the particle size. The minor sensitivity of the breakthrough curve to the particle size might reflect the relative importance of the micropore diffusion within the particle as compared to the macropore diffusion. The sensitivity of the breakthrough curves to the particle size can also be explained by the clinoptilolite content of the natural zeolite.

5.3.3. Effect of Activation Period on NO Adsorption

Prior to an adsorption capacity measurement, the adsorbent must be activated in order to remove any preadsorbed material on the adsorbent. Activation conditions (temperature, pressure, purge gas flow rate, heating rate, and period of activation) required to attain a clean surface depend on the nature of the adsorption system and the purpose of the investigation. The desorption rate of the preadsorbed material strongly depends on the temperature so elevated temperature is desirable. The temperature should be increased slowly while purging the adsorbent under high gas flow rate so that the preadsorbed materials are removed as soon as they are desorbed. However deciding on the temperature and rate to reach this temperature for activation, changes that may occur in the adsorbent structure must be taken into consideration. Furthermore in the case of clinoptilolite, the number of exchangeable cations and water molecules in the channels are interdependent. Therefore the changes in the amount of water in the channels affect the positions of the cations (Bish and Boak, 2001). It was reported in the literature that preadsorption of polar molecules affects the adsorption properties of zeolite. The polar water molecule has strong electrostatic interactions with the oxygen atoms of the zeolite framework as well as with the cations present in the zeolite framework. Even small amounts of water present in a zeolite cause adsorption of an adsorbate to severely reduce. A diffusion block by clustering of water molecules about the cation in the channels is produced upon the strong interaction between the cations in the zeolite structure and the dipole moment of water (Breck, 1974).

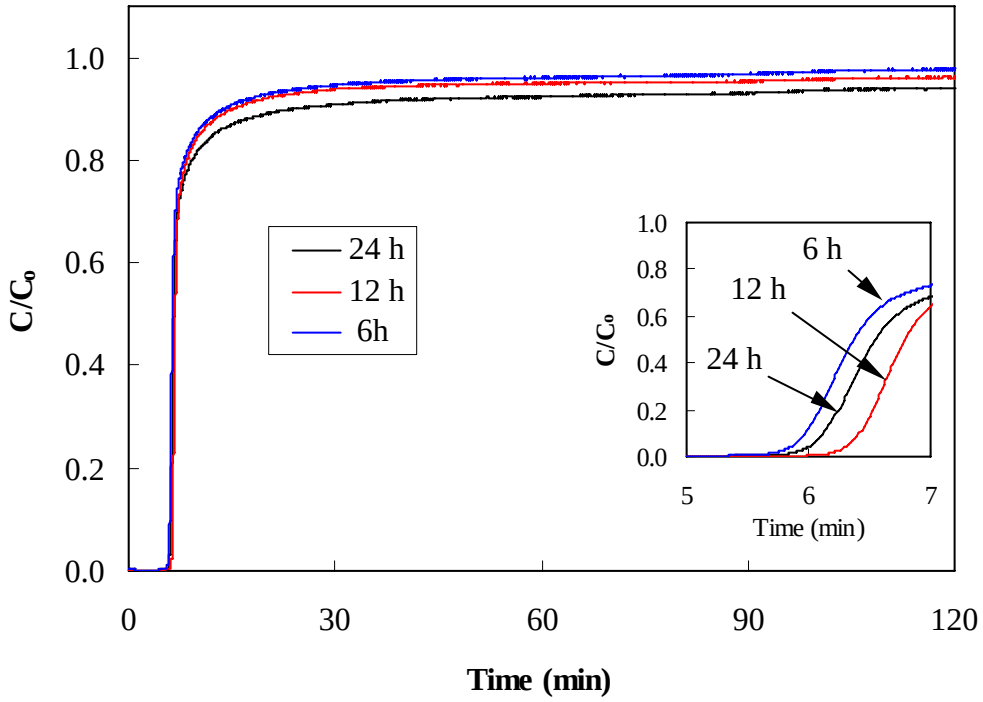

Figure 5.49. Effect of activation period on the NO adsorption by Washed zeolite.

The adsorption profiles for Washed zeolite activated at 400 ^{o}C, under the same helium flow of 50 ml/min for different periods (6, 12 and 24 hours) are shown in Figure 5.49. Due to the limitation of the gas chromatograph, it was not possible to increase the activation temperature above 400 ^{o}C. After the activation has been completed, the temperature was decreased to the adsorption temperature (30 ^{o}C) and NO was passed through the column at flow rate of 20 ml/min for 120 minutes. The breakthrough time did not change with the activation period, whereas the equilibrium adsorption capacity decreased when the zeolite was activated in shorter periods implying that more preadsorbed species could be removed from the adsorbent by activation for longer period thereby providing more sites for interaction of NO. The equilibrium adsorption capacities were calculated as 7.87, 8.09 and 9.32 mmol/g for the zeolite activated for 6, 12 and 24 hours, respectively. The results revealed that that the sites for NO and water adsorption are probably competing with each other. The competitive adsorption of NO and water probably

led to the inhibition of NO adsorption sites by water molecules. It was also stated that for microporous zeolites, diffusion in micropores is very susceptible to small differences in activation procedure which may lead to slight difference in cation locations. Thus the zeolite activated under slightly different conditions exhibits large differences in micropore diffusivity (Ruthven, 1984). But for practical purposes and regarding the activation periods reported in the literature, the activation period of 12 hours was selected and applied in all adsorption runs. The profiles within the first 7 minutes as well as the degree of approach to saturation were not in the same order as the activation periods.

5.3.4. Effect of Adsorption Temperature on NO Adsorption

The effect of adsorption temperature on the adsorption profile is shown in Figure 5.50. As the adsorption temperature increased, the breakthrough curve became sharper implying the higher adsorption rate. An increase in the adsorption temperature from 30 ^{o}C to 90 ^{o}C caused a decrease in the breakthrough time from 3.2 minute to 1.8 minute. This is due to exothermic nature of the adsorption. As the adsorption temperature increased, the equilibrium is attained faster (Shams, et al., 2008). The breakthrough curves were coincided at about 30 minutes of the adsorption and the curves were overlapped in the later portion of the adsorption. The temperature did not affect the time of saturation of the bed.

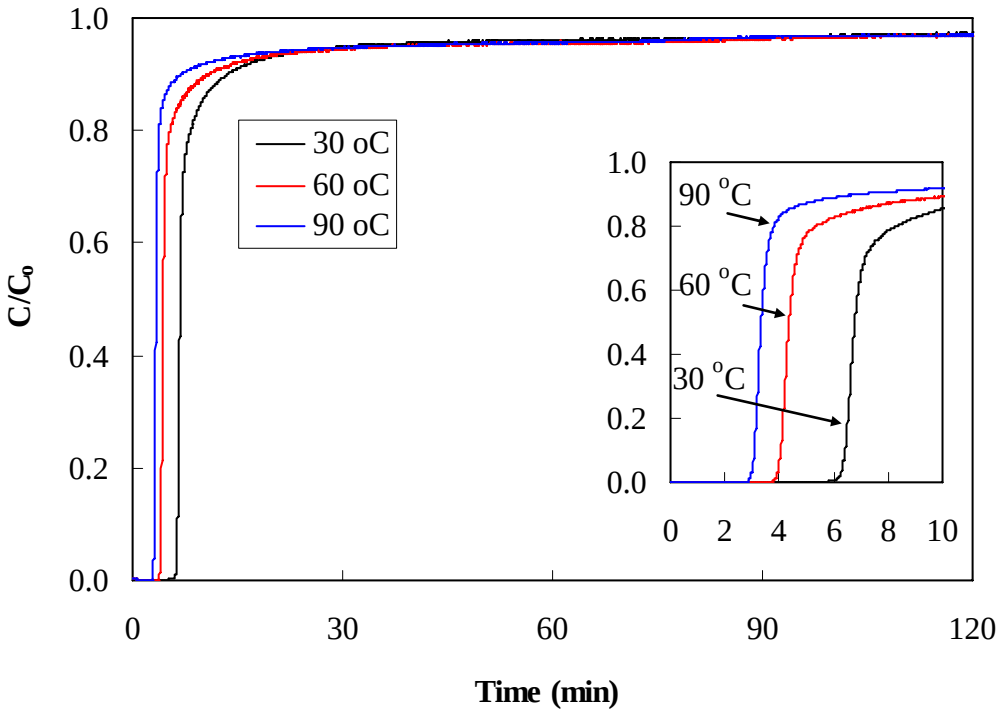

Figure 5.50. Effect of temperature on the NO adsorption breakthrough curve.

The dependencies of total, reversible and irreversible adsorption capacities of Washed zeolite for NO on adsorption temperature are shown in Figure 5.51. The total adsorption capacity decreased with the adsorption temperature indicating that physical adsorption is the dominant mechanism of adsorption. The irreversibly adsorbed NO amount decreased gradually up to 60 ^{o}C and then continued to decrease more gradually. The reversible adsorption capacity increased gradually and reached a maximum at 60 ^{o}C and decreased in similar trend with further increase in the temperature. The temperature dependence of the NO adsorption properties of the zeolite requires further investigation.

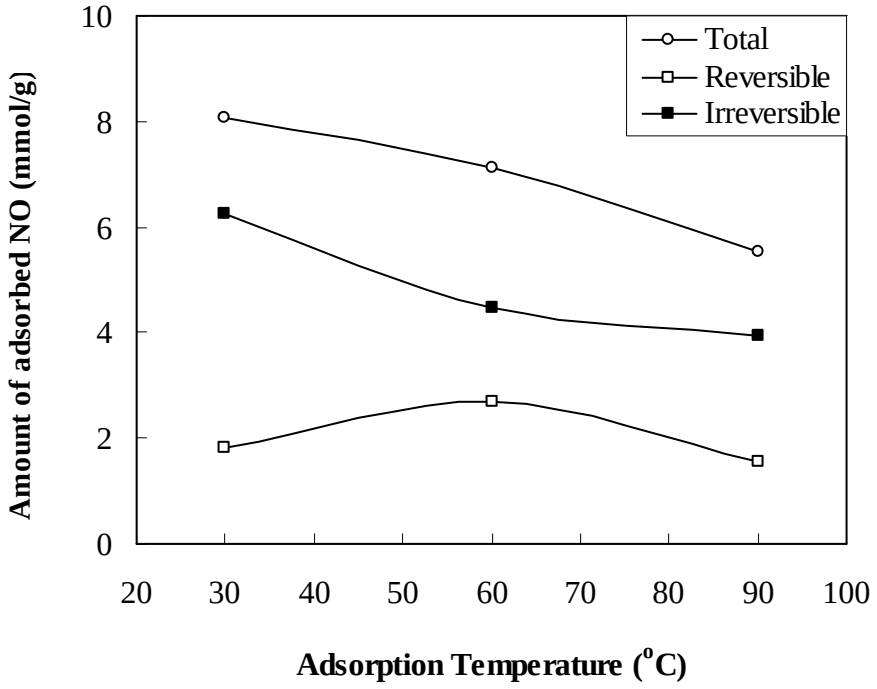

Figure 5.51. Total, reversibly and irreversibly adsorbed NO amounts as a function of adsorption temperature.

5.3.5. Effect of Clinoptilolite Content of the Zeolite on NO Adsorption

The particles with particle diameter of 75-150 μm obtained from the pure kaolin pellets were also tested for the NO adsorption characteristics under the same conditions and the breakthrough curves obtained are shown in Figure 5.52. The breakthrough curve for Washed zeolite was also included in the figure for comparison purposes and to evaluate the effect of clinoptilolite content of the zeolite on the adsorption.

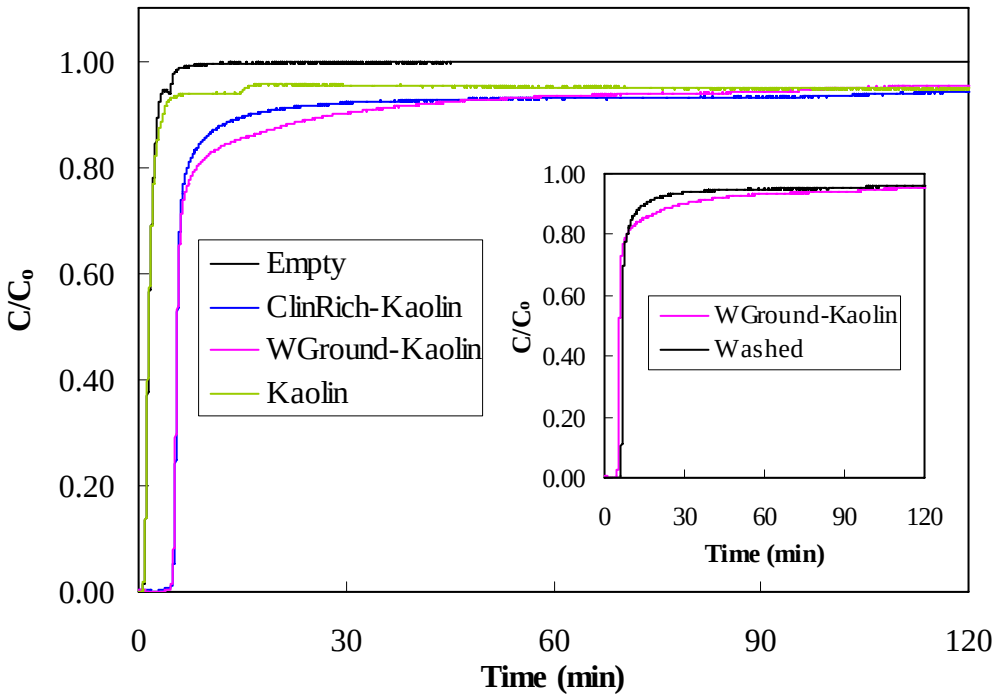

Figure 5.52. Effect of clinoptilolite content of the zeolite on its NO adsorption kinetics.

The breakthrough curve obtained for the kaolin packed column confirmed that the contribution of the binder to the adsorption of NO was negligible. Therefore, the kaolin was considered as inert filler. The breakthrough times for WGround-Kaolin and Washed zeolites were determined as 2.5 and 3.1 minutes, respectively. This slight difference can be attributed to the differences in the transport properties of the natural filler in Washed zeolite (biotite, quartz, feldspars) and the additional second filler (kaolin) in WGround-Kaolin particles. The differences in the size of clinoptilolite crystals in the prepared and natural zeolite particles might have also affected the adsorption properties. From the electron micrographs the size of the clinoptilolite crystals in Washed zeolite was determined in the range of 5-10 μm, while the average size of the crystals of ground Washed zeolite (WGround) was determined to be in the range of 0.5-50 μm. Moreover, blinding of the crystal surface might have occurred during production of the pellets and coking due to the catalytic activity of the binder which led to decrease in mass transfer rates (Ruthven, 1984; Jasra et al., 1991; Breck, 1974; Yang, 1997). Furthermore, the secondary pores are formed

in the pellets due to the presence of the binder during pellet formation and subsequent calcination processes. These pores may have different and nondefined sizes, and serve as channels for transfer of the adsorbate molecules to the micropores (primary pores).

The TPD profiles for WGround-Kaolin, ClinRich-Kaolin and pure Kaolin particles are compared with that of Washed zeolite in Figure 5.53. Regarding the peak maxima and heights especially for the second peak, the discrepancies between WGround-Kaolin and Washed zeolites can be related to the clinoptilolite crystal size as well as to the binder. In the TPD spectrum of ClinRich-Kaolin, the second peak was detected at temperature about 20 ^{o}C higher than that for WGround-Kaolin. It was not possible to correlate either the positions or the heights of the peaks to the clinoptilolite content of the zeolites. The detector signal recorded for Kaolin particles during the temperature programmed desorption was at the same level with that for the empty column confirming the inertness of the binder.

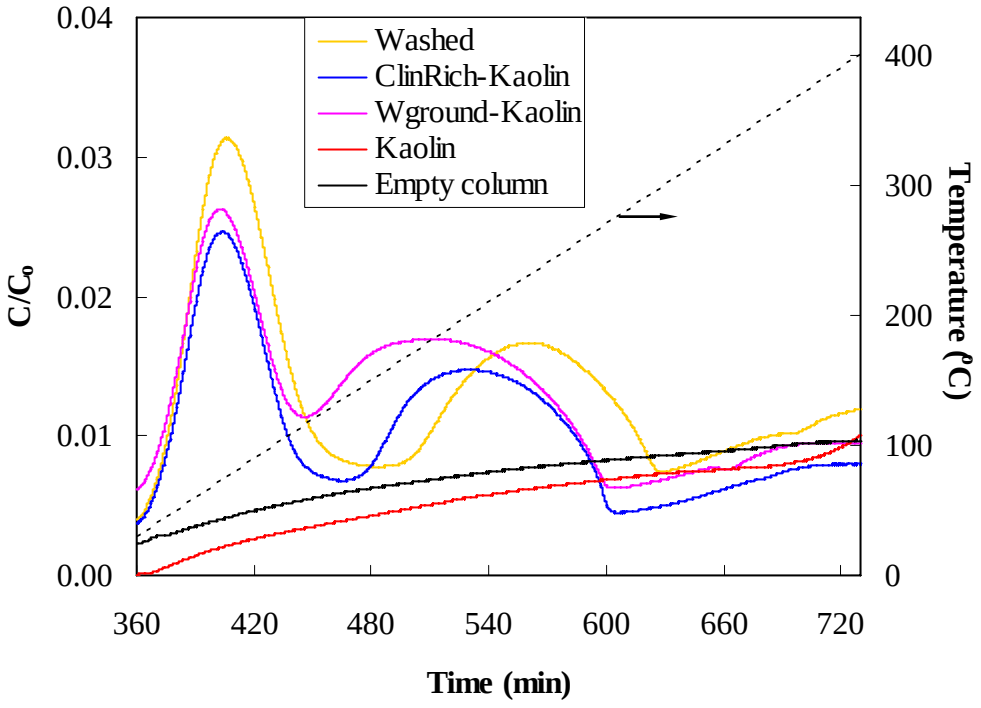

Figure 5.53. Effect of the clinoptilolite content on the TPD profiles.

5.3.6. Effect of NO Adsorption Period on NO Adsorption

The breakthrough curves obtained for different periods of NO adsorption are illustrated in Figure 5.54. It can be seen that saturation of the zeolite with NO has not been achieved even after 5 hours. The composition of the column outlet did not significantly change after 120 minutes as indicated by the gradual increase of the detector signal. The total amount of NO adsorbed increased only by 1 % between the 120th minute and the 5th hour.

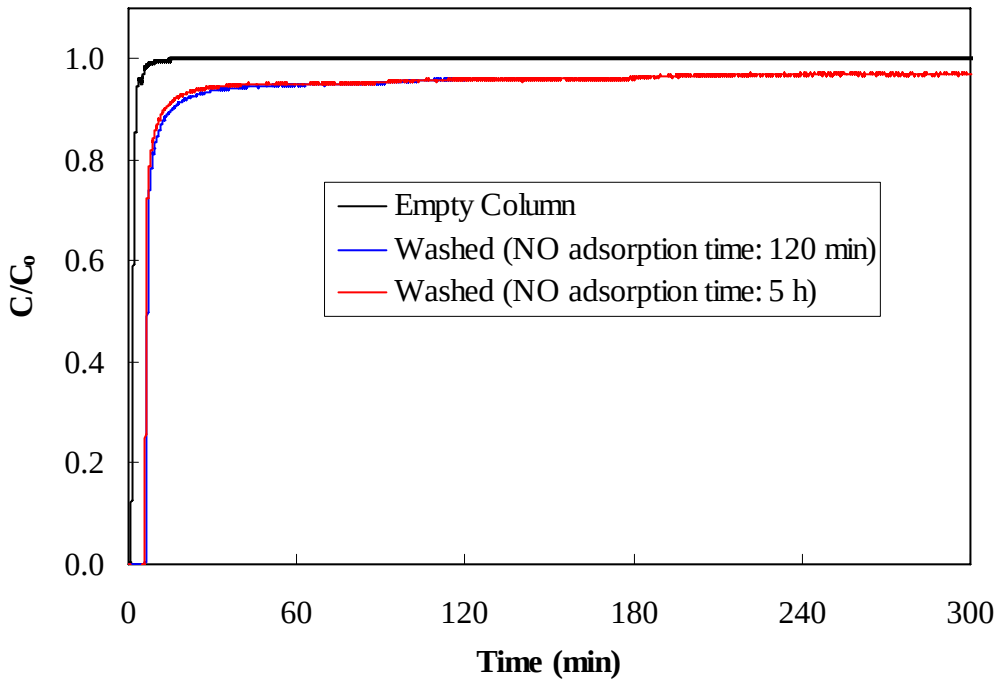

Figure 5.54. Effect of NO adsorption time on the breakthrough curve.

For all the zeolites and under the different experimental conditions of concern in this thesis, the NO adsorption rate was slow and the adsorbents were not saturated

completely within 120 minutes of adsorption. The slow rate of NO diffusion in the Washed zeolite could not be indicative of a kinetic barrier since the kinetic diameter of NO molecules are much smaller than the channel dimensions of the zeolite. On the other hand, adsorption in micropores is strongly affected by the internal electrostatic fields that envelop the entire pore space. The contributions of the framework and extra-framework cations and adsorbate molecules to these internal fields are all important and interdependent (Ackley and Yang, 1991a). It was reported that changing the cations in a zeolite, the pore openings can be effectively modified as a result of reduction in the cation population and/or a relocation of cations which are normally located near the pore openings (Breck, 1974). The interactions between the cations in the pores and the NO gas molecules play an important role in both diffusion and adsorption (Ma and Mancel, 1972). Therefore, the differences in the breakthrough profiles can be interpreted regarding the types, locations and amounts of the cations present in the zeolite.

The influence of cation type and content on the adsorption breakthrough curves can be seen in Figure 5.55. The breakthrough curves exhibited dissimilarities especially in the initial period of adsorption. The adsorption uptake curve of Na-Clin was also included in the figures to evaluate the effect of metal sorption. The breakthrough time was found to be the same for all the zeolites as 2.6 minutes. The slope of the breakthrough curves was smooth within the first 2-5 minutes of the adsorption indicating the low mass transfer rate. After the first 5 minutes, the NO concentration in the column outlet steeply increased and this increase ended at different times for each zeolite: 5.1 minutes for Na-Clin, 5.4 minutes for 0.05 M Fe, 6.8 minutes for 0.05 M Ag, 7.3 minutes for Washed, 9.7 minutes for 0.05 M Co and 10.1 minutes for 0.05 M Cu samples. The time at which the profile reached a more gradual increase was found to be 5.3, 5.5 and 6.6 minutes for 0.01 M Fe, Ag and Co samples, respectively. After about 45 minutes, the NO concentration at the outlet almost approached a steady value indicating that free sites are no longer available for further adsorption. The steep breakthrough curves implied that the adsorption isotherm of NO on the zeolites was favorable.

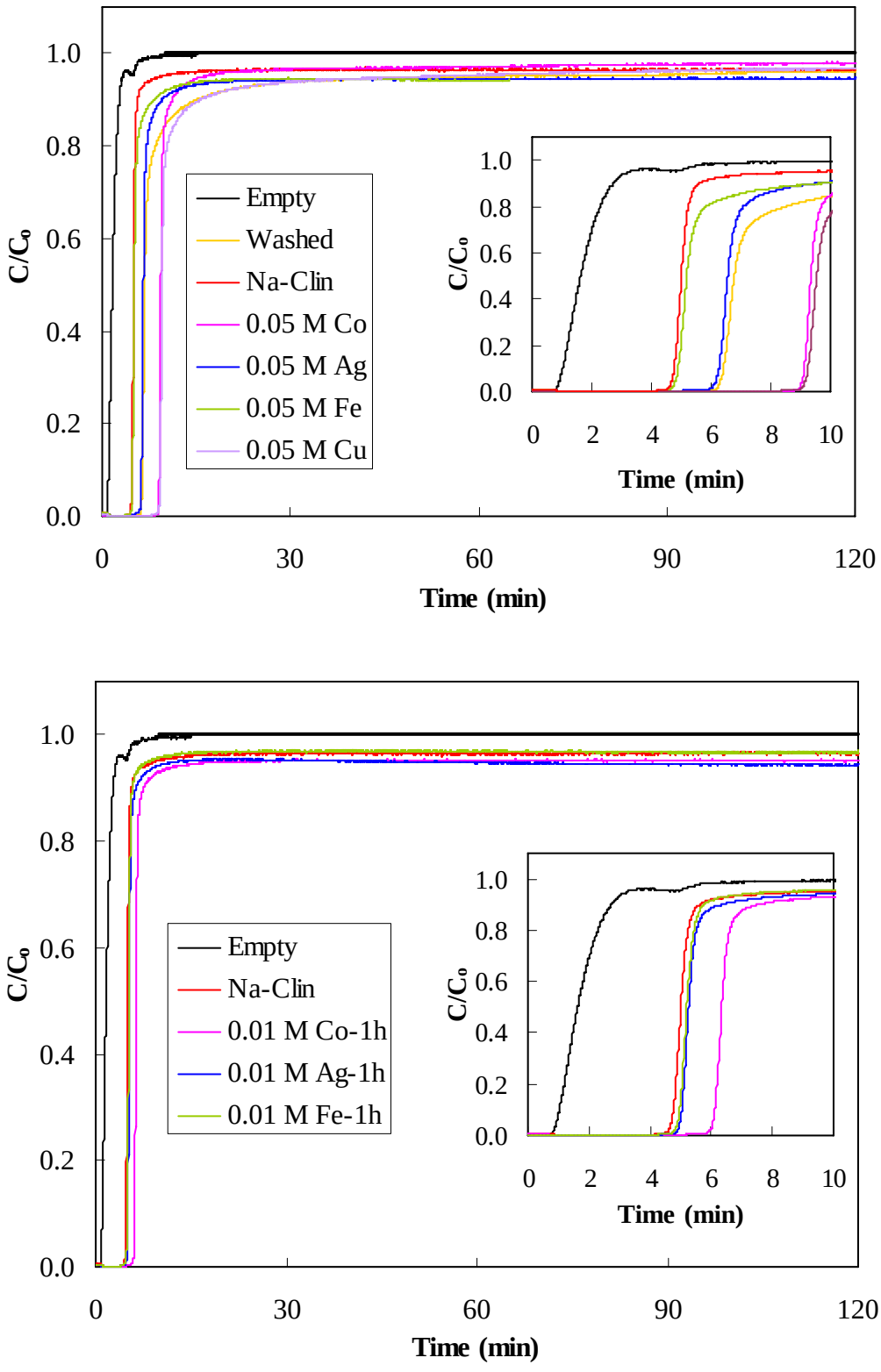

Figure 5.55. Adsorption profiles for the zeolite samples with different cation contents.

The time required to reach the 10 % of the feed NO concentration (C/C_o=0.1) was determined as 1.1 minutes for the empty column, 4.9 minutes for 0.05 M Fe, 4.8 minutes for Na-Clin, 6.3 minutes for 0.05 M Ag, 6.4 minutes for Washed, 9.1 minutes for 0.05 M Co and 9.3 minutes for 0.05 M Cu sample. For 0.01 M-1h samples, 10 % of the inlet concentration was achieved after 4.9 minutes for Fe, 5.1 minutes for Ag, and 6.1 minutes for Co sample. Regarding the longer times required to reach C/C_o=0.1 by the zeolites with higher metal content, there might be a relationship between the metal content of the zeolite and the adsorption rate in the initial period of the adsorption, except for the iron-sorbed zeolites. For these zeolites, the time required to reach C/C_o=0.1 was found to be independent of the iron content of the zeolite.

After 120 minutes of adsorption, the feed flow was switched to a 20 ml/min flow of pure helium in order to remove the gas-phase and reversibly (weakly) adsorbed NO. The desorption breakthrough curves obtained in this manner are shown in Figure 5.56. The decrement in the TCD signal during helium purge at adsorption temperature was attributed to desorption of reversibly adsorbed species. Approximately 2 minutes after switching the flow from pure NO to pure helium a peak with two maxima were observed. Since those peaks were also inspected for the empty column, it is not possible to attribute them to the reversibly adsorbed NO species. The amounts of reversibly adsorbed NO by the adsorbents were calculated by subtracting the area under the empty column desorption breakthrough curve from those of the packed columns.

The adsorption and desorption profiles are compared in Figure 5.57. It was revealed that the adsorption profiles were sharper than the desorption profiles which indicates that the adsorption equilibrium isotherm is in favorable form. For the systems with linear adsorption isotherm, the adsorption and desorption breakthrough curves are symmetrical. The deviation from the symmetry indicates deviations from linearity in the equilibrium isotherm (Ruthven, 2004).

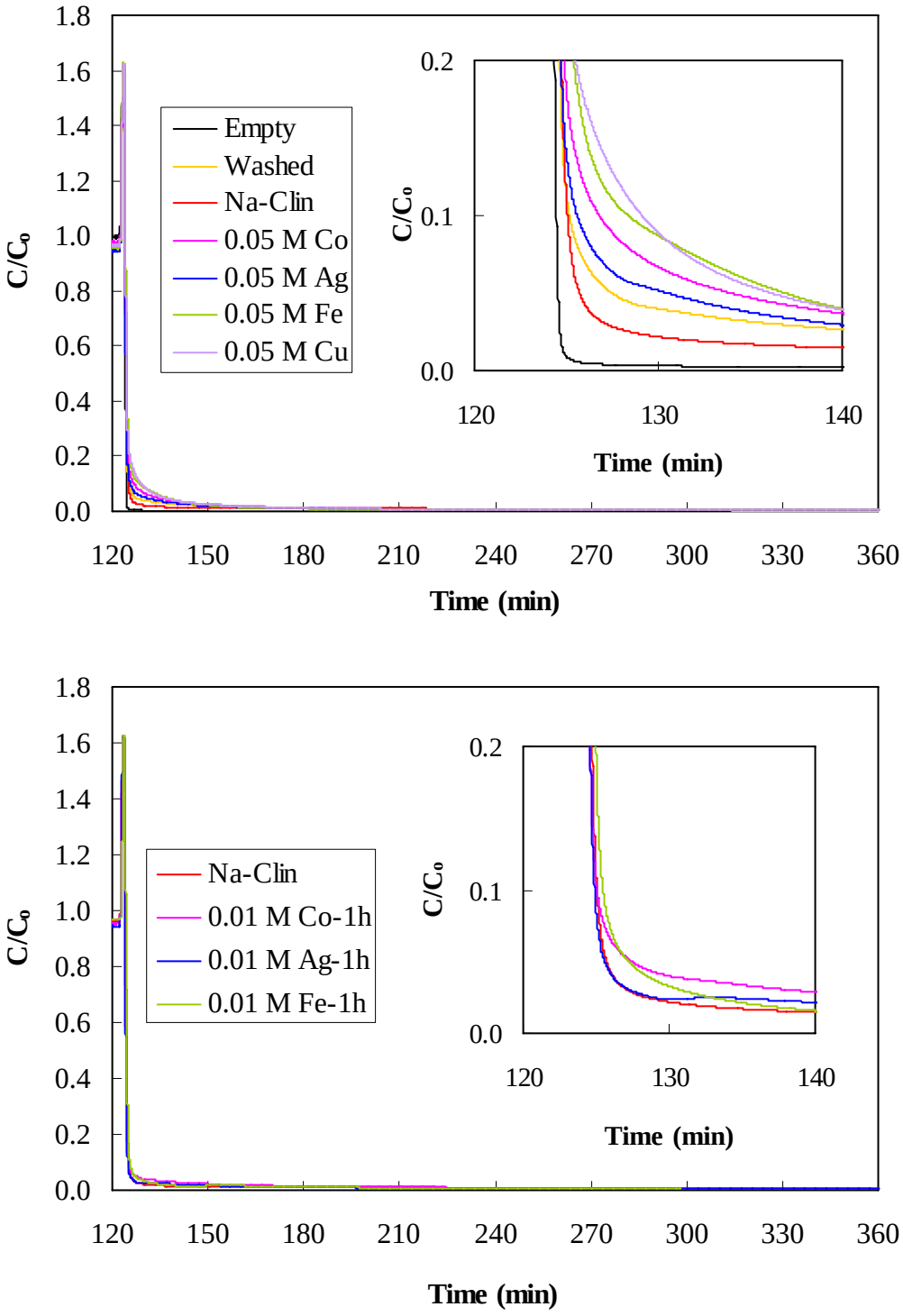

Figure 5.56. NO desorption profiles of the zeolites.

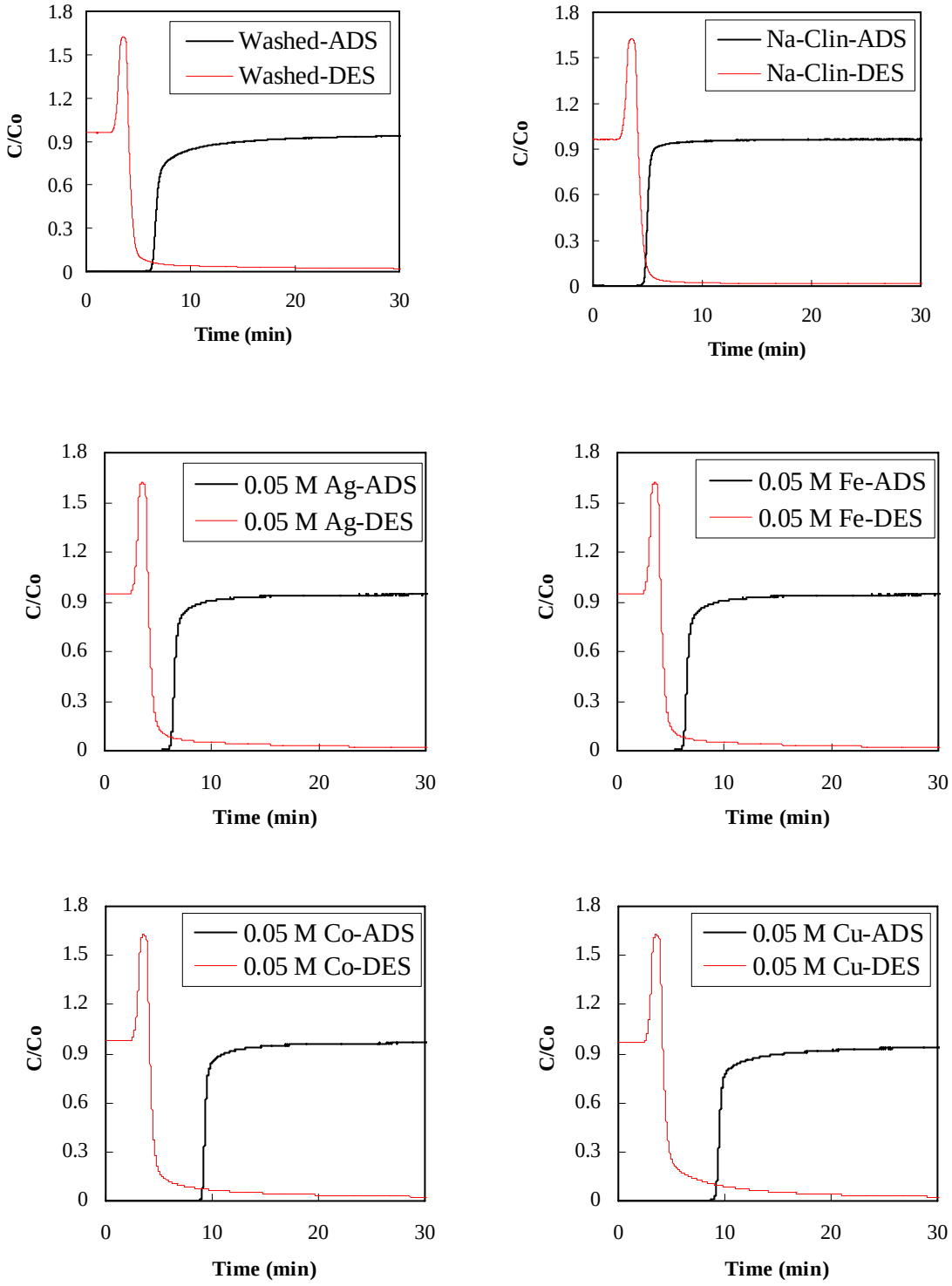

Figure 5.57. NO adsorption and desorption profiles.

(cont. on next page)

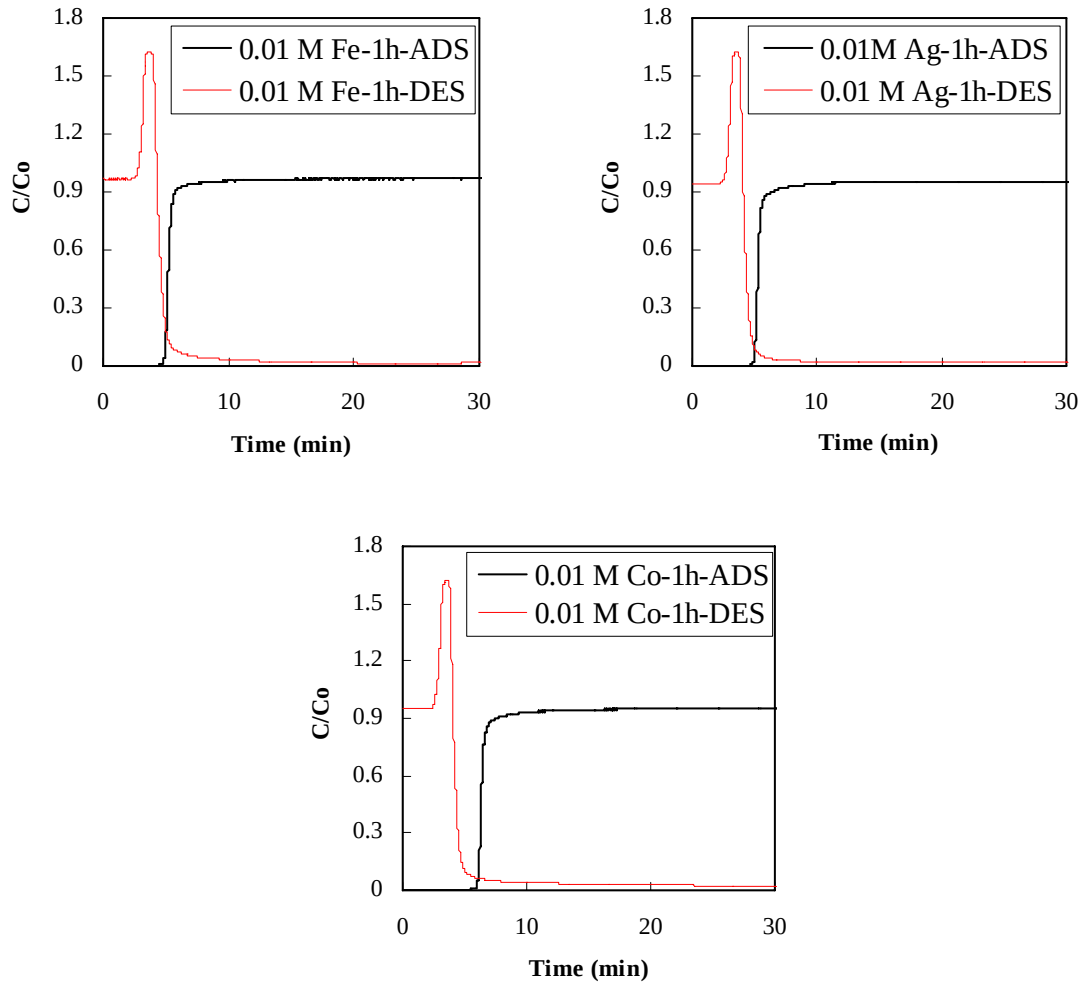

Figure 5.57. (cont.) NO adsorption and desorption profiles.

The total, reversible and irreversible NO adsorption capacities of the zeolites calculated from the adsorption and desorption breakthrough curves in the manner mentioned in Appendix A are given in Table 5.26. The irreversibly adsorbed amounts were calculated by subtracting the reversibly adsorbed amounts from the total amounts.

Table 5.26. Equilibrium NO adsorption capacities of the zeolites.

Samples	Amount of NO adsorbed (mmol/g)			Percent irreversibly adsorbed NO (%)
	Total	Reversible	Irreversible	
Washed	8.08	1.69	6.39	79.07
Na-Clin	5.73	2.15	3.58	62.48
0.05 M Co	7.77	2.35	5.42	69.77
0.05 M Ag	6.41	1.45	4.96	77.37
0.05 M Fe	6.49	2.24	4.26	65.54
0.05 M Cu	8.53	1.91	6.63	77.66
0.01 M Co-1h	7.94	2.38	5.56	70.02
0.01 M Ag-1h	6.71	1.87	4.84	72.09
0.01 M Fe-1h	5.52	1.92	3.60	65.16
0.1 M Co-24h	7.48	2.68	4.80	64.15
0.01 M Co-24 h	8.36	2.91	5.45	65.19

The comparison of the adsorption capacities obtained in this thesis with the reported data is not possible due to the lack of data in the literature as far as we know. But just for comparison, the local clinoptilolite-rich zeolite and its metal-sorbed forms have total equilibrium NO capacity in the range of those reported for the MFI and its metal modified forms obtained under dynamic flow conditions (adsorption time: 45 minutes, desorption time: 60 minutes, concentration of NO: 997 ppm, adsorbent weight: 0.5 g, flow rate: 100 cm^3/min) at 0 ^oC (0.16–21.21 cm^3/g) (Zhang et al., 1993) and higher than that reported for the Na-mordenite at 0 ^oC obtained under static conditions (0.09 cm^3/g) (Matsumoto et al., 2000). In Table 5.27, the NO adsorption capacities of Washed and the cobalt-sorbed zeolites determined in this study were compared with those for cobalt-exchanged zeolite A reported in the literature. The total adsorption capacities were almost 5 times higher than those in the literature, but the contribution of the reversible adsorption capacities to the total adsorption capacities exhibited good agreement.

Table 5.27. Comparison of the NO adsorption capacity of Washed and the cobalt-sorbed natural zeolite with those reported for cobalt-exchanged zeolite A.

Adsorbent	Co-exchanged zeolite A	Washed	0.05 M Co	0.01 M Co-1h
Adsorption temperature (^{o}C)	25	30		
Adsorption system	static (gravimetric)	dynamic (chromatographic)		
Pressure (mmHg)	800	760		
Total NO adsorbed (mmol/g)	1.7	8.08	7.77	7.94
Reversibly adsorbed NO (mmol/g)	0.4-0.5	1.69	2.35	2.38
Percent reversibly adsorbed (%)	24-29	20.9	30.2	30.0
Irreversibly adsorbed NO (mmol/g)	1.2-1.3	6.39	5.42	5.56
Reference	Wheatley et al., 2006	present study		

From Table 5.26, it is clear that copper-sorbed zeolite has the highest total adsorption capacity for NO compared to the other zeolites. Enrichment of Washed zeolite with sodium ions caused the adsorption capacity to decrease, especially the reversible one. The total adsorption capacity decreased in the following order: 0.05 M Cu ≈0.01 M Co-24 h>Washed>0.01 M Co-1h≈0.05 M Co>0.1 M Co-24 h >0.01 M Ag-1h≈0.05 M Ag≈0.05 M Fe>Na-Clin≈0.01 M Fe-1h. The reversible adsorption capacities of the zeolites did not show significant divergence, but there was a notable difference in their irreversible adsorption capacities. The relationship between the total versus reversible and irreversible adsorption capacities is shown in Figure 5.58. From the good correlation (r^2=0.95) between the total and irreversible adsorption capacities, it was revealed that the irreversible adsorption has higher contribution to the total adsorption capacity of a zeolite. The irreversible adsorption capacity decreased in the same order as the total adsorption capacity.

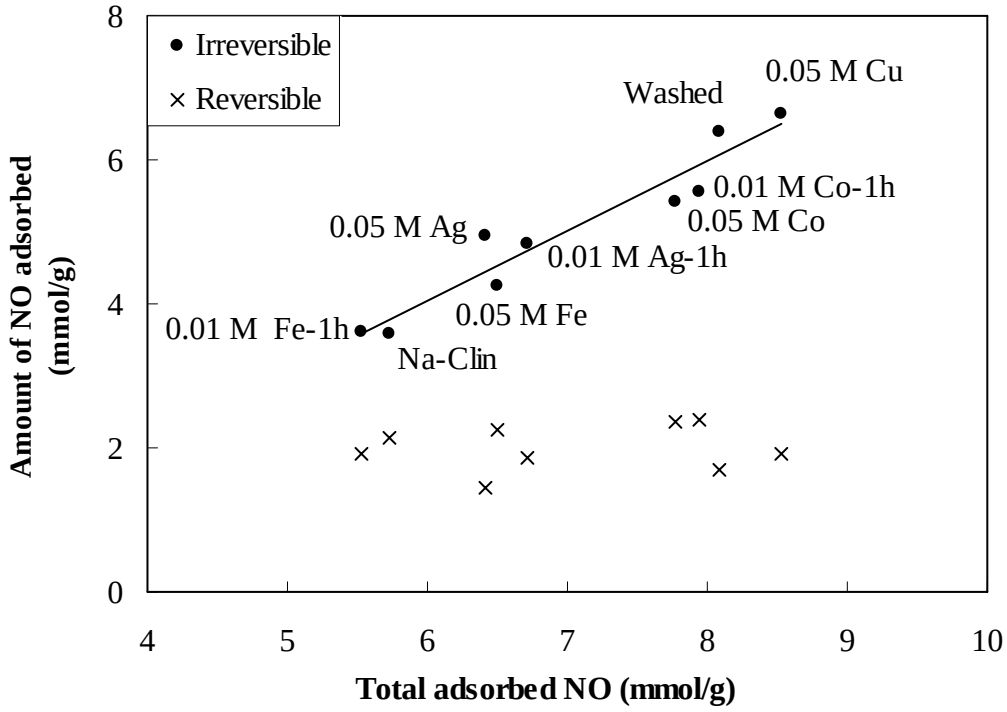

Figure 5.58. Relationship between the total, reversible and irreversible adsorption capacities of the zeolites.

The adsorbed amount of NO was expressed in terms of volume of NO adsorbed per unit mass of zeolite in Table 5.28. This conversion was performed based on the assumption that the density of the adsorbed NO is equal to its liquid density at the adsorption temperature of 30 ^{o}C (corrected density) which was calculated from Equation (4.14) as 0.543 g/cm^{3}.

In fact, there is some debate on which density value should be used in the calculations. For adsorption below the critical temperature of the adsorbate, liquid density at the same temperature can be used for the adsorbed phase density. Kaneko compared the amount of NO adsorbed on the modified ACF at 30 ^{o}C with that of N_2 at -196 ^{o}C and revealed that the anomalously high NO adsorption capacity of the adsorbent regarding the normal boiling and critical temperatures of NO. Almost all NO molecules was assumed to be adsorbed in the micropores and occupied the micropore volume in the same way as with N_2 adsorption. Hence, the pore volume for NO was calculated assuming that the density of

NO adsorbed in micropores was equal to the bulk liquid density of NO at the normal boiling temperature (1.28 g/cm^3 at 121 K). However, the apparent density of the adsorbed NO was found to be 0.5 g/cm^3 which was much smaller than the bulk liquid density (Kaneko, 1987a,b). Zhang and colleagues estimated the apparent densities of adsorbed NO on Cu-MFI(23.3)-157 and Co-MFI(23.3)-90 from the total adsorbed amounts of NO and the micropore volumes as 0.143 and 0.175 g/cm^3, respectively at 0 ^{o}C. These values corresponded to 11 % and 14 % of the liquid density of NO at the normal boiling point, respectively (Zhang et al., 1993). Matsumoto et al. calculated the saturation NO adsorption capacities of H, Na and Ca mordenites at 0 ^{o}C and -70 ^{o}C from the adsorption isotherms obtained gravimetrically under the assumption that the density of adsorbed NO was equal to that of liquid phase at the critical temperature (180 K) (Matsumoto et al., 2000).

Table 5.28. Total, reversible and irreversible adsorption capacities of the zeolites for NO.

Sample	Amount NO adsorbed (cm^3/g)		
	Total	Reversibly	Irreversibly
Washed	0.447	0.094	0.353
Na-Clin	0.317	0.119	0.198
0.05 M Co	0.429	0.130	0.300
0.05 M Ag	0.354	0.080	0.274
0.05 M Fe	0.359	0.124	0.235
0.05 M Cu	0.472	0.105	0.366
0.01 M Co-1h	0.439	0.132	0.307
0.01 M Ag-1h	0.371	0.103	0.267
0.01 M Fe-1h	0.305	0.106	0.199
0.1 M Co-24h	0.413	0.148	0.265
0.01 M Co-24 h	0.462	0.161	0.301

The total NO adsorption capacities calculated corresponds to the total pore volume of the zeolites according to the Gurvitsch Rule. When compared with the total pore volumes based on the thermogravimetric and CO_2 adsorption data, the total pore volumes calculated using the NO adsorption data were found to be almost 5 times higher. The total

pore volumes based on the NO adsorption capacities were also found to be almost twice the theoretically calculated ones.

From the total pore volumes of the zeolites previously calculated, it is possible to estimate the density of the adsorbed NO within the pores (apparent density) as stated by the Gurvitsch Rule. The estimated apparent densities of adsorbed NO based on the adsorption data for the different adsorbates and on the theoretical pore volume were presented in Table 5.29. The apparent densities estimated based on the thermal gravimetric analysis, N_2 and CO_2 adsorption data were remarkably higher than the liquid density of NO at 30 ^oC. On the other hand, the apparent density values estimated based on the total pore volume calculated from the water content at the fully hydrated state and on the theoretical pore volume fell in the range of density of liquid NO at the normal boiling point (1.28 g/cm^3) and at the adsorption temperature (30 ^oC) (0.543 g/cm^3). Hence it can be suggested that the adsorbed NO present in the micropores in a denser state than that in the liquid state (Kaneko, 1987a,b; Zhang et al., 1993; Matsumoto et al., 2000).

Table 5.29. Density estimations for the adsorbed NO.

Sample	Apparent density of adsorbed NO (g/cm^3)				
	TG data	Water content at the fully hydrated state	Theoretical	N_2 adsorption	CO_2 adsorption
Washed	2.91	1.21	1.22	4.31	2.27
Na-Clin	2.23	0.86	0.87	2.43	2.24
0.05 M Co	2.10	1.16	1.17	3.37	2.93
0.05 M Fe	2.38	0.97	0.98	1.45	2.27
0.05 M Ag	1.89	0.96	0.97	3.81	3.27
0.05 M Cu	2.59	1.27	1.29	3.59	3.13
0.01 M Co-1h	2.77	1.19	1.20	3.61	3.18
0.01 M Fe-1h	1.70	0.82	0.83	2.61	2.01
0.01 M Ag-1h	2.10	1.00	1.01	3.41	2.63
0.1 M Co-24h	2.16	1.12	1.13	3.21	
0.01 M Co-24 h	2.38	1.25	1.26	4.20	

Considering that the adsorption temperature of above the critical temperature of NO, it is expected that the adsorption occurs in the micropores and the adsorption capacity is related to the micropore volume. The relationship between the total, reversible, and irreversible adsorption capacities of the zeolites and their limiting micropore volumes calculated from the CO_2 adsorption data by the application of the D-R model is illustrated in Figure 5.59. The lack of correlation between the NO adsorption capacity and the micropore volume made the explanation of the differences in the NO adsorption capacities among the zeolites by the limiting micropore volumes impossible. The NO adsorption capacities were 5 times higher than the micropore volumes.

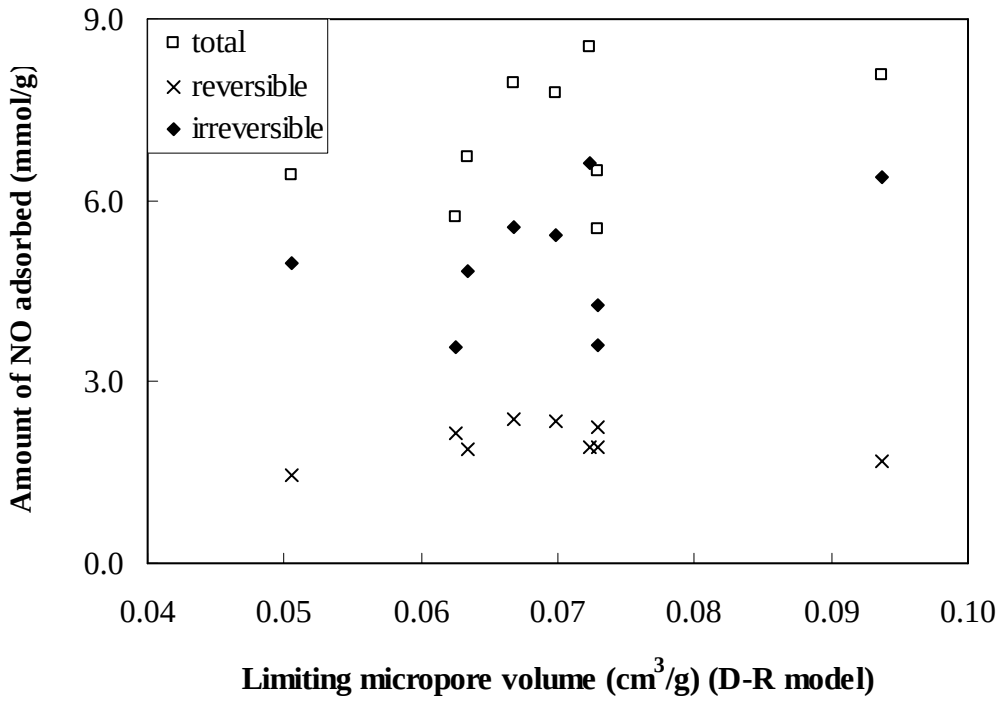

Figure 5.59. Dependence of the NO adsorption capacity on the limiting micropore volumes.

The effectiveness of each cation in the zeolite for NO adsorption can be interpreted from the adsorbed NO per cation relations as shown in Figure 5.60. The total and irreversible adsorption capacities decreased with the increase in the cation content of the zeolite regardless the type of the cation. The reversible adsorption capacity did

not change significantly also with the cation content. The zeolites with lower cation content exhibited higher adsorption capacities. The cation content particularly affected the irreversibly adsorbed amount of NO per cation. It can be figured out that the increased cation content hindered the irreversible adsorption of NO. The low adsorption capacity of Na-Clin may suggest that the Na^+ cations occupied positions in the zeolite structure that caused diffusional restrictions to the NO molecules.

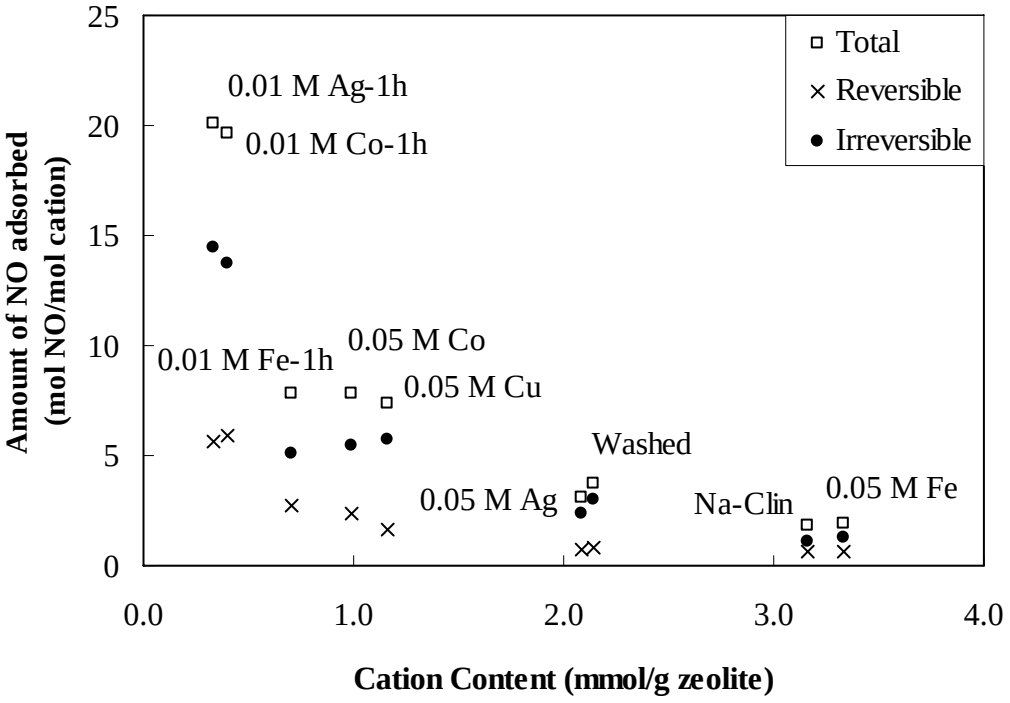

Figure 5.60. Dependence of total, reversible and irreversible adsorption capacities on the cation contents of the zeolites.

The influence of the cations in the partially calcium, sodium, magnesium, strontium, lithium, and cesium exchanged clinoptilolites on the capacity and kinetics of adsorption for CH_4 and N_2 was examined in the literature and the differences in adsorption capacity and rate were attributed to the ionic radius and location of the cations in the cationic sites which led to molecular sieving effect depending on the partial or complete blockage of the channels (Jayaraman et al., 2005). The dependence of the total, reversible and irreversible adsorption of the zeolites on the ionic radii of the

cations contained is shown in Figure 5.61. The ionic radius of the cation did not influence the reversible adsorption capacity of the zeolite.

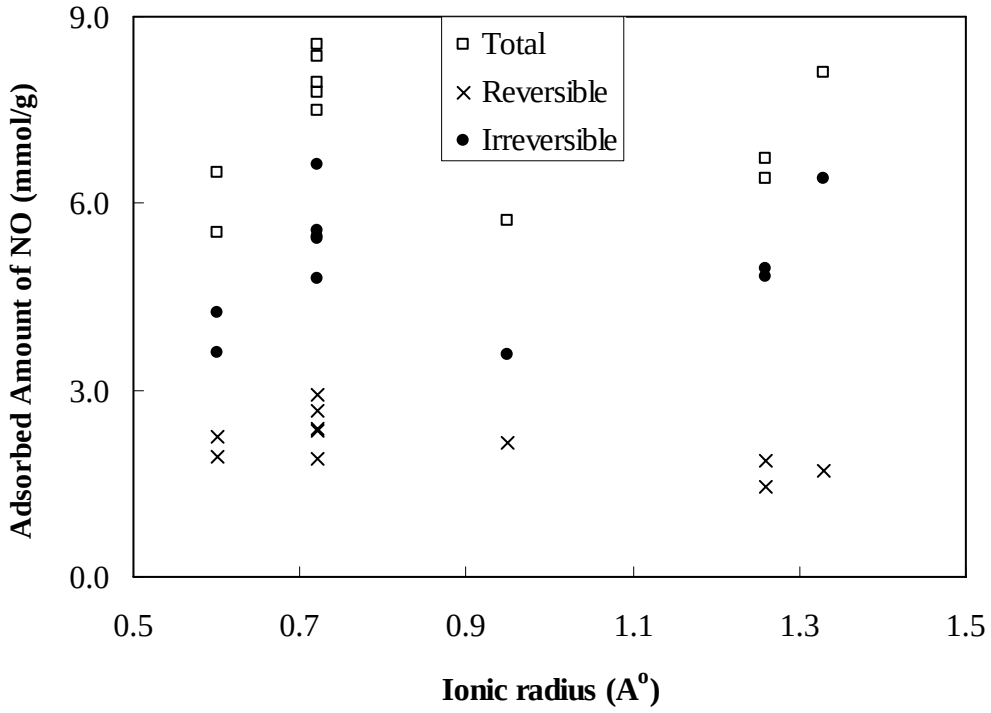

Figure 5.61. Effect of ionic radius on the NO adsorption capacity of the zeolites.

The appreciably lower adsorption capacity of 0.05 M Fe zeolite might be attributed to the presence of oxidized iron species which decreased the interaction between the metal and NO molecules. Recently, the importance of the nature of the iron species for NO adsorption was reported. In that study, it was shown that the sample with reduced iron species (Fe, FeO) showed the highest NO adsorption capacity, indicating that the reduced iron species were very active in NO adsorption. As a consequence, the nature of the iron species present on the samples was proposed to be a key factor for NO adsorption. If the metal cations present in hydroxyl form, the electrostatic interaction with the NO molecules is zero (Alcañiz-Monge et al., 2008).

The effectiveness of a cation in the zeolite for NO adsorption can be more obviously seen in Figure 5.62. In this figure, the total amount of adsorbed NO

molecules per cation atom declined in the similar trend with that in Figure 5.60, except for Na-Clin, 0.05 M Fe and 0.05 M Ag samples.

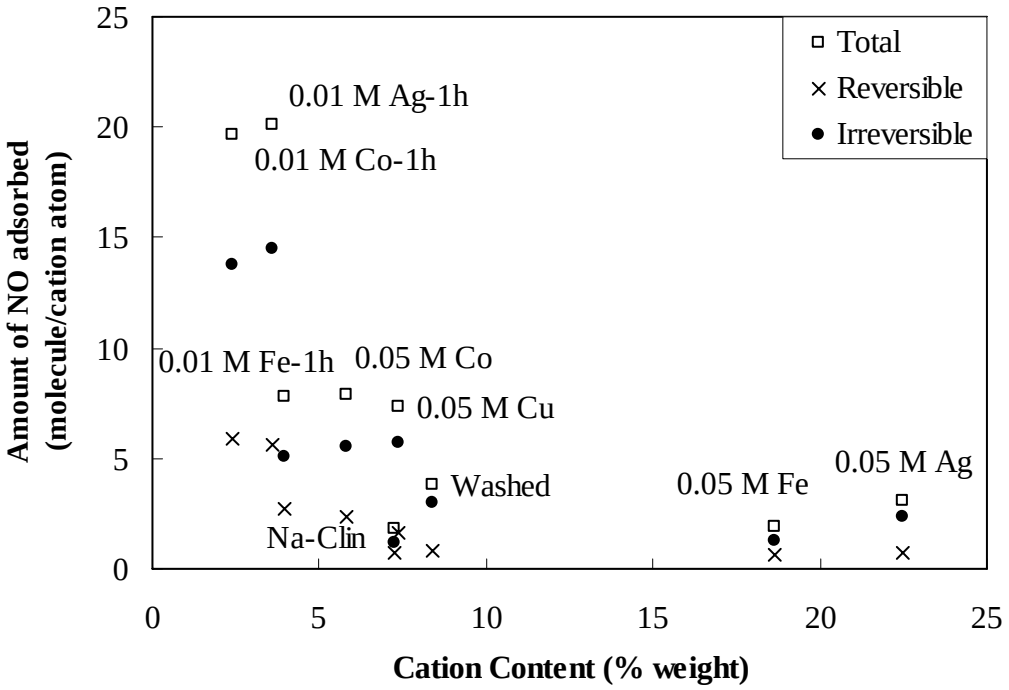

Figure 5.62. Effect of cation type and amount on the NO adsorption capacity in terms of molecule NO adsorbed per cation atom.

In order to examine the effect of cation content on the NO adsorption capacity of the zeolite, cobalt was selected as a model cation since there is relatively large data on its interaction with NO in the literature. The two more cobalt-sorbed zeolite samples were prepared in the manner as described in Chapter 4. The adsorption experiments were performed on these zeolites under the same conditions. The activation was performed in the same manner as for the other zeolites. Figure 5.63 shows the dependencies of the total, reversible and irreversible NO adsorption capacities on the cobalt content of the zeolite. It was found that as the both total and irreversible adsorption capacities increased with the increasing cobalt content up to certain cobalt content. That cobalt content was 5.11 % by weight for the total adsorption capacity, while 2.38 % by weight for the irreversible one. Further increase in the cobalt content of

the zeolite caused the total adsorption capacity to decrease slightly. The irreversible adsorption capacity was not significantly affected by the further increase in the cobalt content up to 5.38 % by weight, but higher cobalt content resulted in a decline in the irreversibly adsorbed NO amount.

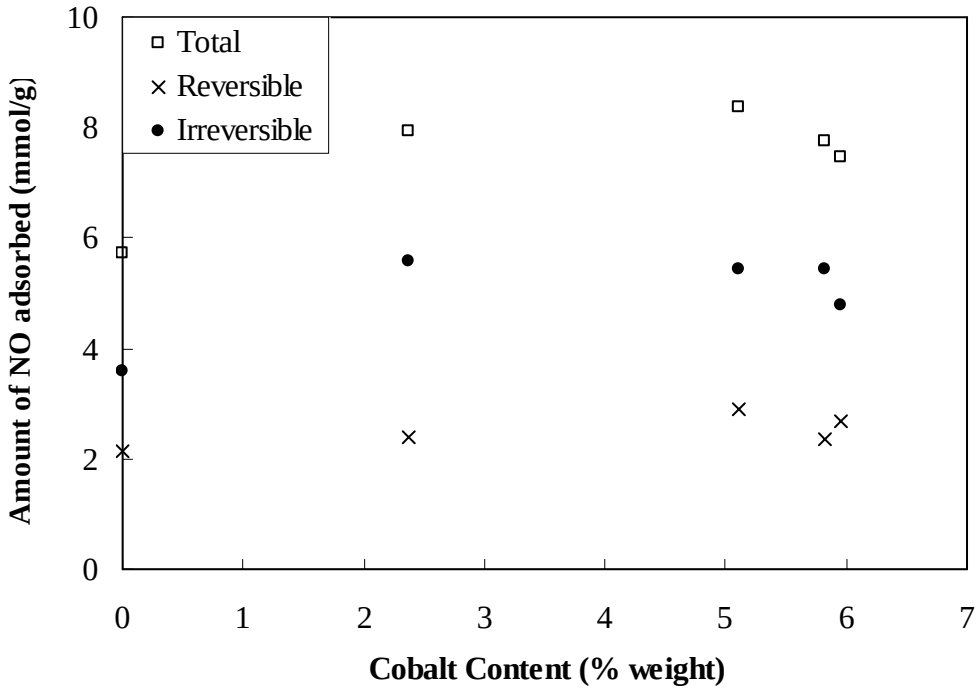

Figure 5.63. Relationship between the NO adsorption capacity and the cobalt content of the zeolite.

In order to examine the effectiveness of each cobalt cation for NO adsorption, the ratio of adsorbed amount of NO to the cobalt content (mol/mol) was examined from Figure 5.64. It followed that the effectiveness of each cobalt ion in the zeolite for NO adsorption was strongly dependent on its loading level. The total, reversibly and irreversibly adsorbed NO amounts were found to be inversely proportional to the cobalt content of the zeolite. The decline in the NO adsorption capacity of the zeolite with the increasing cobalt content can be attributed to the presence of some cobalt oxides and locations of the cobalt cations in the zeolite structure. The presence of cobalt oxides decreased the electrostatic interaction of the zeolite with NO molecules and also these

oxides may block the zeolite pores. The location of cations in the structure affects the accessibility of the adsorbate molecules to these cations. It is known from the literature that cations may change position during activation which might cause the cobalt cations to move to sites inaccessible to NO.

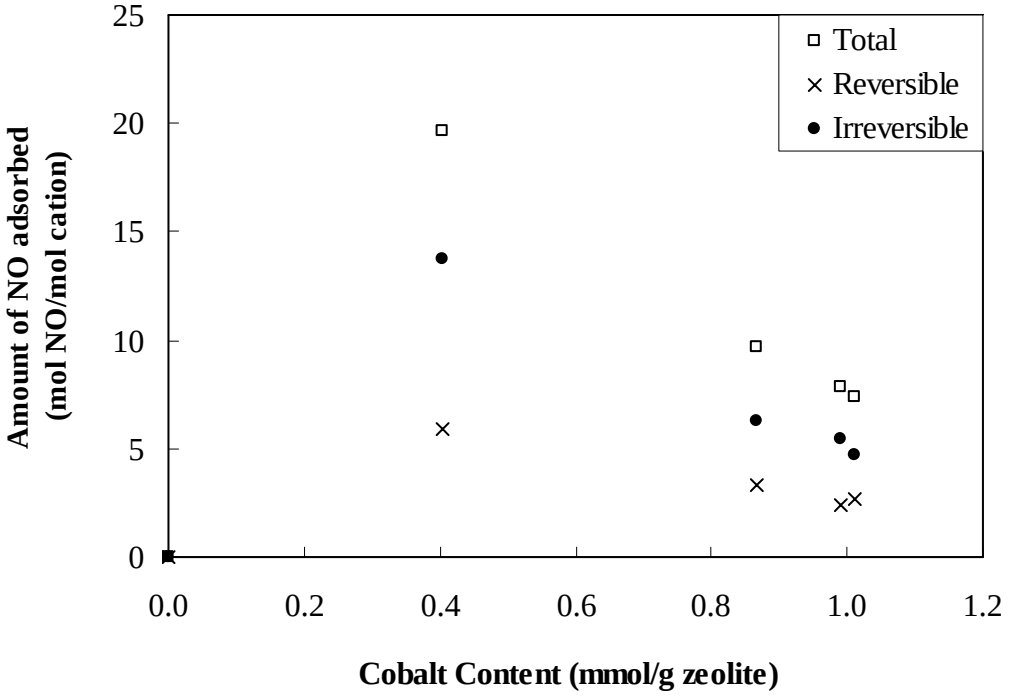

Figure 5.64. Dependence of the total, reversible and irreversible NO adsorption capacities per cobalt cation on the zeolite cobalt content (r^2 is 0.997 for the total adsorption and 0.988 for reversible adsorption).

Ackley et al. emphasized that the nature of the adsorbent-adsorbate and adsorbate-adsorbate interactions is important as much as the pore dimensions (Ackley et al., 2003). NO is a polar molecule so with high dipole and strong quadrupole moment, so it is strongly adsorbed by polar zeolites, but only weakly adsorbed by nonpolar adsorbents (Ruthven, 1984). In the case of the polar adsorbents, high field-gradient-quadrupole and field-dipole interaction prevail between the cations in the zeolite and the NO molecules. Furthermore due to polarizability of NO molecules, polarization energy also contributes to the adsorption energy. The energetic field strength of a zeolite is

determined by the polarizing power of the cations. The polarizing power of the cations is inversely proportional to their ionic radius (Cotton and Wilkinson, 1966).

The adsorption properties of the zeolites also depend on the positions of the cations in the structure that influence the local electric field. Cations located in larger channels have greater accessibility to adsorbate molecules (Yang, 1997). It has been shown that the adsorption capacity and selectivity of zeolites for the polar molecules also increases when the Si/Al ratio decreases (Calleja et al., 1998). A zeolite with smaller Si/Al ratios (higher Al^{3+} content) requires more cations to neutralize the structure so that electric field in the pores increases. Hence, it has higher adsorption capacity for a polar molecule. It is worthless to try to correlate the NO adsorption capacity to the Si/Al ratio of the zeolites in the present study, since the Si/Al ratios of the zeolites were in a very narrow range (5.21-5.81 % by weight).

NO is a strong Lewis base and, when it has a σ-bonded interaction it is more firmly adsorbed on cationic sites. Furthermore, due to an unpaired electron in the NO molecule, NO is adsorbed as dimers (Hadjiivanov et al., 1999). The NO coordination to the unsaturated metal cations in dehydrated zeolites is different from the physical adsorption since it involves electron transfer between them. The chemisorption of NO can be dissociative or molecular, depending on the surface and other conditions. The d-block transition metals on the zeolite surface form a type of bonding referred to as π-complexation due to their partly filled d-orbitals (Yang, 2003). NO has an unpaired electron in the π* orbital. NO forms complexes with all transition metals to give metal nitrosyls. The interaction of d-block transition metals with NO often involves a d-electron and/or an empty d-orbital, which leads to the formation of metal nitrosyls (Richter-Addo and Lezdins, 1992). This species is supposed to be susceptible to decomposition depending on the mode of d-transition metals for NO coordination. NO can bond to one, two or three metal centers, and with the further degree of freedom in the case of single metal center bonding, of being linear or bent at the nitrogen. The most common bonding mode of NO is the terminal linear type (M-NO). The angle of the M-N-O group can vary from 160-180° but are still termed as "linear". In this case the NO group is formally considered a 3-electron donor. Alternatively, one can view such complexes as derived from NO^+, which is isoelectronic with CO. NO can serve as a one-electron pseudohalide. In such complexes, the M-N-O group is characterized by an angle between 120-140°. The NO group can also bridge between metal centers through

the nitrogen atom in a variety of geometries. In a complex with a metal center, the character of the NO ligand can range from that of a nitrosyl cation (NO^+), which binds to the metal with a M-NO angle of ~180°, to that of a nitroxyl anion (NO^-), for which a bond angle of ~120° might be anticipated. In the former case, considerable charge transfer to the metal has occurred, while in the latter, charge transfer is in the opposite direction. The NO group geometry is governed by the charge of NO group together with other parameters such as the coordination number, the coordination geometry and the nature of the highest occupied molecular orbital (Enemark and Feltham, 1974a,b; Feltham and Enemark, 1981).

5.4. Temperature-Programmed Desorption

After the purging the column with pure helium gas flow, the temperature of the adsorbent was increased to 400 °C at a rate of 1 ^oC/min. The composition of the column outlet was continuously monitored by the thermal conductivity detector. As the temperature rises, particular absorbed species were detected as a peak in the TPD profile. The TPD profiles for the zeolites are shown in Figure 5.65. The TPD profiles were found to be significantly different from each other. In these profiles, at least one peak were observed implying the presence of distinct adsorption sites, formation of various surface species, and/or existence of interactions between the adsorbed molecules leading to a variation of the activation energy for the desorption of NO as a function of the coverage. 0.05 M Fe and 0.05 M Co zeolites exhibited significantly different TPD profiles than other zeolites.

The desorption temperatures and the areas of the peaks observed in the TPD spectra are given in Table 5.30. All the zeolites exhibited a peak in the 80-90 ^oC range. This low-temperature peak indicated the presence of relatively weakly adsorbed species on the zeolite surface. The area of the peak is related to the concentration of the weakly adsorbed species. This peak was symmetrical for all zeolites except for 0.05 M Co sample. In the profile of 0.05 M Co, the peaks at 85 ^oC and at 121 ^oC could not be resolved. 0.05 M Fe sample showed a very weak peak in this temperature range. The

small difference in the desorption temperature of the first peak indicated that the active sites of the zeolites for this weakly adsorbed species were very similar.

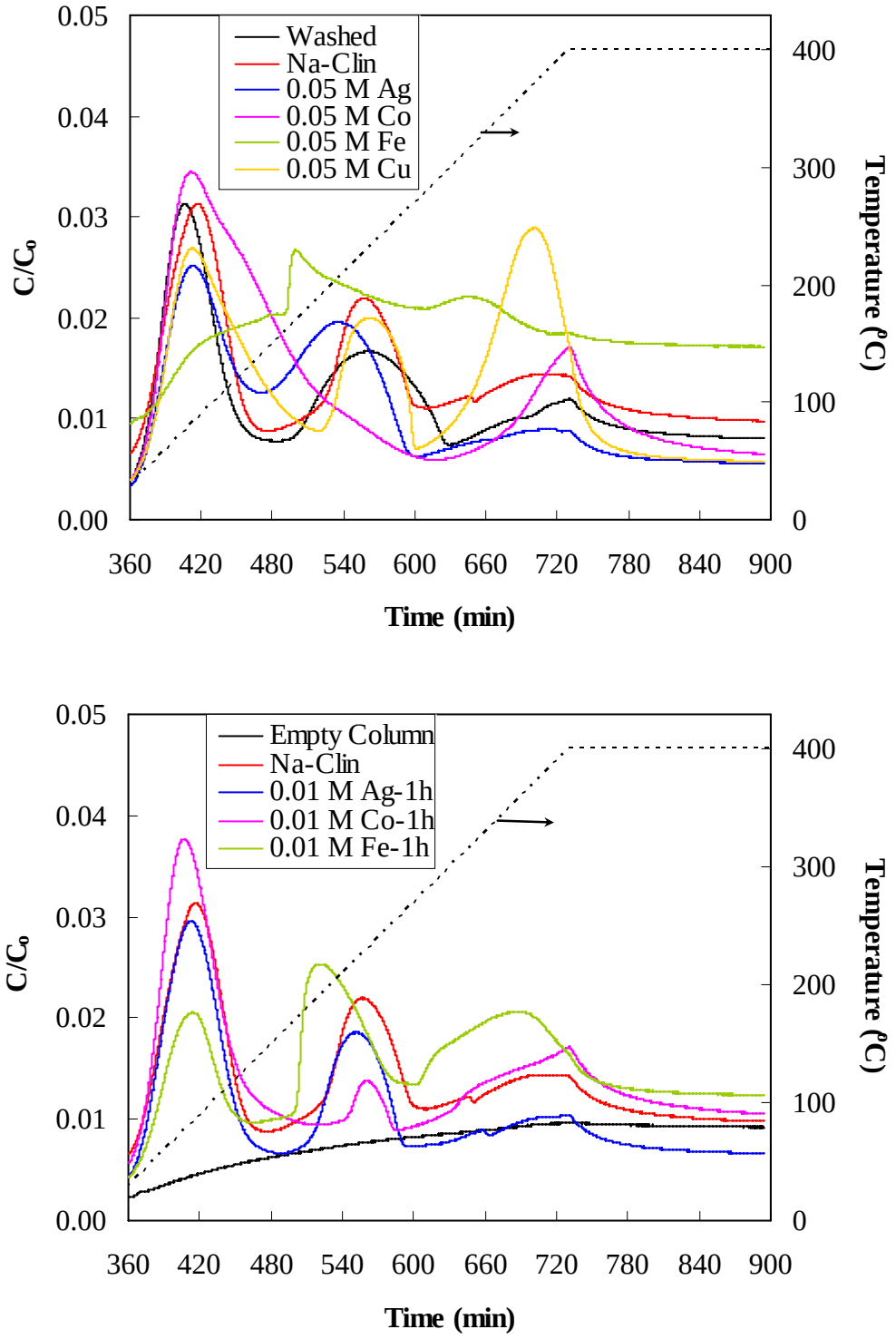

Figure 5.65. TPD profiles for the zeolite samples with different cation content.

The zeolites exhibited another common peak in the temperature range of 150-240 ^{o}C. The desorption temperature and area of this peak was significantly lower for 0.05 M Fe sample implying the lower and weaker interaction of NO with 0.05 M Fe sample. The area of this peak was notably higher in the profile of 0.01 M Fe-1h. The difference between the two iron-sorbed zeolites might be attributed to the iron content as well as the state and location of the iron species in the zeolite. The same explanation may be valid for the cobalt-sorbed zeolites. In the TPD spectra of 0.05 M Cu sample, a peak observed at 376 ^{o}C which was not observed in any other spectra designated the formation of more stable species on this sample. The presence or absence of desorption peak can also be interpreted in terms of accessibility of the active sites to NO molecules.

Table 5.30. Desorption temperatures and areas of the peaks in the TPD spectra.

Sample	Temperature of peak maxima (^{o}C) and Peak Area				
	1st peak	2nd peak	3th peak	4th peak	5th peak
Washed	80	235	357 (sh)	366 (sh)	400 (w)
Peak Area	1604760	889835			532621
Na-Clin	91	231	319 (sh)	380 (sh)	400 (w)
Peak Area	1599070	778280			472458
0.05 M Co	85	121 (sh)	210 (sh)		400
Peak Area	3845850				1085950
0.05 M Ag	87	210	334 (sh)	384 (sh)	400 (w)
Peak Area	1126620	927328			399549
0.05 M Fe	82	152	327 (w)		400 (w)
Peak Area	245879	342674	145664		7718.32
0.05 M Cu	87	236			372
Peak Area	1851440	814688			1991550
0.01 M Co-1h	80	233 (w)	318 (sh)		400
Peak Area	2200340	164851			1117570
0.01 M Ag-1h	87	226	331 (sh)		400 (w)
Peak Area	1643840	759667			433101
0.01 M Fe-1h	84	194	288 (sh)		361
Peak Area	823843	923868			967504
w: weak, sh: shoulder					

The desorption temperatures for 0.05 M Co zeolite were similar to those reported for Co-A obtained by ion exchange. In the TPD spectra for Co-A zeolite after NO adsorption three peaks were observed at 77, 137 and 217 ^{o}C. It was shown by mass spectrometer detector that most of adsorbed NO desorbed as NO_2 at 289 ^{o}C. The peak at 77 ^{o}C was assigned to physically adsorbed NO and that at 137 ^{o}C to adsorption of NO on sites different from tricoordinated Co^{2+} (Henao et al., 2004). This type of interaction is possible by either migration of metal cations to more accessible positions during NO adsorption (Lunsford et al., 1978) or ability of NO to form nitrosyl complexes with sodium cations remained in the zeolite structure after ion exchange (Pöppl et al., 2000).

It was expected that the sum of the peak areas in the TPD spectra is related to the irreversibly adsorbed NO amount, but very poor correlation (r^2 =0.31) was obtained.

5.5. Diffuse Reflectance Infrared Spectroscopy (DRIFTS)

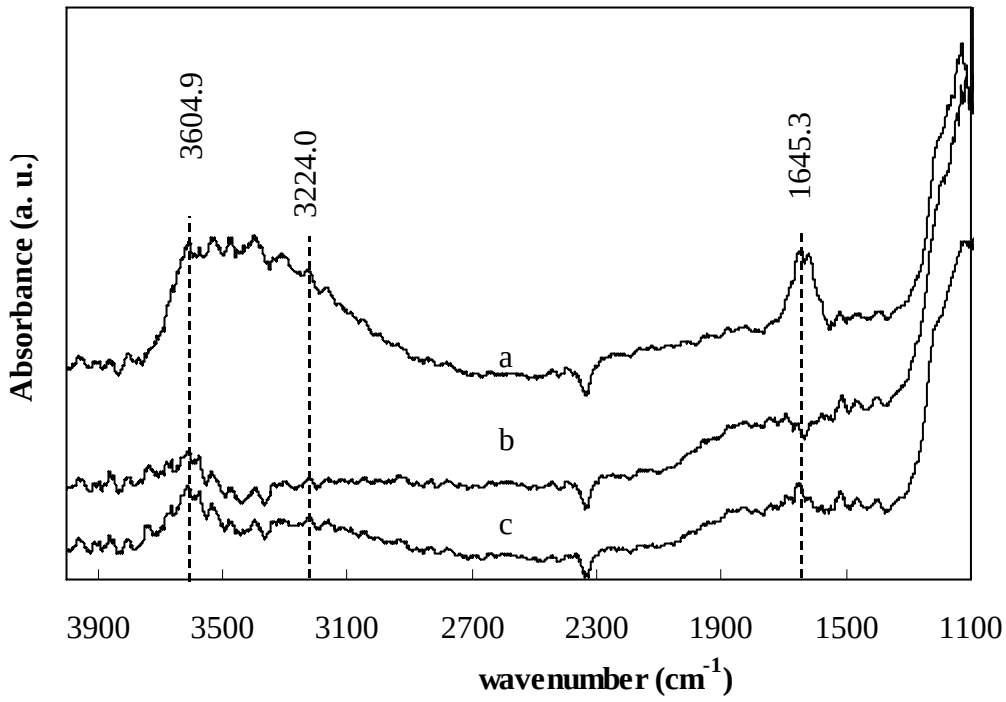

Figure 5.66. DRIFT spectra of Washed zeolite-KBr mixture a, before activation (at 30 ^{o}C, 1 atm); b, after heating to 400 ^{o}C under 2×10^{-4} mbar for 24 hours; and c, after activation (cooled to the adsorption temperature under vacuum).

The DRIFT spectra of Washed zeolite before and after the insitu activation (at 400 ^{o}C, under 2×10^{-4} mbar, overnight) are shown in Figure 5.66. The spectrum c which shows the state of the zeolite surface before adsorption was used as a background for the assignments of the bands to the species adsorbed. The degree of activation can be evaluated based on the absence or presence of the band at 1645.3 cm^{-1} which is assigned to the usual bending vibration of water (Breck, 1974). This peak was not detected in the spectrum collected at 400 ^{o}C (spectrum b). However, during cooling the zeolite to the adsorption temperature, the intensity increased slightly.

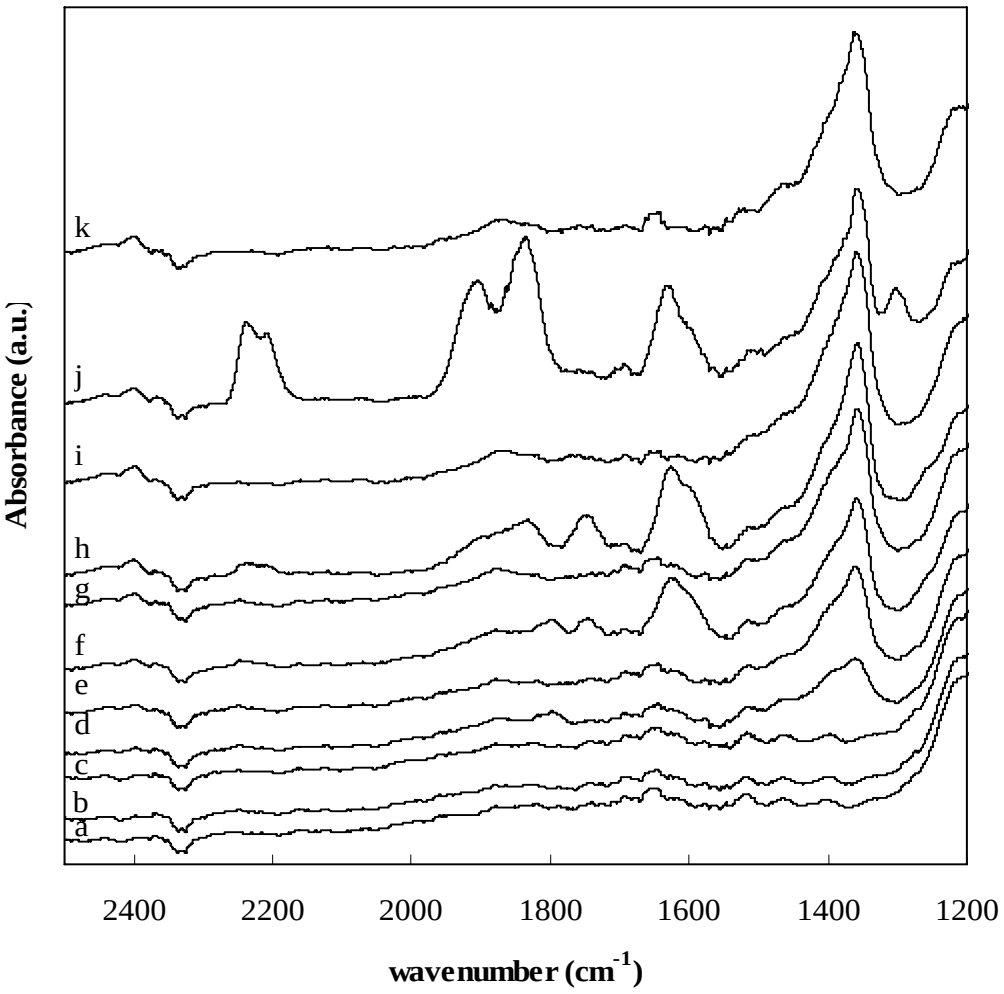

Figure 5.67. DRIFT spectra of Washed-KBr mixture during NO adsorption and successive evacuation at 30 ^{o}C: a, activated; b, 45 mbar NO; c, vacuum after 45 mbar NO; d, 100 mbar NO; e, vacuum after 100 mbar NO; f, 200 mbar NO; g, vacuum after 200 mbar NO; h, 500 mbar NO; i, vacuum after 500 mbar NO; j, 1000 mbar NO; k, vacuum after 1000 mbar NO (vacuum at 10-1 mbar for 15 minutes).

DRIFT spectra of Washed zeolite-KBr mixture after the weakly adsorbed species were removed following the introduction of 45, 100, 200, 500 and 1000 mbar NO were shown in Figure 5.67. Exposure of Washed zeolite-KBr mixture to NO at 30 ^{o}C produced various IR-bands in the range of 1300-2400 cm^{-1}.

When NO at 45 mbar was introduced to the sample, no change was observed in the spectrum. After increasing the NO pressure to 100 mbar a strong band appeared at 1358.8 cm^{-1} with shoulder bands at 1390.7, 1464.0 and 1520.9 cm^{-1}. A weak band at 2399.4 cm^{-1} was also appeared in the spectra. A weak band at 1794.8 cm^{-1} was also observed. When the reaction cell was evacuated for 15 minutes, the intensities of 1358.8 and 1390.7 cm^{-1} increased significantly and that of 1464.0 cm^{-1} slightly. The intensity of the band at 1520.9 cm^{-1} did not change. The band at 1801.6 cm^{-1} disappeared. The intensity of the 2399.4 cm^{-1} increased slightly.

Following the introduction of 200 mbar NO to the sample, a new strong band was detected at 1627.9 cm^{-1} with a shoulder at 1608.3 cm^{-1}. The intensities of the bands at 1358.8, 1390.7, 1464.0 cm^{-1} and 2399.4 cm^{-1} continued to increase. The intensity of the band at 1520.9 cm^{-1} did not change. A new band appeared 1750.4, and 1878.7 cm^{-1} and the band at 1794.8 cm^{-1} reappeared. Following the evacuation, the bands at 1750.4 and 1794.8 cm^{-1} disappeared. No changes were observed either intensity or frequency of the band at 1878.7 cm^{-1}. The intensities of the bands at 1358.8, 1390.7, 1464.0 cm^{-1} and 2399.4 cm^{-1} continued to increase. The intensity of the band at 1520.9 cm^{-1} did not change. The band at 1627.9 cm^{-1} with a shoulder at 1608.3 cm^{-1} disappeared.

Upon introduction of 500 mbar NO, the intensity of the band 1358.8 cm^{-1} increased significantly, while that of 1390.7 cm^{-1} slightly. The intensities of the bands at 1464.0 and 1520.9 cm^{-1} did not change. The band previously occurred at 1627.9 cm^{-1} reappeared with higher intensity and with prominent shoulder band at 1608.3 cm^{-1}. The bands at 1750.4 cm^{-1} reappeared, and a new band occurred at 1835.3 cm^{-1} with a shoulder at 1900.0 cm^{-1}. A weak band was detected at 2237.4 cm^{-1}. Slight increase was observed in the intensity of the band at 2399.4 cm^{-1}. After evacuation the intensities of the bands at 1358.8, 1392.6, 1464.0 and 1520.9 cm^{-1} did not change further. The band at 1627.9, 1750.4, 1835.3, 1900.0 and 2237.4 cm^{-1} vanished. The intensity of the band at 2399.4 cm^{-1} increased slightly.

Introduction of 1000 mbar NO increased, a new band appeared at 1303.9 cm^{-1}. The band at 1510.2 cm^{-1} shifted to 1520.9 cm^{-1}. The band at 1627.9 cm^{-1} shifted to 1631.8 cm^{-1} and its intensity increased. The shoulder to this band appeared previously

was detected again with slightly lower intensity and at the same frequency, 1608.3 cm^{-1}. A very weak band appeared at 1694.5 and a shoulder appeared at 1761.0 cm^{-1}. Similarly a broad band with two peaks at 2237.4 and 2208.5 cm^{-1} appeared in the spectrum. The intensity of the 2399.4 cm^{-1} band continued to increase gradually with a shoulder at 2362.8 cm^{-1}. Upon evacuation at the adsorption temperature, the 1303.9 cm^{-1} band disappeared. A minor increase was observed in the intensity of the 1358.8 cm^{-1} band. No change was observed in the intensity of 1464.0 cm^{-1}. The band appeared at 1510.2 cm^{-1} returned to previous frequency (1520.9 cm^{-1}) and intensity. The broad band at 1631.8 cm^{-1} and the shoulder band 1608.3 cm^{-1} vanished. The weak bands at 1694.5 and 1761.0 cm^{-1} disappeared. By the disappearance of the bands at 1835.3 cm^{-1} and 1905.7 cm^{-1}, the band at 1878.7 cm^{-1} was detected in the spectrum again. The broad band with peaks at 2237.4 and 2208.5 cm^{-1} disappeared. The intensities of the bands at 2399.4 cm^{-1} and 2362.8 cm^{-1} declined.

Figure 5.68 shows the changes in the spectra upon the evacuation, heating and exposure to the atmosphere successive to the saturation at 1000 mbar NO. The bands appeared in the spectrum after adsorption of NO at 1000 mbar (at 1303.9, 1358.8, 1390.7, 1464.0, 1510.2, 1608.3, 1631.8, 1694.5, 1761.0, 1835.3, 1905.7, 2208.5, 2237.4, 2362.8 and 2399.4 cm^{-1}) were accepted as both the weakly and strongly adsorbed species at saturation. At this stage, the surface of the zeolite can be accepted in the equal state as that after the saturation of the column and before the helium purge in the packed column experiments.

After evacuation at 30 ^{o}C under 10^{-1} mbar, the bands at 1358.8, 1390.7, 1464.0, 1520.9, 1878.7, 2362.8 and 2399.4 cm^{-1} remained. When the vacuum was increased to 2×10^{-4} mbar at the adsorption temperature, the intensity of the band at 1358.8 slightly decreased. A minor rise in the intensity of the band at 2362.8 cm^{-1} was observed. The surface of the zeolite can be assumed is in the same state as that after the helium purge successive to the saturation in the packed column runs. Therefore, the bands vanished during the evacuation (under 2×10^{-4} mbar, at 30 ^{o}C) can be accepted as to belong the reversibly (weakly) adsorbed species, i.e. the 1303.9, 1510.2, 1608.3, 1631.8, 1761.0, 1835.3, 1905.7, 2208.5, and 2237.4 cm^{-1} bands. The species that were remained on the zeolite surface after the evacuation step (under 2×10^{-4} mbar, at 30 ^{o}C) corresponding to the bands at 1358.8, 1390.7, 1464.0, 1520.9, 1878.7, 2362.8 and 2399. 4 cm^{-1} can be accepted as irreversibly (strongly) adsorbed ones. At this stage, the surface of the zeolite

can be accepted at the same state as that after the helium purge step in the packed column experiments. Hence, the zeolite obtained after the evacuation step at the adsorption temperature was assumed to correspond to those tested for the release (Washed-NO), however exposure of the sample to the atmosphere during depacking of the column and exposure during weighing for the release experiments must be taken into account.

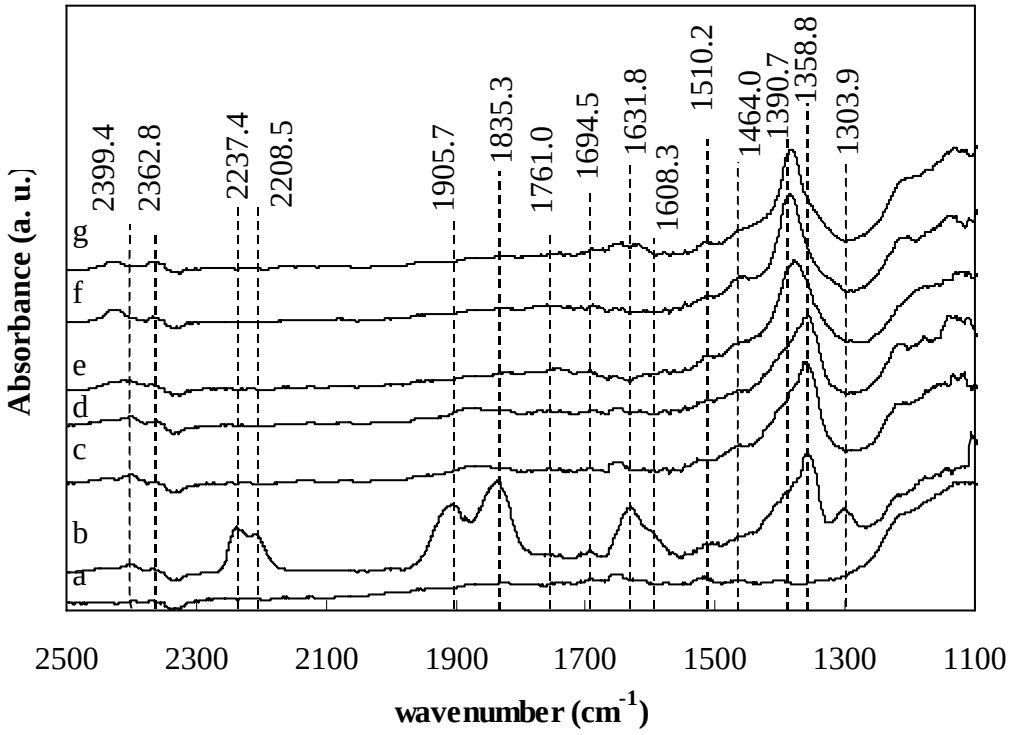

Figure 5.68. DRIFT spectra of Washed zeolite-KBr mixture obtained successive to the saturation with 1000 mbar NO: a, activated zeolite; b, after 1000 mbar NO adsorption; c, after vacuum at 10^{-1} mbar, 30 ^{o}C successive to the 1000 mbar NO adsorption; d, after vacuum at 2×10^{-4} mbar, 30 ^{o}C successive to the 1000 mbar NO adsorption; e, after vacuum at 2×10^{-4} mbar, 400 ^{o}C; f, cooling to 30 ^{o}C under vacuum; and g, after the sample was opened to the atmosphere.

When the temperature increased to 400 ^{o}C under vacuum, the band at 1358.8 cm^{-1} (this band) shifted to 1378.1 cm^{-1}. The bands at 1390.7 and 1878.7 cm^{-1} disappeared. A new band at 1750.4 cm^{-1} was detected. No change in either intensity or frequency of the band at 2399.4 cm^{-1} was observed. The intensities of the bands at

1464.0 and 1520.9 cm^{-1} increased. This state of the surface can be accepted to correspond to that after the TPD run before the cooling step. Therefore the bands that were removed during the evacuation at 400 ^{o}C (1390.7 and 1878.7 cm^{-1}) can be correlated with the peaks in the TPD profile.

After cooling the zeolite to 30 ^{o}C under vacuum, the band at 1358.8 cm^{-1} further shifted to 1385.9 cm^{-1} without significant change in the intensity. The intensities of the 1464.0, 2362.8 and 2399.4 cm^{-1} remained unchanged. The band at 1750.4 shifted to 1761.0 cm^{-1} without change in its intensity. The 1520.9 cm^{-1} lost intensity.

When the sample was opened to the atmosphere, the band at 1761.0 cm^{-1} disappeared. The band at 1645.3 cm^{-1} reappeared. It should be noted that the bending mode of water is also associated with a band in this region. No variation was observed in the intensities of the bands at 1520.9, and 2362.8 cm^{-1}. The intensities of the bands at 1385.9, 1464.0 and 2399.4 cm^{-1} decreased. The bands at 1385.9, 1464.0, 1520.9, 2362.8 and 2399.4 cm^{-1} that remained in the spectrum were those stable to evacuation and heating. The surface of the zeolite can be accepted as the same as that of “Washed-NO-Des” sample.

The zeolites that were used in the antibacterial, bactericidal or release in PBS/water experiments were those obtained at the different stages of the adsorption, purging (removal of weakly or reversibly adsorbed species at adsorption temperature either under vacuum or under helium flow) and the successive thermal treatment at 400 ^{o}C steps. The sample obtained after the evacuation step correspond to “Washed-NO” sample that was obtained under the dynamic adsorption runs with only exception that the zeolite obtained at the end of the evacuation step was not exposed to the atmosphere. The sample obtained after the evacuation at 400 ^{o}C, cooling and exposure to the atmosphere corresponded to “Washed-NO-Des”.

All the spectra collected were for the mixture of Washed zeolite and KBr. The DRIFT spectra of the KBr collected under the same conditions revealed that NO interacts with KBr and the bands due to this interaction are common to those in the spectrum of the mixture. Therefore the spectra of Washed zeolite-KBr must be corrected for the KBr, in order to determine the bands belong to the reversibly and irreversibly adsorbed species on Washed zeolite.

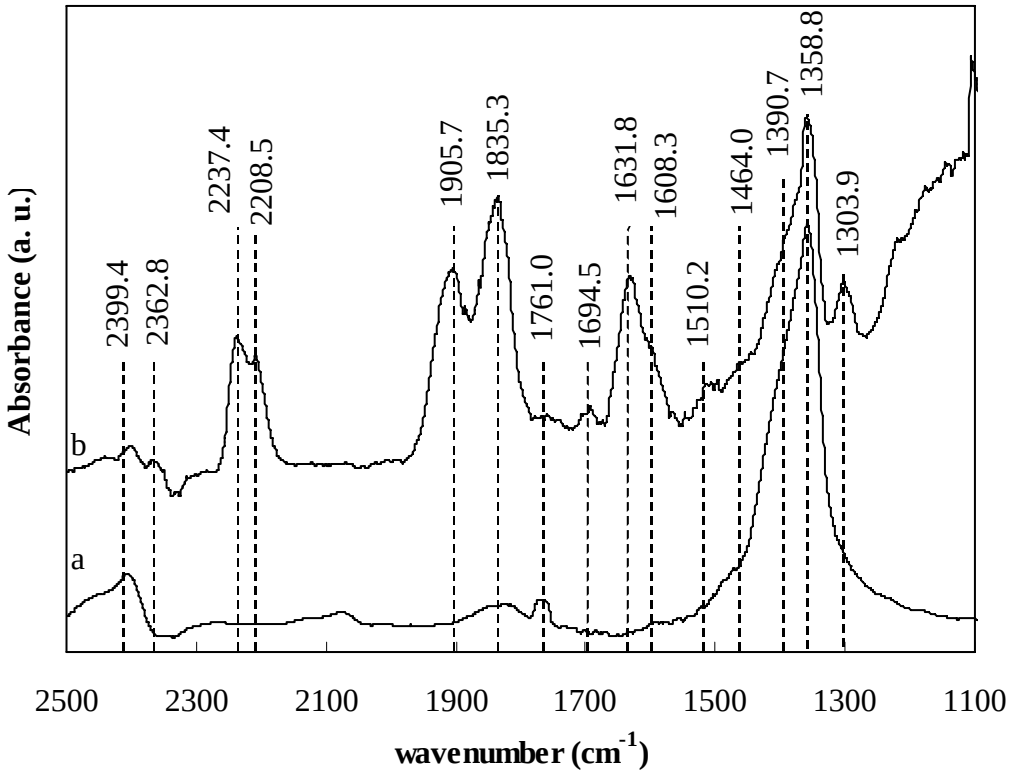

Figure 5.69. DRIFT spectra collected after 1000 mbar NO adsorption at 30 ^{o}C, a, pure KBr ; b, Washed zeolite-KBr mixture.

The spectrum of Washed zeolite-KBr mixture after saturation with NO at 1000 mbar was compared with tat of pure KBr collected under the same conditions in Figure 5.69. When the DRIFT spectrum of the Washed zeolite-KBr collected after 1000 mbar NO adsorption was compared with the corresponding spectrum of pure KBr, it was revealed that the bands at 1358.8, 1464.0, 1761.0, and 2399.4 cm^{-1} were common. The uncommon bands (at 1303.9, 1390.7, 1510.2, 1608.3, 1631.8, 1694.5, 1835.3, 1905.7, 2208.5, 2237.4 and 2362.8 cm^{-1}) can be attributed to the reversibly and irreversibly adsorbed species on Washed zeolite.

The spectra of Washed zeolite-KBr mixture and pure KBr after evacuation under 2×10^{-4} mbar at 30 ^{o}C following the saturation (after the reversibly adsorbed species were removed from the surface) were compared in Figure 5.70. The bands at 1390.7, 1520.9, 1645.3, 1878.7 and 2362.8 cm^{-1} were detected only in the spectra of Washed zeolite-KBr mixture, therefore they were assigned to the irreversibly adsorbed species on Washed zeolite.

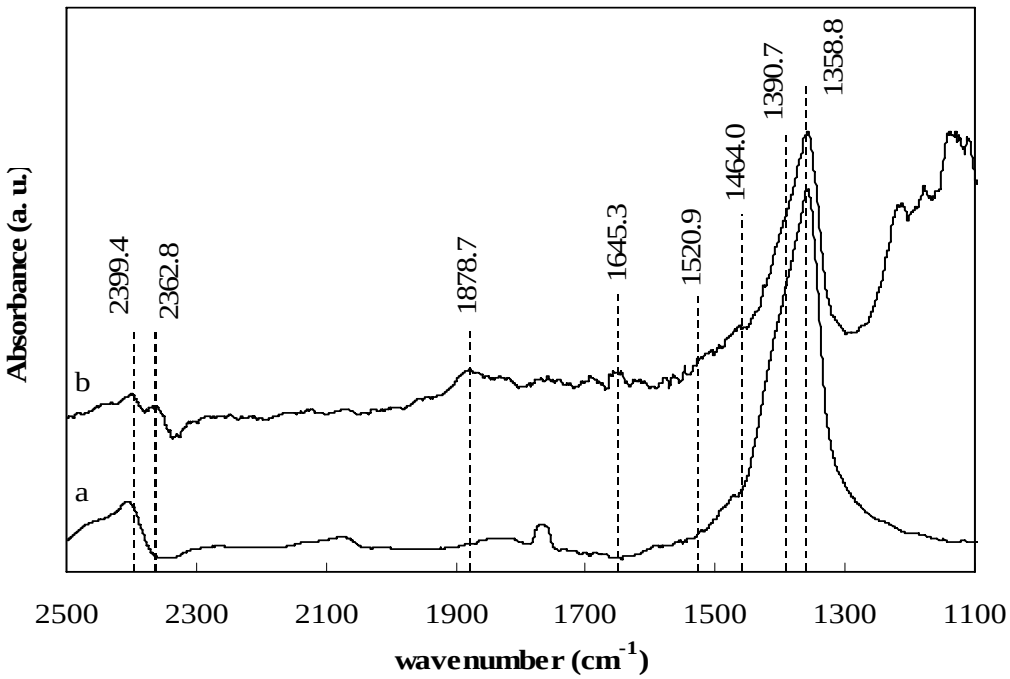

Figure 5.70. DRIFT spectra collected after evacuation at 30 ^{o}C successive to the 1000 mbar NO adsorption, a, pure KBr ; b, Washed zeolite-KBr mixture.

The band at 1358.8 cm^{-1} is close to the bands of NO_3^- species induced upon adsorption of NO on NaY and CaY zeolites (1400 cm^{-1}) (Chao and Lunsford, 1971). The surface nitrate species exhibited two bands together, one in the 1250-1350 cm^{-1} region and the other in the 1540-1558 cm^{-1} range. The detection of this peak in the absence of oxygen was attributed to the oxidation of NO using the surface hydroxyls or lattice oxygen atoms as oxidation source. The nitrates and nitrospecies are formed with the participation of lattice oxygen (Ivanova et al., 2001).

Table 5.31 summarizes the changes in the frequency and area of 1358.8 cm^{-1} band detected in the spectra of Washed zeolite-KBr mixture under different conditions.

Table 5.31. Change in the area and the frequency of the 1358.8 cm^{-1} band.

NO pressure (mbar)	Area		wavenumber (cm^{-1})
	before vacuum	after vacuum	
45	0	0	-
100	12.29	33.66	1358.8
200	39.36	44.53	1358.8
500	40.66	59.44	1358.8
1000	32.05	46.88	1358.8
30 ^{o}C, 2×10^{-4} mbar	-	42.39	1358.8
400 ^{o}C, 2×10^{-4} mbar	-	39.58	1378.1
30 ^{o}C, 2×10^{-4} mbar	-	40.69	1385.9
30 ^{o}C, open to atmosphere	-	51.80	1385.9

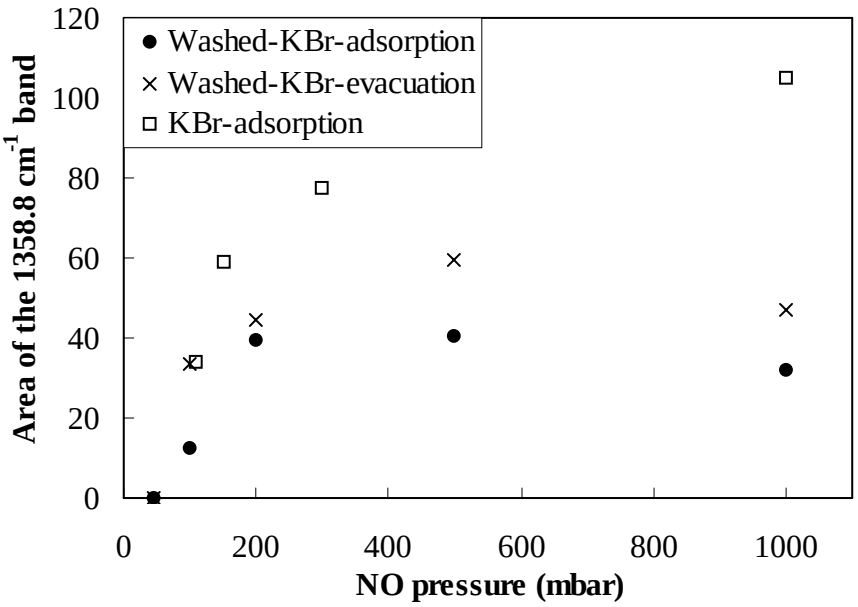

Figure 5.71. Change in the area of 1358.8 cm^{-1} band upon NO adsorption and evacuation for Washed-KBr mixture and pure KBr.

Figure 5.71 shows the variation of the area of 1358.8 cm^{-1} band upon NO adsorption as well as upon evacuation. The data was also given in Table 5.32. For Washed-KBr, the area of the band increased with increasing NO pressure and started to decrease upon adsorption of NO at 1000 mbar. The evacuation caused the band area to increase. The areas for pure KBr were higher than those for the mixture within the

entire NO pressure range. It increased continuously with NO pressure in the spectra of pure KBr. The ratio of the area for Washed-KBr mixture to that for pure KBr was around 35% for the entire pressure range. Regarding the KBr content of the powder (90 % by weight), the ratio cannot be explained by the individual contributions from the constituents of the powder. On the other hand the integration limits for the area calculations were 1305.8 cm^{-1} and 1558.5 cm^{-1}, so the bands at 1390.7, 1464.0 and 1520.9 cm^{-1} were also included within the area. This was unavoidable due to the broadness of the band and determination of the area requires deconvolution of this broad band.

Table 5.32. Change in the area and the frequency of the 1358.8 cm^{-1} band for pure KBr.

NO pressure (mbar)	Area (before vacuum)	Wavenumber (cm^{-1})
110	33.95	-
150	58.87	1358.8
300	77.37	1358.8
1000	105.12	1358.8
30 ^{o}C, 2×10^{-4} mbar	117.01	1358.8

The course of intensity of the same band was also investigated. Figure 5.72 illustrates the variation of the intensity with NO pressure and compares the trend for Washed-KBr mixture with that for pure KBr. The intensity in the spectra of pure KBr was higher than that of Washed-KBr indicating the significant contribution from the KBr. Contrary to the area ratio, the intensity ratio was not constant in the NO pressure range. It can be suggested that the Washed-KBr mixture exhibited a behavior different from the pure KBr regarding the intensity of 1358.8 cm^{-1} band.

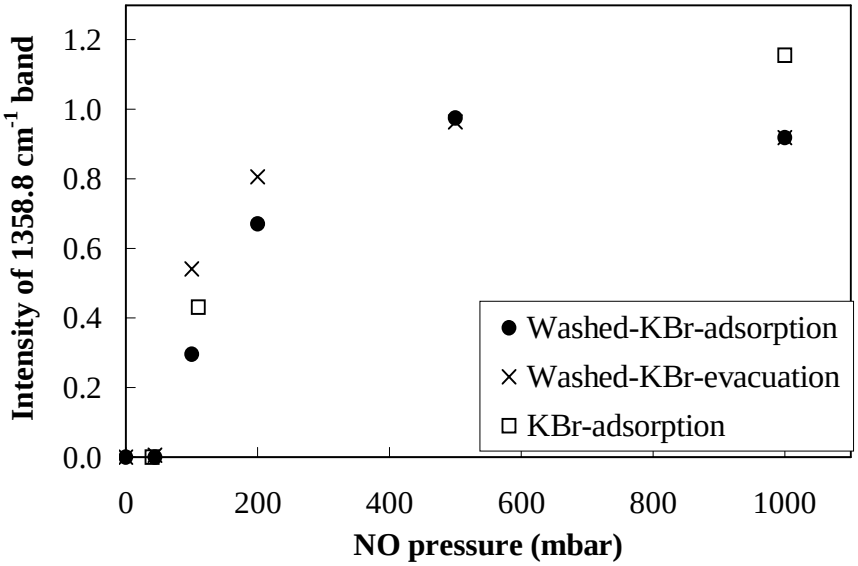

Figure 5.72. Change in the intensity of 1358.8 cm^{-1} band as a function of NO pressure for pure KBr and for Washed-KBr mixture.

In order to eliminate the effect of KBr, Washed zeolite without diluted with KBr was used, but no interpretable spectrum could be acquired even Washed zeolite of different particle sizes was tested. The level of DRIFTS signal is dependent on the scattering coefficient, which is strongly dependent of the particle size and the packing density of the sample. Therefore, only qualitative comparisons of the band intensities were made from one sample to another. However, the quantitative evaluation of the signals is justified for a single sample at different gas loading.

In the transmission spectra of the NO loaded zeolites, the sharp and intense band was detected at 1384.9 cm^{-1}. Therefore the 1384.9 cm^{-1} band was attributed to the species formed on the zeolites upon NO adsorption. Although there was no relationship between the intensity of the band and the NO adsorption capacities of the zeolites, it was applied for qualitative analysis: The detection of the band with decreased intensity in the transmission spectra collected after heating the NO-loaded zeolite to 400 ^{o}C can be inferred as the partial desorption of the species. The absence of the band in the transmission spectra of the zeolites those were used in the release experiments can be explained by the release of the species related to this band to the solution.

The transmission spectra were collected using KBr pellets. The zeolite amount in the pellets was in 0.5 % by weight which is 20 times lower than that in the powder

mixture used in the DRIFTS studies. Furthermore the KBr that was used for the preparation of the pellets was not exposed to NO. Therefore it can be suggested that the species adsorbed on the zeolite must have contributed to the band at 1358.8 cm^{-1} in the DRIFTS spectra, but quantitative analysis is not reliable based on this band. On the other hand, the band was not detected in the transmission spectra of the zeolites that were heated to 400 ^{o}C under helium flow, but the DRIFT studies showed the thermal stability of this band. Regarding the thermal stabilities, the 1358.8 cm^{-1} does not correspond to the band observed at 1384.9 cm^{-1} in the transmission spectra.

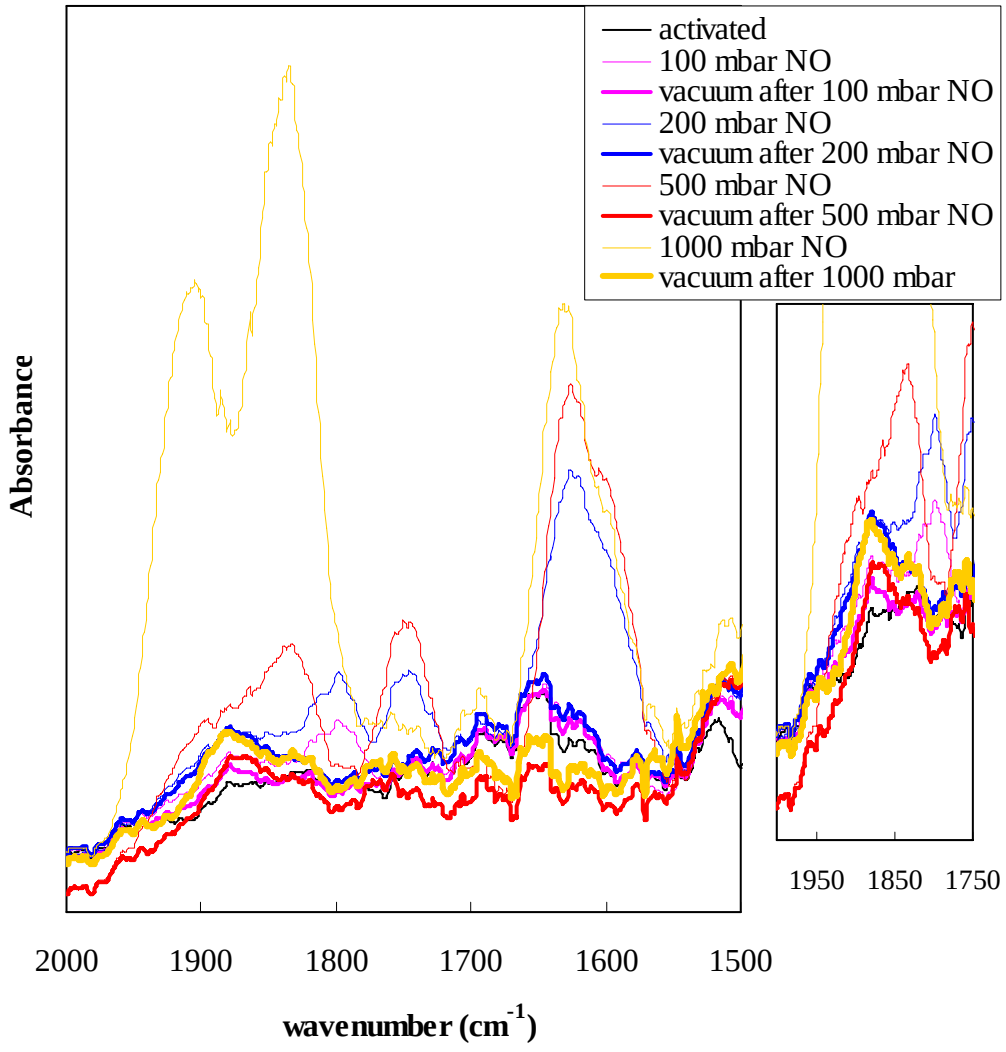

Figure 5.73. DRIFT spectra of Washed zeolite-KBr mixture collected during NO adsorption and evacuation.

The 1500-2000 cm^{-1} region of Washed zeolite-KBr mixture collected during adsorption and evacuation is shown in Figure 5.73. The progress of 1878.8 cm^{-1} band can be followed more evidently from the inset figure. This band first appeared in the spectra after admission of 100 mbar NO and after evacuation remained in the spectra. Adsorption of NO at 200 mbar, the intensity of this band increased. New bands appeared at 1878.8, 1794.8, 1750.4, and 1627.9 with a shoulder at 1608.3 cm^{-1}. Following the evacuation the intensity of the 1878.8 cm^{-1} band did not change, all other bands vanished. When NO was introduced at 500 mbar, the intensity of 1878.8 cm^{-1} band did not change. New bands were detected at 1835.3, 1750.4, and 1627.9 with a shoulder at 1608.3 cm^{-1}. After evacuation all the bands were removed from the spectra, but 1878.8 cm^{-1} band remained without change in the intensity. The detection of this band in the transmission spectra is impossible due to its low intensity. Therefore the comparison between the transmission and DRIFT spectra based on this band is not possible.

Upon introduction of 1000 mbar NO, very broad and strong band with two peaks appeared at 1905.7 and 1835.3 cm^{-1}. The 1878.8 cm^{-1} band was masked by this band so could not be detected. The band previously observed at 1627.9 cm^{-1} was detected at 1631.9 cm-1 with a shoulder at 1608.3 cm^{-1}. After evacuation, by the disappearance of the broad band at 1905.7 and 1835.3 cm^{-1}, 1878.8 cm^{-1} band became visible with the same intensity. Upon evacuation 1878.8 cm^{-1} band remained unchanged while the other bands vanished.

When the zeolite was heated to 400 ^{o}C under vacuum, 1878.8 cm^{-1} band disappeared and a broad but weak band appeared in that region with a peak at 1750.4 cm^{-1}. The cooling of the zeolite under vacuum did not cause a significant change in this region of the spectrum. Upon exposure of the zeolite to the atmosphere all the bands disappeared and a weak band was observed at 1645.3 cm^{-1} which was assigned to usual bending vibration of water.

The stability of species formed on Washed zeolite upon exposure to the atmosphere was also examined. Figure 5.74 shows the changes in the spectrum of Washed zeolite-KBr mixture upon exposure to 1000 mbar NO, successive evacuation and exposure to the atmosphere for 15 minutes and for 12 hours. The 1878.7 cm^{-1} band shifted to 1855.5 cm^{-1} upon exposure the sample to the atmosphere and disappeared from the spectrum after 12 hours.

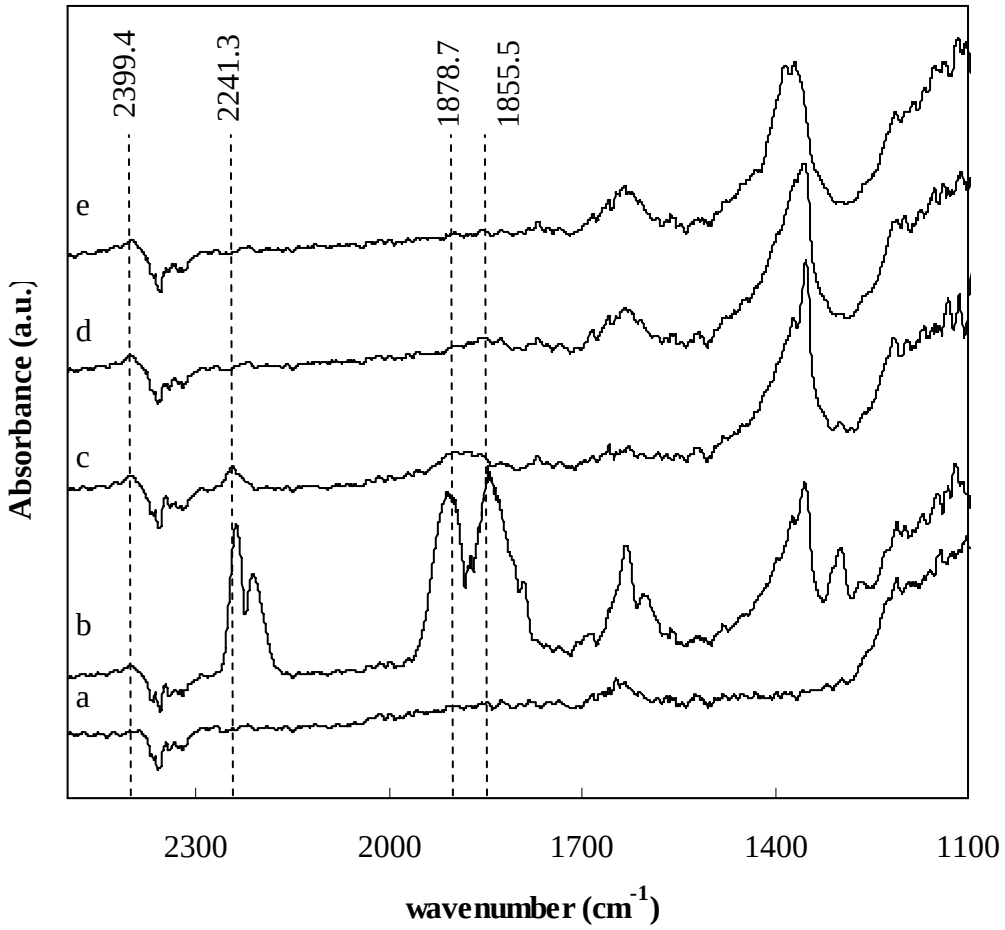

Figure 5.74. DRIFT spectra of Washed zeolite-KBr mixture for adsorption of 1000 mbar NO. a, activated; b, adsorption of 1000 mbar NO; c, evacuation; d, exposure to the atmosphere for 15 minutes; e, exposure to the atmosphere for 12 hours.

Regarding the changes in 1878.8 cm^{-1} band upon different treatments, this band seems responsible for the antibacterial and bactericidal properties of Washed-NO. The 1878.7 cm^{-1} band present in the nitrosyl-stretching region (2100-1680 cm^{-1}). This band can be assigned to the symmetric vibration of metal-nitrosyls formed on the zeolite. But no band that can be assigned to the asymmetric stretching vibration could be detected in the 1835-1691 cm^{-1} range of the spectra. The symmetric (ν_s) and asymmetric (ν_{as}) vibrations of the nitrosyls were reported in the 1940-1765 cm^{-1} and 1835-1691 cm^{-1} regions respectively. For $Ni^{2+}(NO)_2$, ν_s was reported at 1870 cm^{-1} and ν_{as} at 1842 cm^{-1}. For $Co^{2+}(NO)_2$, the ranges of symmetric and asymmetric vibrations were reported as 1900-1894 cm^{-1} and 1819-1812 cm^{-1}, respectively (Hadjiinavov, 2000). The symmetric

and asymmetric vibrations of $Co^{2+}(NO)_2$ on CoY were found to be at 1900 cm^{-1} and at 1819 cm^{-1} , respectively (Ivanova et al., 2001). The gaseous NO also stretches at 1876 cm^{-1}.

The irreversibly adsorbed NO is chemisorbed and was not spontaneously released from the zeolite even at 2×10^{-4} mbar and 400 ^{o}C. This type of adsorption is a good method of storing a gas in an adsorbent. It was stated that the NO interacts with the extraframework cations in zeolites through the nitrogen atom to form either mononitrosyl or dinitrosyl complexes (Lunsford et al., 1978).

5.6. NO Release

5.6.1. Antibacterial Properties of the NO-Loaded Zeolites

The antibacterial activity tests on the zeolites aimed to investigate the effects of type and amount of metal sorbed in the zeolite, NO loading and thermal treatment applied successive to the NO loading on the strength and stability of antibacterial activities of the zeolites. Figure 5.75 shows the effect of the type and amount of the metal sorbed in the zeolite on the antibacterial action against *E. coli*. Washed, Na-Clin and iron-sorbed samples did not exhibit antibacterial activity. The 0.01 M Co-1h sample exhibited the strongest antibacterial activity followed by 0.05 M Cu sample. As the cobalt content of the zeolite increased, the antibacterial activity decreased. For the silver-sorbed zeolites, the strength of the antibacterial activity increased with the increasing silver content of the zeolite. The reduced antibacterial activities of silver and cobalt-sorbed zeolites with high metal content zeolites can be attributed to the reduction of some metal cations (Ag^{+}, Co^{2+}) exchanged in the zeolitic material to Ag^{0} and Co^{0}, respectively. In the literature, the reduced antibacterial activity was also observed for the silver-exchanged Mexican clinoptilolite-heulandite with high silver content. The small particles were observed on the surface of the silver-zeolite with high silver loading by electron microscope. The microanalysis of these particles revealed a high concentration of silver as 86.78 %. It was proposed that the Ag^{+} exchanged in the zeolitic material reduced to Ag^{0} in the presence of light (Rivera-Garza et al., 2000).

Some zeolite samples changed the color of the agar: A yellow ring was observed around the silver-sorbed zeolites, the cobalt-sorbed zeolites turned the color of the agar to red, 0.05 M Cu made the agar bluish. The iron-, silver- and cobalt-sorbed zeolite particles with high metal content aggregated during filling of the wells.

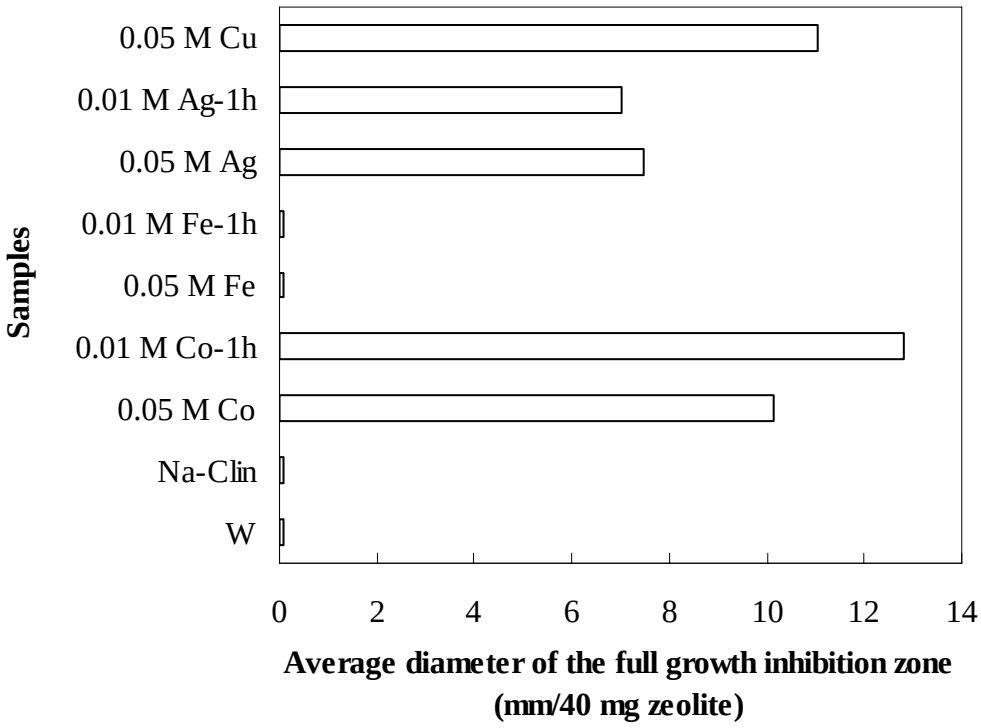

Figure 5.75. Antibacterial activity of the metal-sorbed zeolites against *E. coli.*

The effects of NO loading and the thermal treatment applied successive to the NO loading (heating insitu to 400 ^{o}C at a rate of 1 ^{o}C/min, under 20 ml/min helium flow in gas chromatograph oven, cooling to 30 ^{o}C) on the antibacterial strength of the parent and metal-sorbed zeolites can be seen in Figure 5.76. Washed and iron-sorbed zeolites gained antibacterial activity after NO loading. For 0.05 M Co and 0.05 M Cu zeolites, the NO loading resulted in stronger antibacterial activity. On the other hand, the strength of antibacterial activities of 0.01 M Co-1h and 0.01 M Ag-1h samples declined after NO loading. Either NO loading or the thermal treatment following the NO loading did not cause a significant change in the antibacterial activity of 0.05 M Ag sample. The antibacterial activities of Washed and iron-sorbed zeolites vanished after the zeolites

were subjected to the thermal treatment successive to the NO loading. The thermal treatment applied after NO loading caused the antibacterial activities of 0.05 M Co and 0.05 M Cu zeolites to decline. The strength of the antibacterial activities of 0.01 M Ag-1h and 0.01 M Co-1h increased after the samples were subjected to the thermal treatment. The rise in the strength was remarkable for 0.01 M Ag-1h sample. The negative change in the antibacterial strength of the zeolites after the thermal treatment can be attributed to removal of the species responsible for the antibacterial activity from the zeolite surface. Similarly, an increase in the antibacterial strength can be deduced to species formed during the thermal treatment.

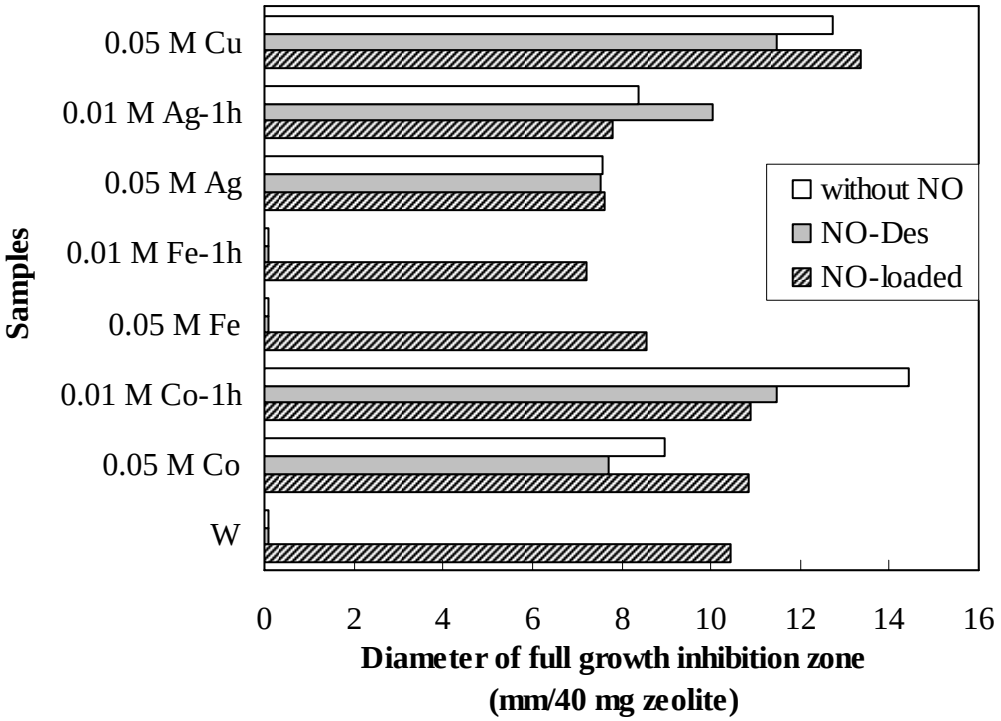

Figure 5.76. Antibacterial activity of the zeolite samples before and after NO loading (NO-loaded), and after the thermal treatment (NO-Des).

The variation of the species on the zeolite surface can be followed from the DRIFT spectra collected during heating to 400 ^{o}C, cooling to 30 ^{o}C under vacuum and after exposure the zeolite to the atmosphere subsequent to the NO adsorption. From those spectra for Washed zeolite it was obvious that the changes in frequency and

intensity of the bands occurred. The disappearance of the bands at 1390.7 and 1878.7 cm^{-1} in the DRIFT spectra of Washed zeolite during heating to 400 ^{o}C confirmed the removal of the species from the zeolite surface. On the other hand since no DRIFT spectrum was available for the other samples, it is not possible suggest a mechanism explaining the higher antibacterial activities.

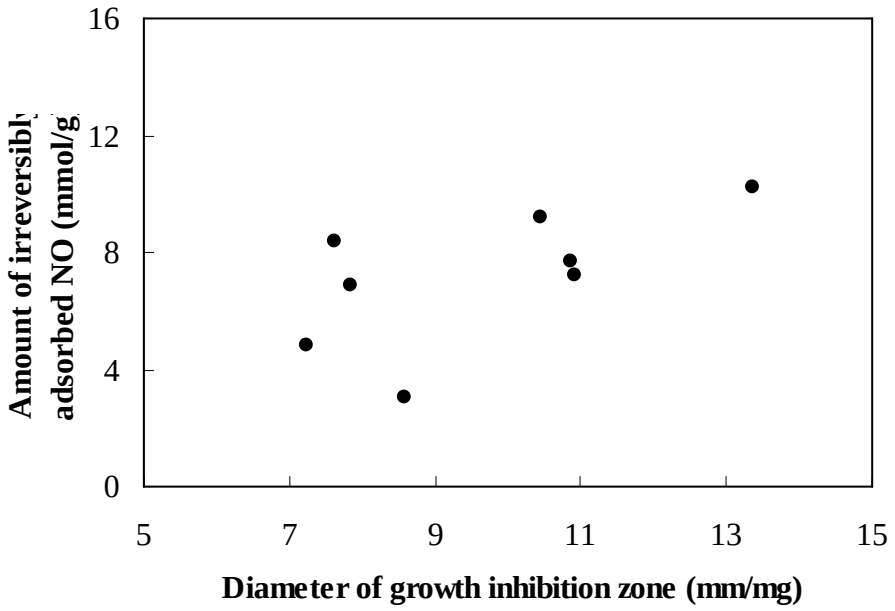

Figure 5.77. Relationship between the irreversibly adsorbed NO and the antibacterial strength of the zeolites against *E. coli*.

The strength of the antibacterial activity against *E. coli* was found to be poorly correlated with the irreversible adsorption capacity of the zeolites (shown in Figure 5.77) and not related with the intensity of the 1384.9 cm^{-1} band detected in the transmittance spectra of the NO loaded zeolites (Figure 5.78).

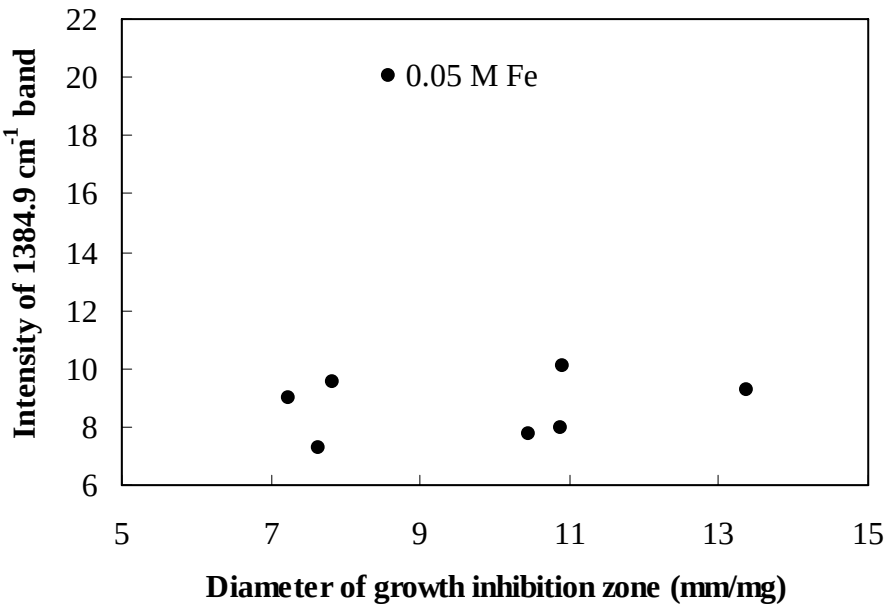

Figure 5.78. Relationship between the intensity of the 1384.9 cm^{-1} band and the antibacterial strength of the zeolites against *E. coli*.

The antibacterial activity of Washed zeolite on the reference culture of representative Gram-positive bacteria (*Bacillus subtilis*, NRLLB 4378) was also tested and the results are presented in Figure 5.79. The results of the stability of antibacterial activity tests are also shown in the same figure. For the investigation of the stability of the antibacterial activity of the NO-loaded zeolite sample, the antibacterial activity of Washed zeolite that was stored in 20 ml gas tight vials in the desiccator for different periods after being loaded with NO was tested. The average diameter of the full growth inhibition zone exhibited by Washed-NO on *B. subtilis* cells has decreased slightly (10 % decrease in the average diameter of the full growth inhibition zone) on the 6^{th} weeks of NO loading when stored in a gas-tight vial. Furthermore, the results of the tests on the stability of the antibacterial activity of Washed-NO against *E. coli* after 6 weeks of NO loading revealed that Washed-NO still exhibited stable antibacterial effect also on *E. coli* without loss in the strength.

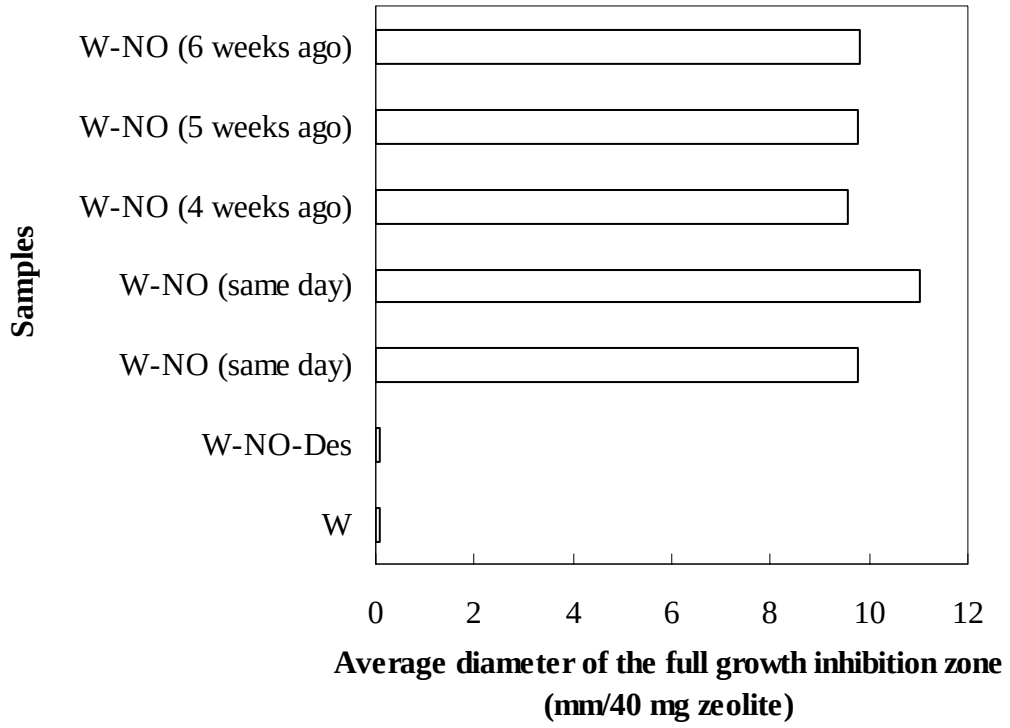

Figure 5.79. Antibacterial activity of Washed-NO against *B. subtilis* (The time passed between the NO loading and antibacterial tests are indicated in the parentheses.).

The antibacterial properties of NO and its reactive byproducts are attributed to either nitrosative or oxidative stress (Fang, 1997). Since NO is a lipophilic molecule like O_2, it is capable of rapidly crossing cell membranes. NO and O_2 tend to concentrate in cell membranes, accelerate oxidation of NO's to N_2O_3 and generated higher nitrosative stress within and near the bacterial cell membrane (Fang, 1997, 2004; Wink and Mitchell, 1998; Stamler et al., 2001). The reaction of NO with superoxide (O_2^-) forms peroxynitrite (-OONO), a potent oxidizing agent that can disrupt the structural integrity of bacterial cell membranes (Wink and Mitchell, 1998). NO and its reactive byproducts cause DNA deamination, nitrosative species such as N_2O_3 may nitrosate thiols (*S*-nitrosation) on proteins and initiate disulfide bridging with other thiols on the protein, thereby directly altering protein function. Nitrosation of both cell surface proteins and intracellular proteins (including enzymes) has been shown to cause bacterial cell death (Fang, 1997).

5.6.2. Bactericidal Activity Test

Washed-NO sample was tested for its bactericidal activity against *E. coli* and *B. subtilis* and the results are presented in Figure 5.80. Although Washed did not exhibit bactericidal effect on both bacteria before being NO loaded, it exhibited bactericidal activity after NO loading. Washed-NO exhibited complete bactericidal effect against *E. coli* and *B. subtilis* above the concentration of 12.5 mg zeolite/ml PBS and 7.5 mg zeolite/ml PBS, respectively. The bactericidal activity of the zeolite has been vanished after the thermal treatment employed following the NO adsorption.

It was reported in the literature that the bactericidal effects of NO and NO_2 are due to their reaction with water to form nitrous and nitric acids, but this only appears at high concentrations (Shank et al., 1962). Mancinelli and Mckay explained the lack of toxicity of NO and NO_2 at low concentrations by the concentrations of the acids which are not enough to act as toxic agents (Mancinelli and Mckay, 1983). In the present study, pH of the PBS-zeolite suspensions showing complete bactericidal effect was measured as around 2.5 at the end of the contact. In order to elucidate whether the bactericidal activity is associated with the formation of the acids causing decrease in the pH of the PBS, a bacterial test was performed in the absence of the zeolite in a PBS for which the pH was adjusted to 2.5. The pH adjustment was performed using concentrated HCl in small amount and the PBS was inoculated to get the same initial bacteria concentrations. At end of the contact period, the viable cells were counted by the pour plate method and no viable cells could be observed.

The difference in activity against the two types of bacteria can be attributed to different organization of the cell wall. Gram-positive bacteria typically have one cytoplasmic membrane and thick wall composed of multilayers of peptidoglycan. On the other hand, gram-negative bacteria have more complex cell wall structure, with a layer of peptidoglycan between outer membrane and cytoplasmic membrane. Thus, the cell membrane of gram-positive bacteria can be damaged more easily. This mechanism was proposed for the bactericidal activity of the silver-zeolite in the literature (Rivera-Garza, 2000; Silver, 1992; Viarengo, 1985).

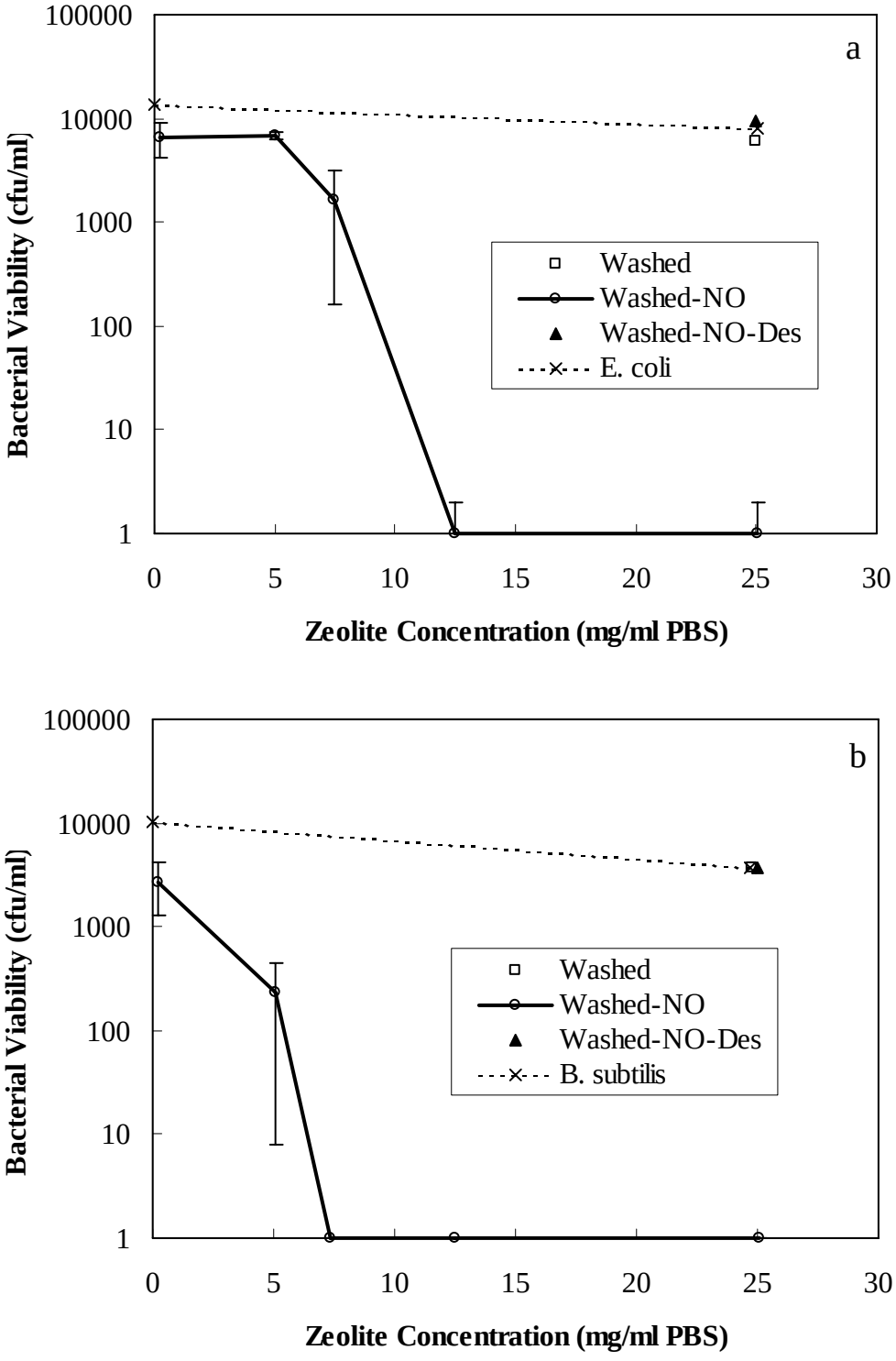

Figure 5.80. Bactericidal activity of Washed-NO in PBS (pH 7.4, at 37 ^{o}C). a, against *E. coli*; b, against *B. subtilis*.

5.6.3. NO Release in PBS

The calibration curve constructed for nitrite concentration measurements in PBS with good regression coefficient (r^2=0.998) is shown in Figure 5.81. The change in nitrite concentration of PBS as a function of the amount of Washed-NO added to PBS is shown in Figure 5.82. The release profiles of the control (Washed) and Washed-NO-Des were also included for comparison purpose.

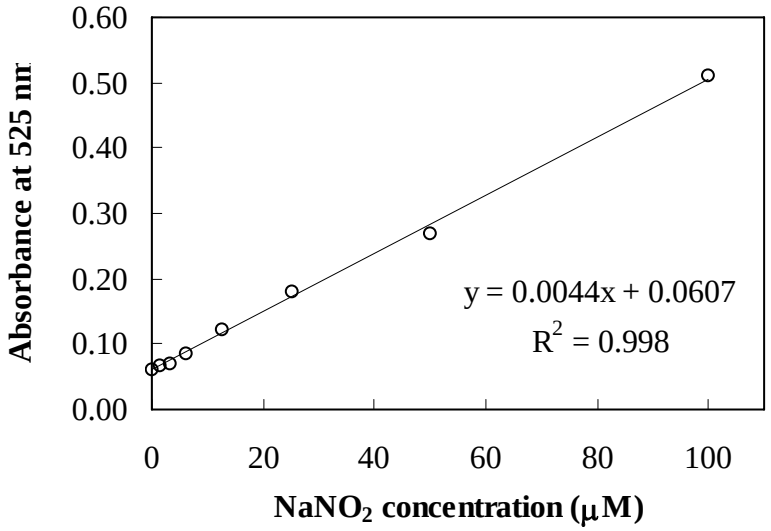

Figure 5.81. Calibration curve obtained for the nitrite concentration measurements by the spectrophotometric Griess method ($NaNO_2$ in PBS).

The interaction of Washed-NO with PBS immediately induced the nitrite concentration in PBS to increase. Washed-NO released most of the NO within first 60 minutes of contact. The change in nitrite concentration was more gradual after 180 minutes. The nitrite concentration reached in the PBS at the end of the contact period was found to be linearly related to the amount of the zeolite contacted with PBS (r^2=0.967). Washed and washed-NO-Des samples exhibited very low absorbance with the Griess assay corresponding to 10.64 and 11.79 μM nitrite concentration at the end of the contact period, respectively.

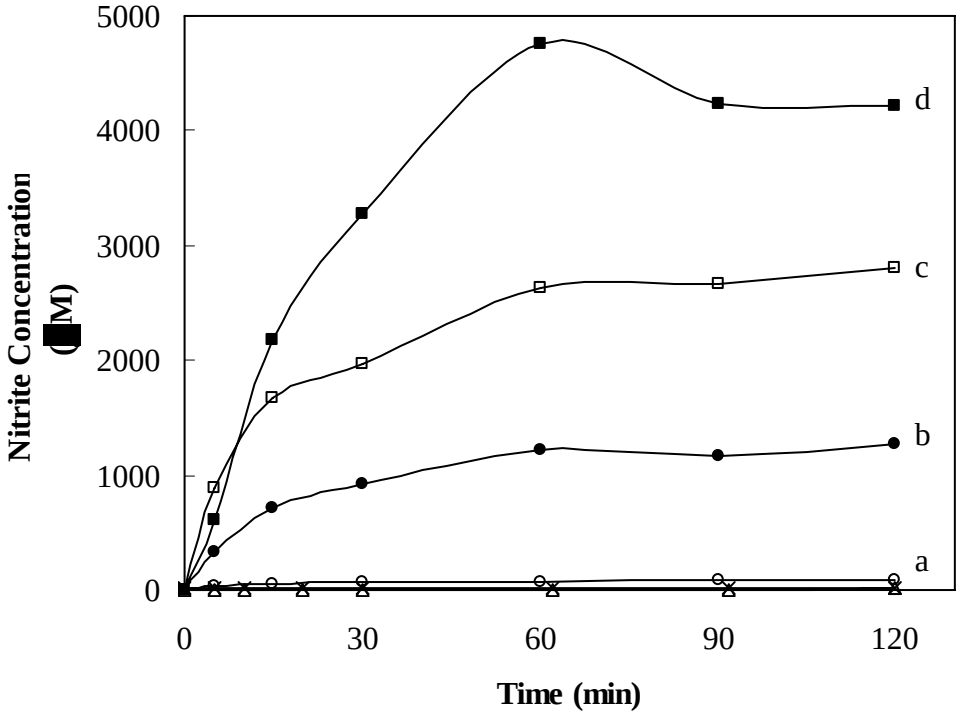

Figure 5.82. Cumulative NO release profiles for Washed, Washed-NO and Washed NO-Des samples in PBS (37 ^{o}C, pH 7.4). Washed-NO in a, 0.26 mg/ml; b, 5.1 mg/ml; c, 12.44 mg/ml; d, 24.78 mg/ml.

The amount of NO released per unit weight of Washed-NO decreased as the amount of zeolite in the PBS increased and found to be in the range of 0.17-0.33 mmol/g. Comparing with the irreversibly adsorbed amount of NO obtained from the dynamic adsorption studies, it was revealed that the irreversibly adsorbed NO is about 30 times higher than the released NO amount

Although the release of NO was performed under very different conditions, the comparison of the total amount of NO released measured in the present study with the values in the literature (0.02–1 mmol/g zeolite) revealed that our values fell within the range.

5.6.4. NO Release in Deionized Water

The calibration curve prepared dissolving $NaNO_2$ in deionized water for the determination of the nitrite concentrations in the deionized water was shown in Figure 5.83.

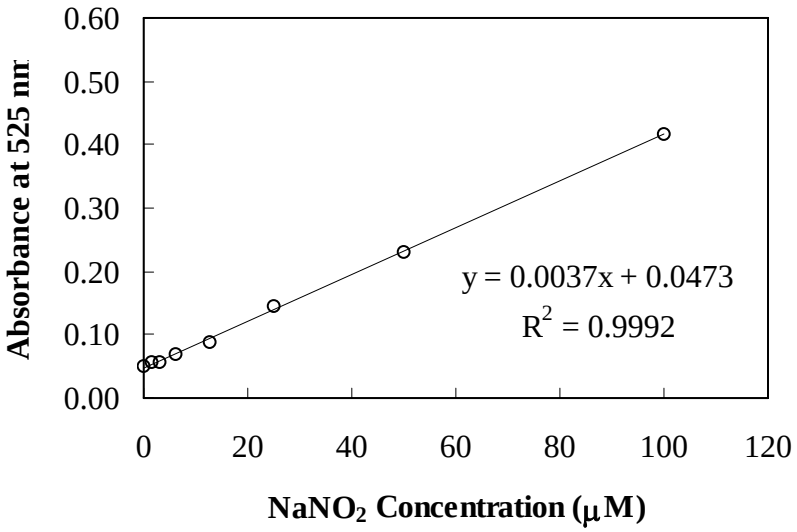

Figure 5.83. Calibration curve obtained for the nitrite concentration measurements by the spectrophotometric Griess method (NaNO2 in deionized water).

The change in the cumulative nitrite concentration in the deionized water upon addition of Washed-NO is shown in Figure 5.84. Washed-NO released most of the loaded NO within first 240 minutes of contact. The change in nitrite concentration in the deionized water after 240 minutes is negligible. The half-life of NO release from Washed-NO was determined as 10 minutes. Washed and Washed-NO-Des samples exhibited no signal with the Griess assay (not shown). The total amount of NO released from Washed-NO was found to be approximately 0.220 mmol/g. The cumulative release profiles for the same zeolite loaded with NO three and five months ago were also shown in the inset of the figure and the first 180 minutes of the releases were compared with the profile for the freshly loaded zeolite. The total amounts of NO

released were found as 0.061 and 0.005 mmol/g for Washed-NO loaded before 3 months and 5 months before the release experiments, respectively. After 3 months the amount of released NO decreased approximately by 70 %, and by 97 % after 5 months of the NO loading.

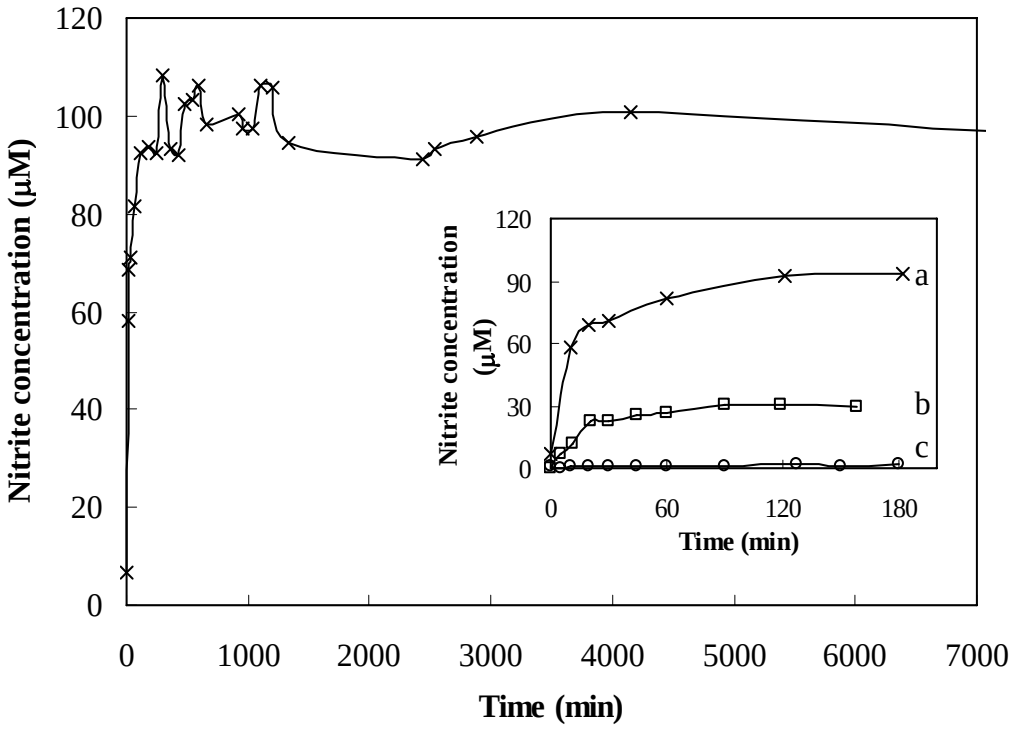

Figure 5.84. Cumulative NO release profile for Washed-NO in deionized water (37 ^{o}C). The NO loading was performed a, on the same day of the release measurements; b, 3 months ago; and c, 5 months ago.

The cumulative NO release profile for Washed-NO was compared with that for 0.05 M Co-NO in Figure 5.85. The NO loading was completed on the same day with the release analysis for both zeolites. The total amount of NO released was found to be almost at the same level for both zeolites, 0.22 mmol/g. This value again was lower than the irreversible adsorption capacity of 0.05 M Cu zeolite that was calculated as 10.23 mmol/g from the dynamic adsorption experiments. For both zeolites release on NO continued for 300 minutes. The half-life of NO release from 0.05 M Cu-NO was found and 35 minutes. In the inset of this figure, the stability of NO release properties of 0.05

M Cu-NO sample was shown. The total amount of NO released decreased to 0.07 mmol/g at the end of the first week of the loading although the sample was stored under the same conditions as Washed-NO zeolite (gas-tight vial, in a desiccator, at room temperature).

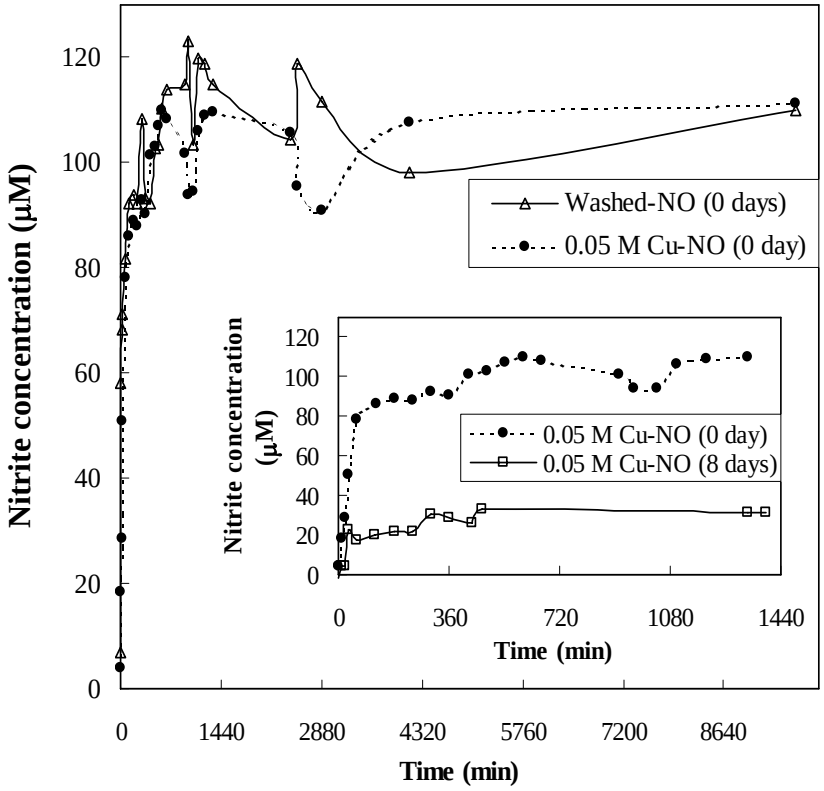

Figure 5.85. Cumulative NO release profiles for freshly loaded Washed-NO and 0.05 M Cu-NO in deionized water (37 ^{o}C).

The cumulative NO release profiles measured for WGround-Kaolin-NO and ClinRich-Kaolin-NO particles in deionized water under the same conditions were compared with that of Washed-NO in Figure 5.86. The total amount of NO released was determined as 0.156 and 0.168 mmol/g. The lower amount of NO released was attributed to the inert binder (kaolin) used in the preparation of the pellets. It was shown previously that kaolin does not adsorb NO. However, the presence of kaolin did not affect the NO release kinetics of the zeolite significantly. The half-life of NO release retarded only by 5 minutes.

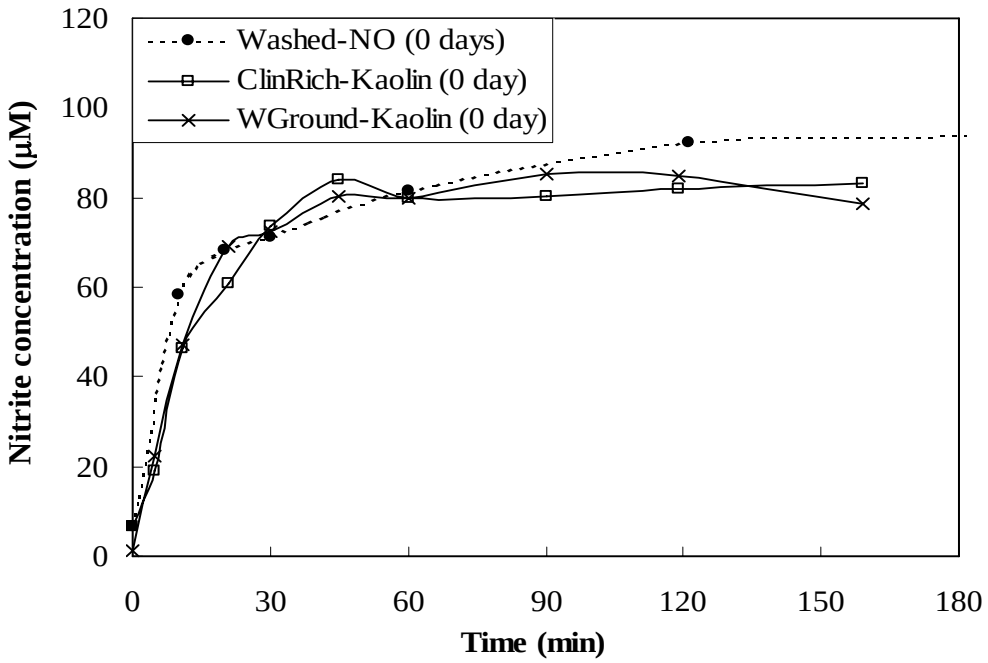

Figure 5.86. Cumulative NO release profiles for freshly NO loaded WGround-Kaolin-NO and ClinRich-Kaolin-NO particles in deionized water at 37 ^{o}C.

The NO release kinetics of Washed-NO in deionized water and PBS were compared in Figure 5.87. The release was slower in PBS which might be attributed to the presence of salts which affect the solubility. The solubility of NO in deionized water at 25°C is given as $(1.94\pm0.03)\times10^{-6}$ mol/ml atm^{-1} and in PBS as $(1.75\pm0.02)\times10^{-6}$ mol/ml atm^{-1}. The total amount of NO released at the end of the 120 minute-contact period was not different in both liquids.

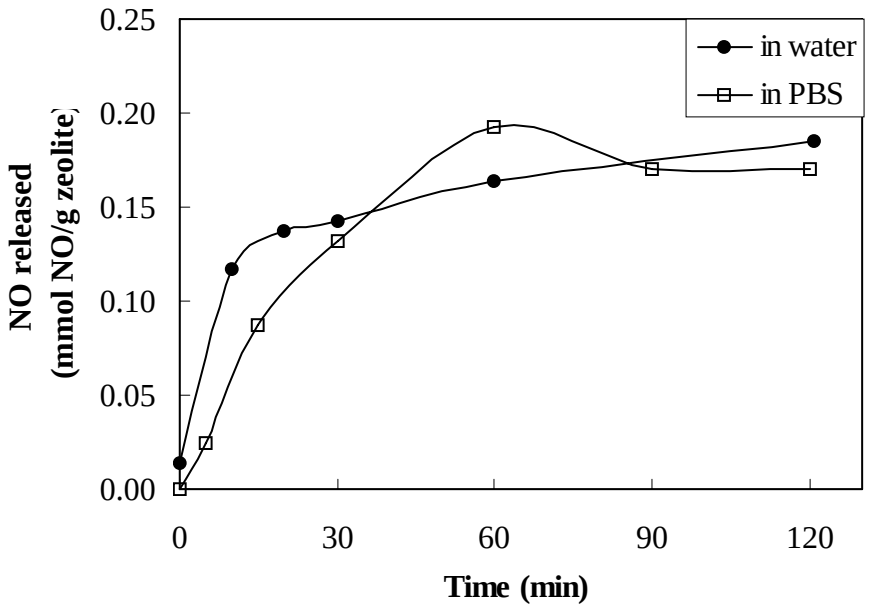

Figure 5.87. NO release profiles for Washed-NO in deionized water (~0.5 mg zeolite/ml PBS) and in PBS (~25 mg zeolite/ml PBS) at 37 ^{o}C.

5.6.5. Mathematical Modeling of NO Release

In the present study, a mathematical model based on Fick's second law of diffusion was used to quantitatively describe the NO release kinetics from the zeolites particles:

$$\frac{\partial q}{\partial t} = \frac{1}{R_p^2}\frac{\partial}{\partial R}\left(R^2 D_{NO}\frac{\partial q}{\partial R}\right) \tag{5.11}$$

Here, q is the concentration of NO in the zeolite, D_{NO} is the effective diffusivity of NO within the zeolite particle and R is the radial coordinate within the particle. Assuming constant diffusion coefficient which is valid at low concentrations of NO diffusivity, Equation (5.11) becomes:

$$\frac{\partial q}{\partial t} = \frac{D_{NO}}{R_p^2} \frac{\partial}{\partial R}\left(R^2 \frac{\partial q}{\partial R} \right) \tag{5.12}$$

For the following initial and boundary conditions:

$$\begin{gathered} \text{at } t = 0,\ q = M_e \\ \text{for } t > 0 \text{ and at } R = R_p,\ q = M_t \\ \text{for } t > 0,\ \left(\frac{\partial q}{\partial R} \right)_{R=0} = 0 \end{gathered} \tag{5.13}$$

The solution for Equation (5.12) is given by (Crank, 1979):

$$\frac{M_t}{M_e} = 1 - \frac{6}{\pi^2} \sum_{n=1}^{\infty} \frac{1}{n^2} \exp\left(- \frac{n^2 \pi^2 D_{NO} t}{R_p^2} \right) \tag{5.14}$$

where M_t and M_e are the cumulative amounts of NO released at time t and at equilibrium, respectively, and R_p is the particle radius. It was assumed that the NO is homogeneously distributed throughout the zeolite initially (before the NO-loaded zeolite is exposed to the release medium).

Approximate solution for the initial region of the diffusion is obtained by neglecting the higher terms:

$$\frac{M_t}{M_e} \approx \frac{6}{\sqrt{\pi}} \sqrt{\frac{D_{NO} t}{R_p^2}} \tag{5.15}$$

In the long time region, all terms except the first in the series of exponential terms in Equation (5.16) become negligible so that the release curve approaches the asymptotic form:

$$\frac{M_t}{M_e} \approx 1 - \frac{6}{\pi^2} \exp\left(- \frac{\pi^2 D_{NO} t}{R_p^2} \right) \tag{5.16}$$

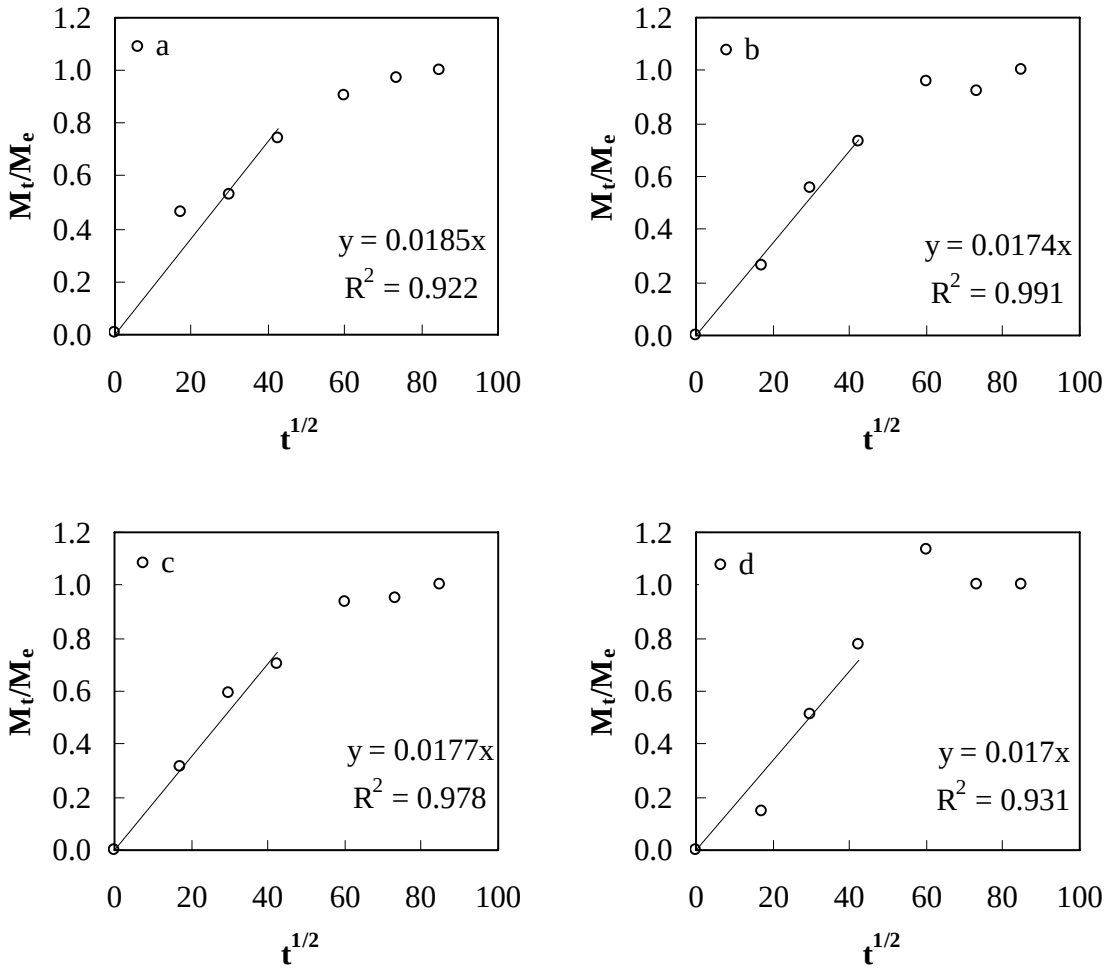

Figure 5.88. NO release kinetics from Washed-NO in PBS fitted to the spherical particle model (short time region) (Zeolite/PBS: a, 0.26 mg/ml; b, 5.10 mg/ml, c, 12.44 mg/ml; d, 24.78 mg/ml).

The diffusion coefficients of NO in the zeolite particles were determined by fitting the short time approximation to the solution (Equation 5.15) to the experimentally measured NO release kinetics. The results are shown in Figure 5.88 and the slopes of initial release functions with the diffusion coefficients calculated are given in Table 5.33.

Table 5.33. The diffusion coefficients calculated for the NO release from Washed-NO sample in PBS.

Sample	D_{NO} (cm^2/s)
W-NO (0.26 mg/ml)	8.87×10^{-10}
W-NO (5.1 mg/ml)	7.84×10^{-10}
W-NO (12.44 mg/ml)	8.12×10^{-10}
W-NO (24.78 mg/ml)	7.49×10^{-10}

The experimental kinetic data for NO release in deionized water was also analyzed in the same manner. The plots in Figure 5.89 shows fitting of the analytical solution of the spherical particle model to the experimental NO release data for Washed-NO and 0.05 M Cu-NO zeolite particles. Good agreement was observed for both samples (r^2=0.90 for both samples). The calculated diffusion coefficients are given in Table 5.34.

Table 5.34. The diffusion coefficients calculated for the NO release from Washed-NO and 0.05 M Cu-NO samples in deionized water.

Sample	D_{NO} (cm^2/s)
Washed-NO	7.84×10^{-10}
0.05 M Cu-NO	2.34×10^{-10}

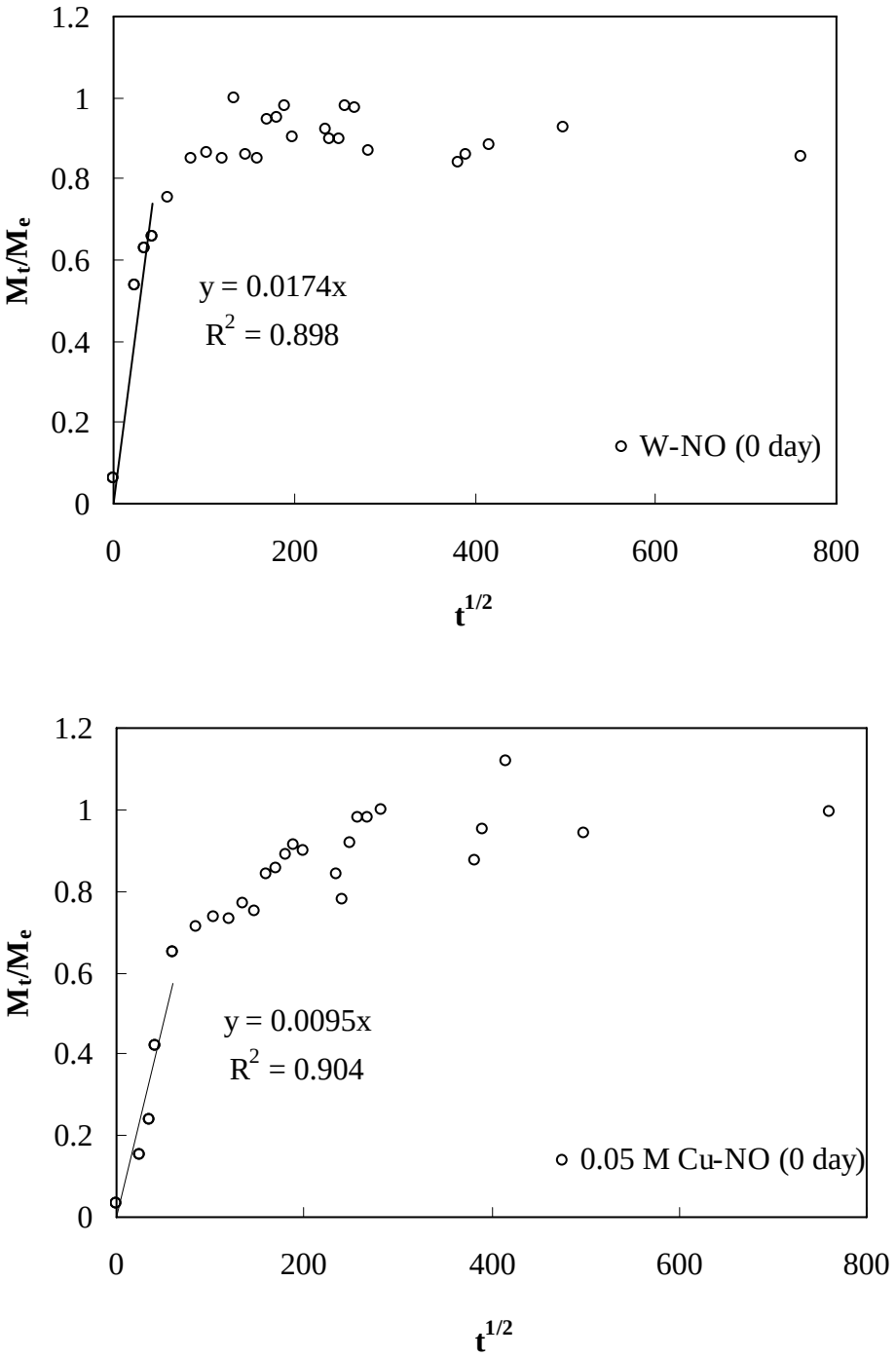

Figure 5.89. NO release kinetics from Washed-NO and 0.05 M Cu-NO samples in deionized water fitted to the spherical particle model (short time region) (Zeolite/deionized water: 50 mg/100 ml).

5.7. Color Change

The changes in the colors of the zeolites were observed after metal sorption, NO loading, the subsequent thermal treatment and contact with deionized water and PBS. The changes in the colors were summarized in Table 5.35 and the photos of the samples after different treatments were represented in Appendix B.

Table 5.35. Color changes observed in the zeolites after different treatments.

Sample	Original	After NO loading	After thermal treatment
Washed	beige	yellowish	brownish
0.05 M Cu	green-beige	darker	yellowish green
0.05 M Fe	red-brown	dark red-brown	no further change
0.05 M Co	pink-beige	lilac	brownish beige
0.05 M Ag	dark gray	yellowish- light gray	yellowish
0.01 M Fe-1h	yellow	darker yellow	Lighter, turned to a more reddish color than that before NO load
0.01 M Co-1h	light pink-beige	darker	yellowish-green
0.01 M Ag-1h	light gray	lighter gray-yellowish	yellowish

It was clearly observed that metal sorbed zeolites are self-indicating. These color changes emphasize the importance of the metal-NO interactions in the storage of the gas and the replacement of these by heating at 400 ^{o}C. The color changes can be attributed to the binding and release of NO.

Padden et al reported the design and synthesis of a new polymeric material that reversibly binds nitric oxide (NO) is reported. The polymer contains discrete metal sites with a high affinity for NO. It is composed of isolated four-coordinate Co^{II} complexes immobilized in a highly cross-linked and porous methacrylate host. The differences in the absorbance properties of P-1[Co^{II}] and P-1[Co(NO)] led to striking color changes in these materials. In the presence of NO, the orange P-1[Co^{II}] changed to the brown-green P-1[Co- (NO)] polymer. They attributed the rapid and vivid color change of the material to the NO binding event. This dramatic color change confirmed the presence of nitric oxide in gas and solution phases. It was noted that porous poly(EGDMA) without

immobilized Co^{II} (salen) sites remains colorless in the presence of NO. Binding of NO causes an immediate color change, indicating coordination of NO to the site-isolated Co^{II} centers. The conversion back to the orange P-1[Co^{II}] was accomplished in ~1 hour when P-1[Co(NO)] is heated to 120 °C under vacuum (0.05 Torr). Moreover, it was shown that the immobilized Co^{II} sites have a significantly greater affinity for NO over other biologically important gaseous compounds such as O_2, CO_2, and CO. The vivid color change resulting from the conversion of P-1[Co^{II}] to P-1[Co(NO)] suggests the potential of this system for the detection of NO. This polymer can be recycled, retaining high binding affinity for NO, and functions equally well in the solid state or as a suspension in a liquid. These properties lend this system to use in a variety of detection applications and efforts to incorporate materials of this kind into sensor technology are ongoing (Padden et al. 2001).

Wheatley et al. also reported that the while dried Co-exchanged zeolite-A has a bright blue color, when loaded with NO the color has turned to gray/blue and changed to pink as the NO is displaced by water. These color changes were explained by the metal-NO interactions in the storage of the gas and the replacement of these by metal-water interactions on delivery of the NO (Wheatley et al., 2006).

CHAPTER 6

CONCLUSION

This thesis aims to investigate the applicability of the clinoptilolite-rich local natural zeolite for nitrogen monoxide adsorption, storage and release purposes.

The clinoptilolite-rich local natural zeolite was used as a starting material to prepare adsorbents for NO adsorption. After crushing, grinding, sieving and washing, the zeolite was treated with concentrated sodium chloride for long periods to get a material in homoionic form. Successively metal sorption was performed on this zeolite. The starting material and its modified forms were characterized in terms of particle size distribution, density, porosity, mineral and elemental composition, surface, particle and crystal morphology, behavior on heating, pore size and volume, surface area, adsorption capacity for N_2, CO_2 and NO, chemical behavior in aqueous metal salt solutions and infrared spectroscopic properties (in both transmission and diffuse reflectance modes).

The clinoptilolite phase in the zeolite was separated from the tuff and characterized. The high clinoptilolite content of the purified phase was confirmed by quantitative x-ray diffraction and thermal stability analysis. In order to get this phase in manageable sizes, the powder was aggregated in to pellet form using kaolin binder in 10% by weight. After the crushing, calcination and sieving, these particles were used to examine the effect of the clinoptilolite content of the zeolite on the NO adsorption and release properties.

The NO adsorption, desorption and temperature-programmed desorption studies were performed on the prepared zeolites in a dynamic adsorption system, as well as by *insitu* diffuse reflectance infrared spectroscopy method.

The NO storage and release properties of the zeolites subjected to different treatments were tested for their antibacterial and bactericidal activities on the reference cells of gram positive (*Bacillus subtilis*) and gram negative (*Escherichia coli*) bacteria, as well as NO release kinetics in both water and phosphate buffered saline solution (PBS, pH 7.4) at 37 ^{o}C.

The average diameters of the zeolite particles were measured as 109 μm and 190 μm for the larger and smaller particles. The particle diameter of the purified zeolite was determined as around 9 μm. The true solid densities of the starting material and the purified phase were measured by helium pycnometer as 2.330 g/cm^3 and 2.625 g/cm^3, respectively. The particle and bulk densities of the starting zeolite were determined as 1.587 g/cm^3 and 1.298 g/cm^3, respectively. The bulk density of the pellets of the purified zeolite was determined as 1.601 g/cm^3. The total pore volume of the parent zeolite measured by using different probe molecules (water, nitrogen, carbon dioxide) in the range of 0.06-0.201 cm^3/g and showed consistency with the theoretically calculated value of 0.199 cm^3/g. The discrepancies were attributed to the properties of the probe molecules that affect the interactions with the zeolite.

The mineral composition of the parent zeolite was determined by qualitative X-ray powder diffraction analysis and it was found that the zeolite contains predominantly clinoptilolite as well as quartz, feldspars (microcline, sanidine) and biotite. The semi-quantitative analysis revealed the clinoptilolite content of 67 % by weight.

The treatment of the zeolite with sodium chloride did not change the crystal structure, but sorption of iron and silver ions at high concentration drastically affected the crystalline structure. The presence of different cations in the structure of the zeolite mainly affected the 2θ=9.82^o peak of the clinoptilolite. Heating of the zeolites to 400 ^{o}C under helium flow did not cause remarkable changes in their crystalline structures. None of the zeolites exhibited sharp peaks in the X-ray diffractograms indicating the presence of the metal oxides.

The interaction of the sodium chloride treated zeolite with water of high acidity caused dissolution of feldspars and biotite and decationization of the zeolite structure. It was shown that different reactions prevailed during the interaction including proton binding and exchange, dissolution and decationization. The surface charge of the zeolite was found to be negative in the pH range of 2-10.

The bulk elemental analysis revealed that the zeolite was rich in potassium ions and has theoretical cation exchange capacity of 2.08 meq/g, SiO_2/Al_2O_3 ratio of 5.9. The theoretical exchange capacity was well correlated with the clinoptilolite content. It was not possible to get the zeolite in homoionic form after the sodium chloride treatment, but this treatment increased the theoretical cation exchange capacity to 2.20 meq/g,

The metal oxide contents of the cobalt, iron, silver and cupper-sorbed zeolites using the metal salt solutions with high concentrations were determined as 3.77, 13.87, 13.43 and 4.74 % by weight in terms of the relevant metal cation. The cobalt, iron and silver oxide contents of the zeolites treated with the metal salt solutions with low concentrations were determined as 1.53, 2.86 and 1.98 % by weight, respectively.

Well-defined clinoptilolite crystals of tabular morphology and of average size of 5 μm were observed on the surface of the zeolite particles. In the scanning electron micrographs, drastic precipitation of needle-like phase on the surface of the zeolite with high iron content was observed. The EDX analysis depicted that the precipitated phase has high iron content. No such a precipitation was observed in the micrographs of the other samples. On the surface of the zeolite with high silver content, relatively large clusters were observed and the high silver content of these clusters was confirmed by the EDX analysis.

The zeolites gave Type IV adsorption isotherms with nitrogen at –196 ^{o}C and Type I isotherm with carbon dioxide at 30 ^{o}C. The fitting of the experimental nitrogen adsorption data to the BET model showed the microporous character of the zeolites, therefore the BT surface areas were used only for comparison purposes. BET The BET surface area determined from the nitrogen adsorption data of the zeolite with high iron content was found to be remarkably higher than those for other zeolites. The decrease in the BET surface area of some samples was explained by by the presence of metal oxide species in the channels of the zeolite which might cause the blocking of some pores. The Langmuir model was found capable of describing the N_2 adsorption isotherms for up to $P/P_o \leq 0.31$. The differences in the CO_2 adsorption capacities of the zeolites were attributed to the cationic densities in the low-pressure range and to the micropore volume in the high relative pressure regions. The type of cations in the zeolite structure also affected the CO2 adsorption capacity. The Langmuir model was able to fit the CO_2 adsorption isotherms over the entire relative pressure range. The micropore volume of the zeolites was calculated by the application of the Dubinin-Raduskevich model to the experimental data in the relative pressure range of 0.001-0.1. The high silver content zeolite has lower micropore volume due to the same reason given for the low surface area. The higher micropore volumes of the iron-sorbed zeolites was attributed to the decationization and to the dissolution of amorphous silica blocking the channels in the clinoptiolite structure considering the highly acidic conditions under which metal sorption was performed. The low adsorption capacities of the zeolites for N_2 as

compared to those for CO_2 was due to limitation by steric factor. The pore size distribution in the meso-macropore range was determined from the N2 desorption data and in the micropore region from the CO_2 adsorption data. All the zeolites exhibited bimodal mesopore size distribution at around 30 Å and 70 Å. The size and volume of the mesopores increased after iron sorption. The micropore size distribution of the zeolites was determined by the application of Saito–Foley (S-F) model on the CO_2 adsorption data. The pore size distribution in the micropore region was in good agreement with the channel dimensions of the clinoptilolite. The metal sorption changed the pore size distribution mainly in the micropore range. This implied that broader pores were less sensitive to the metal sorption, except for the iron sorption. The pore size distributions of the parent, sodium chloride zeolites and zeolites with low iron and cobalt content were trimodal while the others have showed bimodal pore size distribution.

The continuous and uninterrupted thermogravimetric curves implied the reversibility of dehydration for the zeolites without destruction of the structure. Total water capacity of the parent zeolite was measured as about 8.5 % by weight. The externally adsorbed water was desorbed from the zeolite upto 85 ^{o}C. Desorption of the loosely bound water occurred between 85-285 ^{o}C and above 285 ^{o}C, slow desorption of tightly bound water took place. The minimum In the D-TG curves was observed at different temperatures for different zeolites. From the D-TG curves, the rate of weight loss was found to be the highest for the iron-sorbed zeolites.

Transmittance infrared spectroscopy analyses revealed the bands due to internal and external bonds of the clinoptilolite structure. In the OH stretching region (3000–3700 cm^{-1}), noticeable changes were detected in both positions and intensities of the bands depending upon the cation content of the zeolite. The drastic increase in the intensities of the bands in this region for the zeolite with high iron content was attributed to the addition of some acidic protons during metal sorption. A strong band was detected at 1384.9 cm^{-1} in the transmission spectra of the zeolites after NO loading. No relationship was found between the intensity of this band and the amount of irreversibly adsorbed amount of NO. This band either lost intensity or disappeared in the spectra of the NO-loaded zeolites after heated to 400 ^{o}C under helium flow and after the NO-loaded zeolites were contacted with water.

The inertness of the dynamic adsorption system to NO gas was confirmed. It was also proved that helium was not adsorbed by the zeolite. The irreversibility of the

NO adsorption in the parent zeolite was shown through successive adsorption of NO on the zeolite. Between the successive adsorption runs, no thermal treatment was applied. The equilibrium adsorption capacity of the zeolite in the 2nd adsorption cycle was found to be 28 % of that in the 1st cycle. This indicated the formation of the species that were adsorbed irreversibly during the 1st cycle and thereby prevention of further adsorption of the NO molecules during the 2nd cycle. Furthermore, the helium-purging step applied was not effective in removal of all the species formed. These results were supported by the TPD profiles. The total higher NO adsorption capacity of the natural zeolite as compared to those of the synthetic zeolites was explained by the type, size, amount and location of the cations, Si/Al ratio, size and shape of the pores, and by different electrostatic interactions between the surface and the polar NO molecules. As the NO flow rate increased, the breakthrough curve has become steeper and the breakthrough time was found to be inversely proportional to the flow rate. For larger zeolite particles, the breakthrough occured earlier. The breakthrough time did not change with the activation period, whereas the equilibrium adsorption capacity was decreased when the zeolite was activated in shorter periods implying that more preadsorbed species could be removed from the adsorbent by activation for longer period thereby providing more sites for interaction of NO.

As the adsorption temperature increased, the breakthrough curve became sharper implying the higher adsorption rate. The total adsorption capacity decreased with increasing adsorption temperature, indicating the exothermic character of the adsorption.

The particles with particle diameter of 75-150 μm obtained from the pure kaolin pellets were also tested for the NO adsorption characteristics. The breakthrough curve obtained for the kaolin packed column confirmed that the contribution of the binder to the adsorption of NO was negligible. It was stated that the differences in the adsorption profiles of the starting zeolite and the purified zeolites could not be explained only by the mineral purity of the zeolites. The differences in the transport properties of the natural filler in the starting zeolite (biotite, quartz, feldspars) and the additional filler (kaolin) in the particles prepeared from the purified zeolite contribute to the differences in the adsorption kinetics. the secondary pores are formed in the pellets due to the presence of the binder during pellet formation and subsequent calcination processes. These pores may have different and nondefined sizes, and serve as channels for transfer of the adsorbate molecules to the micropores (primary pores). Furthermore, the size of

the microparticls forming the particles was also different for these two particles. From the electron micrographs the size of the clinoptilolite crystals in the starting zeolite was determined in the range of 5-10 μm, while that of the purified zeolite was determined to be in the range of 0.5-20 μm. The blinding of the crystal surface might have occurred during production of the pellets and coking due to the catalytic activity of the binder that led to decrease in mass transfer.

The breakthrough curves obtained for different periods of NO adsorption on the parent zeolite showed that the saturation of the zeolite with NO has not been achieved even after 5 hours. The composition of the column outlet did not significantly change after 120 minutes as indicated by the gradual increase of the detector signal. The total amount of NO adsorbed increased only by 1 % between the 120^{th} minute and the 5^{th} hour. It was not possible to attribute the slow adsorption rate of NO to a kinetic barrier since the kinetic diameter of NO molecules is much smaller than the channel size of the zeolite. On the other hand, adsorption in microporous channels is strongly affected by the internal electrostatic fields that envelop the entire pore space. The contributions of the framework cations, charge-balancing cations and adsorbate molecules to these internal fields are all important and interdependent.

The cation type and content of the zeolite affectd the adsorption kinetic profiles especially in the initial period of adsorption. The steep breakthrough curves implied that the adsorption isotherm of NO on the zeolites was favorable. The slope of the breakthrough curves was smooth within the first 2-5 minutes of the adsorption indicating the low mass transfer rate. Regarding the longer times required to reach C/C_o=0.1 by the zeolites with higher metal content, it can be suggested that there is a relationship between the metal content of the zeolite and the time required to reach the 10% of the inlet NO concentration at the column outlet, except for the iron-sorbed zeolites. After the first 5 minutes, the NO concentration in the column outlet steeply increased and this increase ended at different times for each zeolite. After about 45 minutes, the NO concentration at the outlet almost approached the inlet concentration, indicating that free sites are no longer available for further adsorption. The breakthrough time was found to be independent of the cation type and amount. The desorption profiles of the zeolite were found to be smoother than the corresponding adsorption profiles which designated the favorable natural of the adsorption equilibrium isotherm. The total and reversible adsorption capacities of the zeolites were determined by the numerical integration of the area above the adsorption profile and of the area

under the desorption profile, respectively. The irreversible adsorption capacities were calculated by subtracting the reversible adsorption capacity from the total adsorption capacity. These values were corrected for the extra column effects and normalized with respect to the dehydrated weights of the zeolites packed into the column.

The total NO adsorption capacities of the zeolites were found to be in the 5.5-8.5 mmol/g range. The copper-sorbed zeolite has the highest total adsorption capacity for NO compared to the other zeolites. The reversible adsorption capacities of the zeolites did not shown significant divergence, but there was a notable difference in their irreversible adsorption capacities. It was revealed that the irreversible adsorption has higher contribution to the total adsorption capacity of a zeolite. The irreversible adsorption capacity decreased in the same order as the total adsorption capacity.

The adsorbed amount of NO was expressed in terms of volume of NO adsorbed assuming that the density of the adsorbed NO is equal to its liquid density at the adsorption temperature of 30 ^{o}C (0.534 g/cm^{3}). The total NO adsorption capacities calculated corresponds to the total pore volume of the zeolites according to the Gurvitsch Rule. When compared with the total pore volumes based on the thermogravimetric and CO_2 adsorption data, the total pore volumes calculated using the NO adsorption data were found to be 5 times higher. From the total pore volumes of the zeolites previously calculated it is possible to estimate the density of the adsorbed NO within the pores (apparent density). The estimated apparent densities of adsorbed NO were remarkably higher than the liquid density of NO at 30 ^{o}C. The total adsorption capacity was found to be independent of the micropore volume of the zeolite calculated from the CO_2 adsorption data. The NO adsorption capacities were 6-12 times higher than the micropore volumes.

The total, reversible and irreversible adsorption capacities decreased with the increase in the cation content of the zeolite regardless the type of the cation. The zeolites with lower cation content exhibited higher adsorption capacities. It can be figured out that the increased cation content hindered the irreversible adsorption of NO.

The appreciably lower adsorption capacity of 0.05 M Fe zeolite might be attributed to the presence of oxidized iron species which decreased the interaction between the metal and NO molecules.

It was found that as the cobalt content of the zeolite increased both the total and reversible adsorption capacities increased up to a certain cobalt content (5.11 % by weight) and then although the difference was not significant. As the cobalt content of

the zeolite was further increased the total adsorption capacity for NO declined. The decline in the NO adsorption capacity of the zeolite with the increasing cobalt content can be attributed to the presence of some cobalt oxides and locations of the cobalt cations in the zeolite structure. The presence of cobalt oxides decreased the electrostatic interaction of the zeolite with NO molecules and also these oxides may block the zeolite pores. The location of cations in the structure affects the accessibility of the adsorbate molecules to these cations.

The peaks observed in the temperature-programmed desorption profiles implied the presence of distinct adsorption sites, formation of various surface species, and/or existence of interactions between the adsorbed molecules leading to a variation of the activation energy for the desorption of NO as a function of the coverage. There was no correlation between the total areas of the peaks and the irreversible adsorption capacities of the zeolites.

DRIFTS studies revealed that upon exposure of the zeolite to 100 mbar NO, a strong band was appeared at 1358.8 cm^{-1}. The bands detected at 1390.7, 1520.9, 1645.3, 1878.7 and 2362.8 cm^{-1} were assigned to the reversibly adsorbed species. The bands at 1358.8 and 1878.8 cm^{-1} were assigned to the irreversibly adsorbed species. The stability of these species to evacuation and heating to 400 ^{o}C was investigated. The band at 1878.8 cm^{-1} was found to be stable to evacuation but not to the heating. The band at 1358.8 cm^{-1} was common for the zeolite and for KBr. The quantitative analysis based on this band exhibited no relation between the irreversible adsorption capacity and either the intensity or the area of the band. Regarding the lack of antibacterial and bactericidal activities of the zeolites subjected to 400 ^{o}C successive to NO loading, these properties were related to the presence and absence of the band at 1878.8 cm^{-1}. This band could not be detected in the transmission spectra of the zeolites due to the low intensity.

The natural and iron-sorbed zeolites gained antibacterial activity after NO loading. The antibacterial activities of these samples vanished after the zeolites were subjected to the thermal treatment successive to the NO loading. For other zeolites, NO loading and thermal treatment resulted in either stronger or weaker antibacterial activity. The decline in the antibacterial strength after the thermal treatment can be attributed to removal of the species responsible for the antibacterial activity from the zeolite surface. Similarly, an increase in the antibacterial strength can be deduced to

species formed during the thermal treatment. The antibacterial activities of the natural zeolite on *E. coli* and *B. subtilis* were found to be stable at least 6 weeks.

The natural zeolite exhibited bactericidal effect against *E. coli* and *B. subtilis* after NO loading above the concentration of 12.5 mg zeolite/ml PBS and 7.5 mg zeolite/ml PBS, respectively. The bactericidal activity of the zeolite has been vanished after the thermal treatment employed following the NO adsorption. The amount of NO released per unit weight of NO-loaded zeolite in the PBS was found to be in the range of 0.17-0.33 mmol/g. No release was detected for the natural and copper-sorbed zeolites before NO loading. The natural zeolite subjected to the thermal treatment successive to the NO loading also did not release NO. Comparing with the irreversibly adsorbed amount of NO obtained from the dynamic adsorption studies, it was revealed that the irreversibly adsorbed NO is about 40 times higher than the released NO amount.

The total amount of NO released from the natural and copper-sorbed zeolites in water was found to be almost at the same level, 0.22 mmol/g. The total amounts of NO released from these zeolites decreased significantly after storage for 3 months under dry atmosphere. The NO release kinetics of the natural zeolite in deionized water and PBS were not significantly different from each other.

The changes in the colors of the zeolites were observed after metal sorption, NO loading, the subsequent thermal treatment and contact with deionized water and PBS. The color changes were explained by the metal-NO interactions in the storage of the gas and the replacement of these by metal-water interactions on delivery or thermal desorption of the NO.

CHAPTER 7

RECOMMENDATIONS FOR FUTURE STUDY

For the detailed analysis of the adsorbate-adsorbent pair of NO-natural zeolite, adsorption equilibrium isotherm data is required. This information is also an input to the dynamic model. For this purpose special set-up which is inert to NO is needed. In the literature, NO adsorption/desorption isotherms were generally obtained on a gravimetric adsorption system.

Regarding the adsorption of NO by the diluant (KBr) observed in the insitu adsorption studies by infrared spectroscopic method, it was not possible to get quantitative information on the kinetics of NO adsorption on the zeolite surface. A method that does not require dilution of the zeolite with a dilutant (e.g. KBr) should be employed. For this purpose gas reaction chambers in which the zeolite is loaded in the form of self-supported pellets were used in the literature and the spectrum is collected in the transmission mode.

The biological activity of NO released from the zeolites in anti-thrombosis applications can be investigated. It is known that NO is produced by endothelial cells and serves to prevent platelet adhesion and activation (Siney and Lewis, 1992; Salvemini et al., 1990; Radomski et al., 1992, 1987c), and to promote vasodilation of the surrounding blood vessels (Radomski, 1987). These researches suggested that it should be possible to create polymeric surfaces that mimic the inner surface of the blood vessel by locally generating NO.

Regarding the involvement of NO in a wide range of biochemical reactions, increases or decreases in NO levels might be therapeutically desirable depending on the type or stage of disease provides a considerable challenge for drug development. The therapeutic approach targeting promotion of endogenous NO is important particularly in the cardiovascular system. Since NO has a short half-life in vivo, the development of NO donors which have the capacity to release NO selectively, with a prolonged half-life and with a reduced incidence of drug tolerance has paramount importance.

The NO releasing polymeric materials have had some success, but NO might be expected to be efficient if delivered at the appropriate rate for a sufficient duration. Another concern in the delivery of exogenous NO is the target specificity. For this purpose, materials that can store significant quantities of NO and then deliver it to specific sites in the body are under development.

Although these benefits support the use of NO-releasing coatings for medical devices, the implications of NO release on neighboring tissue is still a concern. Prolonged exposure to NO at elevated concentrations has been associated with many detrimental physiological conditions, including septic shock, apoptosis, cytotoxicity, DNA damage, and carcinogenesis.

Further study may include the investigation of the NO release kinetics of zeolites in blood and in gastrointestinal system in powder form or as blended with different polymers. Furthermore, the mechanism of antibacterial and bactericidal activities of the NO-loaded zeolites must be elucidated.

REFERENCES

Abusafa, A.; Yücel, H. Removal of ^{137}Cs from Aqueous Solutions Using Different Cationic Forms of a Natural Zeolite: clinoptilolite. Sep. Purif. Technol. 2002, 28, 103-116.

Ackley, M. W.; Yang, R. T. Adsorption Characteristics of High-Exchange Clinoptilolites. Ind. Eng. Chem. Res. 1991a, 30, 2523-2530.

Ackley, M. W.; Yang, R. T. Diffusion in Ion-Exchanged Clinoptilolites. AlChE J. 1991b, 37, 1645-1656.

Ackley, M. W.; Giese, R. F.; Yang, R. T. Clinoptilolite: Untapped Potential for Kinetic Gas Separations. Zeolites. 1992, 12, 780-788.

Ackley, M. W.; Rege, S. U.; Saxena, H. Application of Natural Zeolites in the Purification and Separation of Gases. Microporous Mesoporous Mater. 2003, 61, 25-42.

Addison, W. E.; Barrer, R. M. Sorption and Reactivity of Nitrous Oxide and Nitric Oxide in Crystalline and Amorphous Siliceous Sorbents. J. Chem. Soc. 1955, 757-769.

Aguilar-Armenta, G.; Hernandez-Ramirez, G.; Flores-Loyola, E.; Ugarte-Castaneda, A.; Silva-Gonzalez, R.; Tabares-Munoz, C.; Jimenez-Lopez, A.; Rodriguez-Castellon, E. Adsorption Kinetics of CO_2, O_2, N_2, and CH_4 in Cation-Exchanged Clinoptilolite. J. Phys. Chem. B. 2001, 105, 1313-1319.

Akdeniz, Y.; Ülkü, S. Microwave Effect on Ion-Exchange and Structure of Clinoptilolite. J. Porous Mater. 2007, 14, 55-60.

Akdeniz, Y.; Ülkü, S. Thermal Stability of Ag-exchanged Clinoptilolite Rich Mineral. J. Therm. Anal. Calorim. 2008, 94, 703-710.

Alcañiz-Monge, J.; Bueno-López, A.; Lillo-Rodenas, M. A.; Illán-Gómez, M. J. NO Adsorption on Activated Carbon Fibers from Iron-Containing Pitch. Microporous Mesoporous Mater. 2008, 108, 294-302.

Alietti, A.; Gottardi, G.; Poppi, L. The Heat Behavior of the Cation Exchanged Zeolites with Heulandite Structure. Mineral. Petrol. 1974, 21, 291-298.

Andrew, P. J.; Mayer, B. Enzymatic Function of Nitric Oxide Synthases. Cardiovasc. Res. 1999, 43, 521-531.

Annich, G. M.; Meinhardt, J. P.; Mowery, K. A.; Ashton, B. A.; Merz, S. I.; Hirschl, R. B.; Meyerhoff, M. E.; Bartlett, R. H. Reduced Platelet Activation and Thrombosis in Extracorporeal Circuits Coated with Nitric Oxide Release Polymers. Crit. Care Med. 2000, 28, 915-920.

Armbruster, T. Clinoptilolite-heulandite: Applications and Basic Research. In *Studies in Surface Science and Catalysis-Zeolites and Mesoporous Materials at the Dawn of the 21st Century;* Galarneau, A.; Di Renzo, F.; Fajula, F.; Vedrine, J., Eds.; Elsevier: Amsterdam, 2001; Vol. 135; p 13.

Baerlocher, Ch.; Meier, W. H.; Olson, D. H. *Atlas of Zeolite Framework Types*, Elsevier Science, New York, 2001.

Baeyens, B.; Bradbury, M. H. A Mechanistic Description of Ni and Zn Sorption on Na-montmorillonite Part I: Titration and Sorption Measurements. J. Contam. Hydrol. 1997, 27, 199-222,

Bamford, C. H.; Middleton, I. P.; Al-Lamee, K. G.; Paprotny, J. J. Modification of Biomaterials to Improve Blood Compatibility. Int. J. Artif. Organs. 1992, 15, 71-78.

Barrer, R. M. *Zeolites and Clay Minerals as Sorbents and Molecular Sieves,* Academic Press, New York, 1978.

Barrett, E. P.; Joyner, L. G.; Halenda, P. H. The Determination of Pore Volume and Area Distributions in Porous Substances. I. Computations from Nitrogen Isotherms. J. Am. Chem. Soc. 1951, 73, 373-380.

Bedioui, F.; Villeneuve, N. Electrochemical Nitric Oxide Sensors for Biological Samples-principle, Selected Examples and Applications. Electroanalysis. 2003, 15, 5-18.

Bish, D. L.; Chipera, S. J. Problems and Solutions in Quantitative Analysis of Complex Mixture by X-ray Powder Diffractions. Adv. X-ray Anal. 1988, 31, 295-308.

Bish, D. L.; Boak, J. M. Clinoptilolite-Heulandite Nomenclature. In *Natural Zeolites: Occurrence, Properties, Applications*; Bish, L.; Ming, D. W., Eds.; Reviews in Mineralogy and Geochemistry, Volume 45, Mineralogical Society of America, Washington, DC, 2001, p 207.

Bish, D. L. Effects of Exchangeable Cation Composition on the Thermal Expansion/Contraction of Clinoptilolite. Clays Clay Miner. 1984, 32, 444-452.

Blanchard, G.; Maunaye, M.; Martin, G. Removal of Heavy Metals from Waters by Means of Natural Zeolites. Water Res. 1984, 18, 1501-1507.

Bremmer, P. R.; Schultze, L. E. Ability of Clinoptilolite Rich Tuffs to Remove Metal Cations Commonly Found in Acidic Drainage. In *Natural Zeolites'93: Occurrence, Properties, Use*; Ming, D. W.; Mumpton, F. A., Eds.; Brackport: New York, 1995.

Breck, D. W. *Zeolite Molecular Sieves*, John Wiley and Sons, New York, 1974.

Bruch-Gerharz, D.; Ruzicka, T.; Kolb-Bachofen, V. Nitric Oxide in Human Skin: Current Status and Future Prospects. J. Invest. Dermatol. 1998, 110, 1-7.

Brunauer, S.; Emmett, P. H.; Teller, E. Adsorption of Gases in Multimolecular Layers. J. Am. Chem. Soc. 1938, 60, 309-319.

Cabrera, C.; Gabaldon, C.; Marzal, P. Sorption Characteristics of Heavy Metal Ions by a Natural Zeolite. J. Chem. Technol. Biotechnol. 2005, 80, 477-481.

Calleja, G.; Pau, J.; Calles, J. A. Pure and Multicomponent Adsorption Equilibrium of Carbon Dioxide, Ethylene, and Propane on ZSM-5 Zeolites with Different Si/Al Ratios. J. Chem. Eng. Data. 1998, 43, 994-1003.

Carberry, J. J. *Chemical and Catalytic Reaction Engineering*, McGraw-Hill, New York, 1976.

Castaldi, P.; Santona, L.; Cozza, C.; Giuliano, V.; Abbruzzese, C.; Nastro, V.; Melis, P. Thermal and Spectroscopic Studies of Zeolites Exchanged with Metal Cations. J. Mol. Struct. 2005, 734, 99-105.

Cazorla-Amorós, D.; Alcañiz-Monge, J.; de la Casa-Lillo, M. A.; Linares-Solano, A. CO_2 as an Adsorptive to Characterize Carbon Molecular Sieves and Activated Carbons. Langmuir. 1998, 14, 4589-4596.

Chao, C. C.; Lunsford, J. H. Infrared Studies of the Disproportionation Reaction of Nitric Oxide on Y-Type Zeolites. J. Am. Chem. Soc. 1971, 93, 71-77.

Chao, C. C.; Lunsford, J. H. Electron Paramagnetic Resonances Study of the Cu^{+}-NO Complex in a Y-type Zeolite. J. Phys. Chem. 1972, 76, 1546-1548.

Chao, C. C.; Lunsford, J. H. Infrared and Electron Paramagnetic Resonance Study of Some Silver-nitric Oxide Complexes in Y Type Zeolites. J. Phys. Chem. 1974, 78, 1174-1177.

Chapman, S.; Cowling, T. G. *The Mathematical Theory of Non-Uniform Gases*, 3rd Edition; Cambridge University Press: Cambridge, 1970.

Chen, J. W.; Buege, J. A.; Cunningham, F. L.; Northam, J. I. Scale-up of Column Adsorption Process by Computer Simulation. Ind. Eng. Chem. Proc. Design Dev. 1968, 7, 26-31.

Chilton, T. H.; Colburn, A. P. Pressure Drop in Packed Tubes. Ind. Eng. Chem., 1931, 23, 913-931.

Chmielewska-Horvathova, E.; Lesny, J. Study of Sorption Equilibrium in the Systems: Water Solutions of Inorganic Ions-Clinoptilolite. J. Radioanal. Nucl. Chem. 1995, 201, 293-301.

Cirino, G. Nitric Oxide Releasing Drugs: From Bench to Bedside. Dig. Liver Dis. 35, 2003, Suppl. 2, S2-S8.

Claudino, A.; Soares, J. L.; Moreira, R. F. P. M.; José, H. J. Adsorption Equilibrium and Breakthrough Analysis for NO Adsorption on Activated Carbons at Low Temperatures. Carbon. 2004, 42, 1483-1490.

Coeuret, F. Percolating Porous Electrode-I. Mass transfer in fixed bed. Electrochim. Acta. 1976, 21, 185-193.

Colman, R. W. Mechanisms of Thrombus Formation and Dissolution. Cardiovasc. Pathol. 1993, 2, Supplement 1, 23S-31S.

Concepción-Rosabal, B.; Rodriguez-Fuentes, G.; Simón-Carballo, R. Development and Featuring of the Zeolitic Active Principle FZ: A Glucose Adsorbent. Zeolites. 1997, 19, 47-50.

Concepción-Rosabal, B.; Rodríguez-Fuentes, G.; Bogdanchikova, N.; Bosch, P.; Avalos, M.; Lara, V. H. Comparative Study of Natural and Synthetic Clinoptilolites Containing Silver in Different States. Microporous Mesoporous Mater. 2005, 28, 249-255.

Cooney, D. Comparison of Simple Adsorber Breakthrough Curve Method with Exact Solution. AIChE J. 1993, 39, 355-358.

Cotton, F. A. Wilkinson, G. *Advanced Inorganic Chemistry,* 2nd ed.; Wiley Interface: New York, 1966.

Crank, J. *The Mathematics of Diffusion*, 2nd ed.; Clarendon Press: Oxford, 1979.

Cunningham, R. E. Williams, R. J. J. *Diffusion in Gases and Porous Media*; Plenum Press: New York, 1980.

Cussler, E. L. *Diffusion: Mass Transfer in Fluid Systems*, 2nd ed.; Cambridge University Press: Cambridge, 1997.

Çağın, V. Use of Clinoptilolite for Copper and Nickel Removal from Aqueous Solutions. M.S. Dissertation, Middle East Technical University, Ankara, Turkey, 2006.

Çakıcıoğlu-Özkan, F.; Ülkü, S. Adsorption Characteristics of Lead-, Barium- and Hydrogen-Rich Clinoptilolite Mineral. Adsorpt. Sci. Technol. 2003, 21, 309-317.

Çakıcıoğlu-Özkan, F.; Ülkü, S. The Effect of HCl Treatment on Water Vapor Adsorption Characteristics of Clinoptilolite Rich Natural Zeolite. Microporous Mesoporous Mater. 2004, 77, 47-53.

Çakıcıoğlu-Özkan, F.; Ülkü, S. Diffusion Mechanism of Water Vapour in a Zeolitic Tuff Rich in Clinoptilolite. J. Therm. Anal. Calorim. 2008, 94, 699-702.

Çulfaz, M.; Yağız, M. Ion Exchange Properties of Natural Clinoptilolite: Lead–sodium and Cadmium-sodium Equilibria. Sep. Purif. Technol. 2004, 37, 93-105.

Dahm, A.; Eriksson, H. Ultra-stable Zeolites-a Tool for In-Cell Chemistry. J. Biotechnol. 2004, 111, 279–290.

Despres, J.; Koebel, M.; Kröcher, O.; Elsener, M.; Wokaun, A. Adsorption and Desorption of NO and NO_2 on Cu-ZSM-5. Microporous Mesoporous Mater. 2003, 58, 175-183.

Doula, M. K. Synthesis of a Clinoptilolite–Fe System with High Cu Sorption Capacity. Chemosphere. 2007, 67, 731-740.

Du, Q.; Liu, S.; Cao, Z.; Wang, Y. Ammonia Removal from Aqueous Solution Using Natural Chinese Clinoptilolite. Sep. Purif. Technol. 2005, 44(3), 229-234.

Dubinin, M. M.; Radushkevich, L. V. The Equation of the Characteristic Curve of Activated Charcoal. Proc. Acad. Sci. USSR Phy. Chem. Sect. 1947, 55, 331-333.

Dubinin, M. M. The Potential Theory of Adsorption of Gases and Vapors for Adsorbents with Energetically Nonuniform Surfaces. Chem. Rev. 1960, 6, 235-241.

Dubinin, M. M.; Astakhov, V. A. Development of the Concepts of Volume Filling of Micropores in the Adsorption of Gases and Vapors by Microporous Adsorbents. Russ. Chem. Bull. 1971, 20, 3-7.

Dwivedi, P. N.; Upadhyay, S. N. Particle-fluid Mass Transfer in Fixed and Fluidized Beds. Ind. Eng. Chem. Proc. Design Dev. 1977, 16, 157-165.

Edwards, M. F.; Richardson, J. F. Gas Dispersion in Packed Beds. Chem. Eng. Sci. 1968, 23, 109-123.

Elliott, H. A.; Huang, C. P. Adsorption Characteristics of Some Cu(II) Complexes on Aluminosilicates. Water Res. 1981, 15, 849–855.

Enemark, J. H.; Feltham, R. D. Stereochemical Control of Valence. II. Behavior of the {MNO}n [Metal Mononitrosyl] Group in Ligand Fields. J. Am. Chem. Soc. 1974a, 96, 5002-5004.

Enemark, J. H.; Feltham, R. D. Stereochemical Control of Valence. III. The $\{CoNO\}^8$ Group in Ligand Fields of C_{4v}, C_{2v}, and C_s Symmetry. J. Am. Chem. Soc. 1974b, 96, 5004-5005.

Englert, A. H.; Rubio, J. Characterization and Environmental Application of a Chilean Natural Zeolite. Int. J. Miner. Process. 2005, 75, 21-29.

Ergun, S. Fluid Flow through Packed Columns. Chem. Eng. Prog. 1952, 48, 9-94.

Ersoy, B.; Çelik, M. S. Electrokinetic Properties of Clinoptilolite with Mono- and Multivalent Electrolytes. Microporous Mesoporous Mater. 2002, 55, 305-312.

Esenli, F. Natural zeolite reserves, mining, production, and market situation. *National Zeolite Symposium*. Tubitak-mam, Gebze, Kocaeli (in Turkish). 2002.

Evans, E. V.; Kenney, C. N. Gaseous Dispersion in Laminar Flow Through a Circular Tube. Proc. Roy. Soc. London Ser.A. 1965, 284, 540-549.

Everett, D. H.; Powl, J. C. Adsorption in Slit-Like and Cylindrical Micropores in the Henry's Law region. A Model for the Microporosity of Carbons. J. Chem. Soc., Faraday Trans. 1. 1976, 72, 619-636.

Faghihian, H.; Marageh, M. G.; Kazemian, H. The Use of Clinoptilolite and Its Sodium rm for Removal of Radioactive Cesium, and Strontium from Nuclear Wastewater and Pb^{2+}, Ni^{2+}, Cd^{2+}, Ba^{2+} from Municipal Wastewater. Appl. Radiat. Isot. 1999, 50, 655-660.

Fang, F. C. Mechanisms of Nitric Oxide-Related Antimicrobial Activity. J. Clin. Invest. 1997, 99, 2818-2825.

Fang, F. C. Antimicrobial Reactive Oxygen and Nitrogen Species: Concepts and Controversies. Nat. Rev. Microbiol. 2004, 2, 820-832.

Farías, T.; Ruiz-Salvador, A. R.; Rivera, A. Interaction Studies Between Drugs and a Purified Natural Clinoptilolite. Microporous Mesoporous Mater. 2003, 61, 117-125.

Feltham, R. D.; Enemark, J. H. Structures of Metal Nitrosyls. In *Topics in Stereochemistry: Topics in Inorganic and Organometallic Stereochemistry;* Geoffroy, G. L., Ed.; Wiley: New York: 1981; Vol. 12, p 155.

Feng, J.; Chaikof, E. L. Reconstitution of Thrombomodulin into Polymerizable Phospholipid Vesicles. Polym. Prepr. 2000, 41, 16-17.

Feelisch, M.; Stamler, J. S. Donors of Nitrogen Oxide. In *Methods in Nitric Oxide Research*; Feelisch, M.; Stamler, J. S., Eds.; John Wiley and Sons, New York, 1996.

Filippidis, A.; Godelitsas, A.; Charistos, D.; Misaelides, P.; Kassoli-Fournaraki, A. The Chemical Behavior of Natural Zeolites in Aqueous Environments: Interactions between Low-silica Zeolites and 1 M NaCl Solutions of Different Initial pH-values. Appl. Clay Sci. 1996, 11, 199-209.

Flanigen, E. M.; Khatami, H.; Szimansky, H. A. Molecular Sieve Zeolites. In *Advances in Chemistry Series*; Flanigen, E. M.; Sand L. B., Eds.; American Chemical Society: Washington, 1971; Vol. 101, p 201.

Fleming, I.; Banersachs, J.; Fischthaler, B.; Busse, R. Ca^{2+}-Independent Activation of the Endothelial Nitric Oxide Snthase in Response to Tyrosine Phosphatase Inhibitors and Fluid Shear Stress. Circ. Res. 1998, 82, 686-695.

Fogler, H. S. *Elements of Chemical Reaction Engineering*, 3rd Edition; Prentice Hall: New York, 1999.

Frost, M. C.; Reynolds, M. M.; Meyerhoff, M. E. Polymers Incorporating Nitric Oxide Releasing/Generating Substances for Improved Biocompatibility of Blood-contacting Medical Devices. Biomaterials. 2005, 26, 1685-1693.

Furchgott, R. F. Studies on Relaxation of Rabbit Aorta by Sodium Nitrite: the Basis for the Proposal That the Acid-activatable Inhibitory Factor from Retractor Penis is Inorganic Nitrite and the Endothelium-derived Relaxing Factor is Nitric Oxide. In *Vasodilation: Vascular Smooth Muscle, Peptides, and Endothelium;* Vanhoutte, P. M.; Ed.; Raven Press: New York, 1988; p 401.

Furuyama, S.; Morimoto, T. Sorption of Nitric Oxide, Carbon Monoxide, and Nitrogen by Sodium Mordenite. J. Phys. Chem. 1978, 82, 1748-1752.

Furuyama, S.; Nagato, M. Sorption of Argon, Oxygen, Nitrogen, Nitric Oxide, and Carbon Monoxide by Magnesium, Calcium, and Barium Mordenites. J. Phys. Chem. 1984, 88, 1735-1740.

Furuyama, S.; Miyazaki, M.; Inoue, H. Sorption of Argon, Oxygen, Nitrogen, Nitric Oxide, and Carbon Monoxide by Hydrogen Mordenite, Hydrogen ZSM-5 Synthetic Zeolite, and Sodium Hydrogen Mordenites. J. Phys. Chem. 1984, 88, 1741-1744.

Galán, M. A. Adsorption Characteristics of Nitric Oxide on Various Adsorbents Determined by Gas-solid Chromatography. Chem. Eng. J. 1984, 28, 105-113.

Garg, D. R.; Ruthven, D. M. Theoretical Prediction of Breakthrough Curves for Molecular Sieve Adsorption Columns-I. Asymptotic Solutions. Chem. Eng. Sci. 1973, 28, 791-798.

Ghaffari, A.; Neil, D. H.; Ardakani, A.; Road, J.; Ghahary, A.; Miller, C. C. A Direct Nitric Oxide Gas Delivery System for Bacterial and Mammalian Cell Cultures. Nitric Oxide. 2005, 12, 129-140.

Godelitsas, A.; Armbruster, T. HEU-type Zeolites Modified by Transition Elements and Lead. Microporous Mesoporous Mater. 61, 2003, 3-24.

Godelitsas, A.; Charistos, D.; Tsipis, A.; Tsipis, C.; Filippidis, A.; Triantafyllidis, C.; Manos, G.; Siapkas, D. Characterization of Zeolitic Materials with a HEU-type Structure Modified by Transition Metal Elements: Definition of Acid Sites in Nickel-Loaded Crystals in the Light of Experimental and Quantum-Chemical Results. Chem.-Eur. J. 2001, 7, 3705-3721.

Golden, T. C.; Sircar, S. Gas Adsorption on Silicalite. J. Colloid Interface Sci. 1994, 162, 182–188.

Gottardi, G.; Galli, E. *Natural Zeolites*, Springer-Verlag, Berlin, 1985.

Gradev, G.; Avramova, A.; Stefanova, I. Silver Sorption on Clinoptilolite and Vermiculite and Their Modifications. In *Occurrence, Properties and Utilization of Natural Zeolites*; Kallo, D.; Sherry, H. S., Eds.; Akademia Kiado: Budapest, 1988, p 463.

Green, L. C.; Wagner, D. A.; Glogowski, J. Jr.,; Skipper, P. L.; Wishnok, J. S.; Tannenbaum, S. R. Analysis of Nitrate, Nitrite, and [^{15}N] Nitrate in Biological Fluids. Anal. Biochem. 1982, 126, 131-138.

Gregg, S. J.; Sing, K. S. W. *Adsorption, Surface Area, and Porosity*, Academic Press: London, 1982.

Gruberg, L.; Waksman, R.; Satler, L. F.; Pichard, A. D.; Kent, K. M. Novel Approaches for the Prevention of Restenosis. Expert Opin. Invest. Drugs. 2000, 9, 2555-2578.

Gunn, D. J. Mixing In Packed and Fluidized Beds. The Chemical Engineer, 1968, 6, 153-172.

Gurvitsch, L. G. Physicochemical Attractive force. J. Phys. Chem. Russia. 1915, 47, 805-827.

Hadjiivanov, K.; Klissurski, D.; Ramis, G.; Busca, G. Fourier Transform IR Study of NO_x Adsorption on a CuZSM-5 DeNO_x Catalyst. Appl. Catal. B. 1996, 7, 251-267.

Hadjiivanov, K. IR Study of CO and NOx Sorption on Ag-ZSM-5. Microporous Mesoporous Mater. 1998, 24, 41-49.

Hadjiivanov, K.; Knozinger, H.; Tsyntsarski, B.; Dimitrov, L. Effect of Water on the Reduction of NOx with Propane on Fe-ZSM-5, An FTIR Mechanistic Study. Catal. Lett. 1999, 62, 35-40.

Hadjiivanov, K.; Tsyntsarski, B.; Nikolova, T. Stability and Reactivity of the Nitrogen-oxo Species Formed After NO Adsorption and NO+O_2 Coadsorption on Co-ZSM-5: An FTIR Spectroscopic Study. PCCP. 1999, 1, 4521-4528.

Hadjiivanov, K. Identification of Neutral and Charged N_xO_y Surface Species by IR Spectroscopy. Catal. Rev.-Sci. Eng. 2000, 42, 71-144.

Haggerty, G.M.; Bowman, R. S. Sorption of chromate and other inorganic anions by organo zeolites. Environ. Sci. Technol. 1994, 28, 452-458.

Hand, D. W.; Crittenden, J. C.; Asce, M.; Tracker, W. E. Simplified Models for Design of Fixed-bed Adsorption Systems. J. Environ. Eng. 1984, 110, 440-456.

Hashimoto, N.; Smith, J. M. Diffusion in Bidisperse Porous Catalyst Pellets. Ind. Eng. Chem. Fundam. 1974, 13, 115-120.

Hattori, T.; Kaneko, K.; Ishikawa, T.; Inouye, K. Adsorption of Nitrogen Monoxide on Iron Oxide Hydroxides and Their Calcinated Products. Journal of Chemical Society of Japan. 1979, 423-426.

Henao, J. D.; Córdoba, L. F.; de Correa, C. M. Theoretical and Experimental Study of NO/NO_2 Adsorption over Co-exchanged Type-A Zeolite. J. Mol. Catal. A: Chem. 2004, 207, 195-204.

Hernandez, M. A.; Corona, L.; Rojas, F. Adsorption Characteristics of Natural Erionite, Clinoptilolite and Mordenite Zeolites from Mexico. Adsorption. 2000, 6, 33-45.

Hernández-Huesca, R.; Díaz, L.; Aguilar-Armenta, G. Adsorption Equilibria and Kinetics of CO_2, CH_4 and N_2 in Natural Zeolites. Sep. Purif. Technol. 1999, 15, 163-173.

Hirschfelder, J. O.; Curtiss, C. F.; Bird, R. B. *Molecular Theory of Gases and Liquids*, John Wiley and Sons: New York, 1954.

Ho, Y.-S. Citation review of Lagergren kinetic rate equation on adsorption reactions, Scientometrics, 2004, 59, 171-177.

Hsu, L. K. P.; Haynes, H. W. Effective Diffusivity by the Gas-chromatography Technique: Analysis and Application to Measurements of Diffusion of Various Hydrocarbons in Zeolite NaY. AIChE J. 1981, 27, 81-91.

http://www.uksaf.org/tech/edx.html

http://webmineral.com

http://www.chem.ox.ac.uk/teaching/Exams2005/PartIBGenIn.org.pdf

Huang, Y. Y. Adsorption in AgX and AgY Zeolites by Carbon Monoxide and Other Simple Molecules. J. Catal. 1974, 32, 482-491.

Huang, H. Y.; Yang, R. T. Removal of NO by Reversible Adsorption on Fe-Mn Based Transition Metal Oxides. Langmuir. 2001, 17, 4997-5003.

Ignarro, L. J.; Buga, G. M.; Wood, K. S.; Byrns, R. E.; Chaudhuri, G. Endothelium-derived Relaxing Factor Produced and Released from Artery and Vein is Nitric Oxide. PNAS. 1987, 84, 9265-9269.

Ignarro, L. J. *Nitric Oxide: Biology and Pathobiology*, Academic Press, San Diego, 2000.

Inglezakis, V. J.; Grigoropoulou, H. P. Applicability of Simplified Models for the Estimation of Ion Exchange Diffusion Coefficients in Zeolites. J. Colloid Interface Sci. 2001, 234, 434-441.

Inglezakis, V. J.; Hadjiandreou, K. J.; Loizidou, M. D.; Grigoropoulou, H. P. Pretreatment of Natural Clinoptilolite in a Laboratory-scale Ion Exchange Packed Bed. Wat. Res. 2001, 35, 2161-2166.

Inglezakis, V. J.; Loizidou, M. D.; Grigoropoulou, H. P. Equilibrium and Kinetic Ion Exchange Studies of Pb^{2+}, Cu^{2+}, Fe^{3+}, and Cr^{3+} on Natural Clinoptilolite. Wat. Res. 2002, 36, 2784-2792.

Inglezakis, V. J.; Loizidou, M.; Grigoropoulou, H. Ion Exchange Studies on Natural and Modified Zeolites and the Concept of Exchange Site Accessibility. J. Colloid Interface Sci. 2004, 275, 570-576.

Inglezakis, V. J. The Concept of "Capacity" in Zeolite Ion-Exchange Systems. J. Colloid Interface Sci. 2005, 281, 68-79.

Inglezakis, V. J.; Poulopoulos, S. G. *Adsorption, Ion Exchange and Catalysis, Design of Operations and Environmental Applications*, Elsevier: The Netherlands; 2006.

Ivanova, E.; Hadjiivanov, K.; Klissurski, D.; Bevilacqua, M.; Armaroli, T.; Busca, G. FTIR Studies of Species Arising After NO Adsorption and $NO+O_2$ Co-adsorption on CoY: Comparison with Co-ZSM-5. Microporous Mesoporous Mater. 2001, 46, 299-309.

Iwamoto, M.; Yahiro, H.; Mizuno, N.; Zhang, W. X.; Mine, Y.; Furukawa, H.; Kagawa, S. Removal of Nitrogen Monoxide Through a Novel Catalytic Process. 2. Infrared Study on Surface Reaction of Nitrogen Monoxide Adsorbed on Copper Ion-Exchanged ZSM-5 Zeolites. J. Phys. Chem. 1992, 96, 9360-9366.

Iwamoto, M.; Yahiro, H. Zeolites in the Science and Technology of Nitrogen Monoxide Removal. In *Handbook of Zeolite Science and Technology*, Auerbach, S. M.; Carrado, K. A; Dutta, P. K., Eds.; Marcel Dekker: New York, 2003; p 951.

Jama, M. A.; Yücel, H. Equilibrium Studies of Sodium-ammonium, Potassium-ammonium, and Calcium-ammonium Exchanges on Clinoptilolite Zeolite. Sep. Sci. Technol. 1990, 24, 1393-1416.

Jasra, R. V.; Choudary, N. V.; Bhat, S. G. T. Separation of Gases by Pressure Swing Adsorption. Sep. Sci. Technol. 1991, 26, 885-930.

Jayaraman, A.; Yang, R. T.; Chinn, D.; Munson, C. L. Tailored Clinoptilolites for Nitrogen/Methane Separation. Ind. Eng. Chem. Res. 2005, 44, 5184-5192.

Jentys, A.; Lercher, J. A. Techniques of Zeolite Characterization. In *Introduction to Zeolite Science and Practice;* van Bekkum, H.; Flanigen, E. M.; Jacobs, P. A.; Jansen, J. C., Eds.; Elsevier: Amsterdam, 2001.

Jermyn, J. W.; Johnson, T. J.; Vansant, E. F.; Lunsford, J. H. Iron-nitrosyl Complexes Formed in Zeolites. J. Phys. Chem. 1973, 77, 2964-2969.

Joshi, M.; Joshi, V.; Choudhari, A.; Kasture, M. Structural Studies of Natural Heulandite Using Infrared Spectroscopy. Mater. Chem. Phys. 1997, 48, 160-163.

Joithe, W.; Bell, A. T.; Lynn, S. Removal and Recovery of NO_x from Nitric Acid Plant Tail Gas by Adsorption on Molecular Sieves. Ind. Eng. Chem. Proc. Design Dev. 1972, 11, 434-439.

Kaneko, K.; Inouye, K. Effect of Heat Treatment in Vacuo on the NO Adsorption Activity of α-FeOOH-dispersed Activated Carbon Fibers. Carbon. 1986, 24, 772-774.

Kaneko, K. Anomalous Micropore Filling of NO on α-FeOOH Dispersed Activated Carbon Fibers. Langmuir. 1987a, 3, 357-363.

Kaneko, K.; Fukuzaki, N.; Ozeki, S. The Concentrated NO Dimer in Micropores above Room Temperature. J. Chem. Phys. 1987b, 87, 776-777.

Kaneko, K. Anomalous Micropore Filling of NO on Fe_2O_3-dispersed Activated Carbon Fibers. In *Characterization of Porous Solids*, Unger, K. K.; Rouquerol, J.; Sing, K. S. W.; Krol, H., Eds.; Elsevier: Amsterdam, 1988; p 183.

Kaneko, K.; Inouye, K. Adsorption Activity of Nitric Oxide on Iron Oxide-dispersed Porous Materials. Adsorpt. Sci. Technol. 1988, 5, 239-250.

Kaneko, K. Effect of Temperature on Micropore Filling of Supercritical NO on Fe_2O_3-dispersed Activated Carbon Fibers. Colloid. Surface. 1989, 37, 115-124.

Kaneko, K.; Murata, K. An Analytical Method of Micropore Filling of a Supercritical Gas, Adsorption, 1997, 3, 197-208.

Karabelas, A. J.; Wegner, T. H.; Hanratty, T. J. Use of asymptotic relations to correlate mass transfer data in packed beds. Chem. Eng. Sci. 1971, 26, 1581-1589.

Karge, H. G. Characterization by Infrared Spectroscopy. Microporous Mesoporous Mater. 1998, 22, 547–549.

Kärger, J.; Ruthven, D. M. *Diffusion in Zeolites and Other Microporous Solids*, John Wiley and Sons: New York; 1992.

Kataoka, T.; Yoshida, H.; Ueyama, K. Mass transfer in laminar region between liquid and packing material surface in packed bed. J. Chem. Eng. Japan. 1972, 5, 34-38.

Kavdia, M.; Nagarajan, S.; Lewis, R. S. Novel Devices for the Predictable Delivery of Nitric Oxide to Aqueous Solutions. Chem. Res. Toxicol. 1998, 11, 1346-1351.

Kawazoe, K.; Suzuki, M.; Chihara, K. Chromatographic Study of Diffusion in Molecular Sieving Carbon. J. Chem. Eng. Jpn. 1974, 7, 151-157.

Keane, M. A. Role of the Alkali Metal Co-cation in the Ion Exchange of Y Zeolites III. Equilibrium Properties of the Ni/Cu/Na-Y and Ni/Cu/K-Y Zeolite Systems. Microporous Mater. 1995, 4, 359-368.

Kelm, M. The l-arginine-nitric Oxide Pathway in Hypertension. Current Hypertension Reports. 2003, 5, 80-86.

Kesraoui-Ouki, S.; Kavannagh, M. Performance of Natural Zeolites for the Treatment of Mixed Metal-contaminated Effluents. Waste Manage. Res. 1997, 15, 383-394.

Kesraoui-Ouki, S.; Cheeseman, C.; Perry, R. Effects of Conditioning and Treatment of Chabazite and Clinoptilolite Prior to Lead and Cadmium Removal. Environ. Sci. Technol. 1993, 27, 1108-1116.

Khare, M.; Bukhari, S.; Swann, A.; Spiers, P.; McLaren, I.; Myers, J. Reduction of Catheter-related Colonization by the Use of a Silver Zeolite-impregnated Central Vascular Catheter in Adult Critical Care. J. Infection. 2006, 54, 146-150.

Kim, Y. G.; Kim, Y. C.; Hong, S. B.; Kim, M. H.; Kim, Y. P.; Uh, Y. S. Selective Reduction of Nitric Oxide by Methane on Cobalt-ion-Exchanged Synthetic Clinoptilolite Zeolite in Oxygen-rich Atmosphere. Catal. Lett. 1999, 57, 179-185.

Knowlton, G. D.; White, T. R. Thermal Study of Types of Water Associated with Clinoptilolite. Clays Clay Miner. 1981, 29, 403-411.

Korkuna, O.; Leboda, R.; Skubiszewska-Zięba, J.; Vrublevs'ka, T.; Gun'ko, V. M.; Ryczkowski, J. Structural and Physicochemical Properties of Natural Zeolites: Clinoptilolite and Mordenite. Microporous Mesoporous Mater. 2006, 87, 243-254.

Koyama, K.; Takeuchi, Y. Clinoptilolite: The Distribution of Potassium Atoms and Its Role in Thermal Stability. Z. Kristallogr. Bd. 1977, 145, 216-239.

Kumar, S.; Upadhyay, S. N.; Mathur, V. K. Low Reynolds number mass transfer in packed beds of cylindrical particles. Ind. Eng. Chem. Proc. Des. Dev. 1977, 16, 1-8.

Kurkovic, L.; Cerjan-Stefanovic, S.; Philipan, T. Metal Ion Exchange by Natural and Modified Zeolites. Water Res. 1997, 31, 1379-1382.

Laane, J.; Ohlsen, J. R. Characterization of Nitrogen Oxides by Vibrational Spectroscopy. In *Progress in Inorganic Chemistry*, Lippard, S. J., Ed.; John Wiley: New York, 1980; Vol. 27; p 465.

Lam, A.; Sierra, L. R.; Rojas, G.; Rivera, A.; Rodriguez-Fuentes, G.; Montero, L. A. Theoeretical Study of the Physical Adsorption of Aspirin on Natural Clinoptilolite. Microporous Mesoporous Mater. 1998, 23, 247-252.

Langella, A.; Pansini, M.; Cappelletti, P.; Gerraro, B.; Gennaro , M.; Collela, C. NH_4^+, Cu^{2+}, Zn^{2+}, Cd^{2+} and Pb^{2+} Exchange for Na^+ in a Sedimentary Clinoptilolite, North Sardinia, Italy. Microporous Mesoporous Mater. 2000, 37, 337-343.

Langer, G.; Roethe, A.; Roethe, K.-P.; Gelbin, D. Heat and Mass Transfer in Packed Beds-III. Axial Mass Dispersion. Int. J. Heat Mass Transfer. 1978, 21, 751-759.

Levenspiel, O. *Chemical Reaction Engineering*, 2nd Edition, Wiley Eastern Limited, India, 1972.

Li, Y.; Slager, T. L.; Armor, J. N. Selective Reduction of NOx by Methane on Co-Ferrierites: II. Catalyst Characterization. J. Catal. 1994, 150, 388-399.

Lide, D. R. *Handbook of Chemistry and Physics*, 72nd ed.; CRC Press, 1991.

Lin, C. Y.; Yang, D. H. Removal of Pollutants from Wastewater by Coal Bottom Ash. J. Environ. Sci. Health. Part A Toxic/Hazard. Subst. Environ. Eng. 2002, 37, 1509-1522.

Long, R. Q.; Yang, R. T. Selective Catalytic Reduction of NO with Ammonia over Fe^{3+}-exchanged Mordenite (Fe–MOR): Catalytic Performance, Characterization, and Mechanistic Study. J. Catal. 2002, 207, 274-285.

Lunsford, J. H.; Hutta, P. J.; Lin, M. J.; Windhorst, K. A. Cobalt Nitrosyl Complexes in Zeolites A, X, and Y. Inorg. Chem. 1978, 17, 606-610.

Ma, Y. H.; Mancel, C. Diffusion Studies of CO_2, NO, NO_2, and SO_2 on Molecular Sieve Zeolites by Gas Chromatography. AIChE J. 1972, 18, 1148-1153.

Makrides, S. C.; Ryan, U. S. Overview of the Endothelium. In *Thrombosis and Hemorrhage;* Loscalzo, J.; Schafer, A. I. Eds.; Williams and Wilkins, 2nd Edition, Baltimore, 1998, p 295.

Mancinelli, R. L.; Mckay, C. P. Effects of Nitric Oxide and Nitrogen Dioxide on Bacterial Growth. Appl. Environ. Microbiol. 1983, 46, 198-202.

Mateo, A. O.; De Artinano, M. A. A. Nitric Oxide Reactivity and Mechanisms Involved in Its Biological Effects. Pharmacol. Res. 2000, 42, 421-427.

Matsumoto, A.; Sano, M.; Nishimiya, N.; Tsutsumi, K. Adsorption Characteristics in Zeolite Nano-pore Evaluated by Use of Nitrogen Monoxide as a Probe Adsorbate. Adsorption. 2000, 6, 251-257.

McHenry, K. W.; Wilhelm, R. H. Axial Mixing of Binary Gas Mixtures Flowing in a Random Bed of Spheres. AIChE J. 1957, 3, 83-91.

Mihaylov, M.; Hadjiivanov, K.; Panayotov, D. FTIR Mechanistic Studies on the Selective Catalytic Reduction of NOx with Methane over Ni-containing Zeolites: Comparison between NiY and Ni-ZSM-5. Appl. Catal. B. 2004, 51, 33-42.

Milan, Z.; Sanchez, E.; Weiland, P.; de Las Pozas, C.; Borja, R.; Mayari, R.; Rovirosa, N. Ammonia Removal from Anaerobically Treated Piggery Manure by Ion Exchange in Columns Packed with Homoionic Zeolite. Chem. Eng. J. 1997, 66, 65-71.

Ming, D. W.; Dixon, J. B. Zeolites: Recent Developments in Soil Mineralogy, Transactions XIII Congress of the International Society of Soil Science: Symposia Papers, 1987; Vol. V, p 371.

Ming, D. W.; Allen, E. R.; Galindo, C.; Henninger, D. L. M. Methods for Determining Cation Exchange Capacities and Composition of Native Cations for Clinoptilolite. In Memories of the 3rd International Conference on the Occurrence Properties, and Utilization of Natural Zeolites, Fuentes, G. R.; González, J., Eds.; Havana, 1995; Vol. 2, p 31.

Mishchenko, K. P.; Poltoratskii, G. M. *Short Handbook of Physicochemikal Parameters,* Khimiya: Leningrad, 1972.

Misk, M.; Poly, G., Magnoux, P.; Guisnet, M.; Jullian, S. Formation of Coke from Propene over 5A Adsorbents-Influence of the Binder on the Coke Compositon, Location and Removal. Microporous Mesoporous Mat. 2000, 40, 197-204.

Miura, K.; Hashimoto, K. Analytical Solutions for the Breakthrough Curves of Fixed-bed Adsorption Under Constant Pattern and Linear Driving Force Approximations. J. Chem. Eng. Jpn. 1977, 10, 490-493.

Moncada, S.; Palmer, R. M. J.; Higgs, E. A. Endogenous Nitric Oxide: Physiology, Pathology and Clinical Relevance. Eur. J. Clin. Invest. 1991, 43, 109-141.

Moreno-Tost, R.; Santamaria-González, J.; Rodriguez-Castellón, E.; Jiménez-López, A.; Autié, M. A.; González, E.; Glacial, M. C.; De las Pozas, C.;Selective Catalytic Reduction of Nitric Oxide by Ammonia over Cu-exchanged Cuban Natural Zeolites. Appl. Catal. B. 2004, 50, 279-288.

Moulijn, J. A.; van Swaaij, W. P. M. The Correlation of Axial Dispersion Data for Beds of Small Particles. Chem. Eng. Sci. 1976, 31, 845-847.

Moulijn, J. A. Stimulus/response experimenten in gepakte bedden. Ph.D. Dissertation, University of Amsterdam, Amsterdam, 1974.

Mozgawa, W.; Sitarz, M.; Rokita, M. Spectroscopic Studies of Different Aluminosilicate Structures. J. Mol. Struct. 1999, 512, 251-257.

Mozgawa, W. The Influence of Some Heavy Metals Cations on the FTIR Spectra of Zeolites. J. Mol. Struct. 2000, 555, 299–304.

Mozgawa, W.; Z. Fojud, Z.; Handke, M.; Jurga, S. MAS NMR and FTIR Spectra of Framework Aluminosilicates. J. Mol. Struct. 2002, 614, 281-287.

Mozgawa, W.; Bajda, T. Spectroscopic Study of Heavy Metals Sorption on Clinoptilolite. Phys. Chem. Miner. 2005, 31, 706–713.

Mumpton, F. A. Clinoptilolite Redefined. Am. Mineral. 1960, 45, 351-369.

Mumpton, F. A. Development of Uses for Natural Zeolites: A Critical Commentary. In *Occurrence, Properties and Utilization of Natural Zeolites;* Kallo, D.; Sherry, H. S., Eds.; Akademia Kiado: Budapest, 1998; p 333.

Mumpton, F. A. *La roca magica*: Uses of Natural Zeolites in Agriculture and Industry. PNAS. 1999, 96, 3463-3470.

Munson, R. A. *Properties of Natural Zeolites*, Report of Investigations 7744, U.S. Bur. Mines: Washington, 1973.

Naccache, C.; Ben Taarit, Y. Nature of Nitric Oxide and Nitrogen Dioxide Adsorbed on Chromium and Nickel Exchanged Zeolites. Electron Spin Resonance and Infrared Study. J. Chem. Soc. Faraday Trans. I. 1973, 69, 1475-1486.

Nakamoto, K. *Infrared Spectra of Inorganic and Coordination Compounds*, Mir: Moscow, 1966.

Nakamura, T.; Ishikawa, M.; Hiraiwa, T.; Sato, J. X-Ray Diffractometric Determination of Clinoptilolite in Zeolite Tuff using Multiple Analytical Lines. Anal. Sci. 1992, 8, 539-543.

Narin, G. A Chromatographic Study of Carbon Monoxide Adsorption in Clinoptilolite, M.S. Dissertation, Izmir Institute of Technology, İzmir, Turkey, 2001.

Narin, G.; Yılmaz, S.; Ülkü, S. A Chromatographic Study of Carbon Monoxide Adsorption on a Clinoptilolite-Containing Natural Zeolitic Material. Chem. Eng. Commun. 2004, 191, 1411-1425.

Nathan, C.; Xie, Q. W. C. Regulation of Biosynthesis of Nitric Oxide. J. Biol. Chem. 1994, 269, 13725-13728.

Nightingale, Jr. E. R. Phenomenological Theory of Ion Solvation, Effective Radii of Hydrated Ions. J. Phys. Chem. 1959, 63, 1381-1387.

Oelkers, E. H.; Schott, I. Experimental Study of Anorthite Dissolution and the Relative Mechanism of Feldspar Hydrolysis. Geochim. Cosmochim. Acta. 1995, 59, 5039-5053.

Ohashi, H.; Sugawara, T.; Kikuchi, K.-I.; Konno. H. Correlation of liquid-side mass transfer coefficient for single particles and fixed beds. J. Chem. Eng. Jpn. 1981, 14, 433-438.

Olive, H.; Lacoste, G. Application of volumetric electrodes to the recuperation of metals in industrial effluents-I. Mass transfer in fixed beds of spherical conductive particles. Electrochim. Acta. 1979, 24, 1109-1114.

Padden, K. M.; Krebs, J. F.; MacBeth, C. E.; Scarrow, R. C.; Borovik, S. Immobilized Metal Complexes in Porous Organic Hosts: Development of a Material for the Selective and Reversible Binding of Nitric Oxide. J. Am. Chem. Soc. 2001, 123, 1072-1079.

Panayotova, M.; Velikov, B. Influence of Zeolite Transformation in a Homoionic Form on the Removal of Some Heavy Metal Ions from Wastewater. J. Environ. Sci. Health. Part A. 2003, 38, 545-554.

Parlat, S. S.; Yıldız, A. O.; Oğuz, H. Effect of Clinoptilolite on Performance of Japanese Quail (*Coturnix coturnix japonica*) During Experimental Aflatoxicosis. Brit. Poultry Sci. 1999, 40, 495-500.

Pavelic, K.; Hadzija, M.; Bedrica, L.; Pavelic, J.; Dikic, I.; Katic, M.; Kralj, M.; Bosnar, M. H.; Kapitanovic, S.; Poljak-Blazi, M.; Krizanac, S.; Stojkovic, R.; Jurin, M.; Subotic, B.; Colic, M. Natural Zeolite Clinoptilolite: New Adjuvant in Anticancer Therapy. J. Mol. Med. 2001, 78, 708-720.

Pavelic, K.; Katic, M.; Sverko, V.; Marotti, T.; Bosnjak, B.; Balog, T.; Stojkovic, R.; Radacic, M.; Colic, M.; Poljak-Blazi, M. Immunostimulatory Effect of Natural Clinoptilolite as a Possible Mechanism of Its Antimetastatic Ability. J. Cancer Res. Clin. Oncol. 2002, 128, 37-44.

Perry, R. H.; Green, D. *Perry's Chemical Engineer's Handbook*, 7th Edition, McGraw-Hill, 1999.

Petrov, O. E. Cation Exchange in Clinoptilolite: An X-ray Powder Diffraction Analysis. In *Natural Zeolites'93: Occurrence, Properties, Use, International Committee on natural Zeolites*; Ming, D. W.; Mumpton, F. A., Eds.; Brockport: New York, 1995.

Pinna, F. Supported Metal Catalysts Preparation. Catal. Today. 1998, 41, 129-137.

Pozdnyakov, D.; Filiminov, V. Infrared Spectroscopic Study of the Chemisorption of Nitric Oxide and Nitrogen Dioxide on Metal Oxides. Kinet. Katal. 1973, 14, 760-766.

Pöppl, A.; Rudolf, T.; Manikandan, P.; Goldfarb, D. W- and X-band Pulsed Electron Nuclear Double-resonance Study of a Sodium-Nitric Oxide Adsorption Complex in NaA Zeolites. J. Am. Chem. Soc. 2000, 122, 10194-10200.

Prausnitz, J. M.; Lichtenthaler, R. N.; de Azevedo, E. G. *Molecular Thermodynamics of Fluid-Phase Equilibria*, 3rd ed.; Prentice-Hall: New Jersey, 1999.

Privat, C.; Lantoine, F.; Bedioui, F.; Brussel, E. M.; Devynck, J.; Devynck, M. Nitric Oxide Production by Endothelial Cells: Comparison of Three Methods of Quantification. Life Sci. 1997, 61, 1193-1202.

Radomski, M. W.; Palmer, R. M. J.; Moncada, S. The Role of Nitric Oxide and cGMP in Platelet Adhesion to Vascular Endothelium. Biochem. Biophys. Res. Commun. 1987a, 148, 1482-1489.

Radomski, M. W.; Palmer, M. J.; Moncada, S. Comparative Pharmacology of Endothelium-derived Relaxing Factor, Nitric Oxide and Prostacyclin in Platelets. Br. J. Pharmacol. 1987b, 92, 181-187.

Ravikovitch, P. I.; Vishnyakov, A.; Russo, R.; Neimark, A. V. Unified Approach to Pore Size Characterization of Microporous Carbonaceous Materials from N_2, Ar, and CO_2 Adsorption Isotherm. Langmuir. 2000, 16, 2311-2320.

Regar, E.; Sianos, G.; Serruys, P. W. Stent Development and Local Drug Delivery. Brit. Med. Bull. 2001, 59, 227-248.

Rege, S. U.; Yang, R. T.; Buzanowski, M. A. Sorbents for Air Prepurification in Air Separation. Chem. Eng. Sci. 2000, 55, 4827-4838.

Reid, R. C.; Praustnitz, J. M.; Poling, P. E. *The Properties of Gases and Liquids*, 4th Edition, McGraw Hill, Boston, 1987.

Richter-Addo, G. B.; Lezdins, P. *Metal Nitrosyls*, Oxford University Press: Oxford, 1992.

Riddell, D. R.; Owen, J. S. Nitric Oxide and Platelet Aggregation. Vitamin. Hormone.-Advan. Res. App. 1999, 57, 25-48.

Rivera, A.; Rodriguez-Fuentes, G.; Altshuler, E. Characterization and Neutralizing Properties of a Natural Zeolite/Na_2CO_3 Composite Material. Microporous Mesoporous Mater. 1998, 24, 51-58.

Rivera, A.; Rodriguez-Fuentes, G.; Altshuler, E. Time Evolution of a Natural Clinoptilolite in Aqueous Medium: Conductivity and pH Experiments, Microporous Mesoporous Mater., 2000, 40, 173-179.

Rivera-Garza, M.; Olguín, M. T.; García-Sosa, I.; Alcántara, D.; Rodríguez-Fuentes, G. Silver Supported on Natural Mexican Zeolite as an Antibacterial Material. Microporous Mesoporous Mater. 2000, 39, 431-444.

Rivera, A.; Farías, T.; Ruiz-Salvador, A. R.; de Ménorval, L. C. Preliminary Characterization of Drug Support Systems Based on Natural Clinoptilolite, Microporous Mesoporous Mater., 2003, 61, 249-259.

Rivera, A.; Farías, T. Clinoptilolite–surfactant Composites as Drug Support: A New Potential Application. Microporous Mesoporous Mater. 2005, 80, 337-346.

Roberts, P. V.; Cornal, P. External Mass-transfer Rate in Fixed-bed Adsorption. J. Environ. Eng. 1985, 111, 891-905.

Rodriguez-Fuentes, G.; Barrios, M. A.; Iraizoz, A.; Perdomo, I.; Cedre, B. Enterex: Anti-diarrheic Drug Based on Purified Natural Clinoptilolite. Zeolites. 1997, 19, 441-448.

Rodriguez-Iznaga, I.; Gomez, A.; Rodriguez-Fuentes, G.; Benitez-Aguilar, A.; Serrano-Ballan, J.; Natural Clinoptilolite as an Exchanger of Ni^{2+} and NH_4^+ Ions Under Hydrothermal Conditions and High Ammonia Concentration., Microporous Mesoporous Mater. 2002, 53, 71-80.

Rodríguez-Reinoso, F.; Molina-Sabio, M. Activated Carbons from Lignocellulosic Materials. Advan. Colloid Interface Sci. 1998, 76-77, 271-294.

Rouquerol, F.; Rouquerol, J.; Sing, K. S. W. *Adsorption by Powders and Porous Solids*, Academic Press: London, 1999; p. 255

Roque-Malherbe, R. Complementary approach to the volume filling theory of adsorption in zeolites. Microporous Mesoporous Mater. 2000, 41, 227-240.

Rozic, M.; Stefanovic, S. J.; Curkovic, L. Evaluation of Croation Clinoptilolite- and Montmorillonite-rich Tuffs for Ammonium Removal. Croat. Chem. Acta. 2002, 75, 255-269.

Ruthven, D. M. *Principles of Adsorption and Adsorption Processes*, John Wiley and Sons: New York; 1984.

Ruthven, D. M. Sorption Kinetics for Diffusion-controlled Systems with a Strongly Concentration-dependent Diffusivity. Chem. Eng. Sci. 2004, 59, 4531-4545.

Ruthven, D. M. Fundamentals of Adsorption Equilibrium and Kinetics in Microporous Solids. In *Adsorption and Diffusion, Molecular Sieves*; Karge, H. G.; Weitkamp, J.; Eds.; Springer-Verlag: Berlin, 2006; Vol. 7; p 1.

Ryczkowski, J. IR Spectroscopy in Catalysis. Catal. Today. 2001, 68, 263-381.

Saito, A.; Foley, H. C. Curvature and Parametric Sensitivity in Models for Adsorption in Micropores. AIChE J. 1991, 37(3), 429-436.

Salama, T. M.; Mohamed, M. M.; Othman I. A.; El-Shobaky, G. A. Structural and Textural Characteristics of Ce-containing Mordenite and ZSM-5 Solids and FT-IR Spectroscopic Investigation of the Reactivity of NO Gas Adsorbed on Them. Appl. Catal. A. 2005, 286, 85-95.

Sasaki, S.; Miura, T.; Nishikawa, S.; Yamada, K.; Hirasue, M.; Nakane, A. Protective Role of Nitric Oxide in *Staphylococcus Aureus* Infection in Mice. Infect. Immun. 1998, 66, 1017-1022.

Schlünder, E. U. On the Mechanism of Mass Transfer in Heterogeneous Systems-in Particular in Fixed Beds, Fluidized Beds and on Bubble Trays. Chem. Eng. Sci. 1977, 32, 845-851.

Schmidt, H. H. H. W.; Kelm, M. Determination of Nitrite and Nitrate by the Griess Reaction. In *Methods in Nitric Oxide Research;* Feelisch, M.; Stamler, J. S.; Eds.; John Wiley & Sons: Chichester, 1996; p. 491.

Schoenfisch, M. H.; Mowery, K. A.; Rader, M. V.; Baliga, N.; Wahr, J. A.; Meyerhoff, M. E. Improving the Thromboresistivity of Chemical Sensors Via Nitric Oxide Release: Fabrication and in Vivo Evaluation of NO-releasing Oxygen-sensing Catheters. Anal. Chem. 2000, 72, 1119-1126.

Schoonheydt, R. A.; Vandame, L. J.; Jacobs, P. A.; Uytterhoeven, J. B. Chemical, Surface and Catalytic Properties of Nonstoichiometrically Exchanged Zeolites. J. Catal. 1976, 43, 292-303.

Scott, D. S.; Lee, W.; Papa, J. The Measurement of Transport Coefficients in Gas-solid Heterogeneous Reactions, Chem. Eng. Sci., 1974, 29, 2155-2167.

Sefton, M. V.; Gemmell, C. H.; Gorbet, M. B. What Really Blood Compatibility?. J. Biomater. Sci. Polym. Ed. 2000, 11, 1165-1182.

Segawa, K.; Chen, Y.; Kubsh, J. E.; Delgass, W. N.; Dumesic, J. A.; Hall, W. K. Infrared and Mössbauer Spectroscopic Studies of the Interaction of Nitric Oxide with Fe-Y Zeolite. J. Catal. 1982, 76, 112-132.

Seidel, H.; Bartko, P.; Kováč, G.; Pauliková, I.; Nagy, O. Effects of Haemoperfusion on Selected Indices of Blood Biochemistry in Sheep. Acta Vet. Brno. 1997, 66, 213-218.

Semmens, M. J.; Seyfarth, M. The Selectivity of Clinoptilolite for Certain Heavy Metals. In *Natural Zeolites: Occurrence, Properties, Use*; Sand, L. B.; Mumpton, F. A., Eds.; Pergamon Press: New York, 1978.

Semmens, M. J.; Martin, W. P. The Influence of Pretreatment of the Capacity and Selectivity of Clinoptilolite for Metal Ions. Water Res. 1988, 22, 537-542.

Shahwan, T.; Zünbül, B.; Tunusoğlu, Ö.; Eroğlu, A. E. AAS, XRPD, SEM/EDS, and FTIR Characterization of Zn^{2+} Retention by Calcite, Calcite–kaolinite, and Calcite–clinoptilolite Minerals. J. Colloid Interface Sci. 2005, 286, 471-478.

Shams, A.; Dehkordi, A. M.; Goodarznia, I. Desulfurization of Liquid-Phase Butane by Zeolite Molecular Sieve 13X in a Fixed Bed: Modeling, Simulation, and Comparison with Commercial-Scale Plant Data. Energ. Fuel. 2008, 22, 570-575.

Shank, J. L.; Silliker, J. H.; Harper, R. H. The Effect of Nitric Oxide on Bacteria. Appl. Microbiol. 1962, 10, 185-189.

Sheppard, A. O.; Starkey, H. G. The Effect of Exchanged Cations on the Thermal Behavior of Heulandite and Clinoptilolite. Int. Miner. Assoc. 1966, 155-158.

Silver, S. Bacterial Heavy Metal Detoxification and Resistance Systems. In *Biotechnology and Environmental Science: Molecular Approaches*; Mongkolsuk, S., Lovett, P. S., Trempy, J. E., Eds.; Plenum Press: New York, 1992.

Simón-Carballo, R. S.; Rodriquez-Fuentes, G.; Urbina, C.; Fleitas, A. Study of the Reaction of a Ca-clinoptilolite and Human Bile. In *Studies in Surface Science and Catalysis*, Elsevier Science: 2001, Vol. 135, 5268-5275.

Siney, L.; Lewis, M. J. Endothelium-derived Relaxing Factor Inhibits Platelet Adhesion to Cultured Porcine Endocardial Endothelium. Eur. J. Pharmacol. 1992, 229, 223-236.

Sing, K. S. W.; Williams, R. T. Review: The Use of Molecular Probes for the Characterization of Nanoporous Adsorbents. Part. Part. Syst. Char. 2004, 21, 71-79.

Sing, K. S. W.; Everett, D. H.; Haul, R. A. W.; Moscou, L.; Pierotti, R. A.; Rouquerol, J.; Siemieniewska, T. Reporting Physisorption Data for Gas/Solid Systems with Special Reference to the Determination of Surface Area and Porosity, Recommendations. Pure Appl. Chem. 1985, 57, 603-619.

Sneddon, J. M.; Vane, J. R. Endothelium-derived Relaxing Factor Reduces Platelet Adhesion to Bovine Endothelial Cells. PNAS. 1988, 85, 2800-2804.

Sprynskyy, M.; Buszewski, B.; Terzyk, A. P.; Namiésnik, J. Study of the Selection Mechanism of Heavy Metal (Pb^{2+}, Cu^{2+}, Ni^{2+}, and Cd^{2+}) Adsorption on Clinoptilolite.J. Colloid Interface Sci. 2006, 304, 21-28.

Stamler, J. S.; Lamas, S.; Fang, F. C. Nitrosylation: the Prototypic Redox-based Signaling Mechanism. Cell. 2001, 106, 675-683.

Stoeckli, F. The Gas-Solid Interface Calculations of Adsorption Potentials in Slot-like Pores of Molecular Dimensions. Helv. Chim. Acta. 1974, 57, 2195-2199.

Storck, S.; Bretinger, H.; Maier, W. F. Characterization of Micro- and Mesoporous Solids by Physisorption Methods and Pore-size Analysis. Appl. Catal. A. 1998, 174, 137-146.

Stuart, H. A. *Die Struktur des Freien Moleküls*, Vol. 1, Springer: Berlin, 1952.

Stumm, W.; Morgan, J. J. *Aquatic Chemistry: Chemical Equilibria and Rates in Natural Waters*, 3rd ed.; Wiley: New York, 1996.

Stylianou, M. A.; Inglezakis, V. J.; Moustakas, K. G.; Malamis, S. Ph.; Loizidou, M. D. Removal of Cu(II) in Fixed Bed and Batch Reactors Using Natural Zeolite and Exfoliated Vermiculite as Adsorbents. Desalination. 2007, 215, 133-142.

Sundaresan, B. B.; Harding, C. I.; May, F. P.; Hendrickson, E. R. Adsorption of Nitrogen Oxides from Waste Gas. Environ. Sci. Technol. 1967, 1, 151-156.

Suzuki, M. *Adsorption Engineering*, Elsevier: Amsterdam, 1990.

Suzuki, M.; Smith, J. M. Axial Dispersion in Beds of Small Particles. Chem. Eng. J. 1972, 3, 256-264.

Szanyi, J.; Kwak, J. H.; Moline, R. A.; Peden, C. H. F. The Adsorption of NO_2 and the $NO+O_2$ Reaction on Na-Y, FAU: an in Situ FTIR Investigation. PCCP. 2003, 5, 4045-4051.

Tabata, T.; Ohtsuka, H.; Sabatino, L. M. F.; Bellussi, G. Selective Catalytic Reduction of NOx by Propane on Co-loaded Zeolites. Microporous Mesoporous Mater. 1998, 21, 517-524.

Top, A.; Ülkü, S. Silver, Zinc, and Copper Exchange in a Na-clinoptilolite and Resulting Effect on Antibacterial Activity. Appl. Clay Sci. 2004, 27, 13-19.

Top, A. Cation Exchange (Ag^+, Zn^{2+}, Cu^{2+}) Behavior of Natural Zeolites. M.S. Dissertation, Izmir Institute of Technology, İzmir, Turkey, 2001.

Treybal, R. P. *Mass Transfer Operations*, 3rd Edition, McGraw-Hill, International Editions, 1980.

Trgo, M.; Perić, J. Interaction of the Zeolitic Tuff with Zn-containing Simulated Pollutant Solutions. J. Colloid Interface Sci. 2003, 260, 166-175.

Triebe, R. W.; Tezel, F. H. Adsorption of Nitrogen, Carbon Monoxide, Carbon Dioxide and Nitric Oxide on Molecular Sieves. Gas Sep. Purif. 1995, 9, 223-230.

Tsitsishvili, G. V.; Andronikashvili, T. G.; Kirov, G. N.; Filizova, L. D. *Natural Zeolites*, Ellis Horwood: New York, 1992.

Urban, J. C.; Gomezplata, A. Axial Dispersion Coefficients in Packed Beds at Low Reynolds Numbers. Can. J. Chem. Eng. 1969, 47, 353-359.

Ülkü, S. Heat and Mass Transfer in Adsorbent Beds. In *Convective Heat and Mass Transfer in Porous Media*; Kakaç, S., Kilkiş, B., Kulakci, F. A., Arınç, F., Eds.; NATO Series; Kluwer Academic Publishers: Dordrecht, 1991; p 695.

Valyon, J.; Hall, W. K. Studies of the Surface Species Formed from Nitric Oxide on Copper Zeolites. J. Phys. Chem. 1993, 97, 1204-1212.

Van Deemter, J.; Zuiderweg, F.; Klinkenber, A. Longitudinal Diffusion and Resistance to Mass Transfer as Causes of Nonideality in Chromatography. Chem. Eng. Sci. 1956, 5, 271-289.

Van Faassen, E.; Vanin, A. NO Trapping in Biological Systems with a Functionalized Zeolite Network. Nitric Oxide. 2006, 15, 233-240.

Vaughn, M. W.; Kuo, L.; Liao, J. C. Estimation of Nitric Oxide Production and Reaction Rates in Rissue by Use of a Mathematical Model. Am. J. Physiol. 1998, 274, H2163-2176.

Venero, A. F.; Chiou, J. N. Characterization of Zeolites by Gas Adsorption at Low Pressures. In *Microstructural Properties of Catalysis, Materials Research Society Symposium Proceedings*, Boston, 1988, vol. 111, p 235.

Viarengo, A. Biochemical Effects of Trace Metals. Mar. Pollut. Bull. 1985, 16, 153-158.

Wakao, N. Particle-to-fluid Transfer Coefficients and Fluid Diffusivities at Low Flow Rate in Packed Beds. Chem. Eng. Sci. 1976, 31, 1115-1122.

Wakao, N.; Funazkri, T. Effect of Fluid Dispersion Coefficients on Particle-to-fluid Mass Transfer Coefficients in Packed Beds. Chem. Eng. Sci. 1978, 33, 1375-1384.

Wakao, N.; Smith, J. M. Diffusion in Catalyst Pellets. Chem. Eng. Sci., 1962, 17, 825-834.

Wark, M.; Lutz, W.; Schultz-Ekloff, G.; Dyer, A. Quantitative Monitoring of Side Products During High Loading of Zeolites by Heavy Metals via pH Measurements. Zeolites. 1993, 13, 658-662.

Wheatley, P. S.; Butler, A. R.; Crane, M. S.; Fox, S.; Xiao, B.; Rossi, A. G.; Megson, I. L.; Morris, R. E. NO-releasing Zeolites and Their Antithrombotic Properties. J. Am. Chem. Soc. 2006, 128, 502-509.

Wicke, E. Bedeutung der Molekularen Diffusion für Chromatographische Verfahren. Ber. Bunsen Ges. 1973, 77, 160-171.

Wilkin, R. T.; Barnes, H. L. Thermodynamics of Hydration of Na- and K-clinoptilolite to 300 °C. Phys. Chem. Miner. 1999, 26, 468-476.

Williamson, J. E.; Bazaire, K. E.; Geankoplis, C. J. Liquid-phase mass transfer at low Reynolds numbers. Ind. Eng. Chem. Fund. 1963, 2, 126-129.

Wilson, E. J.; Geankoplis, C. J. Liquid mass transfer at very low Reynolds number in packed beds. Ind. Eng. Chem. Fund. 1966, 5, 9-14.

Wingenfelder, U.; Hansen, C.; Furrer, G.; Schulin, R. Rremoval of Heavy Metals from Mine Waters by Natural Zeolites. Environ. Sci. Technol. 2005, 39, 4606-4613.

Wink, D. A.; Mitchell, J. B. Chemical Biology of Nitric Oxide: Insights into Regulatory, Cytotoxic, and Cytoprotective Mechanisms of Nitric Oxide. Free Radical Biol. Med. 1998, 25, 434-456.

Witte, M. B.; Barbul, A. Role of Nitric Oxide in Wound Repair. Am. J. Surg. 2002, 183, 406-412.

Woods, R. M.; Gunter, M. E. Na- and Cs-exchange in a Clinoptilolite-Rich Rock: Analysis of the Outgoing Cations in Solution. Am. Mineral. 2001, 86, 424-430.

Xiao, B.; Wheatley, P. S.; Morris, R. E. The Adsorption, Storage and Release of Nitric Oxide Using Ion Exchanged Zeolites, in: Studies in Surface Science and Catalysis, Xu, R., Gao, Z., Chen, J., Yan, W. Eds.; Volume 170A, Elsevier, 2007.

Yang, R. T. *Gas Separation by Adsorption Processes*, Imperial College Press: UK, 1997.

Yang, P.; Stolz, J.; Armbruster, T.; Gunter, M. E. Na, K, Rb, and Cs Exchange in Heulandite Single Crystals: Diffusion Kinetics. Am. Mineral. 1997, 82, 517-525.

Young, D. M.; Crowell, A. D. *Physical Adsorption of Gases*, Butterworths: London, 1962.

Young, B. D.; van Vliet, B. M. The effect of surface roughness on fluid-to-particle mass transfer in a packed adsorber bed. Int. J. Heat Mass Transfer. 1988, 31, 27-34.

Yun, H. Y.; Dawson, V. L.; Dawson, T. M. Neurobiology of Nitric Oxide. Critical Reviews in Neurobiology. 1996, 10, 291-316.

Zhang, H.; Annich, G. M.; Miskulin, J.; Osterholzer, K.; Merz, S. I.; Bartlett, R. H.; Meyerhoff, M. E. Nitric Oxide Releasing Silicone Rubbers with Improved Blood Compatibility: Preparation, Characterization, and in Vivo Evaluation. Biomaterials. 2002, 23, 1485-1494.

Zhang, W.; Yahiro, H.; Mizuno, N.; Izumi, J.; Iwamoto, M. Removal of Nitrogen Monoxide on Copper Ion-exchanged Zeolites by Pressure Swing Adsorption. Langmuir. 1993, 9, 2331-2343

Zhang, W.; Yahiro, H.; Izumi, J.; Iwamoto, M. Reversible and Irreversible Adsorption of Nitrogen Monoxide on Cobalt Ion-exchanged ZSM-5 and Mordenite Zeolites at 273-523 K. J. Chem. Soc. Faraday Trans. 1995, 91, 767-771.

Zhang, W.; Jia, M.; Yu, J.; Wu, T.; Yahiro, H.; Iwamoto, M. Adsorption Properties of Nitrogen Monoxide on Silver Ion-Exchanged Zeolites. Chem. Mater. 1999, 11, 920-923.

Zamzow, M. J.; Eichbaum, B. R.; Sandgren, K. R.; Shanks, D. E. Removal of Heavy Metals and Other Cations from Wastewaters Using Zeolites. Sep. Sci. Technol. 1990, 25, 1555-1569.

APPENDIX A

ANALYSIS OF THE ADSORPTION SYSTEM

For the packed bed NO adsorption system investigated in this thesis, the following analysis were performed for the packed columns of zeolite particles with two different sizes (75-150 μm and 150-250 μm) and NO feed flow rates (20 and 50 ml/min). Table A.1 gives the Schmidt and Reynolds numbers calculated for the adsorption system under the experimental conditions of concern.

Table A.1. Reynolds and Schmidt numbers characterizing the adsorption system.

Particle diameter range, NO feed flow rate	Reynolds number, Re	Schmidt Number, Sc (NO-NO)	Schmidt Number, Sc (NO-He)
75-150 μm, 20 ml/min	0.087	0.620	0.173
150-250 μm, 20 ml/min	0.152		
75-150 μm, 50 ml/min	0.218		

The pressure drop across the column was calculated from the Ergun's equation as 0.91 and 0.27 mbar for the beds of the smaller and larger particles, respectively and accepted as negligible.

Initially, in the very short time period after NO is introduced to the bed, i. e., at the very start up of the adsorption, the NO molecules diffuse through the interparticle voids and intraparticle pores which are occupied by helium molecules. Since the fluid phase contains two gas species, there exist an external film on the particle through which the NO molecules diffuse. Thereafter, after prolonged period, the fluid phase in the interparticle void spaces and intraparticle pores will contain only NO molecules, so the film surrounding the particles will disappear. For this time period, NO molecules diffuse through NO molecules.

The mean free path of the diffusing NO molecules (λ) was calculated as 7.515 Å. For the calculation of the Knudsen diffusivity (D_K), the mean macropore radius ($\bar{r}$) was determined as 60 Å using the BET surface area obtained from the N_2 adsorption data at -196 ^oC. At the very start up, the NO molecules diffuse through the helium molecules. The collision diameter of the NO-He pair ($\sigma_{NO\text{-}He}$) at 303 K was calculated 3.022 Å using the σ value for NO and He given in the literature (Cussler, 1987). The energy of interaction ($\in_{12}$) was found as 34.54k_B though the application the Equation (3.10). Then $k_BT/\in_{12}$ was found as 8.832 and the corresponding Ω was read from the table as 0.7582 by interpolation (Cussler, 1987). Then, the molecular diffusion coefficient (D_m) for diffusion of NO in helium was calculated as 0.739 cm^2/sec.

After prolonged period following the introduction of NO to the bed, NO molecules diffuse through NO molecules. The collision diameter of the NO-NO pair at 303 K was calculated 3.492 Å using the σ value for NO given in the literature (Cussler, 1987). The energy of interaction ($\in_{12}$) was found as 116.7 k_B though the application the Equation (3.10). Then $k_BT/\in_{12}$ was found as 2.614 and the corresponding Ω was read from the table as 0.9871 by interpolation (Cussler, 1987). Then, the molecular diffusion coefficient (D_m) was determined. The calculated mean free path of the diffusing NO molecules was much smaller that the mean macropore radius. Therefore, collisions between the diffusing NO molecules occur more frequently than collisions between the diffusing NO molecules and the pore walls. This implies that the molecular diffusion is the dominant diffusion mechanism in the macropores. For the estimation of the effective macropore diffusivity, both Knudsen and molecular diffusion were taken into account.

Table A.2. Effective macropore diffusion coefficients calculated using the diffusibility values estimated from different correlations (cm^2/s)

		$\eta_p = \frac{\varepsilon_p}{\varepsilon_p + \chi(1-\varepsilon_p)}$	$\eta_p = \varepsilon_p^2$	
Diffusibility (η_p)		0.30	0.13	
Particle tortuosity factor (τ_p)		1.31	2.58	3
Effective macropore diffusivity (D_P)	NO-He	0.0053	0.0027	0.0023
	NO-NO	0.0050	0.0025	0.0022

In the calculation of the diffusibility (η_p), the particle shape factor was taken as 1.5 assuming that the zeolite particles are spherical. The particle tortuosity factor (τ_p) was calculated from Equation (3.13) using different correlations given for the diffusibility (Equations 3.14 and 3.15). An average value of 3 of the particle tortuosity was also used in the calculation to represent straight, randomly oriented, cylindrical pores with equal probability of all possible orientations (Ruthven, 1984). The tortuosity factor was reported as 3.3 for 5A zeolite (Suzuki, 1990). The calculated effective macropore diffusivities are summarized in Table A.2

There exist an external film surrounding the particles through which the NO molecules diffuse only at the very start up following the introduction of NO to the bed. The Sherwood number and external mass transfer coefficients (k_f) calculated from the empirical correlations given are presented in Table A.3 and A.4, respectively.

Table A.3. Sherwood numbers estimated using different correlations.

Particle diameter, NO flow rate	Kumar et al., 1977	Kataoka et al., 1972	Wilson and Geankoplis, 1966	Dwivedi and Upadhyay, 1977	Ohashi et al., 1981
75-150 μm, 20 ml/min	0.977	0.538	0.703	0.809	2.334
150-250 μm, 20 ml/min	1.056	0.633	0.812	0.909	2.417
75-150 μm, 50 ml/min	1.077	0.691	0.865	0.951	2.482

Table A.4. External fluid film mass transfer coefficients, k_f (cm/s).

Particle diameter, NO flow rate	Kumar et al., 1977	Kataoka et al., 1972	Wilson and Geankoplis, 1966	Dwivedi and Upadhyay, 1977	Ohashi et al., 1981
75-150 μm, 20 ml/min	66.25	36.52	47.68	54.85	158.29
150-250 μm, 20 ml/min	41.08	24.64	31.60	35.36	94.04
75-150 μm, 50 ml/min	73.07	46.88	58.70	64.51	168.32

As previously mentioned, the estimated *Sh* values below 2 may be attributed to the underestimation of axial dispersion for porous particles and the values higher than 2 can be explained by the invalidity of limiting single sphere boundary in the adsorbent bed (Ülkü, 1991). The discrepancies between the *Sh* values estimated from the different correlations can be also attributed to the differences in the chemical and physical characters of the adsorbents (including surface topography and roughness, particle shape, particle porosity) for which the correlations were developed and the zeolites used in this study (Ülkü, 1991; Roberts and Cornal, 1985; Yound and van Vliet, 1988). The crushed zeolite particles are assumed to be spherical with radii R_p. But in fact, the zeolite particles used in the present studies possessed rather irregular shapes ranging from angular to sub-rounded as illustrated in Figure A.1. The sphericity of crushed zeolite was reported as 0.65 (Inglezakis and Poulopoulos, 2006). This representative micrograph also gives qualitative information about the surface roughness of the particles. Cleavages, micro- and macrosteps, cracks which are actually mesopores and macropores, and kinks can be seen on the surface of the particles. No standardized criteria have been established for determining which correlation may be best for a given system, except for hydrodynamic conditions (*Re* and *Sc*). Therefore, the applicability of such correlations for a given situation must be verified.

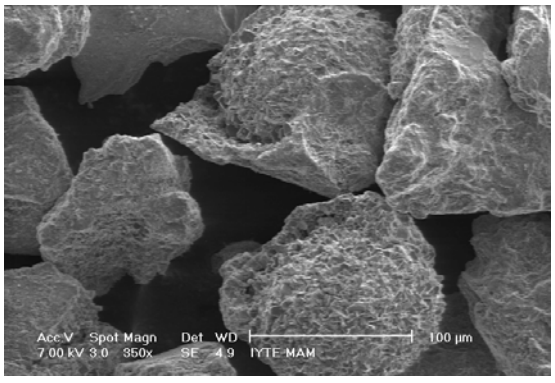

Figure A.1. SEM micrograph of the natural zeolite particles (75-150 μm) (×350).

The Biot numbers for the time period where there exist external film on the particles calculated are given in Table A.5. The particle tortuosity value of 3 was used in the calculation of the effective macropore diffusivities. These values of the Biot number which are much higher than 20 clearly show that the external mass transfer

resistance can be assumed to be negligible and the intraparticle diffusion controls the adsorption process.

Table A.5. Biot numbers for mass transfer, *Bi*.

Particle diameter, NO flow rate	Kumar et al., 1977	Kataoka et al., 1972	Wilson and Geankoplis, 1966	Dwivedi and Upadhyay, 1977	Ohashi et al., 1981
75-150 μm, 20 ml/min	133.61	73.65	96.15	110.63	319.25
150-250 μm, 20 ml/min	144.40	86.61	111.09	124.31	330.61
75-150 μm, 50 ml/min	147.37	94.55	118.39	130.11	339.46

Regarding the flow velocities and particle sizes of interest in the present study, the Reynolds numbers calculated were in the range of 0.087-0.218. Therefore, the dynamic term present in Equation (3.25) was not taken into account and thus the axial dispersion coefficient was assumed to be $D_L \approx \gamma_1 D_m$. Using the value of γ_1 calculated as 0.664-0.685 from Equation (3.27), D_L values were found as 0.491 cm^2/s and 0.137 cm^2/s for the short and long time periods after the introduction of NO to the bed, respectively.

Table A.6. Axial dispersion coefficient, D_L (cm^2/s) (initial).

Particle diameter, NO flow rate	$D_L = \gamma_1 D_m + \gamma_2 v d_p$ $\gamma_1=0.45+0.55\varepsilon$ $\gamma_2=0.5$	$D_L \approx \gamma_1 D_m$ $\gamma_1=0.45+0.55\varepsilon$	Hsu and Haynes, 1981	Edwards and Richardson, 1968 $\gamma_1=0.73$, $\beta=13$, $Pe_\infty=2$	Wakao, 1976	Suzuki and Smith, 1972
75-150 μm, 20 ml/min	0.505	0.491	0.626	0.540	38.061	0.222
150-250 μm, 20 ml/min	0.521	0.497	0.607	0.540	36.616	0.232
75-150 μm, 50 ml/min	0.539	0.506	0.581	0.540	34.653	0.247

Table A.7. Axial dispersion coefficient, D_L (cm^2/s) (later period).

Particle diameter, NO flow rate	$D_L = \gamma_1 D_m + \gamma_2 v d_p$ γ_1=0.45+0.55ε γ_2=0.5	$D_L \approx \gamma_1 D_m$ γ_1=0.45+0.55ε	Hsu and Haynes, 1981	Edwards and Richardson, 1968 γ_1=0.73, β=13, Pe_∞=2	Wakao, 1976	Suzuki and Smith, 1972
75-150 μm, 20 ml/min	0.152	0.137	0.182	0.151	10.650	0.063
150-250 μm, 20 ml/min	0.163	0.139	0.190	0.151	10.253	0.066
75-150 μm, 50 ml/min	0.174	0.142	0.199	0.152	9.710	0.070

The particle diameters of the zeolite particles of interest in the present thesis and the corresponding Reynolds numbers are nearly within the range of interest in the study by Suzuki and Smith (1972), then the correlation given Equations (3.33) and (3.34) was applied for the estimation of the axial dispersion coefficient. Assuming that the zeolite particle is spherical and for the bed voidage of 0.386, δ was calculated as 0.295 from Equation (3.34). Then the axial dispersion coefficient was calculated as 0.063 cm^2/s from Equation (3.33). The contribution from the particle phase to the axial dispersion was found to be 6.6 % of that from the gas phase. Regarding the validity ranges of the correlations reported for estimation of the axial dispersion coefficient, the axial dispersion coefficients were also calculated using the correlation by Equation (3.40) (Hsu and Haynes, 1981). The estimated axial dispersion coefficients initially at the very start up and for the later periods of the adsorption are given in Table A.6 and A.7, respectively.

The calculated Péclet numbers for the bed for the initial period of the adsorption, given in Table A.8, were lower than 100 designated that the axial dispersion effect cannot be neglected according to the criterion given (Levenspiel, 1972). On the other hand, for the later periods of the adsorption the calculated bed Péclet numbers (given in Table A.9) indicated that it is a reasonable approximation to neglect the axial dispersion. It was stated that the axial dispersion coefficients are be very sensitive to packing geometry and vary from one study to another (Hashimoto and Smith, 1974).

Table A.8. Péclet numbers for the column (initial).

Particle diameter, NO flow rate	$D_L = \gamma_1 D_m + \gamma_2 v d_p$ $\gamma_1=0.45+0.55\varepsilon$ $\gamma_2=0.5$	$D_L \approx \gamma_1 D_m$ $\gamma_1=0.45+0.55\varepsilon$	Hsu and Haynes, 1981	Edwards and Richardson, 1968 $\gamma_1=0.73$, $\beta=13$, $Pe_\infty=2$	Wakao, 1976	Suzuki and Smith, 1972
75-150 μm, 20 ml/min	21.39	22.01	38.03	44.76	0.28	48.72
150-250 μm, 20 ml/min	19.94	20.90	31.06	35.82	0.28	44.82
75-150 μm, 50 ml/min	45.59	48.53	67.48	75.19	0.71	99.48

Table A.9. Péclet numbers for the column (later period).

Particle diameter, NO flow rate	$D_L = \gamma_1 D_m + \gamma_2 v d_p$ $\gamma_1=0.45+0.55\varepsilon$ $\gamma_2=0.5$	$D_L \approx \gamma_1 D_m$ $\gamma_1=0.45+0.55\varepsilon$	Hsu and Haynes, 1981	Edwards and Richardson, 1968 $\gamma_1=0.73$, $\beta=13$, $Pe_\infty=2$	Wakao, 1976	Suzuki and Smith, 1972
75-150 μm, 20 ml/min	71.28	78.74	114.67	159.14	1.01	171.31
150-250 μm, 20 ml/min	63.73	74.78	81.94	126.63	1.01	157.77
75-150 μm, 50 ml/min	141.05	173.60	157.83	264.42	2.53	350.65

This approximation was confirmed by calculating the L/d_{column}, d_{column}/d_p and L/d_p as given in Table A.10, regarding the criteria given in Equations (3.42), (3.43) and (3.44), respectively. Furthermore, comparing the value of D_L with the other mass transfer coefficients, it was justified that the contribution of axial dispersion to the overall mass transfer is quite small.

Table A.10. Geometrical criteria to avoid maldistribution of the flow.

Particle diameter, NO flow rate	L/d_{column}	d_{column}/d_p	L/d_p
75-150 μm, 20 ml/min	7.7	48.9	376.2
150-250 μm, 20 ml/min		28.1	215.8

The system on which the NO adsorption kinetics is studied is a nontrace system since the step change in concentration is large. For these systems, the adsorbate molecules are present at high concentration levels and cause a significant variation in the fluid velocity across the mass transfer zone. The system can be assumed as isothermal because a small amount of adsorbent was used in the column. Furthermore, in a dynamic adsorption system, even the heat of adsorption is high, the continuous flow through the column will purge the heat immediately from the adsorbent. Also, the column was enclosed in a temperature-controlled oven of the gas chromatograph during adsorption and desorption runs.

APPENDIX B

CHANGES IN COLOR OF ZEOLITES

The changes in colors of the zeolites observed upon metal sorption, NO loading and thermal treatment at 400 ^{o}C after NO loading can be seen in Figure B.1.

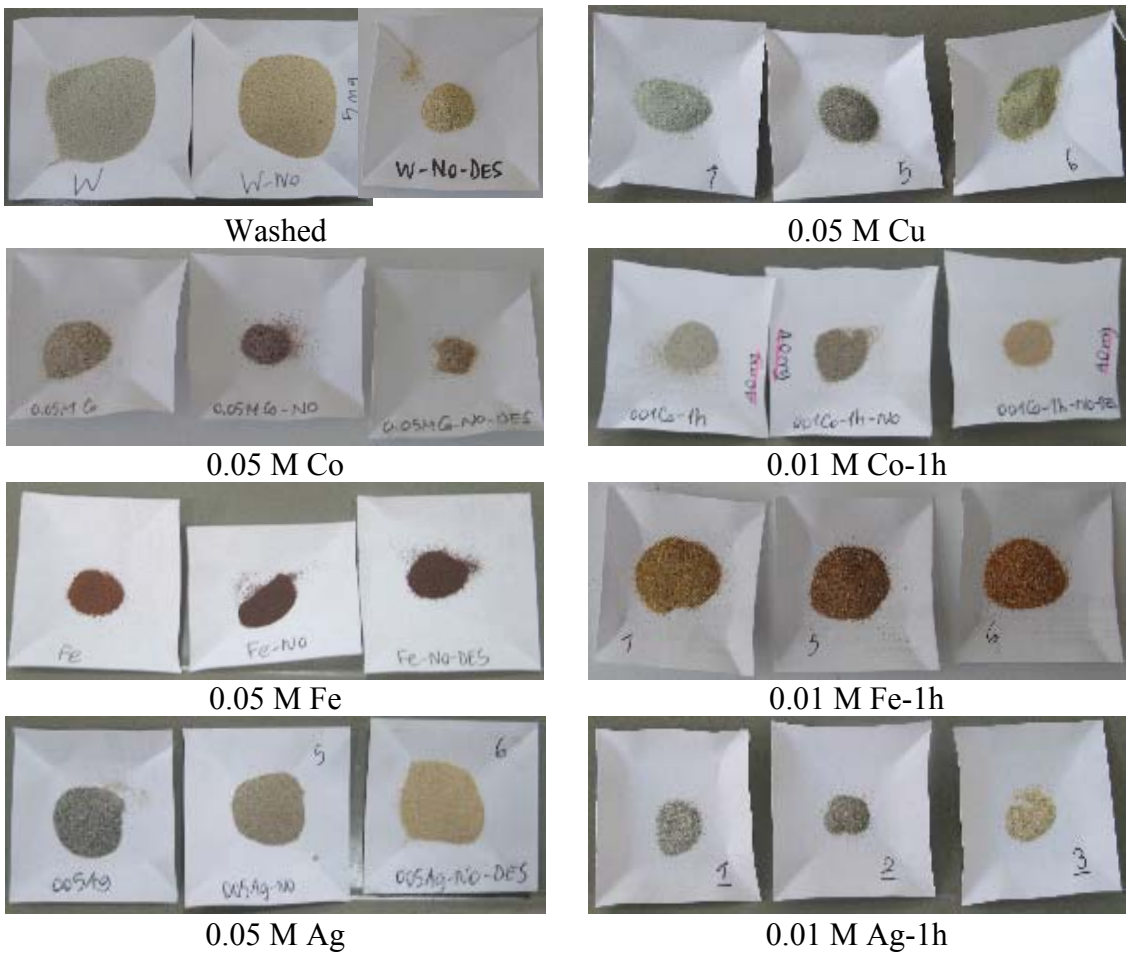

Washed | 0.05 M Cu

0.05 M Co | 0.01 M Co-1h

0.05 M Fe | 0.01 M Fe-1h

0.05 M Ag | 0.01 M Ag-1h

Figure B.1. Changes in color of the zeolites upon metal sorption, NO loading and thermal treatment after NO loading (from left to right).